Promising Novel Therapeutic Strategies for Cisplatin Resistant Bladder Cancer

Inaugural dissertation

for the attainment of the title of doctor
in the Faculty of Mathematics and Natural Sciences
at the Heinrich Heine University Düsseldorf

presented by

Chenyin Wang

from Shandong, P. R. China

Düsseldorf, November 2019

from the Institute for Pharmaceutical and Medicinal Chemistry at the Heinrich Heine University Düsseldorf

Published by permission of the
Faculty of Mathematics and Natural Sciences at
Heinrich Heine University Düsseldorf

Supervisor: Prof. Dr. Matthias U. Kassack
Co-supervisor: Prof. Dr. Dres. h.c. Peter Proksch

Date of the oral examination: 18.12.2019

Erklärung

Hiermit erkläre ich ehrenwörtlich, dass ich die vorliegende Dissertation mit dem Titel „Promising Novel Therapeutic Strategies for Cisplatin Resistant Bladder Cancer“ selbst angefertigt habe. Außer den angegebenen Quellen und Hilfsmitteln wurden keine weiteren verwendet. Diese Dissertation wurde weder in gleicher noch in abgewandelter Form in einem anderen Prüfungsverfahren vorgelegt. Weiterhin erkläre ich, dass ich früher weder akademische Grade erworben habe, noch dies versucht habe.

Düsseldorf, November 13, 2019

Chenyin Wang

献给我亲爱的爸爸妈妈

以及

我爱的人

Contents

Contents

Abstract

Bladder cancer is the most common malignancy of the urinary tract. Depending on the location of the tumors grown into the bladder, it can be divided into superficial and muscle-invasive bladder cancer. Although only 30% of patients have muscle-invasive bladder cancer as initial diagnosis, advanced disease occurs in another 15-30% of patients with a high grade of superficial carcinomas and leads to the development of life-threatening muscle-invasive tumors or metastatic disease. Platinum-based combination chemotherapy is the first-line treatment for advanced bladder cancer. However, the acquisition of cisplatin resistance has been frequently observed in cisplatin treated patients resulting in relapse. Furthermore, cancers including bladder cancer show aberrant epigenetics: increased promotor CpG island methylation and increased histone deacetylase (HDAC) expression both leading to transcriptional silencing, in particular of tumor suppressor and proapoptotic genes. Thus, the aim of this thesis was to establish a cellular model of cisplatin-resistant bladder cancer and to use this *in vitro* model for the discovery of novel therapeutic approaches against bladder cancer, in particular against chemoresistant cancer. Initially, the cisplatin-resistant bladder cancer cell line J82CisR was established from the sensitive cell line J82 by intermittent treatment with cisplatin. Following studies were then undertaken at the bladder cancer cell line J82, J82CisR, and RT-112.

The first part of the thesis deals with combination treatments of the DNA methyltransferase inhibitor (DNMTi) decitabine and the class I HDAC inhibitor (HDACi) entinostat. Whereas decitabine and entinostat or combinations of the two could only partially reverse cisplatin resistance in J82CisR, the combination of decitabine and entinostat was highly synergistic in reducing the viability of bladder cancer cells by inducing cell cycle arrest and caspase 3/7-mediated apoptosis. Mechanistically, expression levels of the transcription factor FoxO1 were up-regulated in all three bladder cancer cell lines upon treatment with decitabine or entinostat or a combination of both. Furthermore, a significant increase in the expression of the pro-apoptotic protein Bim and the cell cycle regulator p21, both downstream targets of FoxO1, was observed upon epigenetic treatment. Importantly, the expression of Bim and p21 was reduced by addition of the FoxO1 inhibitor AS1842856 confirming the essential role of FoxO1 after epigenetic treatment.

In the second part of the thesis, nature-derived compounds were investigated for their cytotoxic potential in bladder cancer, particularly in chemoresistant cancers. The tetrahydroxanthone dimer phomoxanthone A (PXA) isolated from the endophytic fungus *Phomopsis longicolla* exhibited potent anti-cancer activity with low micromolar IC_{50} values in sensitive and cisplatin-resistant cell lines by caspase 3/7-mediated induction of apoptosis. Initially, PXA induces a fast depolarization of the mitochondrial membrane potential which may be due to degradation of the proton gradient along the inner mitochondrial membrane by acting as proton shuttle as computational studies suggest. A number of further natural products were investigated for their anticancer activity as e.g., two indole diterpenoids isolated from *Zingiber officinale* or a diketopiperazine isolated from a mangrove-derived endophytic fungus *Penicillium brocae* MA-231. These compounds showed potent cytotoxicity with sub-μM IC_{50} values.

In conclusion, this thesis first, suggests the use of epigenetic modulation (DNMT- and HDAC-inhibitors) for the management of chemoresistant bladder cancer cells and second, has investigated nature-derived compounds with promising cytostatic activity, especially in resistant cancer cells, in particular phomoxanthone A targeting the mitochondrial potential.

1 Introduction

1.1 Bladder Cancer

Bladder cancer comprises several types of cancers growing from the wall of the urinary bladder and is the 4th most common malignancy in men and the 11th most in women [1]. To date, urothelial carcinoma is the most common type of bladder cancer, which accounts for over 90% cases of bladder cancer. Other types of bladder cancers, including squamous cell carcinoma, adenocarcinoma, small cell carcinoma, account for less than 10% among all of this disease [2]. The stage of bladder cancer is defined by how far they have spread into the bladder wall. Depending on the location of cancers grown into the bladder, it is described as non-muscle invasive bladder cancer (NMIBC) or superficial (cancers only can be found in the inner layer of the bladder wall) and muscle invasive bladder cancer (MIBC, cancers have grown into deeper layers of the bladder wall) [3]. The stages can be specified to T0/T1 (NMIBC) and T2/T3/T4 (MIBC). Although only 30% of newly diagnosed bladder cancer cases are advanced, another 15-30% of high-grade superficial bladder cancers develop to muscle invasive carcinomas with poor long-term survival rate [4].

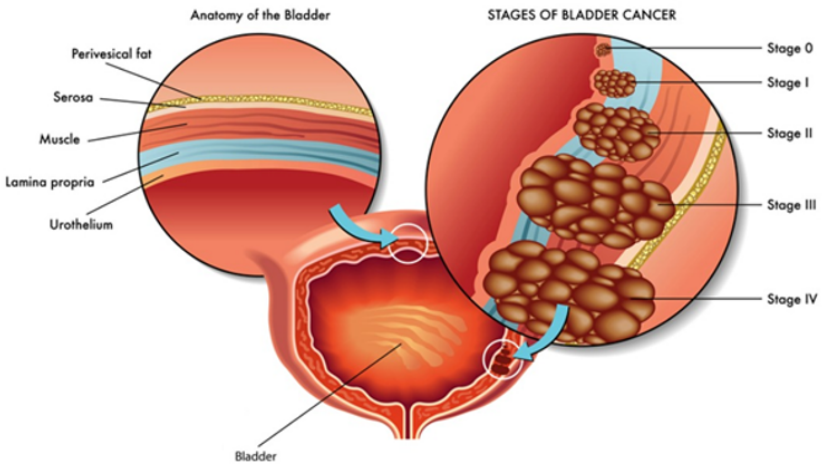

Figure 1. Anatomy of the bladder and stages of bladder cancer

1.1.1 Treatment Options of Bladder Cancer

The treatment of bladder cancer depends on the stage of the disease. A complete

transurethral resection (TUR) is considered the gold standard of the management of NMIBC, with the aim of reducing the risk of cancer progress. NMIBC patients with high risk of recurrence and progression after TUR are recommended to receive adjuvant therapy [3]. Sylvester and colleagues have shown that the risk of progression of superficial bladder cancer to life-threatening MIBC is reduced when bacillus Calmette-Guerin is applied [5]. For patients with MIBC, cisplatin-based neoadjuvant chemotherapy (aiming to reduce the tumor bulk) followed by radical cystectomy is a standard care to prevent metastatic spread and even death [4]. The combined clinical data have shown the evidence that cisplatin-based combination chemotherapy plus radical cystectomy shows beneficial effect in survival rate compared with radical cystectomy alone [6, 7]. As first-line chemotherapy of bladder cancer, the regimens of methotrexate, vinblastine, doxorubicin and cisplatin (MVAC) or gemcitabine and cisplatin (GC) are approved drug combination strategies. The clinical study conducted by von der Maase and colleagues revealed a longer median overall survival in MVAC than in GC group (MVAC, 15.2 months versus GC, 14.0 months). However, GC is less toxic than MVAC, with better tolerance and reduced frequency of adverse effects [8]. Therefore, a number of factors, such as age and past medical history, should be considered to make the treatment decision.

Beyond the conventional transurethral resection and chemotherapy, immune checkpoint inhibitors have been introduced to the treatment of bladder cancer recently. Up to now, several immune checkpoint inhibitors including anti-PD-1 antibodies (nivolumab and pembrolizumab) and anti-PD-L1 antibodies (atezolizumab and durvalumab, avelumab) have been approved by FDA for bladder cancer treatment [9]. A large number of clinical trials are ongoing to evaluate effect of the immune checkpoint inhibitors alone or combined with other treatment in bladder cancer patients [10]. A substantial beneficial effect has been observed in these clinical trials. For instance, 46.4% of patients with refractory tumors after standard platinum-based treatment, showed PD-L1 positive tumors and responded to durvalumab [11]. Additionally, the anti-PD-1 antibody nivolumab was reported to show a 19.6% overall objective response regardless of PD-1 expression in patients with progressed disease after receiving platinum-based chemotherapy [12]. The exciting clinical data of immune checkpoint inhibitors indicate the potential revolution of the standard bladder cancer management in future.

1.2 Cisplatin

1.2.1 Cisplatin in Cancer

Cisplatin [cis-diamminedichloroplatinum (II)] is one of the most widely used chemotherapy drugs for cancer. The history of cisplatin initiates in 1845 by an Italian chemist Michele Peyrone who synthesized it for the first time. However, the inhibition of cell proliferation effect of cisplatin was accidentally discovered by Barnett Rosenberg in 1965, which triggered the study of cisplatin developed as anti-cancer agent eventually [13]. The successful results of clinical trials led the approval of cisplatin for testicular cancer treatment by FDA in 1978 [14]. In the past four decades, cisplatin has been approved for the treatment of a wide range of solid tumors, such as ovarian cancer, bladder cancer, and breast cancer. Moreover, cisplatin-based chemotherapy has become the backbone of drug combination treatments in cancer [15].

Cisplatin induces the cytotoxicity by targeting the DNA directly. Once it enters the cell, the drug is activated when the chloride atoms on cisplatin are displaced by water molecules due to the lower chloride concentration (2-30 mM) within the cell compared to the outside of the cell (100 mM). The positively charged aquated product reacts easily with any nucleophile including the nitrogen donor atoms on nucleic acids [16]. The interaction between aquated cisplatin with N7-positions of purine bases in DNA leads to the formation of DNA adducts and thus induces interstrand and intrastrand crosslinks **(Figure 2)**. It is generally agreed that, the intrastrand DNA adduct is the most prevalent nuclear lesion caused by cisplatin since 1,2-intrastrand ApG and GpG crosslinks account for 85-90% of total lesions [17]. These DNA damages induced by cisplatin lead to accumulation of DNA damage recognition proteins and regulate pathways and finally promote apoptosis and cell cycle arrest [18].

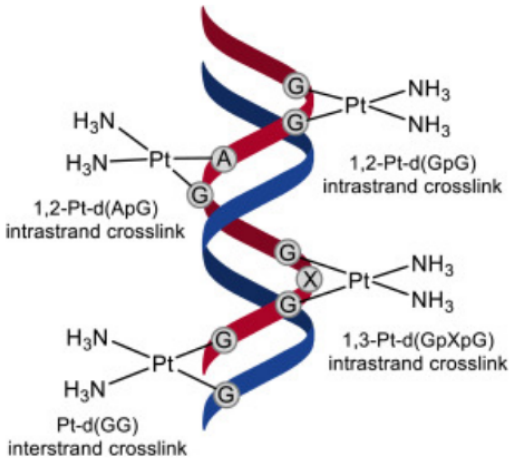

Figure 2. Different types of cisplatin-DNA adducts [19]

1.2.2 Cisplatin Resistance

Although most patients initially have good response to cisplatin, the development of drug resistance, either intrinsic or acquired, attenuates its effectiveness and eventually causes cancer relapse. The development of cisplatin resistance is a multifactorial process with alterations of many proteins and pathways. It is generally accepted that three molecular mechanisms contribute to the reduced sensitivity of tumors to cisplatin. These mechanisms are (**Figure 3**): increased DNA repair, reduced drug accumulation, cytosolic inactivation of cisplatin, and defects in the apoptotic signaling pathway [20, 21].

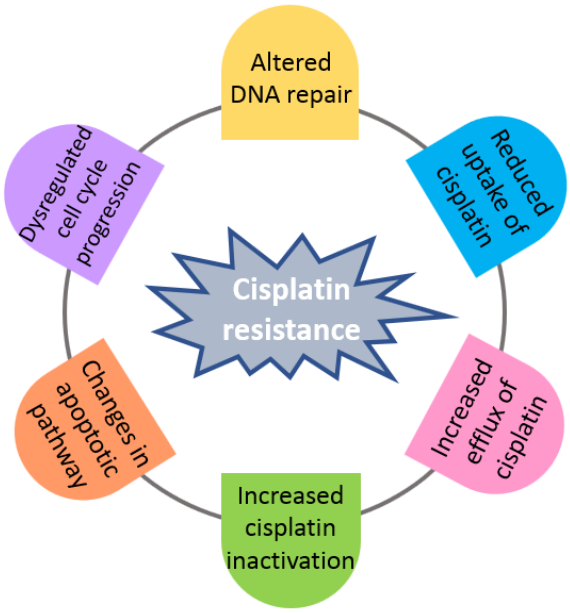

Figure 3. Mechanisms related to cisplatin resistance

a. alteration in DNA repair

As introduced above, the cytotoxic effect of cisplatin is induced through the formation of DNA-platinum adducts and followed by DNA damage. Several mechanisms, such as nucleotide excision repair (NER), base excision repair (BER), and mismatch repair (MMR), have been identified as responsible for the repair of DNA damage [22]. If the DNA repair pathways are increased, less DNA damage induced by cisplatin occurs, and drug resistance inevitably develops.

A number of studies have demonstrated the pivotal role of NER (**Figure 4**) in repair of DNA damage particularly induced by DNA-platinum adducts. More than 30 proteins are involved in NER pathway. The repair processes include detection of the DNA-platinum adducts, verification and buildup of the pre-incision complex, DNA relaxation, incision and removal of damage site, and finally filling the DNA gap. The level of excision repair cross-complementation group 1 (ERCC1), functioning as a scissor to excise the DNA damage site, has been found negatively correlating with cisplatin sensitivity. Up-regulated ERCC1 is associated with increased DNA-platinum removal and consequently reduced efficacy of cisplatin. Conversely, a survival benefit was found in patients with lower levels of ERCC1 [23]. The correlation of high ERCC1 levels and increased cisplatin resistance was firstly reported in ovarian cancer and has been observed in other cancer types, such as cervical, NSCLC, head and neck squamous carcinoma, and bladder cancer as well. and so on [20]. Bellmunt and colleagues have demonstrated low ERCC1 mRNA expression levels in advanced bladder cancer patients correlated with longer median survival than those with high ERCC1 levels (25.4 versus 15.4 months) [24].

Another DNA repair related resistance mechanism is BRCA1/2 mutations. BRCA1/2 play an important role in homologous recombination, a machinery to repair DNA double-strand breaks. Thus, BRCA1/2 deficient cancers tend to be more sensitive to cross-linking agents like cisplatin than BRCA1/2-proficient cells. In ovarian cancers, for instance, the resistance towards cisplatin is consistent with expression status of BRCA2 protein. The ovarian cancer cells with undetectable BRCA2 are responsive to cisplatin while acquired resistance occurred when the BRCA2 protein is positively detected [25]. Furthermore, studies have illustrated that the restoration of BRCA1/2 wild-type function is driven by secondary mutations and eventually

results in the development of cisplatin resistance [21, 26, 27].

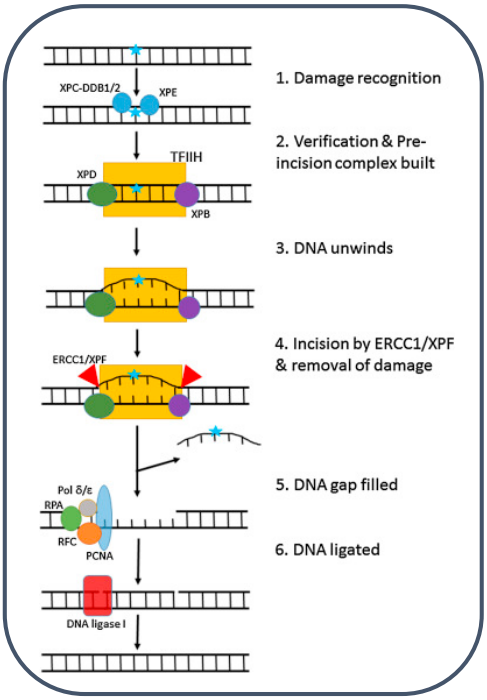

Figure 4. Nucleotide excision repair (NER) pathway [20]

b. reduced cellular accumulation

Cisplatin can cross the cell membrane via both passive diffusion and active transport. Either decreased uptake or increased efflux of cisplatin may contribute to cisplatin resistance due to reduced intracellular drug concentration. CTR1 (copper transporter protein 1) is one of the major proteins controlling cisplatin uptake. Many studies have provided evidences on the positive correlation between CTR1 levels of the cell and its sensitivity to cisplatin. In a CTR1 deleted mouse model, decreased accumulation of cisplatin and increased cisplatin resistance was observed compared to their wild-type counterparts [28]. In clinic, high expression level of CTR1 was associated with better prognosis in ovarian and lung cancer patients treated with cisplatin [29, 30].

As introduced earlier, increased efflux of cisplatin relates to decreased accumulation and consequently promotes cisplatin resistance. MRP2 (multidrug resistance-associated protein 2), also called cMOAT (canalicular multispecific organic anion transporter), has been found overexpressed in many cisplatin resistant cell lines [31]. MRP2 belongs to the family of ABC (ATP-binding cassette) transporters which mediates the ATP-dependent efflux of cisplatin-

glutathione conjugates. A correlation between MRP2 expression and cisplatin resistance has been found in hepatocellular, colorectal, and esophageal cancers. However, no correlation between MRP2 expression level and cisplatin response was found in ovarian and lung cancer [32, 33].

c. increased inactivation of cisplatin

In the cytoplasm, glutathione (GSH) serves as antioxidant by reducing sulfhydryl groups to keep the redox environment. The strong electrophilic property of aquated cisplatin is prone to bind GSH and other cysteine-rich proteins. As a consequence, cisplatin-GSH conjugates, catalyzed by GSTs (Glutathione-S-transferases), are pumped out by MRP transporters, resulting in the reduction of cisplatin binding to DNA [20]. The association between increased cisplatin resistance and increased expression of GSTP1, a member of the GST family, has been demonstrated in ovarian, head and neck, and lung cancers [34]. In addition, MTs (metallothioneins) inactivate cisplatin utilizing its ability to bind heavy metal ions. Up-regulated MTs have been observed in a number of cell lines including lung and bladder cancer cells which are resistant to cisplatin [35, 36].

1.3 Epigenetic Modifications and Cancer

The term “epigenetics” refers to heritable changes in gene expressions that are independent of alterations in the DNA sequence [37]. Over a long period of time, the accumulation of genetic mutations was thought to be the major cause of cancer. However, in recent decades, many studies have focused on epigenetic alterations, such as DNA methylation and histone deacetylation, and elucidated its critical role played in cancer initiation and progression.

1.3.1 DNA Methylation and Cancer

Aberrant patterns of DNA methylation, a methyl group covalently added to the 5’ carbon of cytosine resulting in 5-methylcytosine, 5mC, is one of the most frequently observed epigenetic events in cancer (**Figure 5**).

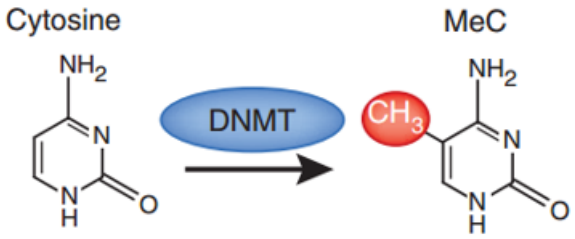

Figure 5. DNMT mediated methylation of the 5-position (C5) of the cytosine ring

The abnormal distribution of 5mC in cancer can be divided into three groups. The first mechanism is known as the global DNA demethylation or hypomethylation. In the human genome, 80% of the cytosine-guanine dinucleotides (CpGs) are methylated. This hypermethylation in genomic DNA is crucial for maintaining the genomic stability. In cancers, conversely, overall genomic hypomethylation disrupts normal transcription and even influences some posttranscriptional processes, finally facilitating tumorigenesis (**Figure 6**) [38]. Secondly, compared with non-tumor cells, DNA hypermethylation is prevalent in CpG islands in promoter regions in a variety of cancer types. In normal cells, the low methylation status in CpG islands in promoter regions correlates with more open chromatin structure thereby actively regulating transcription. If hypermethylation occurs in the promoter regions of tumor suppressor genes, the nucleosomes become condensed resulting in repressed transcription [39]. The last mechanism by which altered DNA methylation patterns can lead to cancer is mutations of 5mC-containing sequences. The methylated cytosine is prone to be deaminated and thus form the deamination product thymine [40].

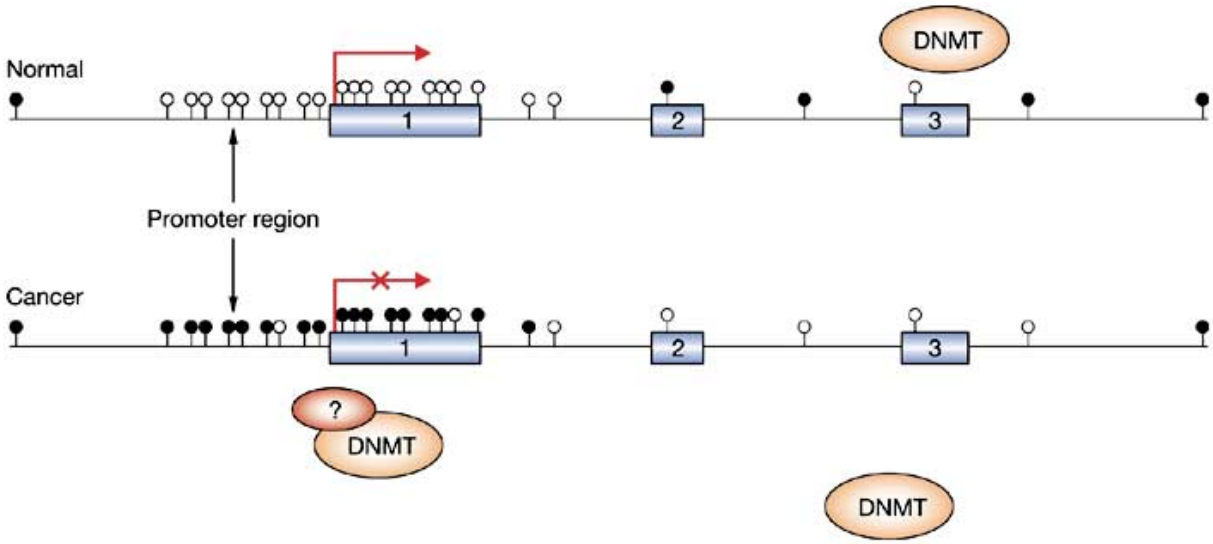

Figure 6. DNA methylation in normal and cancer cells [39]

Furthermore, many studies have shown that DNA hypermethylation-induced gene silencing occurs during long-term exposure to chemotherapeutic agents. For example, in the adriamycin-resistant breast cancer cell line MCF-7, increased DNA methyltransferase activity and global DNA hypermethylation was found when compared with its parental cell line MCF-7. The sensitivity of adriamycin was restored by the treatment of the DNA methylation inhibitor hydralazine [41].

1.3.2 DNA Methyltransferases and Inhibitors

Given that DNA hypermethylation in CpG islands of promoter regions is a common event and essential to tumorigenesis, reversing or inhibiting the aberrant DNA hypermethylation is a therapeutic strategy for cancer. Three DNA methyltransferases (DNMTs), DNMT1, DNMT3a, and DNMT3b, are found in mammalian cells and catalyze the methylation on cytosine. The functional differences among the DNMTs are the responsibilities to either maintain (DNMT1) or establish (DNMT 3a and 3b) DNA methylation [42]. Several DNMT inhibitors, such as the cytosine analogue azacytidine and its deoxy derivative decitabine (**Figure 7**), were developed and some of them have already been approved for cancer treatment. Azacitidine is approved for the treatment of myelodysplastic syndromes and decitabine is approved for acute myeloid leukemia. The mode of action of azacytidine and decitabine is known as follows: both compounds are incorporated into DNA (azacitidine also into RNA) during replication and then bind covalently to the catalytic site of DNMTs [43].

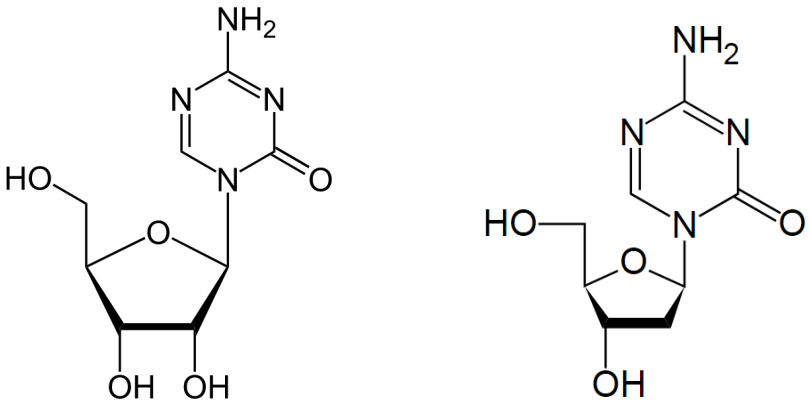

Figure 7. Structure of Azacitidine (Left) and Decitabine (Right)

1.4 Histone Modifications

1.4.1 Histone Deacetylation and Cancer

As the fundamental component of nucleosomes, modifications on histones play a major role in regulating gene expression. Histone acetylation is one of the key molecular events among these modifications. Acetylation of lysine residues of histones is mediated by histone acetyltransferases (HATs) and associated with a relaxed conformation of chromatin and promotes the recruitment of proteins and protein complexes responsible for activating transcription (**Figure 8**). The histone deacetylases (HDACs), on the other hand, are responsible for removing the acetyl groups from lysine residues to maintain a repressive chromatin environment [44]. In general, two mechanisms account for the regulation of transcription achieved by histone acetylation. First, acetylation removes the positive charge on lysine and thereby reduces its interaction with negatively charged DNA phosphate groups, eventually establishing a relaxed chromatin structure [45]. Second, hyperacetylation of histones facilitates the recognition and interaction of bromodomain (BRD)-containing proteins [46]. Binding of BRD-containing proteins with acetylated lysine residues can affect the gene transcription by initiating transcription elongation (BRD4) [47]. However, in cancers, lack or even loss of histone lysine acetylation induced by HDACs has been frequently found and causes a tightly compacted chromatin structure and gene silencing [48]. The dysregulation of the HDACs has been observed in many cancer types including bladder cancer [49, 50]. A study analyzing the mRNA expression level of HDACs in 18 bladder cancer cell lines revealed frequent upregulation of class I HDACs [49]. HDACs comprise separate groups which include class I (HDAC1, 2, 3, and 8), class IIa (HDAC4, 5, 7, and 9), class IIb (HDAC6 and 10), and class IV (HDAC11) [51].

1.4.2 Histone deacetylase inhibitors

Because of the major role of HDACs in gene transcription, HDACs inhibitors have been developed and evaluated in many cancer types. Although the exact mechanism of the anti-tumor effect induced by HDAC inhibitors remains to be elucidated, a number of studies has shown

the upregulation of pro-apoptotic genes and downregulation of anti-apoptotic genes in the presence of HDAC inhibitors [52, 53]. Furthermore, other mechanisms such as the activation of cyclin-dependent kinase inhibitor and induction of DNA damage are also correlated with the anti-tumor activity of HDAC inhibitors [54, 55]. Based on their chemical structures, HDAC inhibitors are generally classified into three major groups: hydroxamic acids (vorinostat, panobinostat), benzamides (entinostat), and cyclic tetrapeptides (romidepsin) (**Figure 9**). Based on their targets, HDAC inhibitors are divided into pan-HDAC inhibitor (vorinostat, panobinostat) and selective HDAC inhibitors. To date, four HDAC inhibitors have been approved by the US-FDA including panobinostat for the treatment of multiple myeloma and romidepsin for cutaneous T cell lymphoma. In addition, a large number of clinical trials with HDAC inhibitors are under investigation in diverse types of solid cancers [56].

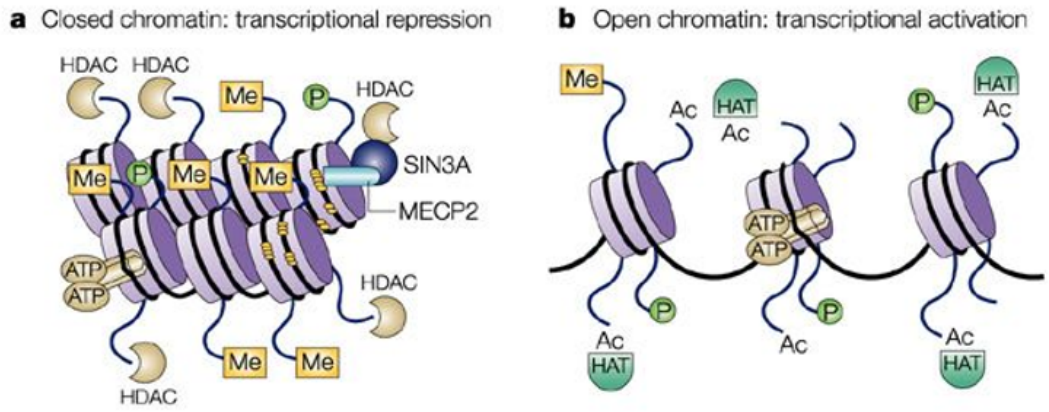

Figure 8. Chromatin conformation and transcriptional state **[57]**
Post-translational modifications of histone tails include methylation (**Me**), phosphorylation (**P**), and acetylation (**Ac**). These modifications can be regulated by histone acetyltransferases (**HAT**s) **or** histone deacetylases (**HDAC**). The connection of methyl-CpG-binding protein (**MECP2**) and methylated DNA facilitates the recruitment of HDACs. **a.** DNA methylation and histone deacetylation induce a tightly compacted chromatin structure. **b.** DNA demethylation and histone acetylation lead to an open chromatin state which allows the interaction with transcription factors.

Very importantly, HDAC inhibitors have been reported to re-sensitize a variety of cisplatin-resistant cancer cell lines. A study published in 2017 by our group analyzed the antiproliferative effects of several novel HDAC1/6 inhibitors (synthesized by the working group of Professor Kurz) in two pairs of cisplatin sensitive and resistant cell lines, namely the ovarian cancer cell lines A2780 and A2780CisR, and the head-neck cancer cell lines Cal27 and Cal27CisR.

Enhanced cytotoxicity of cisplatin was observed in the presence of HDAC inhibitors. Three of those HDAC inhibitors were able to reduce the IC_{50} values of cisplatin in the Cal27 cell line with shift factors of 6.1-8.7. Furthermore, in Cal27CisR treatment with HDAC inhibitors completely resensitized the resistant cells to cisplatin exhibiting IC_{50} values even below the wild-type cell line Cal27 [58]. In addition to the tongue cancer cell line Cal27, a resensitization of bladder cancer against cisplatin was also reported for the HDAC inhibitor trichostatin A [59]. Our group has published further studies reporting complete reversal of cisplatin resistance by HDAC inhibitors [60, 61].

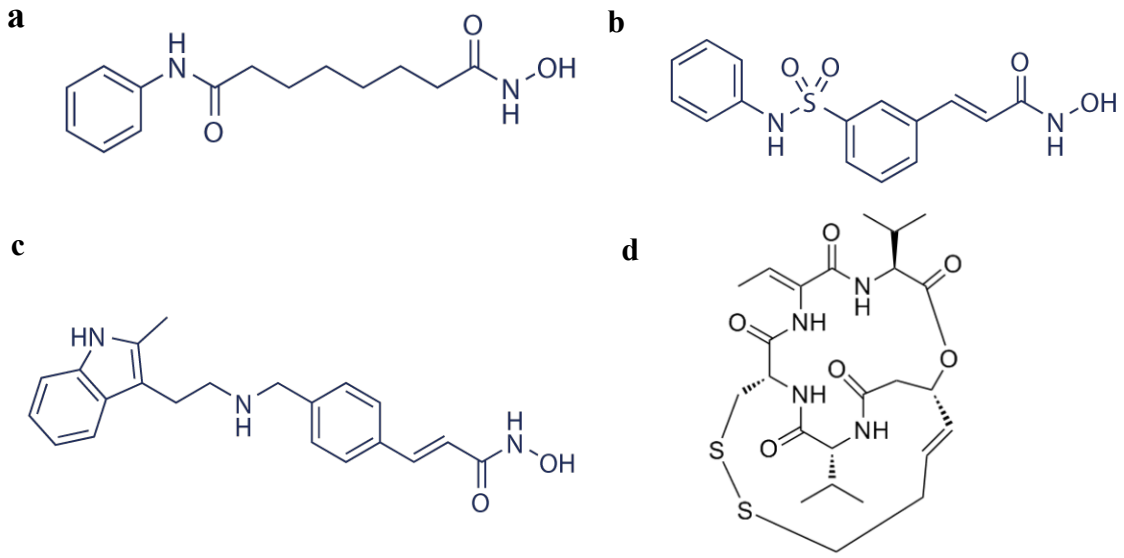

Figure 9. Approved HDAC inhibitors. **a.** Vorinostat. **b.** Belinostat. **c.** Panobinostat. **d.** Romidepsin.

1.5 Natural Products

Plant extracts have been used in human medical care for thousands of years [62]. Regarding cancer treatment, nature-derived compounds in general have been a rich source for the development of anti-cancer drugs either as templates for drug development or for direct therapeutic treatment. Paclitaxel, for instance, was originally extracted from the bark of the Pacific yew *Taxus brevifolia* and emerged from a large-scale screening of natural products in 1967 [63]. Nowadays, paclitaxel remains a commonly used chemotherapy drug in ovarian, breast, lung, and many other types of solid tumors [64]. The mode of action of paclitaxel is to target β-tubulin by stabilizing the microtubules and blocking the cells in G2/M cell cycle progression [65].

Natural products derived from marine organisms are a highly interesting source for the development of anti-cancer agents [66]. For example, eribulin (**Figure 10**) is a structurally simplified synthetic analog of halichondrin B which was originally isolated from the marine sponge *Halichondria okadai* Kadota [67, 68]. It has shown remarkable anti-cancer activity by targeting tubulin and inhibiting microtubule dynamics [68]. Eribulin has been approved by FDA for the treatment of breast cancer and liposarcoma and has been found effective against paclitaxel-resistant cancer cells [69, 70]. Those exciting findings encouraged us to investigate more compounds derived from marine sources for anti-cancer research.

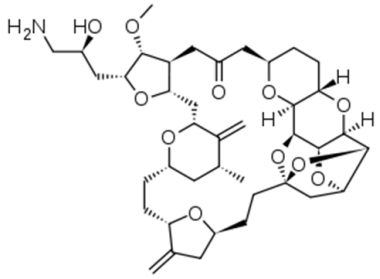

Figure 10. Structure of Eribulin

Another promising natural compound from marine origin is phomoxanthone A (PXA) (**Figure 11**), a tetrahydroxanthone dimer. PXA was isolated from the mangrove-associated fungus Phomopsis longicolla by the working group of Professor Proksch, HHU Duesseldorf [71]. In this previous study, PXA showed potent anti-cancer and antibiotic activity. The cytotoxicity of PXA was investigated in several human cancer cell lines, and IC_{50} values of PXA were in the low micromolar range or even nanomolar range [72]. Interestingly, PXA exerted equipotent effects against cisplatin sensitive as well as cisplatin resistant cancer cell lines. These data prompted us to further investigate PXA as possible anti-cancer agent with the promise to overcome chemoresistance.

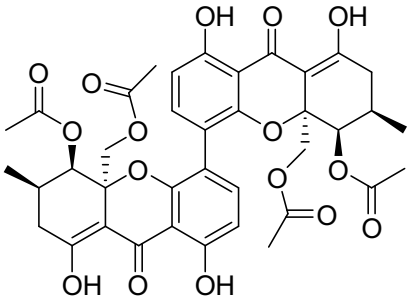

Figure 11. Structure of Phomoxanthone A

2 Aim of the Study

As described in the introduction, bladder cancer is a frequent malignancy. Current platinum-based chemotherapy for bladder cancer is associated with the development of drug resistance leading to tumor relapse. The aim of this study was to set up a cellular model system for chemoresistant bladder cancer and to use this *in vitro* model for the discovery of promising therapeutic approaches to combat bladder cancer, particularly chemoresistant cancer. Two strategies had to be investigated: first, the use of epigenetic treatment for modulation of chemoresistance and second, nature-derived compounds from the group of Professor Proksch to identify novel promising potential cytostatic agents able to overcome chemoresistance. The first goal was to establish a chemoresistant bladder cancer cell line starting from the cisplatin-sensitive epithelial bladder cancer cell line J82. To achieve this aim, a previously published protocol should be applied mimicking clinically relevant treatment conditions for cisplatin [73]. Cisplatin was chosen due to the multiple described resistance mechanisms occurring under cisplatin treatment, thus covering a broad range of resistance mechanisms. After establishing the sensitive and resistant cell pair J82/J82CisR, this cellular model should be characterized and applied for epigenetic modulation of cisplatin sensitivity. Since DNA hypermethylation related gene silencing has been previously shown to correlate with cisplatin resistance [74], the DNMT inhibitor decitabine should be investigated either alone or in combination with cisplatin in the bladder cancer cell lines J82, J82CisR, and RT-112. In addition, HDAC inhibitors should be applied alone and in combination with cisplatin to test for increase in chemosensitivity of cisplatin. As outlined in the introduction, earlier studies from our group have shown that HDAC inhibitors are able to completely reverse cisplatin resistance in various cancer types including human tongue cancer, , ovarian cancer, and breast cancers [58, 60]. These studies were however not yet performed in bladder cancer.

Given the fact that DNA methylation collaborates with histone deacetylation in gene silencing, the combination of a DNMT inhibitor with an HDAC inhibitor should be tested in the three bladder cancer cell lines [56, 75].

The second strategy for the treatment of chemoresistant bladder cancer was the investigation of natural compounds from the group of Professor Proksch. Next to a multitude

of compounds to be tested, this thesis should focus on 3 types of compounds, previously discovered as promising structures. The first was phomoxanthone A (PXA), a tetrahydroxanthone dimer isolated from mangrove endophytes. PXA has previously shown potent anti-cancer activity in various cancer cell lines [64, 72, 76]. In this thesis, the cytotoxic effect of PXA should be deeply investigated in two pairs of cisplatin sensitive and resistant cell lines (A2780, A2780CisR, J82, and J82CisR). This should include descriptive and mechanistic studies such as MTT assays, apoptosis assays, cell cycle analysis, mitochondrial membrane potential assays, and mitochondrial membrane permeation calculations. In another collaborative project, indole diterpenoid analogues and hydroanthraquinone derivatives should be investigated for their cytotoxic potential for cancer treatment including selectivity analysis for cancer over non-cancer cells.

3 Publications

3.1 Publication 1

Combination of Decitabine and Entinostat Synergistically Inhibit Urothelial Bladder Cancer Cells via Activation of FoxO1

Chenyin Wang[1], Alexandra Hamacher[1], Patrick Petzsch[2], Karl Köhrer[2], Günter Niegisch[3], Michele J. Hoffmann[3], Wolfgang Schulz[3], Matthias U. Kassack[1]

1 Institute of Pharmaceutical and Medicinal Chemistry, Heinrich-Heine-University Duesseldorf, Germany
2 Biological and Medical Research Centre (BMFZ), Cluster of Excellence on Plant Sciences (CEPLAS), Heinrich-Heine-University Duesseldorf, Germany
3 Department of Urology, Medical Faculty, Heinrich-Heine-University Duesseldorf, Germany

Contribution: First authorship, performed most of the experiments described in the manuscript. Evaluated the data and wrote the manuscript.

Abstract

Occurrence of cisplatin-resistance in bladder cancer is frequent and results in disease progression. Thus, novel therapeutic approaches are a high medical need for patients suffering from chemotherapy failure. The purpose of this study was to test the combination of the DNA methyltransferase inhibitor decitabine (DAC) with the histone deacetylase inhibitor entinostat (ENT) in bladder cancer cells with different platinum sensitivities: J82, cisplatin-resistant J82CisR, and RT-112. Intermittent treatment of J82 cells with cisplatin resulted in the six-fold more cisplatin-resistant cell line J82CisR. Combinations of DAC and/or ENT plus cisplatin could not reverse chemoresistance. However, the combination of DAC and ENT acted cytotoxic in a highly synergistic manner as shown by Chou-Talalay analysis via induction of apoptosis and cell cycle arrest. Importantly, this effect was cancer cell-selective as no synergism was found for the combination in the non-cancerous urothelial cell line HBLAK. Expression analysis indicated that epigenetic treatment led to up-regulation of forkhead box class O1 (FoxO1) and further activated proapoptotic Bim and the cell cycle regulator p21 and reduced expression of survivin in J82CisR. In conclusion, the combination of DAC and ENT is highly synergistic and has a promising potential for therapy of bladder cancer, particularly in cases with platinum resistance.

cancers

MDPI

Article

Combination of Decitabine and Entinostat Synergistically Inhibits Urothelial Bladder Cancer Cells via Activation of FoxO1

Chenyin Wang [1], Alexandra Hamacher [1], Patrick Petzsch [2], Karl Köhrer [2], Günter Niegisch [3], Michèle J. Hoffmann [3], Wolfgang A. Schulz [3] and Matthias U. Kassack [1,*]

1 Institute of Pharmaceutical and Medicinal Chemistry, Heinrich-Heine-University Duesseldorf, 40225 Duesseldorf, Germany; chenyin.wang@hhu.de (C.W.); alexandra.hamacher@hhu.de (A.H.)
2 Biological and Medical Research Center (BMFZ), Medical Faculty, Heinrich-Heine-University Duesseldorf, 40225 Duesseldorf, Germany; patrick.petzsch@hhu.de (P.P.); koehrer@hhu.de (K.K.)
3 Department of Urology, Medical Faculty, Heinrich-Heine-University Duesseldorf, 40225 Duesseldorf, Germany; guenter.niegisch@med.uni-duesseldorf.de (G.N.); michele.hoffmann@hhu.de (M.J.H.); wolfgang.schulz@hhu.de (W.A.S.)
* Correspondence: matthias.kassack@hhu.de

Received: 10 January 2020; Accepted: 30 January 2020; Published: 3 February 2020

Abstract: Occurrence of cisplatin-resistance in bladder cancer is frequent and results in disease progression. Thus, novel therapeutic approaches are a high medical need for patients suffering from chemotherapy failure. The purpose of this study was to test the combination of the DNA methyltransferase inhibitor decitabine (DAC) with the histone deacetylase inhibitor entinostat (ENT) in bladder cancer cells with different platinum sensitivities: J82, cisplatin-resistant J82CisR, and RT-112. Intermittent treatment of J82 cells with cisplatin resulted in the six-fold more cisplatin-resistant cell line J82CisR. Combinations of DAC and/or ENT plus cisplatin could not reverse chemoresistance. However, the combination of DAC and ENT acted cytotoxic in a highly synergistic manner as shown by Chou-Talalay analysis via induction of apoptosis and cell cycle arrest. Importantly, this effect was cancer cell-selective as no synergism was found for the combination in the non-cancerous urothelial cell line HBLAK. Expression analysis indicated that epigenetic treatment led to up-regulation of forkhead box class O1 (FoxO1) and further activated proapoptotic Bim and the cell cycle regulator p21 and reduced expression of survivin in J82CisR. In conclusion, the combination of DAC and ENT is highly synergistic and has a promising potential for therapy of bladder cancer, particularly in cases with platinum resistance.

Keywords: bladder cancer; cisplatin; DNA methyltransferase inhibitor; drug combination study; histone deacetylase inhibitor; forkhead box class O1

1. Introduction

Bladder cancer is the 6th most common cancer in the United States with an estimated 80,470 new cases and 17,670 deaths in 2019 [1]. Among the different types of bladder cancer, urothelial carcinoma is the most common histological subtype, which can be further divided into superficial and muscle-invasive, based on the depth of the tumor invasion into the wall of the bladder [2]. Although only 30% newly diagnosed bladder cancer cases are advanced, another 15–30% of high-grade superficial bladder cancers develop into muscle-invasive carcinomas with poor long-term survival [3]. Generally, the treatment options of bladder cancer include surgery, radiation therapy, and cisplatin-based chemotherapy [4]. Cisplatin enters cells through passive diffusion and mediated by membrane transporters [5]. The cytotoxic effect is then achieved by the formation of DNA adducts

leading to apoptosis and cell cycle arrest [6]. Although cisplatin is initially effective in most cases, acquisition of cisplatin resistance results in cancer relapse, significantly reducing its clinical usefulness. Development of cisplatin resistance is multifactorial, including pre-target, on-target, and post-target mechanisms, corresponding to diminished intracellular drug accumulation, increased rates of DNA damage repair, and defects in apoptotic signal transduction pathways which are normally activated in response to DNA damage, respectively [7]. Collectively, these processes will then inhibit apoptosis and subsequently lead to drug resistance [7]. Therefore, it is important to search for novel strategies in bladder cancer treatment, also for those patients ineligible for platinum-based therapy. One such approach is epigenetic modulation.

Aberrant epigenetic modifications play a significant role in the genesis, progression, and chemoresistance of cancer, including bladder cancer [8,9]. One fundamental epigenetic mechanism is DNA methyltransferase (DNMT)-mediated DNA methylation occurring by addition of a methyl group to carbon 5 of cytosine. In cancers, aberrant DNA methylation affects promoter regions (CpG islands) with subsequent inhibition of transcription, particularly in tumor suppressor genes [10]. DNMT inhibitors (DNMTi's) such as 5-azacytidine or decitabine have been approved for treatment of acute myeloid leukemia (AML) and myelodysplastic syndrome (MDS) and act in part by reactivating genes silenced by abnormal promotor hypermethylation [11].

In addition to DNA methylation, histone modifications are also a crucial mechanism in transcription regulation. The acetylation or deacetylation of lysine residues on histones regulates chromatin structure and gene transcription. These processes are mediated by two enzyme families known as histone acetyltransferases (HATs) and histone deacetylases (HDACs) [12]. Acetylation of histones is in general correlated with active gene transcription, whereas HDAC-mediated hypoacetylation is associated with transcriptional repression [13]. Depending on sequence similarity, zinc-dependent HDACs can be grouped into class I (HDAC1, 2, 3, and 8), class II (IIa: HDAC4, 5, 7, 9; IIb: 6 and 10), and class IV (HDAC11) [14]. In many types of cancer, including bladder cancer, increased expression levels of HDACs have been observed and frequently relate to poor clinical prognosis [15,16]. As a result, the aim of targeting HDACs has prompted the development of HDAC inhibitors (HDACi's). During the last years, different types of HDACi's, broad-spectrum (pan inhibitors) or selective HDACi's, have been developed and evaluated for treatment of solid tumors and different types of lymphomas [17]. Four HDACi's are US-FDA approved for the treatment of various lymphomas: vorinostat (cutaneous T-cell lymphoma (CTCL)), romidepsin (CTCL), belinostat (peripheral T-cell lymphoma (PTCL)), and panobinostat (multiple myeloma) [17]. The HDACi chidamide is approved by the Chinese FDA for PTCL [18]. Vorinostat, belinostat, and panobinostat are pan HDACi's, whereas romidepsin and chidamide are class I-selective HDACi's [11]. Recently, our group has contributed several highly potent and subtype-selective HDACi's leading to a complete reversal of platinum resistance in ovarian and head-neck cancers [19–22]. In a recent study, we could moreover demonstrate that class I HDAC inhibition by entinostat was superior to pan-HDAC inhibition in high-grade serous ovarian carcinomas in reversing chemoresistance against cisplatin [21]. Notably, class I HDACs show increased expression in many cancer cells and promote tumor cell proliferation [23]. This fact and the results from our study in ovarian cancer cells suggest that selective class I HDAC inhibition is more promising than pan-HDAC inhibition and avoids side effects due to lack of selectivity [21]. Another study of our groups rules out a significant role of class IIa HDACs in bladder cancer [24]. Taken together, these data suggest that it should be worthwhile trying class I HDACi's for chemoresistance reversal in bladder cancer. Thus, we decided to use entinostat, a class I selective benzamide currently undergoing clinical studies in several cancers, including bladder cancer [25,26]. In addition, based on the fact that DNMTi's and HDACi's both serve to regulate transcriptional activity, combining these two types of inhibitors might provide a clinical strategy for bladder cancer treatment, especially for patients who have already developed cisplatin resistance [11]. Thus, the aim of this study was: first, to establish-starting from the J82 bladder cancer cell line-a cisplatin-resistant subline (J82CisR) according to clinically relevant protocols previously published [27]; second, to investigate the efficacy of the DNMTi decitabine (DAC)

and HDACi entinostat (ENT) alone and in combination to inhibit the growth of platinum-sensitive (J82) and platinum-resistant (J82CisR, RT-112) bladder cancer cells.

2. Results

2.1. Combining DNMTi and HDACi Induces Synergistic Cytotoxicity in Urothelial Bladder Cancer Cell Lines

The cisplatin-sensitive J82 cell line (IC_{50} [inhibitory concentration 50%]: 1.61 μM) was intermittently exposed to cisplatin (1.6 μM, reflecting the IC_{50} value of J82) for 6 h. After several treatment cycles, the IC_{50} increased from 1.61 μM (J82) to 9.68 μM (J82CisR) corresponding to a resistance factor of 6 (Figure 1a). Notably, no further cisplatin treatments were needed to maintain the increased IC_{50} of cisplatin in J82CisR indicating a stable resistance. Furthermore, RT-112 cells were used displaying native cisplatin resistance (IC_{50}: 16.8 μM, Figure 1a). Thus, in total, three urothelial bladder cancer cell lines were used as in vitro models.

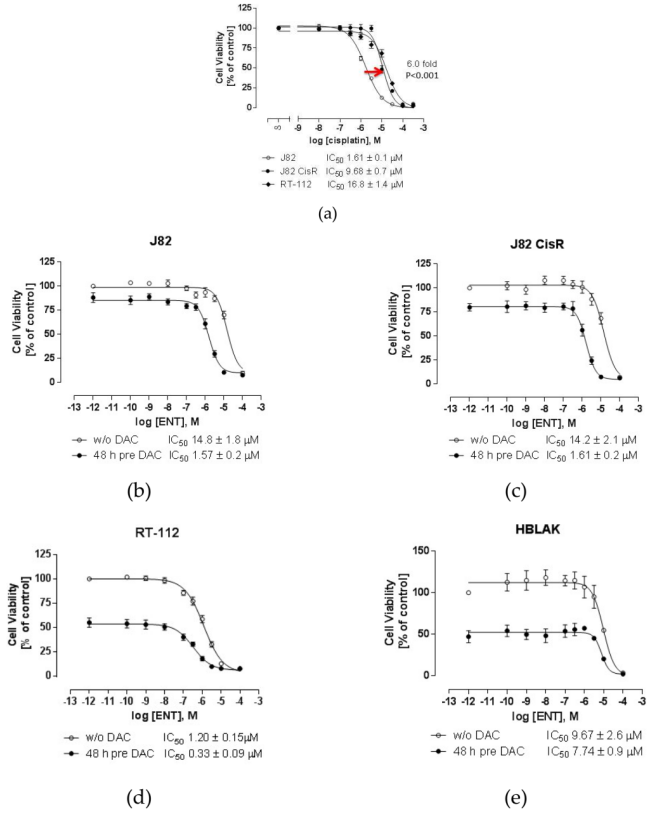

Figure 1. Generation of the cisplatin-resistant cell line J82CisR and combination treatment with DAC and ENT. (**a**) Thirty-four cycles of weekly exposure of J82 with cisplatin for 6 hours resulted in 6-fold ($p < 0.001$) increase in IC_{50} [inhibitory concentration 50%] of cisplatin in J82CisR as indicated by the red arrow. IC_{50} of cisplatin in J82: 1.61 μM; IC_{50} of cisplatin in J82CisR: 9.68 μM. Data shown are mean ± SEM, $n = 3$. (**b**) Forty-eight hours pre-incubation with DAC (1 μM) significantly enhanced the cytotoxicity of ENT in J82 cell line by decreasing IC_{50} from 14.8 μM to 1.57 μM with a shift factor of 9.4. (**c**) Pre-incubation with DAC (1 μM) decreased IC_{50} of ENT from 14.2 μM to 1.61 μM in J82CisR. (**d**) Pre-incubation with DAC (0.1 μM) increased the cytotoxic effect of ENT in RT-112 as shown by a shift factor of 3.6. (**e**) Pre-incubation of DAC (1 μM) did not significantly increase the cytotoxic effect of ENT in the normal human bladder cell line HBLAK. "% of control" on the y-axis means: % of untreated cells.

The cytotoxicity of the DNMTi DAC and the class I HDACi ENT was determined using 3-(4,5-di**m**ethyl**t**hiazol-2-yl)-2,5-diphenyl**t**etrazolium bromide (MTT) assay. In J82 and J82CisR cell lines, DAC showed weak cytotoxicity with IC_{50} values of 30.5 and 28.2 μM, respectively (Table 1; Figure S1). In contrast, RT-112 cells were dramatically more sensitive to DAC showing an IC_{50} value of 0.18 μM. Similarly, the HDACi ENT was more potent in RT-112 compared with J82 and J82CisR cell lines, with IC_{50} values of 3.41, 14.3, and 15.6 μM, respectively.

Table 1. Summary of the IC_{50} and pIC_{50} [-log IC_{50}] values of DAC and ENT in J82, J82CisR, and RT-112 cells (72 h incubation).

Cell Lines	DAC		ENT	
	IC_{50} [μM]	**pIC_{50} ± SEM**	**IC_{50} [μM]**	**pIC_{50} ± SEM**
J82	30.5	4.52 ± 0.08	14.3	4.84 ± 0.06
J82CisR	28.2	4.55 ± 0.18	15.6	4.81 ± 0.06
RT-112	0.22	6.65 ± 0.09	3.41	5.47 ± 0.11

Data shown are the mean of three independent experiments ± SEM.

Next, the combination of DAC with cisplatin or ENT with cisplatin was tested. Similar to our previous studies with HDACi and considering the time-dependent effects of DNMTi and HDACi, DAC or ENT were incubated with the respective cell lines 48 h prior to addition of cisplatin [19,21]. The resulting concentration-effect curves of cisplatin are shown in Figure S2 for all three cell lines. In contrast to our previous studies in head-neck or ovarian cancer cells [19,21], ENT did not completely but only partially reverse cisplatin resistance in J82CisR. While the resistance factor between J82 and J82CisR is 6, the partial reversal of cisplatin resistance gave a shift factor of only 1.5 (Figure S2b).

Thus, we next investigated the dual combination of DAC and ENT (without cisplatin) for synergistic effects. Exploratory experiments investigating different sequences of the two compounds revealed that coincubation or preincubation of an HDACi prior to DAC treatment resulted in an additive but not synergistic effect. Therefore, and given the fact that DNA methylation can even influence the expression of HDACs [10], DAC was incubated prior to the treatment of ENT. Our results show that the cytotoxic effect of ENT was significantly enhanced by pretreatment with DAC in all tested cell lines. In the presence of low-dose DAC (1 μM in J82 and J82CisR, 0.1 μM in RT-112), the IC_{50} values of ENT decreased 9.4-, 8.8-, and 3.6-fold compared to the absence of DAC in J82, J82CisR, and RT-112 cell lines, respectively (Figure 1b–d). To test for cancer selectivity of these observed effects, the spontaneously immortalized normal human urothelial bladder cell line HBLAK was treated with the combination of DAC and ENT as well. In contrast to the results for the bladder cancer cell lines described above, 48 h pre-treatment with 1 μM of DAC did not significantly enhance the cytotoxicity of ENT in HBLAK cells (Figure 1e) [28]. Thus, the highly synergistic effect of DAC and ENT is selective for bladder cancer cells over non-cancerous bladder cells. The drug combination index (CI) of DAC and ENT was calculated using the Chou-Talalay drug combination study method [29]. According to the drug combination model, a synergistic effect is proven if the CI is below 1. Our results indicate that DAC and ENT act synergistically in inhibiting the growth of bladder cancer cells (Figure 2 upper panel). Furthermore, a significantly higher inhibition of cell proliferation by the drug combination compared with either agent alone is illustrated in Figure 2 middle and bottom panels.

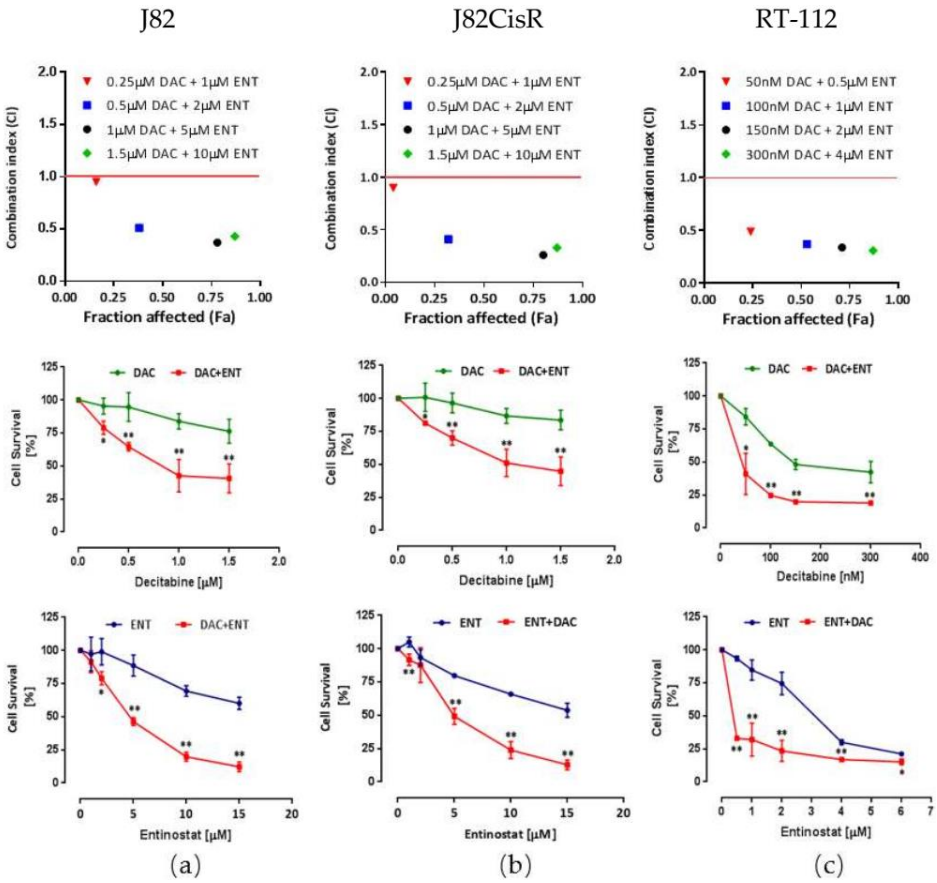

Figure 2. Combination of DAC and ENT elicits synergistic cytotoxic effects in urothelial bladder cancer cells. (**a**) J82; (**b**) J82CisR; (**c**) RT-112 cells. Upper panel: cells were treated for 48 h with DAC, followed by 72 h of ENT, respectively; x axis indicates fraction of cells affected (Fa); y axis indicates combination index (CI). Synergistic effect is defined by a CI below the red line (CI < 1). Middle and bottom panels: percentage of cell survival after treatment with DAC or ENT alone or in combination. Data shown are the mean ± SD of at least three independent experiments. ** $p < 0.01$, * $p < 0.05$, *t*-test, combination treatment compared with single treatments.

2.2. Combination Treatment of DAC and ENT Induces Apoptosis in Urothelial Bladder Cancer Cells Mediated by the Activation of Caspase 3/7

To understand the mechanism of growth inhibition and synergistic cytotoxicity of the combination treatment of DAC and ENT shown above, apoptosis assays (sub-G1 analysis) were performed following DAC and ENT treatment either alone or combined. In agreement with the result of the drug combination study described above, the combination of DAC and ENT led to a strong increase in cells in sub-G1 phase compared to single agent treatment. Importantly, this effect was more pronounced in J82CisR cells with 65.1% sub-G1 population compared with 40.9% and 44.7% in J82 and RT-112 in the combination treatments, respectively (Figure 3a–d). The increased number of cells in sub-G1 after the combination treatment could be reversed by addition of the pan-caspase inhibitor Q-VD-OPh, indicating caspase-driven apoptosis induction. To confirm that the observed effect in sub-G1 assays was not due to other types of cell death, the activity of caspases 3 and 7 was measured using fluorescence-based high content analysis. Under treatment with either agent alone, caspase 3/7 activation was detected in only a few cells. If both drugs were combined, the number of caspase 3/7 positive cells was significantly increased to 66.6%, 49.1%, and 66.3% in J82, J82CisR, and RT-112 cells,

Cancers **2020**, *12*, 337

respectively (Figure 3e–g). Taken together, these results indicate that the combination of DAC and ENT induces caspase 3/7-mediated apoptosis in all three bladder cancer cell lines in a synergistic manner.

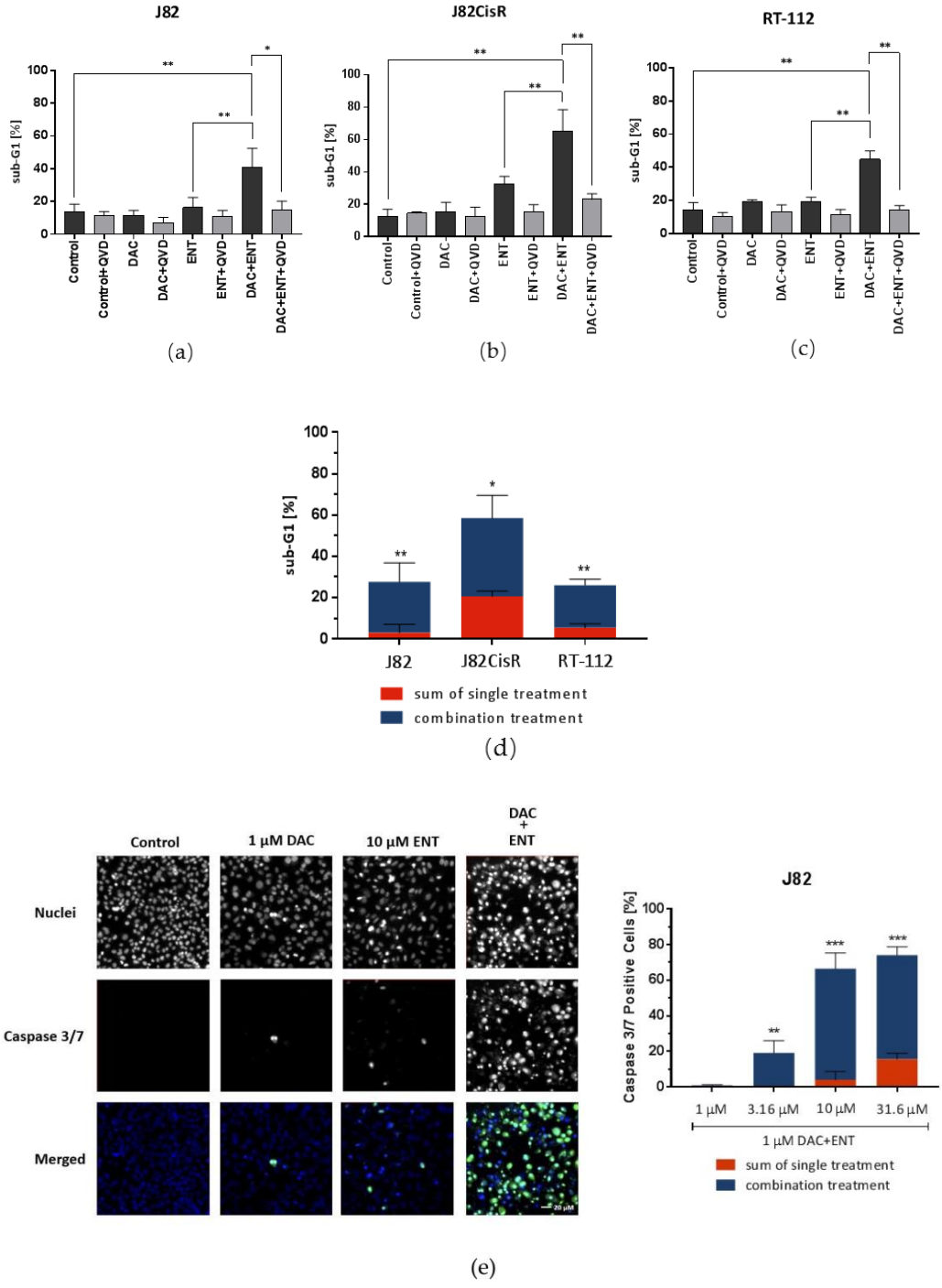

Figure 3. *Cont.*

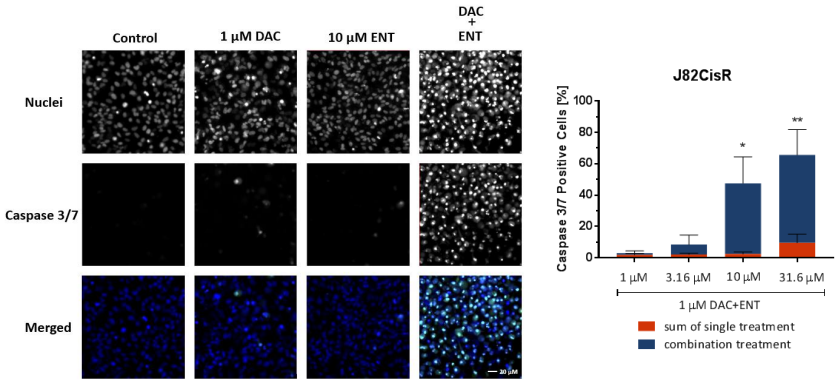

(**f**)

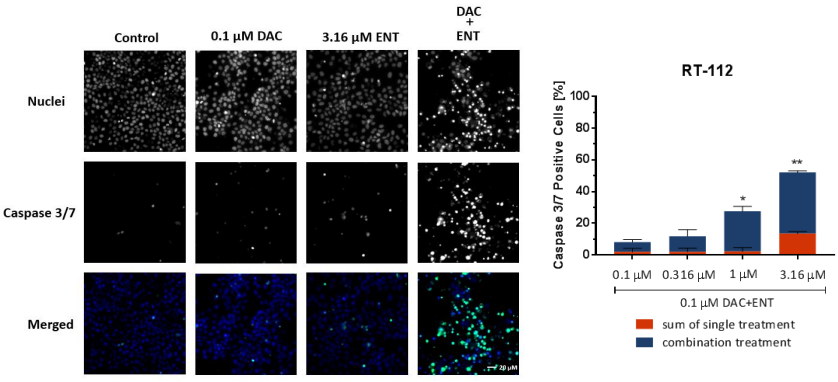

(**g**)

Figure 3. DAC and ENT acted synergistically to induce caspase 3/7-mediated apoptosis. (**a**–**c**) Combinations of DAC (1 µM in J82 and J82CisR, 0.1 µM in RT-112) and ENT (3.16 µM in J82 and J82CisR, 2 µM in RT-112) led to increased sub-G1 fractions, compared with either agent alone in J82, J82CisR, and RT-112 cell lines. In each single experiment, 12,000 cells per condition were analyzed. Medium was used as control. Data shown are the mean ± SD of at least three independent experiments. ** $p < 0.01$, * $p < 0.05$ by *t*-test. (**d**) The sums of sub-G1 signals of single treatments are shown in red bars. The differences between the combination treatment effects and the sums of single treatment effects are shown in extended blue bars (superadditive (=synergistic) part). Data shown are the mean ± SD of at least three independent experiments. ** $p < 0.01$, * $p < 0.05$ by *t*-test. (**e**–**g**) The 48 h treatment of DAC followed by 48 h ENT leads to caspase 3/7 activation in a synergistic manner in J82, J82CisR, and RT-112 cells. A minimum of 500 cells per condition were analyzed in each single experiment. Medium was used as control for untreated cells, and cisplatin (not shown) was used as positive control for caspase 3/7 activation. Cells were stained with Hoechst 33342 (blue) for cell nuclei and CellEvent Caspase-3/7 green detection reagent for the activation of caspase 3/7. Quantification of caspase 3/7 positive cells is displayed in the right panel. The sums of percentages of caspase 3/7 positive cells of single treatment are shown in red bars. The differences between the combination treatment effects and the sums of single treatment effects are shown in extended blue bars (superadditive (=synergistic) part). Data shown are the mean ± SD of at least three independent experiments. *** $p < 0.001$, ** $p < 0.01$, * $p < 0.05$ by *t*-test. Scale bars for (**e**–**g**): 20 µm.

2.3. DAC Combined with ENT Affects the Cell Cycle Distribution in Urothelial Bladder Cancer Cells

To test whether the combined treatment with DAC and ENT has an effect on the cell cycle distribution of bladder cancer cells, J82, J82CisR, and RT-112 cells were analyzed by flow cytometry with PI staining after treatment of DAC and ENT. In J82 cells, the combination treatment led to cell cycle arrest at the G2/M transition, with 20.0% of cells in G2/M in untreated cells versus 40.5% in DAC plus ENT treated cells (Figure 4a,d). Either drug alone failed to change the cell cycle distribution. In J82CisR, combination treatment only slightly (not significantly) increased the cell population in G2/M phase (Figure 4b,e). In the RT-112 cell line, treatment with DAC alone induced an increase in cells in S- und G2/M phase significantly (16.7% in S, 26.9% in G2/M in DAC-treated versus 6.6% in S and 13.5% in G2/M in untreated cells, $p < 0.01$). Treatment with ENT increased the cell population in S phase to 17.4% but no significant changes were observed in G1 and G2/M phase. Combined treatment with DAC and ENT increased the number of cells in S phase to 34.9% and decreased the number of cells in G1 to 45.7% (Figure 4c,f). Taken together, these data indicate that the combination treatment significantly affects the cell cycle distribution in J82 and RT-112 cell lines but not in J82CisR.

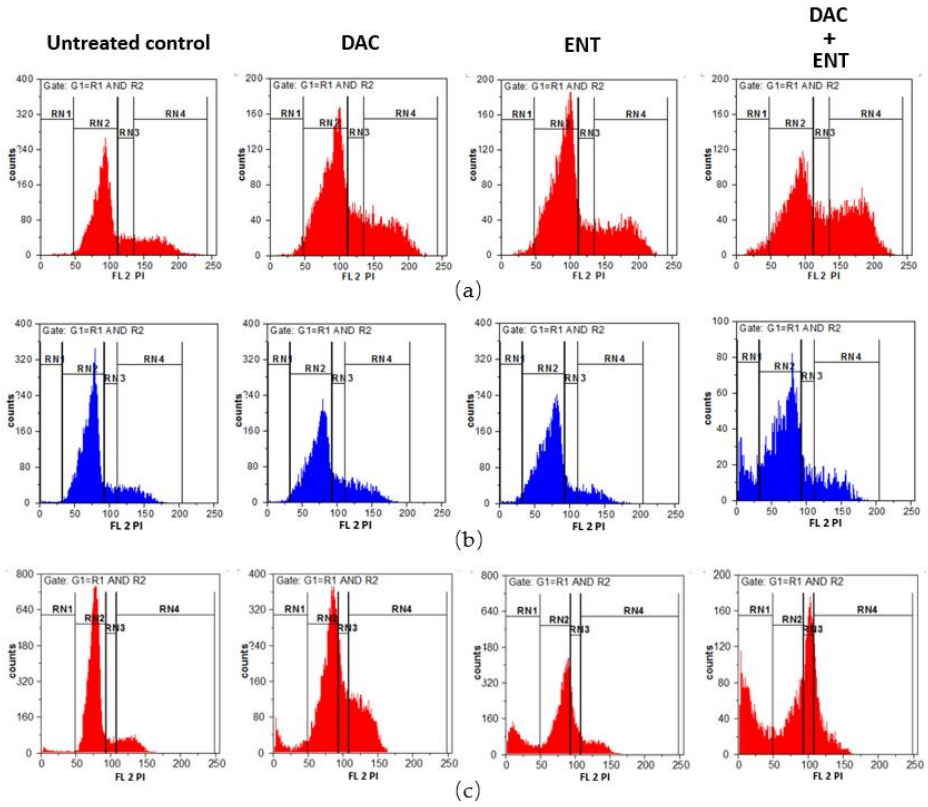

Figure 4. *Cont.*

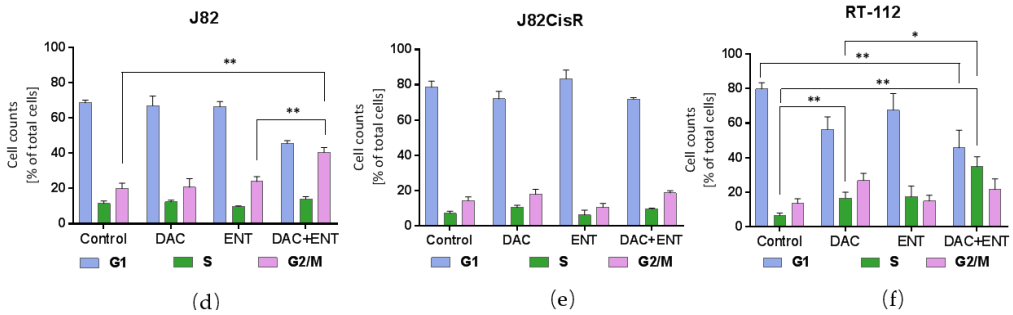

Figure 4. Effect of combination of DAC and ENT on cell cycle progression in J82, J82CisR, and RT-112 cell lines. Cells were incubated with DAC (1 μM in J82 and J82CisR, 0.1 μM in RT-112) or ENT (3.16 μM in J82 and J82CisR, 2 μM in RT-112) or with a combination of DAC and ENT. DMSO was used as a solvent control. RN1, RN2, RN3, and RN4 indicate the cell cycle phases of sub-G1, G1, S, and G2M, respectively. (**a**) Combination treatment led to cell cycle arrest at G2/M phase in J82 cell line. (**b**) Cell cycle distribution of J82CisR cells was not affected by either drug treatment alone or in combination. (**c**) Combination treatment induced cell cycle arrest in S phase in RT-112 cell line. (**d**–**f**) Quantification of the cell cycle distribution after the drug treatments in J82, J82CisR, and RT-112 cell lines. Data shown are the mean ± SD of at least three independent experiments. ** $p < 0.01$, * $p < 0.05$ by *t*-test.

2.4. DAC and ENT Alter RNA- and Protein-Expression and Protein Phosphorylation of Genes Involved in the Akt/FoxO Pathway

Differential gene expression was estimated in response to DAC or ENT or the combination of DAC plus ENT using RNA sequencing. Ingenuity pathway analysis revealed that Akt/FoxO signaling was changed remarkably under epigenetic treatment. AKT1 and AKT2, key regulators of cell survival, were downregulated by DAC or ENT to different extents. Treatment with DAC alone had no significant effect on the expression of AKT1 or AKT2. Treatment with ENT reduced expression of AKT1 and AKT2. The combination of DAC with ENT led to an even greater downregulation of AKT1 and AKT2 (Figure 5a,b). Furthermore, forkhead box class O1 (FoxO1), a transcription factor regulated by AKT, was significantly increased by ENT and by the combination treatment DAC plus ENT in J82, J82CisR, and RT-112 (Figure 5c). Finally, a set of target genes of FoxO1 regulating tumor growth and triggering apoptosis (Bim) or inducing cell cycle arrest (p21) were differentially regulated upon treatment with DAC, ENT, or the combination of DAC plus ENT (Figure 5d–f). Expression of BIM and p21 was induced, whereas expression of survivin was downregulated after drug treatment, especially in J82CisR.

Next, RNA gene expression changes were verified by Western blot analysis. Uncropped Western blots and ratios of integrated densities of proteins of interest and beta-actin from J82, J82CisR, and RT-112 can be found in Figure S3 (J82), Figure S4 (J82CisR), and Figure S5 (RT-112). Consistent with the RNA expression data, FoxO1 was upregulated by either ENT alone or the combination of DAC plus ENT in all three tested cell lines according to Western blots (Figure 6a–c). DAC alone did not (J82CisR) or only slightly increase FoxO1 (J82, RT-112). In accordance with RNA expression, protein levels of Bim, one of the downstream targets of FoxO1, were increased upon treatment with ENT or DAC plus ENT in J82 and RT-112 cells (Figure 6a,b). Bim expression did, however, not increase in J82CisR-neither in RNA nor in protein expression (Figures 5d and 6b). Treatment with ENT or the combination of DAC and ENT significantly increased the protein expression of p21 in J82 and J82CisR, but no significant changes were observed in RT-112 cells. RNA expression of survivin was decreased in all three cell lines upon ENT or DAC plus ENT treatment, whereas a downregulation of survivin protein was only observed in J82CisR (Figure 6b). Next, we analyzed the protein expression of Akt and p-Akt as well as p-FoxO1. While RNA expression suggested a downregulation of Akt in all three cell lines upon ENT and DAC plus ENT treatment, we found a clear reduction of Akt expression in Western blot only in RT-112 cells, whereas in J82 and J82CisR, no treatment-induced changes in Akt

expression were found (Figure 6a–c). Interestingly, Akt, the negative upstream regulator of FoxO1, was less phosphorylated (less p-Akt) by treatment with only ENT and even less by treatment with DAC plus ENT in J82CisR, whereas Akt phosphorylation slightly increased in J82 upon treatment with DAC, ENT, or the combination of both. In RT-112, Akt phosphorylation increased upon DAC or ENT treatment but was reduced to the control level upon combination of DAC plus ENT. Since p-Akt can phosphorylate FoxO1 and lead to inactivation of FoxO1, we examined the phosphorylation of FoxO1 (p-FoxO1) in response to DAC, ENT, or combination treatment.

In J82CisR, Akt was less phosphorylated upon DAC plus ENT treatment. As expected, FoxO1 phosphorylation was also reduced in J82CisR by combination treatment (Figure 6b). In J82 cells, increased expression of FoxO1 upon ENT or DAC plus ENT treatment resulted in increased phosphorylation of FoxO1 because p-Akt remained approximately equal over all treatment conditions and was not reduced upon DAC plus ENT treatment (Figure 6a). In RT-112 cells, FoxO1 phosphorylation was rather low but treatment-induced changes correlated with the phosphorylation of Akt (Figure 6c). Notably, the expression of FoxO1 was reduced by the addition of the FoxO1 inhibitor AS1842856 (Figure 6a–c). Furthermore, AS1842856 reduced expression of p21 (J82, J82CisR) and reduced expression of Bim (J82, RT-112). Taken together, the protein expression results demonstrate that DAC and ENT treatment increase FoxO1 expression in urothelial bladder cancer cells. The pathways by which DAC and ENT induce strong synergistic cytotoxicity are, however, different between the three examined bladder cancer cell lines and involve increased p21 expression, increased Bim expression, reduced phosphorylation of Akt, and reduced expression of survivin.

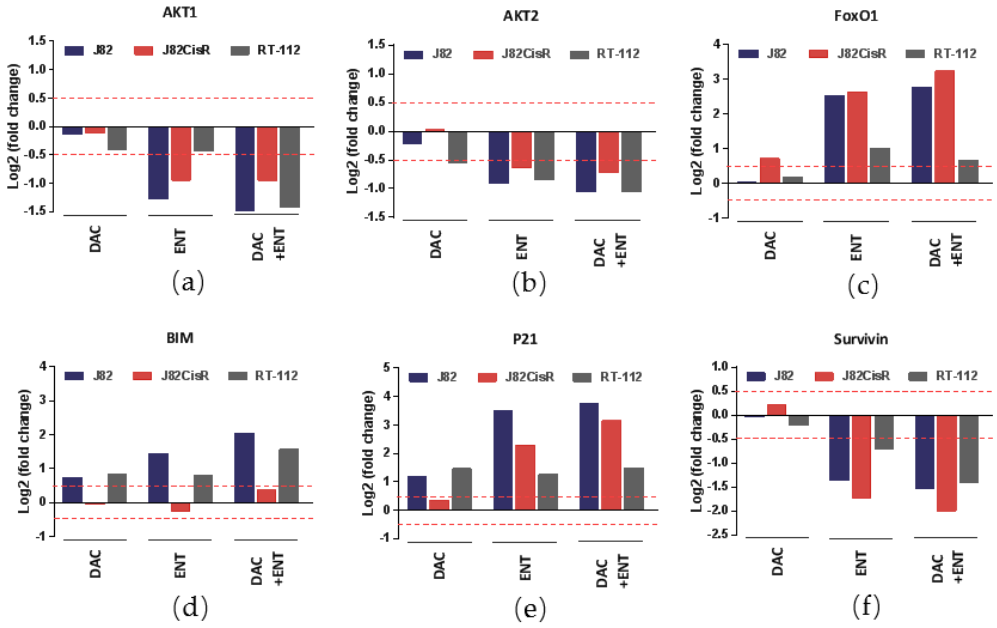

Figure 5. Epigenetic treatments alter gene expression in urothelial bladder cancer cell lines. (**a**–**f**) DAC and ENT resulted in the changes of genes involved in Akt/FoxO pathway. Data shown are RPKM (reads per kilobase per million mapped reads) values normalized from three independent RNA-seq experiments; x axis indicates treatment conditions; y axis indicates log2 fold change of RPKM compared with untreated control.

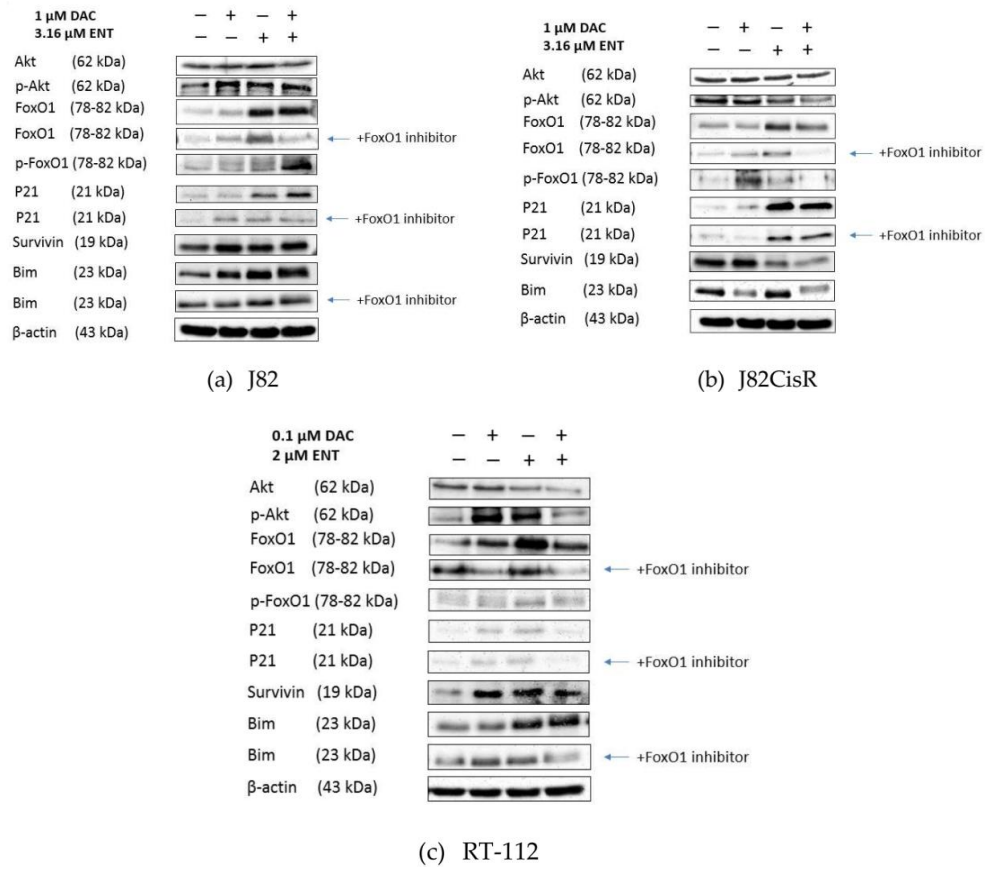

Figure 6. Epigenetic treatments alter protein expression in urothelial bladder cancer cell lines. (**a**–**c**) Western blot analysis of J82, J82CisR, and RT-112 cell lines upon the treatment of DAC and ENT. Cells were treated for 48 h with DAC followed by 48 h treatment with ENT. DMSO was used as a solvent control; the blots shown in (**a**–**c**) are from one representative experiment out of a set of three experiments.

3. Discussion

DNMTs have been long recognized for their role in gene silencing by increasing promotor CpG island methylation. This process occurs particularly in cancer cells resulting in the silencing of genes functioning as tumor suppressors [30]. Consequently, targeting DNMT has become a therapeutic approach for anti-cancer treatment as highlighted by the approval of azacytidine and decitabine for treatment of AML or MDS [11]. Similarly, HDACs have become validated drug targets in particular in cancer [31]. HDAC-mediated low acetylation of histones is associated with a condensed chromatin structure resulting in repressed transcription [32]. Because DNA methylation accompanies histone deacetylation in the regulation of gene expression, the combination of DNMTi's and HDACi's has been studied in several malignancies including, e.g., acute myelogenous leukemia, non-small cell lung cancer, and colorectal cancer [33–35]. In bladder cancer, however, this combination therapy has rarely been investigated. Thus, the aim of the current study was to test the effect of DNMTi's and HDACi's in the two muscle-invasive bladder cancer cell lines J82 and RT-112. Since cisplatin is first-line treatment for advanced bladder cancer and cisplatin resistance occurs frequently in bladder cancer patients eventually leading to relapse, we aimed to set up a cellular model of cisplatin resistance in bladder cancer mimicking the clinical development of cisplatin resistance. Thus, the cisplatin-resistant cell

line J82CisR was developed according to clinical protocols as previously published by our group for head-neck cancer [27].

In a recent study, we have shown that class I-selective inhibitors like entinostat (ENT) were superior in reversing chemoresistance against cisplatin over pan-HDACi in serous ovarian cancer cell lines [21]. Further, exploratory experiments for the current study revealed that the class I-selective HDACi ENT exhibited a stronger synergistic interaction with the DNMTi DAC than the pan-HDACi panobinostat. This is in agreement with findings that expression levels of class I HDACs are higher in cancer versus non-cancerous cells [36]. The superior effect of ENT in combination with DAC compared with other classes of HDACi's may also be explained by the fact that class I HDACs are mainly found in the nucleus and regulate the acetylation status of histones [34].

The main finding of our study is that the DNMTi DAC and the HDACi ENT act synergistically in reducing the viability of urothelial bladder cancer cells by inducing apoptosis and cell cycle arrest (Figures 3 and 4). Importantly, the results from the non-cancerous urothelial bladder cell line HBLAK indicated selectivity of the combination treatment DAC plus ENT for bladder cancer over non-cancer cells (5- to 23-fold for the cell lines J82, J82CisR, and RT-112). Treatment with DAC or ENT alone shows only moderate cytotoxicity and almost no apoptosis induction (Table 1 and Figure 3). Combination of both compounds, however, induced strong apoptosis as seen by sub G1 increase mediated by the activation of caspases 3/7 (Figure 3). These findings are in accordance with previous studies that investigated the effects of DNMTi and HDACi in other malignancies such as acute myelogenous leukemia, non-small cell lung cancer, or colorectal cancer [33,34]. Notably, in contrast to our results from ovarian and head-neck cancers, neither DAC nor ENT nor the combination of DAC plus ENT could completely reverse cisplatin resistance in the bladder cancer cell line J82CisR [19,21] (Figure S2). Gene expression experiments of J82 and J82CisR did not reveal major changes of DNA damage response (DDR) genes, nor did they unravel the exact mechanism of resistance against cisplatin, as typical cisplatin resistance genes such as DNA excision repair gene ERCC-1, the copper transporter CTR1, and multidrug resistance-associated protein 2 ABCC2 remained unchanged. However, rather than further examining the resistance mechanism of J82CisR, we aimed at exploring the novel therapeutic combination of DAC (approved drug) and ENT (late-stage clinical phase 3) for the treatment of chemoresistant bladder cancer. Mechanistically, we found an upregulation of the transcription factor FoxO1 in all three examined bladder cancer cell lines upon epigenetic treatment with DAC, ENT, or the combination of DAC plus ENT. FoxO1 is a transcription factor negatively regulated through phosphorylation by activated Akt (p-Akt) [37]. Multiple downstream targets of FoxO1 play an essential role in controlling cell survival and proliferation, such as the proapoptotic protein Bim, the cell cycle regulator p21, or the survival protein survivin [38], which was confirmed in our study by using the FoxO1 inhibitor AS1842856 (Figure 6a–c).

FoxO1 was upregulated in all three cell lines upon epigenetic treatment albeit to different extents (Figure 6a–c). However, the mechanisms of FoxO1 activation are distinct in the various cell lines upon the treatment with DAC, ENT, or DAC plus ENT. In J82, upregulation of FoxO1 was observed independent of increased p-Akt levels upon epigenetic treatment (Figure 6a). p-FoxO1 increased following increased phosphorylation of Akt after the combination treatment DAC plus ENT. In contrast, in J82CisR cells, the combination of DAC plus ENT reduced the phosphorylation of Akt, subsequently resulting in reduced p-FoxO1 and thus in activation of FoxO1. In RT-112 cells, an increase in FoxO1 expression did not correlate with phosphorylated Akt, similar to the results in J82. We thus conclude that epigenetic modulation with DAC and ENT induced increased expression of FoxO1 independent of the status of p-Akt in J82 and RT-112 cells whereas in J82CisR, increased FoxO1 correlates with reduced phosphorylation of Akt. These findings may have clinical significance, since high FoxO1 expression levels result in increased relapse-free survival of bladder cancer patients as shown by analysis of publicly available bladder cancer expression data (Figure S6). Further, in J82CisR, reduced phosphorylation of Akt also correlated with reduced expression of survivin after combination of DAC plus ENT (Figure 6b), eventually leading to increased apoptosis. These data are also in accordance with literature data [39]

and confirm the distinct mechanisms of the cytotoxicity induced by epigenetic agents in J82, RT-112, and J82CisR cells. Although pharmacological modulation by the FoxO1 inhibitor AS1842856 (Figure 6) should ideally be confirmed by molecular biology studies such as siRNA knockdown experiments, besides clear convincing results obtained with the FoxO1 inhibitor AS1842856 (Figure 6), the clinical importance of FoxO1 expression was shown by analysis of publicly available bladder cancer expression data presented in Figure S6. In the next step, synergy between DAC and ENT needs to be investigated in a larger number of bladder cancer cell lines, in particular in cisplatin-resistant cell lines. Criteria for inclusion of patients in prospective clinical trials may be low FoxO1 expression in tumor specimens and resistance to the first-line therapy cisplatin.

4. Materials and Methods

4.1. Materials

Dulbecco's Modified Eagle Medium (DMEM) was obtained from Gibco (Darmstadt, Germany). Penicillin/streptomycin (pen/strep) (10,000 U/mL; 10 mg/mL) and trypsin-EDTA (0.05% Trypsin, 0.02% EDTA in Phosphate Buffer Saline) were purchased from PAN Biotech (Aidenbach, Germany). Cisplatin was ordered from Sigma (Sigma-Aldrich, Steinheim, Germany). Decitabine, Entinostat, and FoxO1 inhibitor AS1842856 (Selleckchem, Houston, TX, USA) were prepared at 10 mM in DMSO. Cisplatin was dissolved and subsequently diluted in 0.9% saline. The caspase inhibitor Q-VD-OPh (Sigma-Aldrich, Steinheim, Germany) was dissolved in DMSO at 10 mM and diluted in DMEM. Hoechst 33342 (Sigma-Aldrich, Steinheim, Germany) was dissolved in distilled water at 10 mg/mL. 3-(4,5-dimethylthiazol-2-yl)-2,5-diphenyltetrazolium bromide (MTT) was dissolved in PBS at a concentration of 5 mg/mL and obtained from Serva (Heidelberg, Germany). Propidium iodide was obtained from Santa Cruz Biotechnology (Heidelberg, Germany). Triton X-100 was purchased from AppliChem (Darmstadt, Germany). 0.9% NaCl, obtained from Fresenius Kabi (Bad Homburg, Germany) and supplemented with 0.01% sodium azide, was used as sheath fluid for flow cytometry analysis. The CellEvent Caspase-3/7 green detection reagent was purchased from Invitrogen (Carlsbad, CA, USA). HRP-conjugated secondary antibodies used in Western blotting were ordered from R&D Systems (Wiesbaden, Germany).

4.2. Cell Culture

The urothelial bladder cancer cell lines J82, RT-112 and the normal human bladder cell line HBLAK were kindly provided by Prof. Wolfgang A. Schulz (Department of Urology, Medical Faculty, Heinrich Heine University). The J82 cisplatin-resistant (CisR) cell line was generated by exposing the parental cell line to weekly treatment with cisplatin at an IC_{50} concentration over a period of 34 weeks as previously described [27]. The cells were cultured in DMEM supplemented with 10% fetal bovine serum, 120 µg/mL streptomycin, and 120 U/mL penicillin. All cells were cultured at 37°C in a humidified atmosphere containing 5% CO_2. When cells reached a confluence of 80–90%, they were washed with 1× PBS and treated with trypsin-EDTA before use for the respective experiments.

4.3. Cell Viability Assay

The MTT assay was used to test the cell viability and was performed as previously described [40]. Briefly, cells were seeded into 96-well plates (Sarstedt, Nümbrecht, Germany) and incubated overnight. Then, cells were treated with increasing concentrations of test agent. After a certain incubation period, 25 µL of MTT solution (5 mg/mL) was added into each well. After 15 min incubation, the mixture of medium and MTT solution was removed, and 75 µL of DMSO was added to dissolve formazan crystals. Absorbance of each well was measured at 544 nm (test wavelength) and 690 nm (background) using the BMG FLUOstar (BMG Labtechnologies Offenburg, Germany). Background was subtracted from the absorbance of each well.

4.4. Synergistic Study

To determine the synergism of DAC and ENT, the rates of cell growth inhibition were obtained and calculated from MTT assays. The combination indexes (CIs) were calculated using Compusyn software version 1.0 (ComboSyn, Inc., Paramus, NJ, USA) based on the Chou-Talalay method. The synergism, additive effect, and antagonism are defined by CI < 1, CI = 1, and CI > 1, respectively [41].

4.5. Apoptosis Assay

The apoptosis assay was performed as previously described [42]. Briefly, cells were seeded in 24-well plates and incubated overnight. Then the cells were exposed to DAC for 48 h followed by additional 48 h treatment with ENT. The caspase inhibitor Q-VD-OPh was added 1 h prior to the compound treatment (20 μM). To lyse the cells, the plate was centrifuged and the supernatant was removed carefully. To each well, 500 μL of hypotonic lysis buffer (sodium citrate tribasic dihydrate 0.1%, Triton X-100 0.1% (*v*/*v*), PI 100 μg/mL) was added, and the 24-well plate was stored at 4 °C in the dark overnight. The counts in sub-G_1 of the cell nuclei were detected by flow cytometry (CyFlow® space of Partec, Münster, Germany).

4.6. Cell Cycle Analysis

For cell cycle analysis, the cells were plated in 6-well plates 1 day before the drug treatment. The cells were treated with DAC for 48 h and an additional 48 h with ENT either alone or combined with DAC. The cells were then collected and washed with PBS and fixed in 70% ice cold ethanol at –20 °C for 24 h. The fixed cells were washed with cold PBS and incubated in staining solution containing 0.1% (*v*/*v*) Triton X-100, 200 μg/mL DNAse-free RNAse A (Fermentas/Thermo Fisher Scientific, Waltham, MA, USA), and 20 μg/mL propidium iodide for 15 min at 37 °C (protected from light). The DNA content was measured by flow cytometry and the doublet discrimination mode was used.

4.7. Caspase 3/7 Activation

The detection of caspase 3/7 activity after DAC and ENT treatment was performed using high-content analysis (HCA). The cells were treated in the same manner as described in apoptosis assay and cell cycle analysis. After drug incubation, the medium was aspirated, and the cells were labeled with the mixture of CellEvent™ Caspase-3/7 green detection reagent and Hoechst 33342. After 30 min incubation, images were acquired by ArrayScan XTI Live High Content Platform (Thermo Fisher Scientific Inc., Waltham, MA, USA) using excitation filters at 386 and 485 nm for Hoechst 33342 and Caspase-3/7 green detection reagent, respectively. The percentage of activated caspase 3/7 cells was calculated using HCS Studio Cellomics Scan (Thermo Fisher Scientific Inc.).

4.8. Total RNA Extraction and RNA-seq Analysis

Total RNA was isolated using RNeasy Mini Kit (QIAGEN, Hilden, Germany) according to the manufacturer's instruction. The total RNA samples used for transcriptome analyses were quantified (Qubit RNA HS Assay, Thermo Fisher Scientific) and quality-measured by capillary electrophoresis using the Fragment Analyzer and the 'Total RNA Standard Sensitivity Assay' (Agilent Technologies, Inc. Santa Clara, CA, USA). All samples in this study showed high RNA quality numbers (RQN; mean = 9.9). The library preparation was performed according to the manufacturer's protocol using the Illumina® 'TruSeq Stranded mRNA Library Prep Kit'. Briefly, 300 ng total RNA were used for mRNA capturing, fragmentation, the synthesis of cDNA, adapter ligation, and library amplification. Bead purified libraries were normalized and finally sequenced on the HiSeq 3000/4000 system (Illumina Inc. San Diego, CA, USA) with a read setup of 1 × 150 bp. The bcl2fastq tool was used to convert the bcl files to fastq files as well for adapter trimming and demultiplexing.

4.9. Analysis of RNA-Seq Data

Data analyses on fastq files were conducted with CLC Genomics Workbench (version 10.1.1, QIAGEN, Venlo. NL). The reads of all probes were adapter trimmed (Illumina TruSeq) and quality trimmed (using the default parameters: bases below Q13 were trimmed from the end of the reads, with a maximum of two ambiguous nucleotides). Mapping was done against the Homo sapiens (GRCh38) (Mai 25, 2017) genome sequence. After grouping of samples (three biological replicates each) according to their respective experimental condition, multi-group comparisons were made and statistically determined using the Empirical Analysis of DGE (version 1.1, cutoff = 5). The resulting p values were corrected for multiple testing by FDR and Bonferroni-correction. A p value of ≤ 0.05 was considered significant. Data were further evaluated with the Ingenuity-Pathway analysis software (Qiagen Inc. 2016).

4.10. Western Blot Analysis

Total protein extraction and Western blot analysis were performed as previously described with minor modification [43]. Briefly, cells were lysed with RIPA buffer (150 mM NaCl, 1% Triton X-100, 0.5% Na-desoxycholate, 0.1% SDS, 2 mM EDTA, 50 mM Tris-HCl pH 8.0) containing Pierce protease and phosphatase inhibitor mini tablets (Thermo Scientific, Rockford, IL, USA) and boiled at 95 °C with 2× Laemmli-buffer containing β-mercaptoethanol for 5 min. The concentration of the total protein was determined by Pierce BCA protein assay (Thermo Scientific, Rockford, IL, USA). Equal amount of proteins was loaded onto SDS-PAGE for separation. Proteins were transferred on polyvinylidene difluoride membrane (Merck Millipore, Darmstadt, Germany) by semi-dry blotting for 1 h. Blots were blocked in either Tris Buffered Saline-0.1% Tween 20 (TBST) 3% milk or TBST-3% bovine serum albumin (AppliChem, Darmstadt, Germany) for 1 h. Primary antibodies were incubated at 4 °C overnight. For information on the primary antibodies, we refer to the Supplementary Information. Blots were washed twice with TBST and once with TBS followed by the HRP-conjugated secondary antibody incubation for 1 h. Blots were then washed again twice with TBST and once with TBS and detected using the Western Blotting Luminol Reagent (Santa Cruz Biotechnologies, Heidelberg, Germany) and the INTAS Science Imaging Instrument (GeliX Imager, Göttingen, Germany).

4.11. Statistical Analysis

The statistical analysis was carried out with GraphPad Prism 7.0 (GraphPad Software Inc., San Diego, CA, USA). The two-tailed Student's t-test or ANOVA was used, and p-value less than 0.05 was considered as significant. Concentration-effect curves were then generated by nonlinear regression curve fitting using the 4-parameter logistic equation with variable hill slope. The IC_{50} values are the concentration of the cytotoxic agent that led to a decrease of 50% of the recorded signal. The pIC_{50} values are $-\log IC_{50}$. Assays were performed at least in three independent experiments each carried out in triplicates. Values shown are mean ± SEM.

5. Conclusions

In conclusion, our study demonstrated that the combination treatment of DAC plus ENT is cancer-selective and highly synergistic in inhibiting the proliferation of urothelial bladder cancer cells via induction of apoptosis and caspase 3/7 activation. Mechanistically, epigenetic treatment resulted in the increased expression of FoxO1 which then induced cell line-dependent further pathways, such as increased expression of Bim or p21 or reduced expression of survivin. Our findings provide evidence that a combination of the approved drug decitabine and the late-stage trial drug (phase 3) entinostat is a promising therapeutic strategy for bladder cancer, in particular for patients resistant to the first-line therapy cisplatin.

Supplementary Materials: The following are available online at http://www.mdpi.com/2072-6694/12/2/337/s1, Figure S1: Evaluation of the cytotoxic effects of DAC and ENT in bladder cancer cell lines, Figure S2: Combination

treatment of DAC or ENT with cisplatin, Figure S3: Uncropped Western blots and ratios of integrated densities of proteins of interest and beta-actin from J82 cells, Figure S4: Uncropped Western blots and ratios of integrated densities of proteins of interest and beta-actin from J82CisR cells, Figure S5: Uncropped Western blots and ratios of integrated densities of proteins of interest and beta-actin from RT-112 cells, Figure S6: Kaplan-Meier plot showing relapse free survival of 187 bladder cancer patients with low or high FoxO1 expression levels.

Author Contributions: Conceptualization, M.U.K. and A.H.; formal analysis, C.W. and P.P.; investigation, C.W. and P.P.; resources, M.U.K.; writing-original draft preparation, C.W.; writing-review and editing, M.U.K., G.N., M.J.H., W.A.S., and K.K.; visualization, C.W.; supervision, M.U.K.; project administration, M.U.K.; funding acquisition, M.U.K. All authors have read and agreed to the published version of the manuscript.

Funding: This study was supported by grants from the Deutsche Forschungsgemeinschaft (DFG) research training group GRK2158 and from the DFG grant (INST208/690-1) for purchasing the Thermofisher Arrayscan XTI High Content Platform used in this study.

Acknowledgments: C.W. and M.U.K. gratefully acknowledge financial support from the Deutsche Forschungsgemeinschaft (DFG) research training group GRK2158. M.U.K. further acknowledges support from DFG for the Thermofisher Arrayscan XTI (Grant: INST 208/690-1 FUGG to M.U.K.). The authors acknowledge support by the Heinrich Heine University Düsseldorf for covering publication costs.

Conflicts of Interest: The authors declare no conflict of interest.

References

1. Cancer Stat Facts: Bladder Cancer. Available online: https://seer.cancer.gov/statfacts/html/urinb.html (accessed on 20 December 2019).
2. Bellmunt, J.; Orsola, A.; Leow, J.J.; Wiegel, T.; De Santis, M.; Horwich, A. Bladder cancer: ESMO Practice Guidelines for diagnosis, treatment and follow-up†. *Ann. Oncol.* **2014**, *25*, iii40–iii48. [CrossRef] [PubMed]
3. Calabro, F.; Sternberg, C.N. Neoadjuvant and adjuvant chemotherapy in muscle-invasive bladder cancer. *Eur Urol.* **2009**, *55*, 348–358. [CrossRef] [PubMed]
4. Yafi, F.A.; North, S.; Kassouf, W. First- and second-line therapy for metastatic urothelial carcinoma of the bladder. *Curr Oncol.* **2011**, *18*, e25–e34. [CrossRef] [PubMed]
5. Shen, D.W.; Pouliot, L.M.; Hall, M.D.; Gottesman, M.M. Cisplatin resistance: A cellular self-defense mechanism resulting from multiple epigenetic and genetic changes. *Pharmacol. Rev.* **2012**, *64*, 706–721. [CrossRef]
6. Siddik, Z.H. Cisplatin: Mode of cytotoxic action and molecular basis of resistance. *Oncogene* **2003**, *22*, 7265–7279. [CrossRef]
7. Galluzzi, L.; Senovilla, L.; Vitale, I.; Michels, J.; Martins, I.; Kepp, O.; Castedo, M.; Kroemer, G. Molecular mechanisms of cisplatin resistance. *Oncogene* **2012**, *31*, 1869–1883. [CrossRef]
8. Jones, P.A.; Baylin, S.B. The epigenomics of cancer. *Cell* **2007**, *128*, 683–692. [CrossRef]
9. Schulz, W.A.; Koutsogiannouli, E.A.; Niegisch, G.; Hoffmann, M.J. Epigenetics of urothelial carcinoma. *Methods Mol. Biol.* **2015**, *1238*, 183–215.
10. Baylin, S.B. DNA methylation and gene silencing in cancer. *Nat. Clin. Pract. Oncol.* **2005**, *2*, S4–S11. [CrossRef]
11. Jones, P.A.; Issa, J.P.; Baylin, S. Targeting the cancer epigenome for therapy. *Nat. Rev. Genet.* **2016**, *17*, 630–641. [CrossRef]
12. You, J.S.; Jones, P.A. Cancer genetics and epigenetics: Two sides of the same coin? *Cancer Cell* **2012**, *22*, 9–20. [CrossRef]
13. Chueh, A.C.; Tse, J.W.; Togel, L.; Mariadason, J.M. Mechanisms of histone deacetylase inhibitor-regulated gene expression in cancer cells. *Antioxid. Redox Signal.* **2015**, *23*, 66–84. [CrossRef] [PubMed]
14. De Ruijter, A.J.; van Gennip, A.H.; Caron, H.N.; Kemp, S.; van Kuilenburg, A.B. Histone deacetylases (HDACs): Characterization of the classical HDAC family. *Biochem. J.* **2003**, *370*, 737–749. [CrossRef]
15. Montezuma, D.; Henrique, R.M.; Jeronimo, C. Altered expression of histone deacetylases in cancer. *Crit. Rev. Oncog.* **2015**, *20*, 19–34. [CrossRef] [PubMed]
16. Niegisch, G.; Knievel, J.; Koch, A.; Hader, C.; Fischer, U.; Albers, P.; Schulz, W.A. Changes in histone deacetylase (HDAC) expression patterns and activity of HDAC inhibitors in urothelial cancers. *Urol. Oncol.* **2013**, *31*, 1770–1779. [CrossRef] [PubMed]

17. Suraweera, A.; O'Byrne, K.J.; Richard, D.J. Combination therapy with histone deacetylase inhibitors (HDACi) for the treatment of cancer: Achieving the full therapeutic potential of HDACi. *Front. Oncol.* **2018**, *8*, e92. [CrossRef]
18. Wu, Y.F.; Ou, C.C.; Chien, P.J.; Chang, H.Y.; Ko, J.L.; Wang, B.Y. Chidamide-induced ROS accumulation and miR-129-3p-dependent cell cycle arrest in non-small lung cancer cells. *Phytomedicine* **2019**, *56*, 94–102. [CrossRef]
19. Stenzel, K.; Hamacher, A.; Hansen, F.K.; Gertzen, C.G.W.; Senger, J.; Marquardt, V.; Marek, L.; Marek, M.; Romier, C.; Remke, M.; et al. Alkoxyurea-Based Histone Deacetylase Inhibitors Increase Cisplatin Potency in Chemoresistant Cancer Cell Lines. *J. Med. Chem.* **2017**, *60*, 5334–5348. [CrossRef]
20. Krieger, V.; Hamacher, A.; Gertzen, C.G.W.; Senger, J.; Zwinderman, M.R.H.; Marek, M.; Romier, C.; Dekker, F.J.; Kurz, T.; Jung, M.; et al. Design, Multicomponent Synthesis, and Anticancer Activity of a Focused Histone Deacetylase (HDAC) Inhibitor Library with Peptoid-Based Cap Groups. *J. Med. Chem.* **2017**, *60*, 5493–5506. [CrossRef]
21. Bandolik, J.J.; Hamacher, A.; Schrenk, C.; Weishaupt, R.; Kassack, M.U. Class I-Histone Deacetylase (HDAC) Inhibition is Superior to pan-HDAC Inhibition in Modulating Cisplatin Potency in High Grade Serous Ovarian Cancer Cell Lines. *Int. J. Mol. Sci.* **2019**, *20*, 3052. [CrossRef]
22. Pflieger, M.; Hamacher, A.; Oz, T.; Horstick-Muche, N.; Boesen, B.; Schrenk, C.; Kassack, M.U.; Kurz, T. Novel alpha,beta-unsaturated hydroxamic acid derivatives overcome cisplatin resistance. *Bioorg. Med. Chem.* **2019**, *27*, e115036. [CrossRef] [PubMed]
23. Reichert, N.; Choukrallah, M.A.; Matthias, P. Multiple roles of class I HDACs in proliferation, differentiation, and development. *Cell Mol. Life Sci.* **2012**, *69*, 2173–2187. [CrossRef] [PubMed]
24. Kaletsch, A.; Pinkerneil, M.; Hoffmann, M.J.; Jaguva Vasudevan, A.A.; Wang, C.; Hansen, F.K.; Wiek, C.; Hanenberg, H.; Gertzen, C.; Gohlke, H.; et al. Effects of novel HDAC inhibitors on urothelial carcinoma cells. *Clin. Epigenetics* **2018**, *10*, e100. [CrossRef] [PubMed]
25. Malempati, S.; Chang, B.H.; Reid, J.M.; Liu, X.; Minard, C.G.; Keller, C.; Fox, E.; Weigel, B. ADVL1513: Results of a phase 1 trial of entinostat, an oral histone deacetylase inhibitor, in pediatric patients with recurrent or refractory solid tumors. *J. Clin. Oncol.* **2018**, *36*, e10556. [CrossRef]
26. Window of Opportunity Study of Pembrolizumab Alone and in Combinations in Bladder Cancer 2019. Available online: https://clinicaltrials.gov/ct2/show/NCT03978624 (accessed on 9 November 2019).
27. Gosepath, E.M.; Eckstein, N.; Hamacher, A.; Servan, K.; von Jonquieres, G.; Lage, H.; Gyorffy, B.; Royer, H.D.; Kassack, M.U. Acquired cisplatin resistance in the head-neck cancer cell line Cal27 is associated with decreased DKK1 expression and can partially be reversed by overexpression of DKK1. *Int. J. Cancer* **2008**, *123*, 2013–2019. [CrossRef]
28. Hoffmann, M.J.; Koutsogiannouli, E.; Skowron, M.A.; Pinkerneil, M.; Niegisch, G.; Brandt, A.; Stepanow, S.; Rieder, H.; Schulz, W.A. The new immortalized uroepithelial cell line HBLAK contains defined genetic aberrations typical of early stage urothelial tumors. *Bladder Cancer.* **2016**, *2*, 449–463. [CrossRef]
29. Chou, T.-C.; Talalay, P. Quantitative analysis of dose-effect relationships: The combined effects of multiple drugs or enzyme inhibitors. *Adv. Enzym. Regul.* **1984**, *22*, 27–55. [CrossRef]
30. Shen, H.; Laird, P.W. Interplay between the cancer genome and epigenome. *Cell* **2013**, *153*, 38–55. [CrossRef]
31. Yoo, C.B.; Jones, P.A. Epigenetic therapy of cancer: Past, present and future. *Nat. Rev. Drug Discov.* **2006**, *5*, 37–50. [CrossRef]
32. Marks, P.A.; Rifkind, R.A.; Richon, V.M.; Breslow, R.; Miller, T.; Kelly, W.K. Histone deacetylases and cancer: Causes and therapies. *Nat. Rev. Cancer* **2001**, *1*, e194. [CrossRef]
33. Blum, W.; Klisovic, R.B.; Hackanson, B.; Liu, Z.; Liu, S.; Devine, H.; Vukosavljevic, T.; Huynh, L.; Lozanski, G.; Kefauver, C.; et al. Phase I study of decitabine alone or in combination with valproic acid in acute myeloid leukemia. *J. Clin. Oncol.* **2007**, *25*, 3884–3891. [CrossRef] [PubMed]
34. Juergens, R.A.; Wrangle, J.; Vendetti, F.P.; Murphy, S.C.; Zhao, M.; Coleman, B.; Sebree, R.; Rodgers, K.; Hooker, C.M.; Franco, N.; et al. Combination epigenetic therapy has efficacy in patients with refractory advanced non–small cell lung cancer. *Cancer Discov.* **2011**, *1*, e598. [CrossRef] [PubMed]
35. Najem, S.A.; Khawaja, G.; Hodroj, M.H.; Rizk, S. Synergistic effect of epigenetic inhibitors decitabine and suberoylanilide hydroxamic acid on colorectal cancer in vitro. *Curr. Mol. Pharmacol.* **2019**, *12*, 281–300. [CrossRef] [PubMed]

36. Nakagawa, M.; Oda, Y.; Eguchi, T.; Aishima, S.; Yao, T.; Hosoi, F.; Basaki, Y.; Ono, M.; Kuwano, M.; Tanaka, M.; et al. Expression profile of class I histone deacetylases in human cancer tissues. *Oncol. Rep.* **2007**, *18*, 769–774. [CrossRef]
37. Gilley, J.; Coffer, P.J.; Ham, J. FOXO transcription factors directly activate bim gene expression and promote apoptosis in sympathetic neurons. *J. Cell Biol.* **2003**, *162*, 613–622. [CrossRef]
38. Zhang, X.; Tang, N.; Hadden, T.J.; Rishi, A.K. Akt, FoxO and regulation of apoptosis. *Biochim. Biophys. Acta (BBA)-Mol. Cell Res.* **2011**, *1813*, 1978–1986. [CrossRef]
39. Papapetropoulos, A.; Fulton, D.; Mahboubi, K.; Kalb, R.G.; O'Connor, D.S.; Li, F.; Altieri, D.C.; Sessa, W.C. Angiopoietin-1 inhibits endothelial cell apoptosis via the Akt/survivin pathway. *J. Biol. Chem.* **2000**, *275*, 9102–9105. [CrossRef]
40. Gohr, K.; Hamacher, A.; Engelke, L.H.; Kassack, M.U. Inhibition of PI3K/Akt/mTOR overcomes cisplatin resistance in the triple negative breast cancer cell line HCC38. *BMC Cancer* **2017**, *17*, e711. [CrossRef]
41. Chou, T.-C. The combination index (CI<1) as the definition of synergism and of synergy claims. *Synergy* **2018**, *7*, 49–50.
42. Wang, C.; Engelke, L.; Bickel, D.; Hamacher, A.; Frank, M.; Proksch, P.; Gohlke, H.; Kassack, M.U. The tetrahydroxanthone-dimer phomoxanthone A is a strong inducer of apoptosis in cisplatin-resistant solid cancer cells. *Bioorg. Med. Chem.* **2019**, *27*, e115044. [CrossRef]
43. Engelke, L.H.; Hamacher, A.; Proksch, P.; Kassack, M.U. Ellagic acid and resveratrol prevent the development of cisplatin resistance in the epithelial ovarian cancer cell line A2780. *J. Cancer* **2016**, *7*, 353–363. [CrossRef] [PubMed]

3.2 Publication 2

The tetrahydroxanthone-dimer phomoxanthone A is a strong inducer of apoptosis in cisplatin-resistant solid cancer cells

Chenyin Wang[a], Laura Engelke[a], David Bickel[a], Alexandra Hamacher[a], Marian Frank[b], Peter Proksch[b], Holger Gohlke[a,c], Matthias U. Kassack[a]

[a] Institute of Pharmaceutical and Medicinal Chemistry, Heinrich-Heine-University Düsseldorf, 40225 Düsseldorf, Germany

[b] Institute of Pharmaceutical Biology and Biotechnology, Heinrich-Heine-Universität Düsseldorf, 40225 Düsseldorf, Germany

[c] John von Neumann Institute for Computing (NIC), Jülich Supercomputing Centre (JSC) & Institute for Complex Systems - Structural Biochemistry (ICS 6), Forschungszentrum Jülich GmbH, 52425 Jülich, Germany

Published in: Bioorganic and Medicinal Chemistry, 2019.

Contribution: First authorship, performed experiments including MTT assay, apoptosis assay, cell cycle analysis, mitochondrial membrane potential detection, caspase activation, and cytoplasm membrane integrity test. Evaluated the data and wrote the manuscript.

Abstract

Platinum compounds are the first-line therapy for many types of cancer. However, drug resistance has frequently been reported for and is a major limitation of platinum- based chemotherapy in the clinic. In the current study, we examined the anti-tumor activity of phomoxanthone A (PXA), a tetrahydroxanthone dimer isolated from the endophytic fungus *Phomopsis longicolla*, in several solid cancer cell lines and their cisplatin-resistant sub-cell lines. PXA showed strong cytotoxic effects with IC_{50} values in the high nanomolar or low micromolar range in MTT assays. IC_{50} values of PXA were lower than those of cisplatin. Remarkably, equipotent anti-cancer activity was found in cisplatin-sensitive and respective cisplatin-resistant cells. Anticancer effects of PXA were studied in further detail in ovarian cancer (A2780) and bladder cancer (J82) cell pairs. PXA led to rapid depolarization of the mitochondrial membrane potential and strong activation of caspase 3 and 7, eventually resulting in strong induction of apoptosis. These effects occurred again both in sensitive and resistant cell lines. IC_{50} values of PXA from MTT and mitochondrial membrane depolarization assays were in good agreement. Configurational free energy computations indicate that both the neutral and singly negatively charged PXA show membrane partitioning and can penetrate the inner mitochondrial membrane. PXA treatment did not damage the plasma membranes of cancer cells, thus excluding unspecific membrane effects. Further, PXA had neither an effect on intracellular ROS nor on reduction of ROS after hydrogen peroxide treatment. In conclusion, our studies present PXA as a natural compound with strong apoptotic anticancer effects against platinum-resistant solid cancers. This may open new treatment options in clinically resistant malignancies.

Bioorganic & Medicinal Chemistry 27 (2019) 115044

Contents lists available at ScienceDirect

Bioorganic & Medicinal Chemistry

journal homepage: www.elsevier.com/locate/bmc

The tetrahydroxanthone-dimer phomoxanthone A is a strong inducer of apoptosis in cisplatin-resistant solid cancer cells

Chenyin Wang[a], Laura Engelke[a], David Bickel[a], Alexandra Hamacher[a], Marian Frank[b], Peter Proksch[b], Holger Gohlke[a,c], Matthias U. Kassack[a,*]

[a] Institute of Pharmaceutical and Medicinal Chemistry, Heinrich Heine University Düsseldorf, 40225 Düsseldorf, Germany
[b] Institute of Pharmaceutical Biology and Biotechnology, Heinrich Heine Universität Düsseldorf, 40225 Düsseldorf, Germany
[c] John von Neumann Institute for Computing (NIC), Jülich Supercomputing Centre (JSC) & Institute for Complex Systems – Structural Biochemistry (ICS 6), Forschungszentrum Jülich GmbH, 52425 Jülich, Germany

ARTICLE INFO

Keywords:
Phomoxanthone A
Cisplatin resistance
Mitochondrial membrane potential
Apoptosis
Caspase activation
Configurational free energy computations

ABSTRACT

Platinum compounds are the first-line therapy for many types of cancer. However, drug resistance has frequently been reported for and is a major limitation of platinum-based chemotherapy in the clinic. In the current study, we examined the anti-tumor activity of phomoxanthone A (PXA), a tetrahydroxanthone dimer isolated from the endophytic fungus *Phomopsis longicolla*, in several solid cancer cell lines and their cisplatin-resistant sub-cell lines. PXA showed strong cytotoxic effects with IC_{50} values in the high nanomolar or low micromolar range in MTT assays. IC_{50} values of PXA were lower than those of cisplatin. Remarkably, equipotent anti-cancer activity was found in cisplatin-sensitive and respective cisplatin-resistant cells. Anticancer effects of PXA were studied in further detail in ovarian cancer (A2780) and bladder cancer (J82) cell pairs. PXA led to rapid depolarization of the mitochondrial membrane potential and strong activation of caspase 3 and 7, eventually resulting in strong induction of apoptosis. These effects occurred again both in sensitive and resistant cell lines. IC_{50} values of PXA from MTT and mitochondrial membrane depolarization assays were in good agreement. Configurational free energy computations indicate that both the neutral and singly negatively charged PXA show membrane partitioning and can penetrate the inner mitochondrial membrane. PXA treatment did not damage the plasma membranes of cancer cells, thus excluding unspecific membrane effects. Further, PXA had neither an effect on intracellular ROS nor on reduction of ROS after hydrogen peroxide treatment. In conclusion, our studies present PXA as a natural compound with strong apoptotic anticancer effects against platinum-resistant solid cancers. This may open new treatment options in clinically resistant malignancies.

1. Introduction

Cancer is one of the major leading causes of death worldwide. It is predicted that there are approximately 1.7 million new cases of cancer and about 600,000 deaths from cancer are projected to occur in the US in 2018. The treatment options of cancer generally include surgery, radiation therapy, and chemotherapy. Cis- or carboplatin are among the most potent chemotherapeutic drugs and used to treat many types of cancers including ovarian, bladder, and head and neck cancers.[1] The cytotoxicity of platinum compounds is mediated by the formation of DNA adducts leading to apoptosis and cell cycle arrest.[2] The sensitivity or resistance of cancer cells against cisplatin is an important factor for treatment options.[3–4] Acquisition of cisplatin resistance in patients has been observed for many years. Generally, development of platinum resistance is multifactorial, including pre-target mechanisms leading to the reduction in intracellular drug accumulation, on-target mechanisms increasing the rate of DNA damage repair, and post-target effects leading to defects in apoptotic signal transduction pathways which are normally activated in response to DNA damage. These processes will then inhibit apoptosis and subsequently lead to drug resistance.[5] Apoptosis is a vital component for many processes including embryonic development and tissue homoeostasis.[6] Apoptosis mainly proceeds through the activation of intrinsic and/or extrinsic signal transduction pathways. The major characteristic features of apoptosis include cell shrinkage, condensation of chromatin, and DNA fragmentation.[7] The extrinsic apoptosis pathway is triggered by activation of death receptors with recruitment of cytoplasmic adapter proteins followed by activation of caspase-8 and finally activating caspase 3.[8] The intrinsic or

* Corresponding author.
E-mail address: matthias.kassack@uni-duesseldorf.de (M.U. Kassack).

https://doi.org/10.1016/j.bmc.2019.115044
Received 9 May 2019; Received in revised form 18 July 2019; Accepted 6 August 2019
Available online 08 August 2019

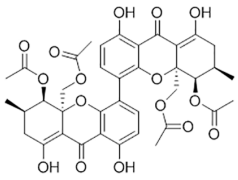

Figure 1. Structure of the mycotoxin phomoxanthone A (PXA) isolated from the fungus *Phomopsis longicola.*

mitochondrial pathway is initiated by a diverse array of stimuli causing reduction in the mitochondrial membrane potential and eventually leading to cellular apoptosis.[9] However, unlike healthy cells, the down regulation or mutation of pro-apoptotic genes are associated with dysregulation of apoptosis in cancer and leads to uncontrolled cell proliferation.[10] Therefore, promoting apoptosis is an important strategy for novel anti-cancer drug discovery.

Natural products have been a great source for anti-cancer drugs. For instance, paclitaxel, a plant-derived diterpenoid interacting with β-tubulin, thus inhibiting the degradation of microtubules and inducing apoptosis, is commonly used for the treatment of many types of cancer.[11] Phomoxanthone A (PXA), a tetrahydroxanthone dimer derived from the mangrove-associated fungus *Phomopsis longicolla*, was previously shown by our groups to exhibit potent cytotoxic and antibiotic activity (Figure 1).[12] A review on the source, stereochemistry, biosynthesis, structure–activity relationships, and anticancer activities of PXA were summarized by Frank et al.[13] PXA demonstrates low micromolar or even 3-digit nanomolar IC_{50} values (MTT assay) in solid and lymphoma cancer cell lines, respectively. Interestingly, PXA retains high selectivity (> 100) for cancer over non-cancer cells as estimated in peripheral blood mononuclear cells (PBMCs).[13] A recent report provided further insight into the mechanism of PXA in lymphoma cells.[4] PXA leads to a rapid depolarization of the mitochondrial potential and disruption of the inner mitochondrial membrane. The molecular target however, is still unknown.[4]

Considering the severity of platinum resistance in clinical patient cases, the findings about PXA encouraged us to study the effects of PXA in models of cisplatin-sensitive and –resistant human cancers. Here, the ovarian cancer cell line A2780 as well as the urinary bladder cancer cell line J82 and their cisplatin resistant sublines were used. Clinically relevant cisplatin resistance was induced by intermittent treatment with cisplatin over several weeks to mimic clinical treatment cycles. Resistance developed after approximately 8 to 14 weeks.[14,15] In contrast to cisplatin which gave clinically relevant resistance factors between sensitive and resistant cell lines of 2 to 4, the potency of PXA was similar in sensitive and resistant cell lines. Furthermore, PXA turned out as a strong depolarizer of mitochondrial membrane potential and strong inductor of apoptosis with similar potency in cisplatin-sensitive and –resistant cell lines whereas cisplatin was much less potent in apoptosis induction in resistant cancer cell lines. PXA may thus serve as a new natural compound to overcome the clinically highly relevant problem of platinum resistance in cancer patients.

2. Results and discussion

2.1 Determination of the cytotoxic potential of PXA

The cytotoxic activity of PXA was tested against a panel of human solid cancer cell lines and their cisplatin resistant sublines using the MTT assay. Results from earlier tests and from this study are summarized in Table 1. PXA showed potent cytotoxicity in all cell lines. IC_{50} values of PXA were 2 to 10-fold lower than IC_{50} values of cisplatin except for the bladder cancer cell line J82. Figure 2 compares the cytotoxicity of cisplatin and PXA in the various cell lines. The ratio of the IC_{50} values of cisplatin and PXA is 2 to 10 (except for J82).

Table 1
Antiproliferative effects of PXA in different human cancer cell lines.

Cell line	IC_{50} [μM]	
	Cisplatin	PXA
A2780*	3.98	0.58
A2780CisR*	12.6	1.38
MDA-MB-231	24.5	3.7
MDA-MB-231CisR	44.7	4.37
Cal27*	10.2	5.25
Cal27CisR*	38.0	5.62
Kyse510*	2.51	0.76
Kyse510CisR*	8.51	0.79
J82	2.29	3.23
J82CisR	7.76	2.04
K562	9.55	1.86
HCT116	16.2	1.82

Values are the mean of three independent experiments each carried out in triplicates. *IC_{50} values were reported previously.[12]

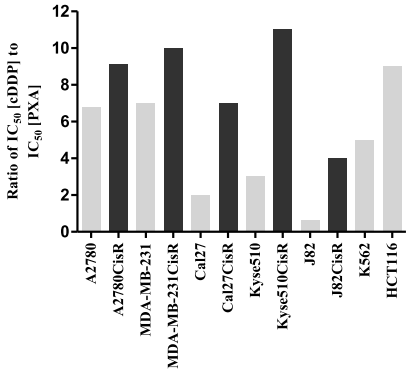

Figure 2. Ratios of IC_{50} values of cisplatin and PXA in different cell lines.

Interestingly, in all resistant cell lines (termed …CisR), the ratio of IC_{50} values increases (e.g. J82, Kyse510). This indicates that PXA is acting equipotent at cisplatin-resistant and cisplatin-sensitive cell lines and may thus serve as a suitable cytotoxic agent to address cisplatin-resistant cancers. In A2780 and A2780CisR cells, IC_{50} values of PXA were 7-fold and 9-fold lower compared to cisplatin, respectively (Table 1). The IC_{50} value of cisplatin was increased 4 times in the esophageal cell line Kyse510CisR cells compared to Kyse510. However, PXA exhibited similar cytotoxic effects in Kyse510 and Kyse510CisR cell lines (approx. 0.8 μM). Furthermore, the cytotoxicity of PXA was also investigated in the chronic myelogenous leukemia cell line K562 displaying an IC_{50} value of 1.86 μM which is 5 times lower than cisplatin (Table 1). PXA exhibited equipotent cytotoxicity against several other pairs of cisplatin-sensitive and cisplatin-resistant cell lines, such as the triple-negative breast cancer cell pair MDA-MB-231 and oral squamous cell carcinoma cell line Cal27. Even though PXA is slightly less potent in J82 cells (human bladder cancer) compared to cisplatin, the IC_{50} value of PXA is still in the low micromolar range and more importantly, PXA showed an even lower IC_{50} value in J82CisR cells.

Since PXA had the highest potency in A2780 cells (0.58 μM) and PXA was even more potent (1.6-fold) in J82CisR compared to J82, further studies on anticancer effects were carried out in these two pairs of cell lines. Remarkably, PXA has a rapid onset of its cytotoxic effect compared to cisplatin. Figure 3 shows the time-dependent concentration-effect curves of PXA and cisplatin in A2780 and A2780CisR. Whereas PXA showed only 2.5-fold (A2780) or 1.4-fold (A2780CisR) differences in IC_{50} values between 24 h and 72 h incubation time (MTT assay), cisplatin gave differences of 10.4-fold (A2780) and 6.9-fold (A2780CisR). These data demonstrate a fast cytotoxic effect of PXA.

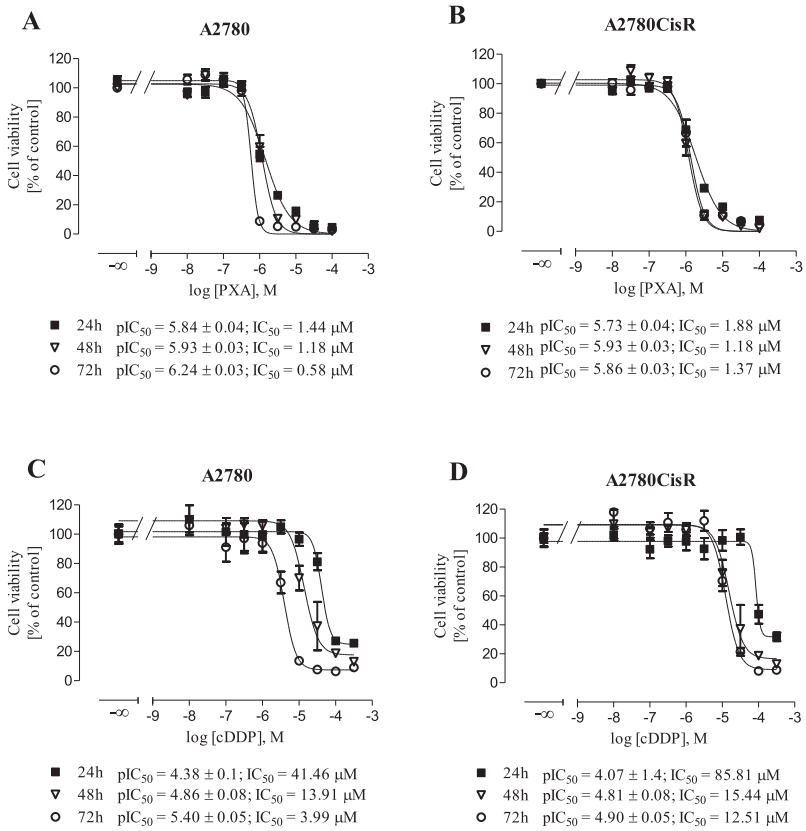

Figure 3. Time-dependent concentration-effect-curves of PXA and cisplatin. A2780 and A2780CisR cells were treated with PXA (A, B) or cisplatin (C, D) for different times. Data shown are average ± SEM of at least three independent experiments.

2.2 PXA induces G1 cell cycle arrest in A2780 and A2780CisR

MTT assays demonstrated a strong inhibition of cell proliferation upon PXA treatment. This prompted us to study cell cycle arrest after PXA treatment. The cell cycle profiles of A2780/A2780CisR and J82/J82CisR after PXA treatment are displayed in Figure 4. In A2780 and A2780CisR, the fraction of cells in G1 phase significantly increased in a dose-dependent manner after 24 h PXA treatment from 61.8% to 78.9% (A2780) and 68.7% to 81.1% (A2780CisR). In J82 and J82CisR cells however, no significant changes occurred in the cell cycle phases upon PXA treatment. These data suggest that the G1 phase cell cycle arrest induced by PXA is a cell type- and concentration-dependent effect.

2.3 PXA is a strong inducer of apoptosis in sensitive and cisplatin-resistant A2780 and J82 cell lines

PXA was further investigated for its effects on induction of apoptosis. Apoptosis induces several morphological changes including membrane blebbing, DNA degradation, and the formation of the apoptosome. Among these events, degradation of DNA characterized by an increased fraction of sub-G1 cells is a good marker for the detection of apoptosis. Figure 5 displays the effects of 24 h PXA treatment on apoptosis. In A2780, sub-G1 fraction increased (from 10% untreated control) dose-dependently up to almost 70%. Approx. 2x IC_{50} of PXA (1 µM) resulted already in 42% sub-G1 whereas 5x IC_{50} of cisplatin (20 µM) was needed to obtain a similar sub-G1 rate (47%), demonstrating the superior potency of PXA over cisplatin to induce apoptosis. In A2780CisR, PXA was even more potent: 0.7x IC_{50} of PXA (1 µM) induced already almost 70% sub-G1 whereas 20 µM cisplatin (approx. 2x IC_{50}) did not significantly increase sub-G1 over untreated control. J82 cells gave a similar result: 1.6x IC_{50} PXA (5 µM) resulted in a similar amount of apoptotic cells (53%) as 8.7x IC_{50} cisplatin (20 µM). J82CisR cells seemed to be slightly more resistant to undergo apoptosis: 2.5x IC_{50} PXA (5 µM) or 2.5x IC_{50} cisplatin (20 µM) resulted in approx. 35% sub-G1 cells. Yet, considering 72 h MTT assay data (Table 1), it is clear that PXA is almost 4-fold more potent than cisplatin in J82CisR.

2.4 PXA treatment leads to rapid depolarization of the mitochondrial membrane potential

Mitochondria are cellular key players in the synthesis of ATP by utilizing the electrochemical gradient under aerobic conditions or as central regulators of apoptosis by maintenance of transmembrane potential and release of apoptogenic proteins.[16,17]

The strong induction of apoptosis by PXA prompted us to examine mitochondrial function by analyzing the mitochondrial membrane potential (ΔΨm) upon PXA treatment. The accumulation of tetramethylrhodamine ethyl ester (TMRE) in mitochondria as surrogate for ΔΨm[18] was detected by flow cytometry or fluorescence microscopy. As shown in Figure 6, PXA induced rapid and concentration-dependent decreases in fluorescence intensity of TMRE (measured by flow cytometry) in both pairs of A2780 and J82 cells after 1 h or 2 h treatment (Figure 6A, B, C, D). IC_{50} values of PXA in ΔΨm breakdown (1 h or 2 h) were remarkably similar to IC_{50} values obtained by MTT (72 h, Table 1). Figure 6E and F show the concentration-dependent effect of 24 h treatment of PXA on ΔΨm in A2780 and A2780CisR, respectively.

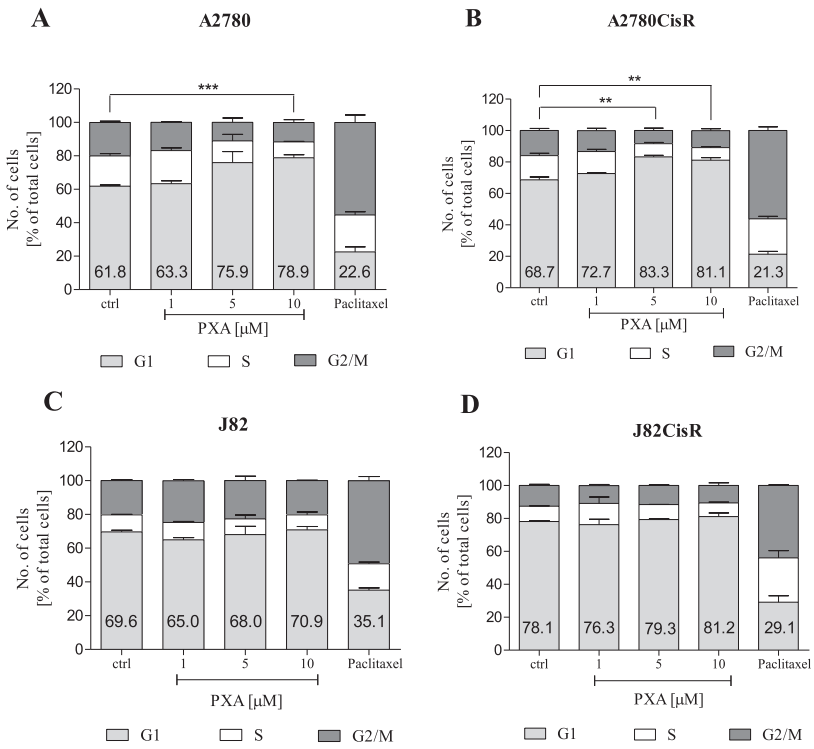

Figure 4. PXA induced cell cycle arrest is concentration and cell line dependent. After a 24 h incubation with the indicated concentrations, PXA was able to induce G1 cell cycle arrest in A2780 (A) and A2780CisR cells (B), but not in the J82 cell lines (C, D). Medium was used as control for untreated cells, paclitaxel as control for G2/M arrest. Data shown are the average ± SEM of three independent experiments. ***P < 0.001, **P < 0.01, *P < 0.05 in comparison to the untreated control.

Further, Figure 6E and F (right part, respectively) show the time-dependent effect of 1 µM PXA. 1 µM PXA for 1 h significantly reduced ΔΨm to approx. 73%, and 2 h incubation reduced to approx. 50% of untreated control, whereas 24 h incubation reduced ΔΨm to positive control (20 µM carbonyl cyanide m-chlorophenyl hydrazine, CCCP).[19] To confirm the approx. 3x lower potency of PXA in J82 and J82CisR compared to A2780 and A2780CisR cells (Figure 6A, B, C, D: IC_{50} values for 2 h incubation were around 1 µM in A2780/A2780CisR and around 3 µM in J82/J82CisR), fluorescence imaging was additionally performed for 2 h incubation in J82 (Figure 6G) and J82CisR (Figure 6H). It was confirmed that 1 µM PXA had no effect (not significantly different from untreated control) whereas 5 and 10 µM PXA led to complete ΔΨm breakdown (not significantly different from CCCP control). These results suggest that PXA is a compound targeting mitochondria and inducing a rapid decrease of ΔΨm in both A2780 and J82 cell lines as well as their cisplatin resistant subclones. Depolarized mitochondrial membrane potential may then trigger the intrinsic apoptotic pathway. These data are in full agreement with data recently published using lymphoma cells.[4]

2.5 PXA increases intracellular Ca^{2+} concentration

Rapid and strong breakdown of the mitochondrial membrane potential may be associated with Ca^{2+} release and increased cytoplasmic Ca^{2+} concentrations. This may in turn lead to the activation of Ca^{2+}-sensitive enzymes, e.g. involved in the apoptotic cascade or activation of caspases.[20] Thus, intracellular Ca^{2+} concentrations were determined in A2780 and A2780CisR in the presence and absence of 1 mM

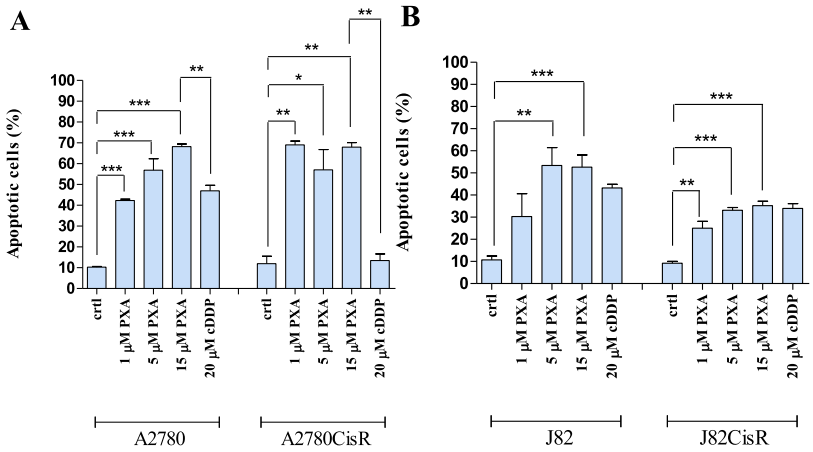

Figure 5. PXA mediates its antiproliferative effects via apoptosis. 24 h incubation with the indicated concentrations of PXA induced apoptosis in A2780 (A), A2780CisR (B), J82 (C), and J82CisR (D). As control, medium was used, and cisplatin served as positive control. Data are means ± SEM. ***P < 0.001, **P < 0.01, *P < 0.05, when compared with the untreated control group.

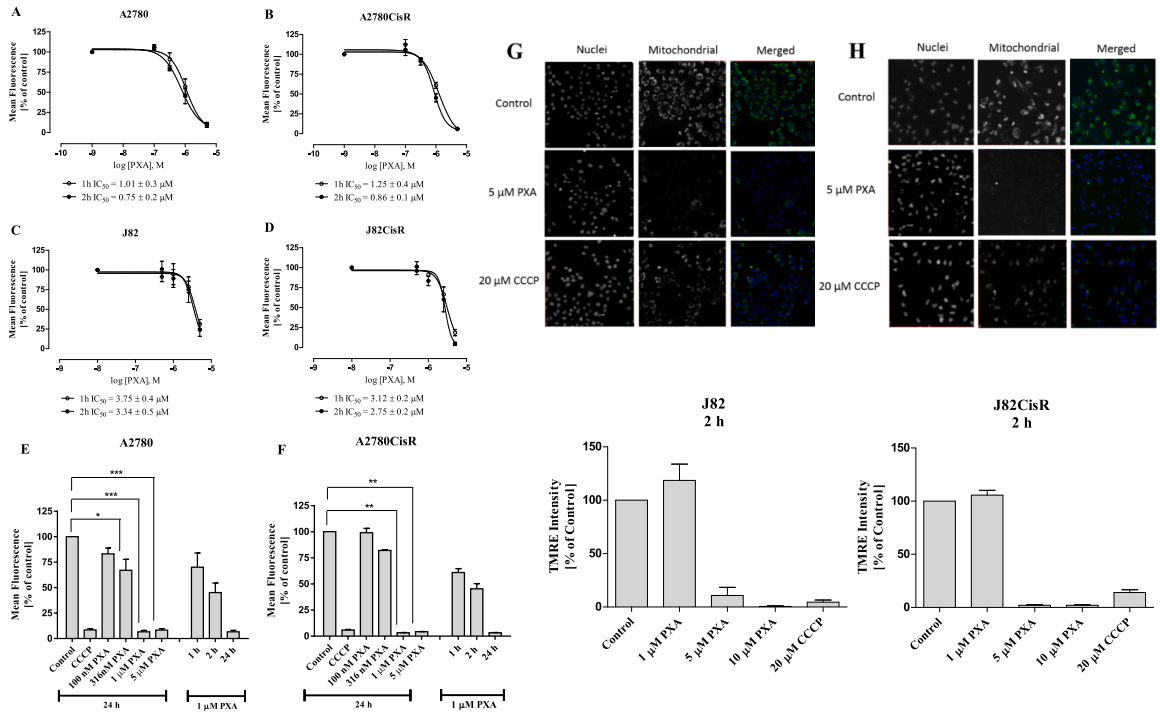

Figure 6. PXA depolarized mitochondrial membrane potential. A2780 (A), A2780CisR (B), J82 (C), and J82CisR (D) were treated for 1 h or 2 h with different concentrations of PXA before the mitochondrial potential was measured by flow cytometry. Medium was used as negative control and 20 µM CCCP was used as positive control. Further, A2780 (E) and A2780CisR cells (F) were treated with increasing concentrations of PXA for 24 h. In addition, Fig. 6E and F show the time-dependent depolarization of the membrane potential (analysis by flow cytometry) at 1 µM PXA. Furthermore, mitochondrial membrane potential was measured by fluorescence imaging in J82 (G) and J82CisR cells (H) after 2 h incubation. Data shown are mean ± SEM. $^{***}P < 0.001$, $^{**}P < 0.01$, $^{*}P < 0.05$ in comparison to the untreated control cells.

extracellular Ca^{2+} over 30 min after addition of PXA. 10 and 30 µM PXA led to a significant increase in intracellular Ca^{2+} in absence or presence of extracellular Ca^{2+} (Figure 7) whereas the Ca^{2+} increase induced by 1 µM PXA was only significant in the absence of extracellular Ca^{2+}. Mitochondrial membrane damage and increase in intracellular Ca^{2+} are thus hallmarks of the effects of PXA. Interestingly, Böhler et al. have reported that Ca^{2+} release upon PXA treatment is likely to be originated from the mitochondria (in lymphoma cells). It thus seems that mitochondrial damage by PXA results in Ca^{2+} release thereof and depolarization of the mitochondrial membrane potential.[4] The molecular target of PXA remains however elusive.

2.6 PXA leads to the activation of caspase 3/7 and reduces expression of anti-apoptotic proteins

The collapse of ΔΨm triggers the process of apoptosis soon after by activation of caspases that among others inactivate negative regulators of apoptosis such as Bcl-2.[21] Caspases are mainly divided into two subgroups known as “initiator caspases” and “executioner caspases” depending on their functions in apoptosis. Caspase 3 and 7, sharing high sequence similarities with each other, belong to the family of executioner caspases. The activation of these caspases is essential for the terminal phase of apoptosis.[22] Because of the finding that PXA results in the depolarization of ΔΨm, we tested the influence of PXA treatment on the activation of caspase 3 and 7 using fluorescence imaging. In untreated cells, basal activation of caspases 3/7 was 1.4%, 0.8%, 1.1%, and 0.5% in A2780, A2780CisR, J82, and J82CisR, respectively (Figure 8). 10 µM PXA (17x IC_{50} in A2780; 7x IC_{50} in A2780CisR) increased caspase 3/7 positive cells to 83% in A2780 and 71% in A2780CisR whereas 100 µM cisplatin gave only 37% (A2780) and 12% (A2780CisR) even though the cisplatin concentration was relatively higher: 25x IC_{50} in A2780 and 8x IC_{50} in A2780CisR (Figure 8F). Similar data were obtained for J82 and J82CisR using 50 or 30 µM PXA, respectively (Figure 8G). Notably, the cisplatin-resistant cell line J82CisR was more sensitive to PXA as can be seen by 90% caspase 3/7 positive cells with 30 µM PXA whereas in J82 cells, the use of 50 µM PXA resulted in only 60% caspase 3/7 positive cells. These data are consistent with our findings described above that PXA is more potent in J82CisR in MTT assay (Table 1). Further, activation of caspase 3/7 was accompanied by nuclear condensation showing reduced size and increased intensity of nuclei (Figure 8A, B, C, D).

In addition to caspase 3/7 activation, we examined differences in the expression of pro- and antiapoptotic proteins after PXA treatment by means of a commercial proteome profiler in A2780 and A2780CisR cell lines (Figure 9). The proteome profiler confirmed an increase in cleaved caspase 3 upon PXA treatment. Additionally, PXA treatment reduced the expression of cIAP-1 (cellular inhibitor of apoptosis protein 1), a member of the IAP family, and of claspin, another anti-apoptotic protein involved in the checkpoint of the cell cycle. Taken together, these results demonstrate that PXA induces apoptosis after collapse of the mitochondrial membrane potential, activation of caspase 3/7 and by suppressing the expression of anti-apoptotic proteins.

2.7 PXA treatment does not rupture the plasma membrane

Disruption of the plasma membrane is a hallmark feature to distinguish between apoptotic and necrotic cell death. It is commonly accepted that cells undergoing apoptosis are phagocytized before

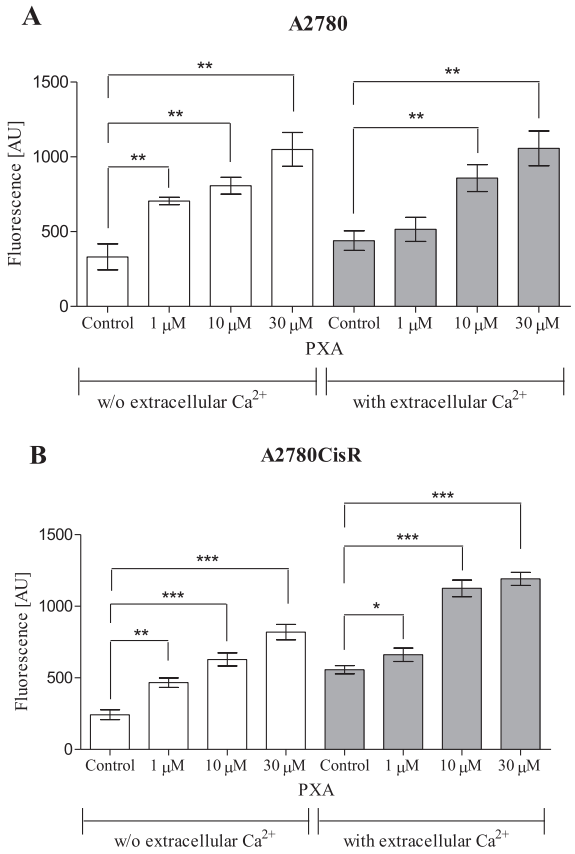

Figure 7. PXA increased concentration of intracellular Ca^{2+}. A2780 (A) and A2780CisR (B) were treated for 30 min with increasing concentrations of PXA while intracellular Ca^{2+} concentration was monitored. Data shown are mean ± SEM of three experiments. $^{***}P < 0.001$, $^{**}P < 0.01$, $^{*}P < 0.05$ in comparison to the untreated control cells.

membrane rupture and a release of intracellular components causing inflammation is prevented. However, a disruption of the cell membrane may occur in apoptotic cells due to secondary necrosis.[23] Therefore, we examined cell membrane integrity after PXA treatment. A2780 and A2780CisR cells were treated with different concentrations of PXA or cisplatin or triton-X-100 as control for 24 h, a time point which has shown an activation of caspase 3/7 and apoptosis induction. As Figure 10 shows, PXA had no effect on membrane integrity up to 10 μM. In contrast, the positive control triton X-100 showed 87% and 92% PI stained cells in A2780 and A2780CisR, respectively, indicating a rupture of the cell membrane. Given the fact that the number of PI stained cells did not raise with increasing concentrations of PXA, we suggest that PXA induces apoptosis but no membrane damage and no secondary necrosis.

2.8 PXA does not affect the generation of reactive oxidative species (ROS)

Many natural products are known to affect ROS levels, e.g. (poly) phenolic compounds. Oxidative stress may play a role in the generation and treatment of cancer cells.[24] We thus wanted to analyze if the tetrahydroxanthone derivative PXA has any impact on intracellular ROS levels. A2780 and A2780CisR cells were treated with PXA for 18 h, then labeled with H_2DCF-DA (2',7'-dichlorodihydrofluoresceine diacetate) treated with or without 250 μM H_2O_2 for 1 h, and then analyzed for ROS by flow cytometry (Figure 11). PXA had no effect on basal ROS levels and showed only a slight, but no significant reduction of ROS induced by H_2O_2.

2.9 Potential of mean force computations indicate that PXA in neutral and singly deprotonated states can penetrate the inner mitochondrial membrane

Due to the lack of experimental pK_a values for PXA, we computed these for PXA in aqueous environment.[25,26] The pK_a values indicate that the hydroxyl groups in 8- and 8′-position are the most acidic functional groups ($pK_a = 5.1 \pm 1.1$, respectively). Thus, the computations do not reveal a mutual influence due to deprotonation of one hydroxyl group onto the pK_a value of the other group, which may be explained by the large separation between the two groups. Therefore, the doubly deprotonated species of PXA is predicted to be the predominant species under physiological conditions in aqueous solution. However, in a low dielectric medium such as a lipid bilayer membrane, pK_a values are known to increase,[27] which would shift the (de)protonation equilibrium to the side of the less charged species.

To address the question if differently charged PXA species can penetrate the inner mitochondrial membrane, which is a prerequisite for transferring protons across the membrane, we performed potential of mean force (PMF) computations of PXA penetration using umbrella sampling[28] and post-processing with the Weighted Histogram Analysis Method.[29] Prior to that, reference points of the sampling path were generated by steered molecular dynamics simulations, starting from the PXA species located at the membrane center and pulling it along the membrane normal (Figure 12A). Note that we paid close attention that the membrane composition in our simulations resembles that of the inner mitochondrial membrane in vivo.[30] As a reaction coordinate, the distance along the z axis between the membrane center and the center of mass of PXA was taken, with $z = \pm 19$ Å indicating the location of the polar head group/solvent interface (Supplementary Fig. 1A). The umbrella windows display considerable overlap regarding the frequency distribution of values for the reaction coordinate (Supplementary Fig. 2A, C, E). Furthermore, computing the PMFs with increasing sampling intervals show that the PMFs appear converged after 30–40 ns of sampling per window (Supplementary Fig. 2B, D, F). Accordingly, the statistical error was estimated by splitting the sampled data into equally sized chunks of 5 ns length, which exceeds the relaxation times in water or a membrane by at least two orders of magnitude. Computing the PMF for each chunk independently, a standard error of the mean of < 0.4 kcal mol^{-1} along the PMFs was obtained.

For both the uncharged and singly charged PXA, the global minima of the PMFs are located at $z = 13$ Å and ~−2.8 kcal mol^{-1} (Figure 12B and C), revealing that a semi-immersed state of PXA within the membrane (state I, Figure 12E) is thermodynamically more favorable than a fully solvent-exposed state. In this state, the hydrophobic part of PXA is located towards the interior of the membrane, whereas the polar part is located close to the head group region, carrying a shell of water molecules. Performing unbiased MD simulations of 500 ns lengths as controls starting from PXA located at the membrane center confirm this finding in that the most frequently sampled distance of PXA from the center is at $z = 12.5$–13.0 Å (Supplementary Figure 1B, C). A small energy barrier of ~1.5 kcal mol^{-1} is observed at $z = 25$ Å, separating the semi-immersed state from the solvent-exposed one. Here, PXA is in proximity to the polar head groups of the lipids (state II, Figure 12E). The height of the energy barrier to pass the membrane is 3.8 and 6.4 kcal mol^{-1} with respect to the fully solvent-exposed state for PXA^0 and PXA^{-1}, respectively, and 6.7 and 9.2 kcal mol^{-1} with respect to state I, respectively. These barrier heights are markedly lower than those found for protein-free phosphatidylcholine, -ethanol, and -glycin lipid flip-flop in respective membranes.[31] Employing Eyring theory[32] at $T = 300$ K, kinetic rates of $1.4 \cdot 10^8$ to $9.9 \cdot 10^9$ s^{-1} are obtained, although obtaining a barrier height pertinent to kinetics via a PMF has been debated.[33] By contrast, the doubly charged species is most favorable in water, and the barrier height with respect to the fully solvent-exposed

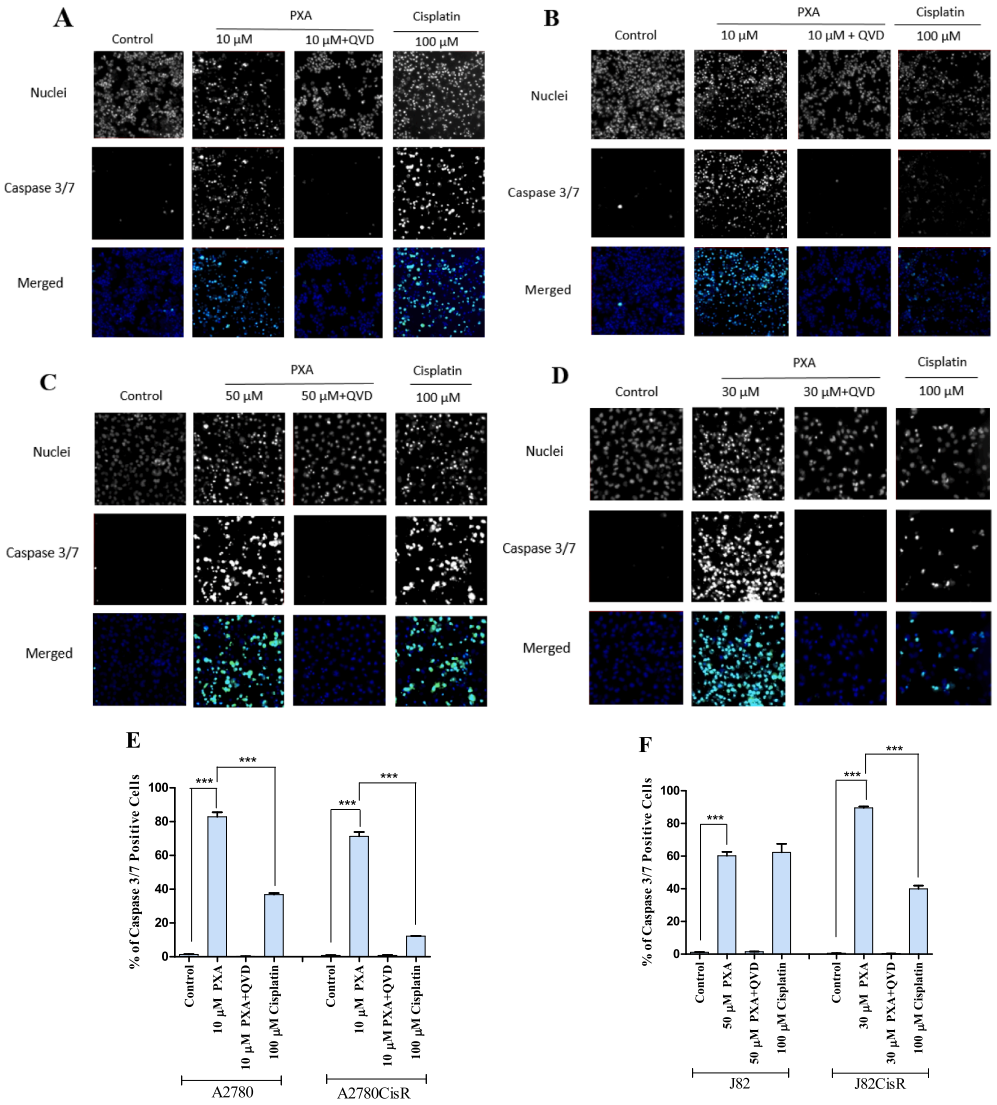

Figure 8. PXA-induced apoptosis is mediated via caspase3/7 activation. A2780 (A), A2780CisR (B), J82 (C), and J82CisR (D) were treated for 24 h with the indicated concentrations of PXA. Medium was used as control for untreated cells and cisplatin and staurosporine were used as positive control for caspase 3/7 activation. Cells were stained with Hoechst 33,342 (blue) for cell nuclei and CellEvent Caspase-3/7 green detection reagent for the activation of caspase 3/7. Quantification of caspase 3/7 positive cells of A2780, A2780CisR, J82, and J82CisR are displayed in (E) and (F). Data shown are mean ± SEM from three experiments. ***$P < 0.001$ in comparison to the untreated control cells. (For interpretation of the references to colour in this figure legend, the reader is referred to the web version of this article.)

state for passage through the membrane is 9.5 kcal mol^{-1} (Figure 12D), 1.5- to 2.5-fold higher than for PXA^0 and PXA^{-1}, leading to a 100-fold slower kinetic rate.

Taken together, our simulation results indicate that both the PXA^0 and PXA^{1-} species, but less so PXA^{2-}, show membrane partitioning and can penetrate the inner mitochondrial membrane with a high rate, similar to what can be estimated from membrane permeabilities of non-electrolyte compounds such as benzoic acid and codeine.[34] These properties of the differently protonated PXA species may contribute to the transfer of protons across the mitochondrial membrane: In our simulations, the membrane potential of the mitochondrial membrane was not considered, which would drive the passage of negatively charged deprotonated PXA towards the intermembrane space, where it can take up a proton and penetrate back as neutral PXA across the membrane. Overall, these processes might allow PXA to act as a proton shuttle and dissipate the proton gradient along the inner mitochondrial membrane.

3 Conclusion

PXA is a strong inducer of mitochondrial membrane potential breakdown, subsequent caspase activation and apoptosis. Remarkably, the effect of PXA is equipotent (or slightly more potent) in cisplatin-resistant and cisplatin-sensitive cancer cell lines. Whereas the mode of action is still not fully understood, PXA leads to an increase in cytosolic Ca^{2+} concentration released from intracellular stores within a time scale that is comparable to the mitochondrial membrane potential

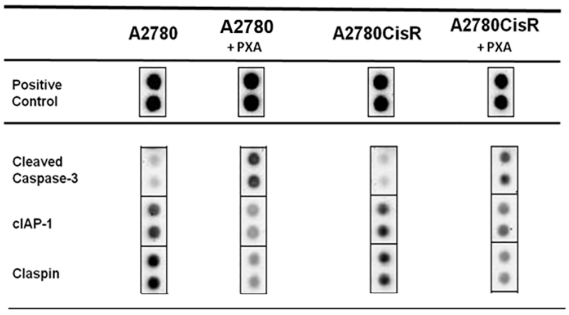

Figure 9. PXA rises the level of pro-apoptotic proteins and inhibits anti-apoptotic proteins. A2780 and A2780CisR cells were treated for 24 h with 5 μM PXA.

breakdown. These events then lead to caspase activation and apoptosis. Potential of mean force computations of PXA in an inner mitochondrial membrane environment suggest that PXA can act as a proton shuttle along the inner mitochondrial membrane and thus degrade the proton gradient and mitochondrial membrane potential. The remarkable effect of PXA in cisplatin-resistant cell lines (three digit nanomolar or low micromolar IC_{50} values) and previously shown selectivity for cancer over non-cancer cell lines[12] warrants further examination of PXA for the treatment of chemoresistant malignancies. Perspectively, mode of action studies need to be undertaken. This includes further studies of PXA on mitochondrial physiology (fusion, fission, potential) and a search for potential (sub)cellular binding proteins (e.g. by chemical modification of PXA to allow crosslinking of PXA with its cellular or subcellular (mitochondrial) binding partners followed by MS analysis). Further, the efficacy of PXA needs to be verified in *in vivo* xenograft models using chemoresistant cell lines such as those used in this study.

4. Experimental

4.1 Materials

Roswell Park Memorial Institute (RPMI) media 1640, Dulbecco's Modified Eagle Medium (DMEM), fetal bovine serum (FBS), penicillin/streptomycin (pen/strep) [10.000 U/ml; 10 mg/ml] and trypsin-EDTA (0.05% Trypsin, 0.02% EDTA in PBS) were purchased from PAN Biotech (Aidenbach, Germany). Cisplatin (cDDP), Pluronic® F-127 and Hoechst 33,342 were purchased from Sigma-Aldrich (Steinheim, Germany). Cisplatin was dissolved and subsequently diluted in 0.9% saline. 3-(4,5-dimethylthiazol-2-yl)-2,5-diphenyltetrazolium bromide (MTT) was purchased from Serva (Heidelberg, Germany) and was dissolved in PBS at a concentration of 5 mg/ml. Oregon Green® 488 BAPTA-1, AM was ordered from life technologies GmbH (Darmstadt, Germany). Propidium iodide was purchased from Santa Cruz Biotechnology (Heidelberg, Germany). Propidium iodide was dissolved in sterile filtered water. 0.9% NaCl, obtained from Fresenius Kabi (Bad Homburg, Germany) and supplemented with 0.01% sodium azide, was used as sheath fluid for flow cytometry analysis. The natural compound phomoxanthone A from fungus Phomopsis longicola was isolated in house (Institute of Pharmaceutical Biology and Biotechnology, Heinrich-Heine-University Duesseldorf, Germany). The compound was dissolved in DMSO and subsequently diluted in medium.

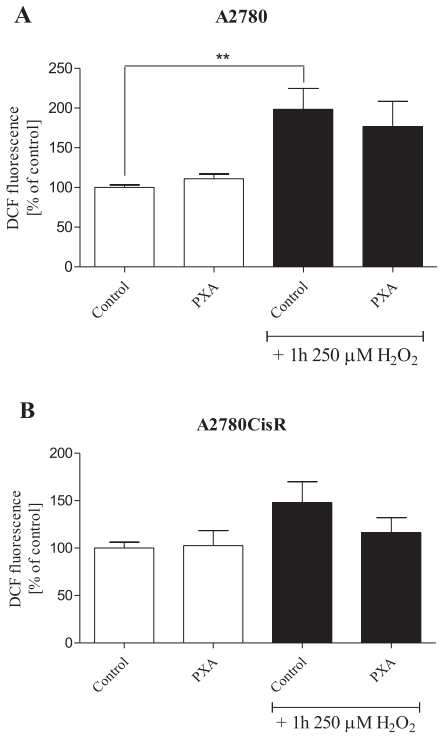

Figure 11. PXA does not affect the concentration of reactive oxidative species. A2780 (A) and A2780CisR (B) were treated for 18 h with a non-toxic concentration of PXA (IC_{10}: 316 nM). Then, cells were labeled with 10 μM H_2DCF-DA for 30 min, followed by 1 h treatment with or without 250 μM H_2O_2. Data shown are mean ± SEM of three independent experiments. $^{**}P < 0.01$ in comparison to the untreated control cells.

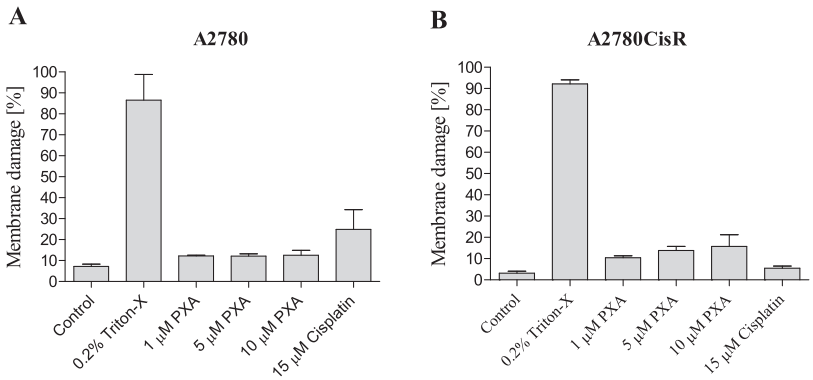

Figure 10. PXA does not damage the plasma membrane. A2780 (A) and A2780CisR (B) were treated for 24 h with different concentrations of PXA. Medium was used as negative control and 0.2% Triton-X was used as positive control. Data shown are mean ± SEM from three experiments.

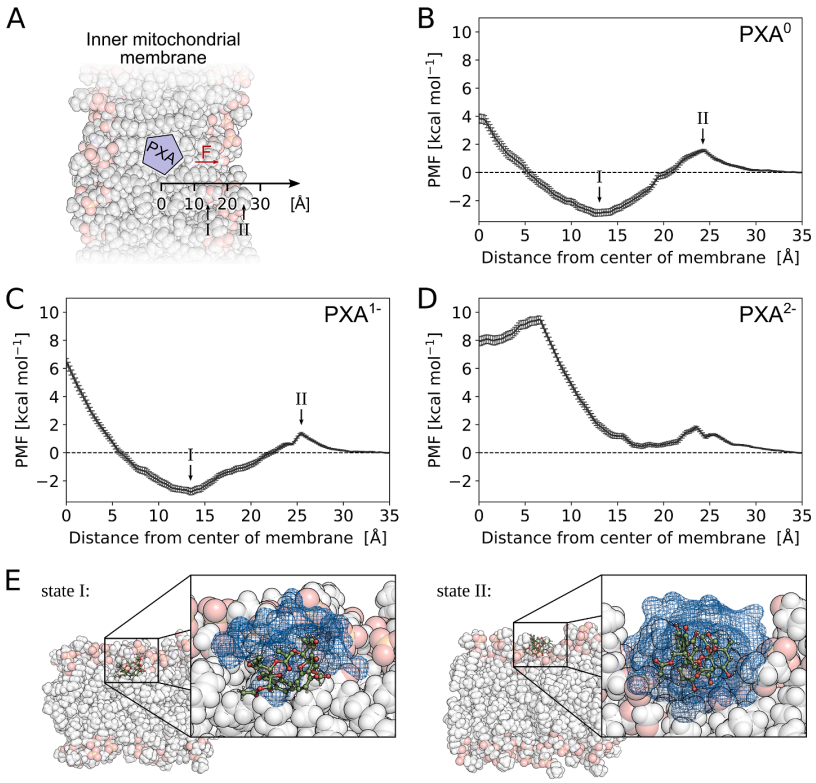

Figure 12. Ability of PXA to penetrate the inner mitochondrial membrane. Potential of mean force for the passage of PXA from the membrane center along the membrane normal to the outside (A) in the uncharged (B), singly (C) and doubly deprotonated (D) states. The PMF values were normalized to zero with respect to the state in the bulk solvent. Error bars indicate the SEM at the respective position. Interesting states in the potentials are marked with I and II, their location is indicated in panel A, and representative snapshots are given in (E), with water molecules solvating the solute displayed as blue meshes. (For interpretation of the references to colour in this figure legend, the reader is referred to the web version of this article.)

4.2 Cell lines

The human epithelial ovarian cancer cell line A2780 (ECACC, Salisbury, Wiltshire/UK), the human esophageal cancer cell line Kyse510 (German Collection of Microorganisms and Cell Cultures (DSMZ, Germany)) and the human myeloid leukemia cell line K562 (DSMZ) were cultivated in RPMI-1640 medium supplemented with 10% fetal bovine serum, 120 µg/ml streptomycin and 120 U/ml penicillin. The human tongue cancer cell line Cal27 and the human colon carcinoma cell line HCT116 were purchased from DSMZ. The urothelial bladder cancer cell line J82 was kindly provided by Prof. Wolfgang A. Schulz (Department of Urology, Medical Faculty, Heinrich Heine University). These cells were cultivated in DMEM supplemented with 10% fetal bovine serum, 120 µg/ml streptomycin and 120 U/ml penicillin. Additionally, the human triple negative breast carcinoma cell line MDA-MB-231 (ATCC, Manassas, USA) was used and cultivated in DMEM supplemented with 15% fetal bovine serum, 120 µg/ml streptomycin and 120 U/ml penicillin. The corresponding cisplatin-resistant (CisR) cell lines were generated by exposing the parental cell lines to weekly intermittent treatments with cisplatin in an IC_{50} concentration over a period of 24 till 30 weeks as previously described.[14] Cells were grown at 37 °C in a humidified atmosphere containing 5% CO_2. When cells reached a confluence of 80–90%, the cells were washed with 1x PBS and treated with Trypsin-EDTA before subculture.

4.3 MTT assay

MTT assays were performed as previously described.[15] Briefly, cells were seeded into 96 well plates (Sarstedt, Nümbrecht, Germany) and incubated overnight. Then, cells were exposed to increasing concentrations of test compound. After 72 h incubation, 25 µl of MTT solution (5 mg/ml) was added into each well and incubated for 15 min. Thereafter, the mixture of medium and MTT solution was discarded and 75 µl of DMSO was added to dissolve formazan crystals. Absorbance of each well was measured at 544 nm (test wavelength) and 690 nm (background) using the BMG FLUOstar (BMG Labtechnologies Offenburg, Germany). Background was subtracted from the absorbance of each well.

4.4 Cell cycle analysis

Cell cycle was analysed using standard procedure as recently described.[35] Briefly, after exposing to various concentrations of PXA, cells were washed in ice-cold PBS and approximately 2 million cells were fixed in cold ethanol 70% and stored for at least 24 h at −20 °C. Then, fixed cells were washed with ice-cold PBS and incubated in staining solution (0.1% (v/v) Triton X-100 in PBS, 200 µg/ml DNAse-free RNAse A (Fermentas/Thermo Fisher Scientific, Waltham, MA, USA), 20 µg/ml propidium iodide) in the dark at 37 °C for 15 min. The DNA content was measured by flow cytometry with the CyFlow® space of Partec (Münster, Germany). The doublet discrimination mode was used.

4.5 Apoptosis assay

To determine apoptosis, nuclei were labeled with propidium iodide (PI). Each cell line was plated out in 24-well plates (approximately 100,000 cells per well) and after one day, cells were exposed to the respective treatments for 24 h. The caspase inhibitor Q-VD-OPh was added 1 h before apoptosis induction (20 µM). The plate was centrifuged and the supernatant was carefully removed. Cells were lysed in a hypotonic lysis buffer (sodium citrate tribasic dihydrate 0.1%, Triton X-100 0.1%, propidium iodide 100 µg/ml) and stored at 4 °C in the dark overnight. Sub-G1 fractions were detected by flow cytometry.

4.6 Analysis of mitochondrial membrane potential

Cells were seeded overnight before compound treatment. Shortly before compound treatment, the complete medium was replaced by FBS free medium to avoid cleavage of the TMRE ester (Biotrend Chemikalien GmbH, Köln, Germany). Treated cells were then stained with TMRE for 20 min and collected by trypsination. The cell suspension was centrifuged at 4° C and 8000 rpm for 4 min and the supernatant was then removed. The samples were stored on ice and protected from light until measurement. The cell pellet was resuspended in sheath fluid and the intensity of accumulated TMRE in each cell was determined using flow cytometry (CyFlow, Partec, Germany). For detection of mitochondrial membrane potential by ArrayScan XTI Live High Content Platform (Thermo Fisher Scientific Inc., USA), cells were labelled with TMRE and Hoechst 33,342 for 20 min after the compound treatment. Images were acquired using 10x magnification and data were analysed using HCS Studio Cellomics Scan (Thermo Fisher Scientific Inc., USA).

4.7 Calcium assay

Calcium assay was performed as previously described.[36] Briefly, cells were seeded into 96 well plates and incubated overnight. On the measurement day, medium was removed, and cells were washed with Krebs-HEPES buffer (KHB) twice. A mixture of Oregon Green BAPTA-1 AM (final concentration of 3 µM) and Pluronic F-127 (3 µl of 20% solution) was prepared in 2 ml of KHB, and 20 µl were added to each well. After 1 h incubation at 37 °C in the dark, the supernatant was removed and replaced by 180 µl pre-warmed KHB. Increasing concentrations of PXA were added (20 µl/well) and fluorescence intensity was measured at 544 nm for 30 min by a NOVOstar plate reader (BMG Labtechnologies Offenburg, Germany).

4.8 Caspase 3/7 activation test

The activity of caspase 3/7 after PXA treatment in A2780 and J82 cells was analysed by fluorescence image analysis. After cells were exposed to PXA for 24 h, medium was aspirated, and the cells were labelled with fluorescent staining solution containing CellEventTM Caspase-3/7 Green Detection Reagent (Invitrogen, Carlsbad, CA, USA) and Hoechst 33342. After 30 min incubation, images were acquired using ArrayScan XTI Live High Content Platform using excitation filters of 386 and 485 nm for Hoechst 33,342 and Caspase-3/7 Green Detection Reagent, respectively. The percentage of activated caspase 3/7 cells was calculated using HCS Studio Cellomics Scan.

4.9 Plasma membrane integrity test

Cells exposed to PXA for 24 h or triton X-100 for 20 min were trypsinized and collected by centrifugation at 4 °C and 266 rcf. The supernatant was removed, and the cell pellet was stained with 100 µg/ml propidium iodide. Samples were diluted with sheath fluid before measurement by flow cytometry. A sample treated with 0.2% Triton X-100 was used as positive control.

4.10 Reactive oxidative species

The measurement of reactive oxidative species was performed as follows: A2780 and A2780CisR were plated in 24-well plates (approximately 150,000 cells/well) (Sarstedt) and pre-incubated with growth medium overnight. Cells were exposed to PXA for 18 h. Cells were washed with PBS and then cultivated in phenolred-free RPMI-1640 (PAN) without FBS and antibiotics. Cells were then treated with 10 µM H2DCF-DA in the dark at 37 °C for 30 min. One aliquot of cells was analysed directly, the other aliquot was first treated with 250 µM H_2O_2 in the dark at 37 °C for 1 h and then analysed. Dichlorofluorescein (DCF) fluorescence was detected by flow cytometry (CyFlow® space, Partec, Münster, Germany).

4.11 Analysis of apoptotic pathway proteins

The functional status of signal pathways was determined by human apoptosis array kit (Proteome ProfilerTM antibody array, biotechne, Germany) according to the manufactureŕs instructions. Relative levels of expression were measured with streptavidin-HRP and chemiluminescent detection reagents.

4.12 Statistical analysis

The statistical analysis was carried out with GraphPad Prism 6.0 (GraphPad Software Inc., San Diego, USA). Concentration-effect-curves were generated by nonlinear regression curve fitting using the 4-parameter logistic equation with variable hill slope. The IC_{50} is the concentration of the cytotoxic agent that led to a decrease of 50% of the recorded signal. pIC_{50} values are –log IC_{50}. Assays were performed at least in three independent experiments each carried out in triplicates. Values shown are mean ± SEM. The two-tailed Studenťs *t*-test was used and a p-value < 0.05 was considered as significant.

4.13 Preparation of the simulations

We used Maestro[37] to prepare the X-ray structure of PXA described in Rönsberg *et al.*.[12] Using the program Epik[25–26], the protonation states at various pH values were evaluated. We generated structures for the uncharged (PXA^0), as well as the singly (PXA^{1-}) and doubly deprotonated (PXA^{2-}) molecule and optimized them with Gaussian09[38] at the B3LYP/6-311G(d) level of theory. Subsequently, atomic charges were calculated according to the RESP procedure[39] by a single point calculation at the HF/6-31G(d) level of theory.

For the setup of the membrane system, the PACKMOL-Memgen module (S. Schott, H. Gohlke, unpublished results) from AmberTools18 and tLEaP were used to generate a lipid bilayer system. LIPID17[40] parameters were used for the membrane lipids, while for the water phase TIP3P water[41] was used. The lipid composition was adjusted to resemble the inner mitochondrial membrane with DOPC, DOPE and DOPG as surrogates for cardiolipin in the ratios of 40:34:18.[30] One molecule of $PXA^{0/1-/2-}$ was placed in the center of the membrane, resulting in three individual systems. For the PXA species GAFF2[40] parameters were used. All following procedures were carried out on each of the systems.

4.14 Thermalization and density adjustment

Thermalization and density adjustment were carried out using pmemd from the Amber18 software package[42] with a time step of 2 fs. Langevin thermostat[43] and Berendsen barostat[44] were used for temperature and pressure control, respectively. For treatment of long-range electrostatic interactions the Particle Mesh Ewald method[45] was used with a cutoff of 8.0 Å. The SHAKE algorithm[46] was used to constrain bond lengths involving hydrogen atoms. Initial relaxation of the membrane, solvent, and both parts were carried out for 3,000 steps using the steepest decent algorithm, and further 2,000 steps with the conjugate gradient algorithm. Other components of the system were held fixed with positional restraints with a force constant of 5.0 kcal·mol^{-1}·$Å^{-2}$. Then, the system was heated to 300 K at a constant heating rate over 20 ps of NVT-MD and simulated for further 5 ps at 300 K. To adjust the system density, 1 ns of NPT-MD was performed.

From here on, the GPU version of pmemd[42,47] was used to further equilibrate the system for 50 ns. During all these steps, $PXA^{0/1-/2-}$ was held in the center of the membrane, using or distance restraints with a force constant of 5.0 kcal·mol^{-1}·$Å^{-2}$.

4.15 Steered molecular dynamics simulations, umbrella sampling, and PMF calculations

After equilibration, $PXA^{0/1-/2-}$ was gradually pulled out of the membrane into the solvent at a rate of 1 Å·ns^{-1} with a force constant of 2.5 kcal mol^{-1} Å^{-2}. The same MD settings as during the last step of the equilibration were applied. From the resulting trajectory, snapshots along the reaction coordinate with 1 Å spacing were extracted with CPPTRAJ[48]. These were used as reference points in umbrella sampling, further sampling each window for 100 ns while keeping $PXA^{0/1-/2-}$ restrained at its respective reaction coordinate value with a harmonic potential and a force constant of 2.5 kcal mol^{-1} Å^{-2}. The first 50 ns of the sampling were discarded as equilibration time. Reaction coordinate values from the last 50 ns of each window were extracted in 500 fs intervals and analyzed by weighted histogram analysis[49]. The error was estimated by performing the same calculation over ten individual windows of 5 ns each. Individual states were visually inspected and figures prepared with PyMOL[50]

4.16 Unbiased molecular dynamics simulations

In addition to the steered molecular dynamics simulations, we started unbiased simulations from the equilibrated structures. In these simulations the three protonation states of PXA were allowed to diffuse freely, from the initial position in the center of the membrane. For each of the systems 500 ns of NPT-MD were performed and analyzed with CPPTRAJ[48].

Acknowledgments

MUK thanks the Bundesminsterium fuer Bildung und Forschung (BMBF) for financial support (Grant 16GW0108). We gratefully acknowledge financial support from the Deutsche Forschungsgemeinschaft (DFG, German Research Foundation) – 270650915 (Research Training Group GRK 2158, TP1 to PP, TP4a to HG). We further acknowledge funding by the DFG for the Thermofisher Arrayscan XTI (Grant: INST 208/690-1 FUGG). We are grateful for computational support by the "Zentrum für Informations und Medientechnologie" at the Heinrich Heine University Düsseldorf and the computing time provided by the John von Neumann Institute for Computing (NIC) to HG on the supercomputer JURECA at Jülich Supercomputing Centre (JSC) (user ID: HKF7).

Appendix A. Supplementary data

Supplementary data to this article can be found online at https://doi.org/10.1016/j.bmc.2019.115044.

References

1. Dasari S, Tchounwou PB. Cisplatin in cancer therapy: molecular mechanisms of action. *Eur J Pharmacol.* 2014;740:364–378.
2. Siddik ZH. Cisplatin: mode of cytotoxic action and molecular basis of resistance. *Oncogene.* 2003;22(47):7265–7279.
3. Cannistra SA. Cancer of the ovary. *N Engl J Med.* 2004;351(24):2519–2529.
4. Bohler P, Stuhldreier F, Anand R, et al. The mycotoxin phomoxanthone A disturbs the form and function of the inner mitochondrial membrane. *Cell Death Dis.* 2018;9(3):286.
5. Galluzzi L, Senovilla L, Vitale I, et al. Molecular mechanisms of cisplatin resistance. *Oncogene.* 2012;31(15):1869–1883.
6. Renehan AG, Booth C, Potten CS. What is apoptosis, and why is it important? *BMJ.* 2001;322(7301):1536–1538.
7. Elmore S. Apoptosis: a review of programmed cell death. *Toxicol Pathol.* 2007;35(4):495–516.
8. Wajant H. The Fas signaling pathway: more than a paradigm. *Science.* 2002;296(5573):1635–1636.
9. Liu FT, Newland AC, Jia L. Bax conformational change is a crucial step for PUMA-mediated apoptosis in human leukemia. *Biochem Biophys Res Commun.* 2003;310(3):956–962.
10. Rogers C, Fernandes-Alnemri T, Mayes L, Alnemri D, Cingolani G, Alnemri ES. Cleavage of DFNA5 by caspase-3 during apoptosis mediates progression to secondary necrotic/pyroptotic cell death. *Nat Commun.* 2017;8:14128.
11. Clark AM. Natural products as a resource for new drugs. *Pharm Res.* 1996;13(8):1133–1144.
12. Rönsberg D, Debbab A, Mandi A, et al. Pro-apoptotic and immunostimulatory tetrahydroxanthone dimers from the endophytic fungus Phomopsis longicolla. *J Org Chem.* 2013;78(24):12409–12425.
13. Frank M, Niemann H, Bohler P, et al. Phomoxanthone A-From Mangrove Forests to Anticancer Therapy. *Curr Med Chem.* 2015;22(30):3523–3532.
14. Gosepath EM, Eckstein N, Hamacher A, et al. Acquired cisplatin resistance in the head-neck cancer cell line Cal27 is associated with decreased DKK1 expression and can partially be reversed by overexpression of DKK1. *Int J Cancer.* 2008;123(9):2013–2019.
15. Engelke LH, Hamacher A, Proksch P, Kassack MU. Ellagic Acid and Resveratrol Prevent the Development of Cisplatin Resistance in the Epithelial Ovarian Cancer Cell Line A2780. *J Cancer.* 2016;7(4):353–363.
16. Green DR, Reed JC. Mitochondria and apoptosis. *Science.* 1998;281(5381):1309–1312.
17. Perry SW, Norman JP, Barbieri J, Brown EB, Gelbard HA. Mitochondrial membrane potential probes and the proton gradient: a practical usage guide. *Biotechniques.* 2011;50(2):98–115.
18. Griffiths EJ. Mitochondria–potential role in cell life and death. *Cardiovasc Res.* 2000;46(1):24–27.
19. Kane MS, Paris A, Codron P, et al. Current mechanistic insights into the CCCP-induced cell survival response. *Biochem Pharmacol.* 2018;148:100–110.
20. Hajnoczky G, Davies E, Madesh M. Calcium signaling and apoptosis. *Biochem Biophys Res Commun.* 2003;304(3):445–454.
21. Thornberry NA, Lazebnik Y. Caspases: enemies within. *Science.* 1998;281(5381):1312–1316.
22. Slee EA, Adrain C, Martin SJ. Executioner caspase-3, -6, and -7 perform distinct, non-redundant roles during the demolition phase of apoptosis. *J Biol Chem.* 2001;276(10):7320–7326.
23. Zhang Y, Chen X, Gueydan C, Han J. Plasma membrane changes during programmed cell deaths. *Cell Res.* 2018;28(1):9–21.
24. Rahal A, Kumar A, Singh V, et al. Oxidative stress, prooxidants, and antioxidants: the interplay. *Biomed Res Int.* 2014;2014:761264.
25. Shelley JC, Cholleti A, Frye LL, Greenwood JR, Timlin MR, Uchimaya M. Epik: a software program for pK a prediction and protonation state generation for drug-like molecules. *J Comput Aid Mol Des.* 2007;21(12):681–691.
26. Schrödinger Release 2018-1: Epik, Schrödinger, LLC: New York, NY, 2018.
27. Sarmini K, Kenndler E. Ionization constants of weak acids and bases in organic solvents. *J Biochem Bioph Methods.* 1999;38(2):123–137.
28. Torrie GM, Valleau JP. Nonphysical sampling distributions in Monte Carlo free-energy estimation: Umbrella sampling. *J Comput Phys.* 1977;23(2):187–199.
29. Kumar S, Rosenberg JM, Bouzida D, Swendsen RH, Kollman PA, THE,. weighted histogram analysis method for free-energy calculations on biomolecules. I. The method. *J Comput Chem.* 1992;13(8):1011–1021.
30. Horvath SE, Daum G. Lipids of mitochondria. *Prog Lipid Res.* 2013;52(4):590–614.
31. Allhusen JS, Conboy JC. The Ins and Outs of Lipid Flip-Flop. *Accounts Chem Res.* 2017;50(1):58–65.
32. Anglin TC, Cooper MP, Li H, Chandler K, Conboy JC. Free Energy and Entropy of Activation for Phospholipid Flip-Flop in Planar Supported Lipid Bilayers. *J Phys Chem B.* 2010;114(5):1903–1914.
33. Dellago C, Bolhuis PG, Csajka FS, Chandler D. Transition path sampling and the calculation of rate constants. *J Chem Phys.* 1998;108(5):1964–1977.
34. Lee CT, Comer J, Herndon C, et al. Simulation-Based Approaches for Determining Membrane Permeability of Small Compounds. *J Chem Inf Model.* 2016;56(4):721–733.
35. Darzynkiewicz Z. Nucleic Acid Analysis. In: Robinson JP, ed. *Current Protocols in Cytometry.* New York: J Wiley & Sons; 1997.
36. Kassack MU, Hofgen B, Lehmann J, Eckstein N, Quillan JM, Sadee W. Functional screening of G protein-coupled receptors by measuring intracellular calcium with a fluorescence microplate reader. *J Biomol Screen.* 2002;7(3):233–246.
37. Schrödinger Release 2018-1: Maestro, Schrödinger, LLC: New York, NY, 2018.
38. Frisch, M. J.; Trucks, G. W.; Schlegel, H. B.; Scuseria, G. E.; Robb, M. A.; Cheeseman, J. R.; Scalmani, G.; Barone, V.; Mennucci, B.; Petersson, G. A.; Nakatsuji, H.; Caricato, M.; Li, X.; Hratchian, H. P.; Izmaylov, A. F.; Bloino, J.; Zheng, G.; Sonnenberg, J. L.; Hada, M.; Ehara, M.; Toyota, K.; Fukuda, R.; Hasegawa, J.; Ishida, M.; Nakajima, T.; Honda, Y.; Kitao, O.; Nakai, H.; Vreven, T.; Montgomery Jr., J. A.; Peralta, J. E.; Ogliaro, F.; Bearpark, M.; Heyd, J. J.; Brothers, E.; Kudin, K. N.; Staroverov, V. N.; Kobayashi, R.; Normand, J.; Raghavachari, K.; Rendell, A.; Burant, J. C.; Iyengar, S. S.; Tomasi, J.; Cossi, M.; Rega, N.; Millam, J. M.; Klene, M.; Knox, J. E.; Cross, J. B.; Bakken, V.; Adamo, C.; Jaramillo, J.; Gomperts, R.; Stratmann, R. E.; Yazyev, O.; Austin, A. J.; Cammi, R.; Pomelli, C.; Ochterski, J. W.; Martin, R. L.; Morokuma, K.; Zakrzewski, V. G.; Voth, G. A.; Salvador, P.; Dannenberg, J. J.; Dapprich, S.; Daniels, A. D.; Farkas, O.; Foresman, J. B.; Ortiz, J. V.; Cioslowski, J.; Fox, D. J. Gaussian 09, Revision A.02, Gaussian, Inc.: Wallingford CT, 2009.
39. Bayly CI, Cieplak P, Cornell W, Kollman PA. A well-behaved electrostatic potential based method using charge restraints for deriving atomic charges: the RESP model. *J Phys Chem.* 1993;97(40):10269–10280.
40. Case DA, Betz RM, Cerutti DS, et al. *AMBER 2016.* San Francisco: University of California; 2016.
41. Jorgensen WL, Chandrasekhar J, Madura JD, Impey RW, Klein ML. Comparison of simple potential functions for simulating liquid water. *J Chem Phys.* 1983;79(2):926–935.
42. Case, D. A.; Ben-Shalom, I. Y.; Brozell, S. R.; Cerutti, D. S.; Cheatham III, T. E.;

Cruzeiro, V. W. D.; Darden, T. A.; Duke, R. E.; Ghoreishi, D.; Gilson, M. K.; Gohlke, H. ; Goetz, A. W.; Greene, D.; R Harris; Homeyer, N.; Izadi, S.; Kovalenko, A.; Kurtzman, T.; Lee, T. S.; LeGrand, S.; Li, P.; Lin, C.; Liu, J.; Luchko, T.; Luo, R.; Mermelstein, D. J.; Merz, K. M.; Miao, Y.; Monard, G.; Nguyen, C.; Nguyen, H.; Omelyan, I.; Onufriev, A.; Pan, F.; Qi, R.; Roe, D. R.; Roitberg, A.; Sagui, C.; Schott-Verdugo, S.; Shen, J.; Simmerling, C. L.; Smith, J.; Salomon-Ferrer, R.; Swails, J.; Walker, R. C.; Wang, J.; Wei, H.; Wolf, R. M.; Wu, X.; Xiao, L.; York, D. M.; Kollman, P. A. AMBER 2018, University of California, San Francisco: 2018.

43. Pastor RW, Brooks BR, Szabo A. An Analysis of the Accuracy of Langevin and Molecular-Dynamics Algorithms. *Mol Phys.* 1988;65(6):1409–1419.
44. Berendsen HJC, Postma JPM, van Gunsteren WF, DiNola A, Haak JR. Molecular dynamics with coupling to an external bath. *J Chem Phys.* 1984;81(8):3684–3690.
45. Darden T, York D, Pedersen L. Particle Mesh Ewald - an N. Log(N) Method for Ewald Sums in Large Systems. *J Chem Phys.* 1993;98(12):10089–10092.
46. Ryckaert JP, Ciccotti G, Berendsen HJC. Numerical-Integration of Cartesian Equations of Motion of a System with Constraints - Molecular-Dynamics of N-Alkanes. *J Comput Phys.* 1977;23(3):327–341.
47. Le Grand S, Gotz AW, Walker RC. SPFP: Speed without compromise-A mixed precision model for GPU accelerated molecular dynamics simulations. *Comput Phys Commun.* 2013;184(2):374–380.
48. Roe DR, Cheatham TE. PTRAJ and CPPTRAJ: Software for Processing and Analysis of Molecular Dynamics Trajectory Data. *J Chem Theory Comput.* 2013;9(7):3084–3095.
49. Grossfield, A. WHAM: an implementation of the weighted histogram analysis method, version 2.0.9.1.
50. PyMOL: The PyMOL Molecular Graphics System, 2.1.0; Schrödinger, LLC.

Appendix A. Supplementary data

The following are the Supplementary data to this article:

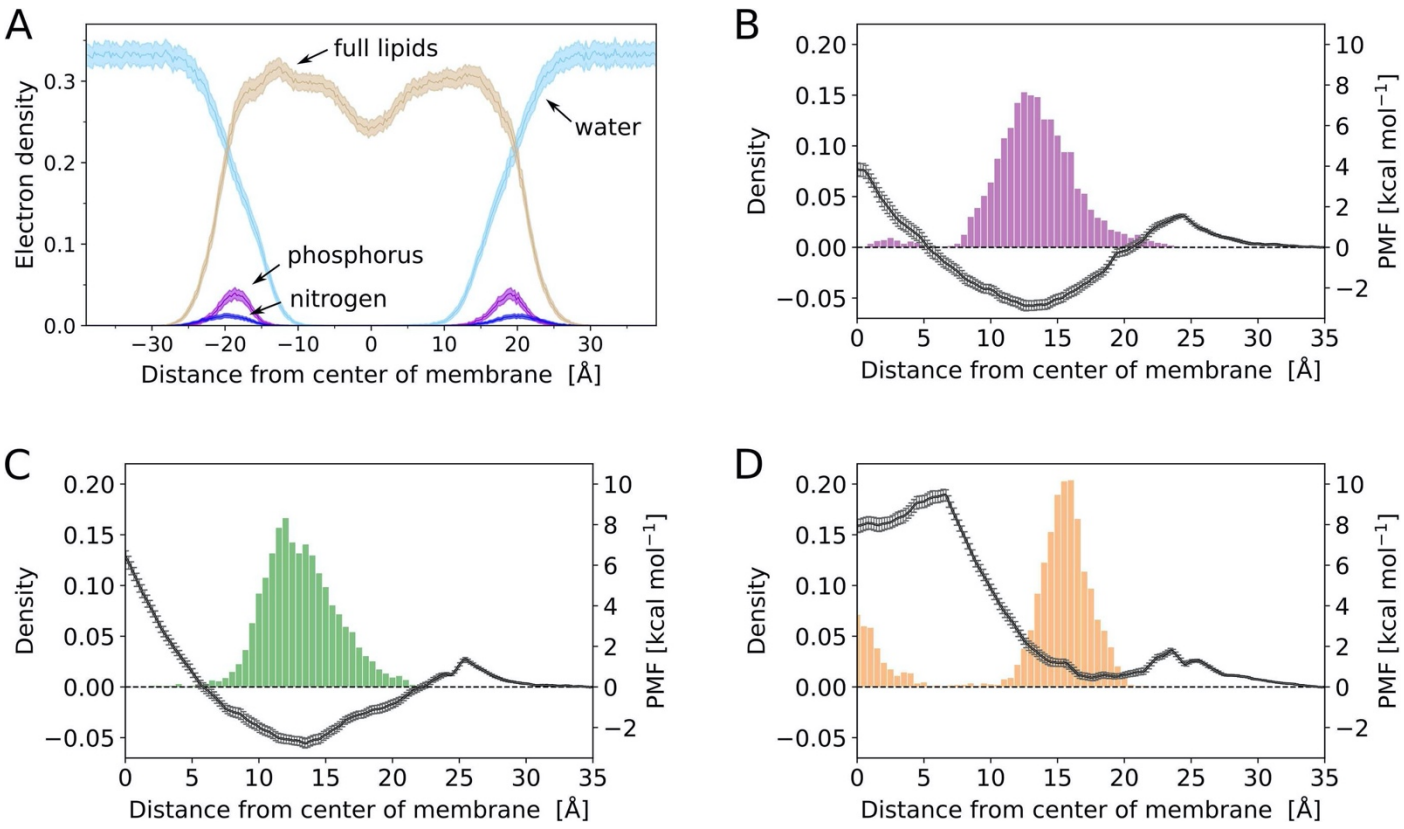

Supplementary Fig. 1.

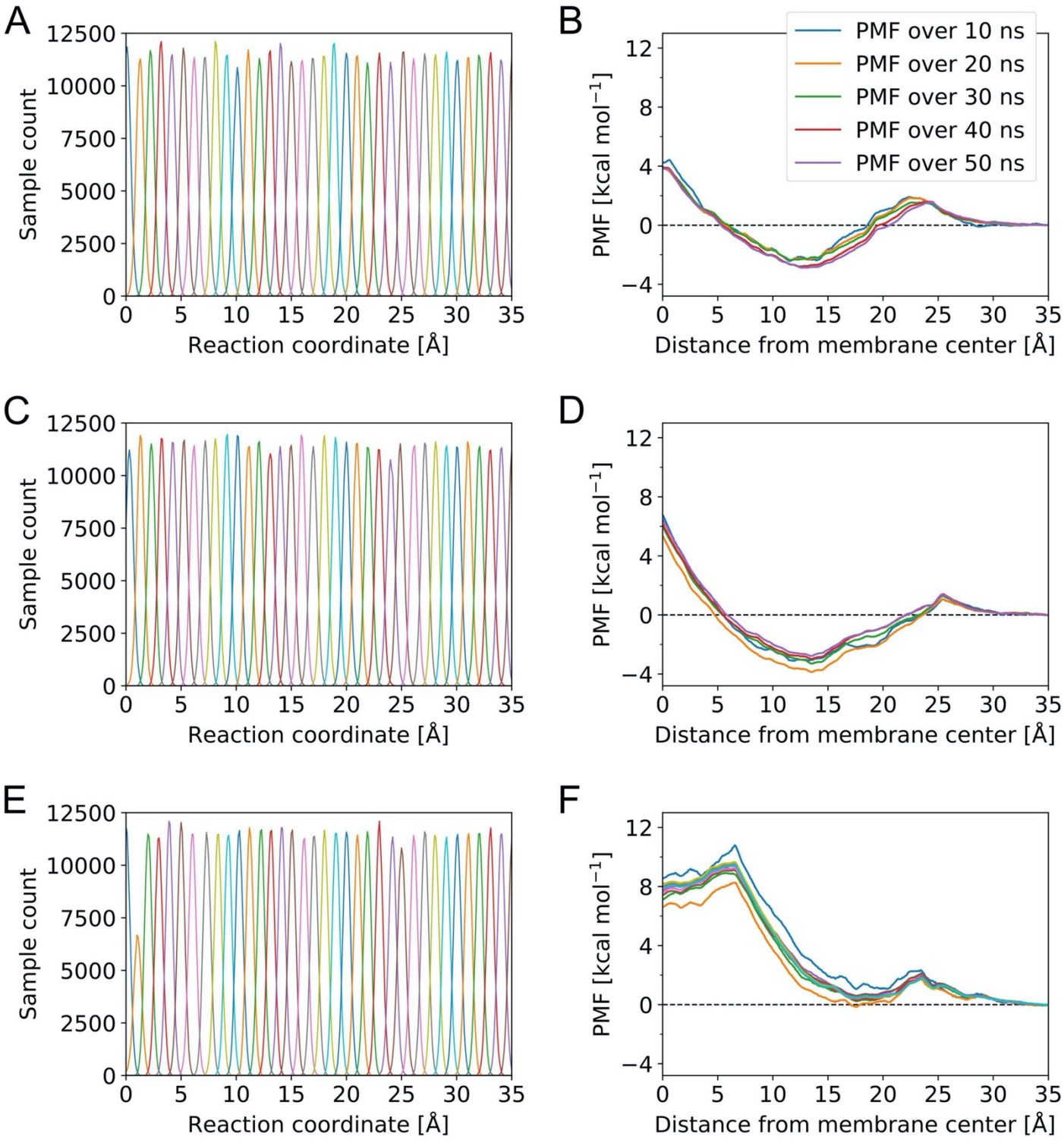

Supplementary Fig. 2.

3.3 Publication 3

Indole Diterpenoids from an Endophytic *Penicillium* sp.

Ni P. Ariantari,[†,‡] Elena Ancheeva,[*,†] Chenyin Wang,[§] Attila Mandi,[´⊥] Tim-O. Knedel,[#] Tibor Kurtan,[´⊥] Chaidir Chaidir,[∥] Werner E. G. Müller,[○] Matthias U. Kassack,[§] Christoph Janiak,[#] Georgios Daletos,[*,†] and Peter Proksch[*,†]

† Institute of Pharmaceutical Biology and Biotechnology, Heinrich Heine University Düsseldorf, Universitatsstrasse 1, 40225¨ Düsseldorf, Germany
‡ Department of Pharmacy, Faculty of Mathematic and Natural Sciences, Udayana University, 80361 Bali, Indonesia
§ Institute of Pharmaceutical and Medicinal Chemistry, Heinrich Heine University Düsseldorf, Universitatsstrasse 1, 40225¨ Düsseldorf, Germany
⊥Department of Organic Chemistry, University of Debrecen, P.O.B. 400, 4002 Debrecen, Hungary
Institute of Inorganic Chemistry and Structural Chemistry, Heinrich Heine University Düsseldorf, Universitatsstraße 1, 40225¨ Düsseldorf, Germany
∥ Center for Pharmaceutical and Medical Technology, Agency for the Assessment and Application Technology, 10340 Jakarta, Indonesia
○ Institute of Physiological Chemistry, Universitatsmedizin der Johannes Gutenberg-Universita¨ t Mainz, Duesbergweg 6, 55128¨ Mainz, Germany

Published in: Journal of Natural Products, 2019.
Contribution: Third authorship, performed experiments including MTT assay, high content analysis. Evaluated the data of cytotoxicity test of the compounds.

Abstract
A chemical investigation of the endophyte Penicillium sp. (strain ZO-R1-1), isolated from roots of the medicinal plant Zingiber officinale, yielded nine new indole diterpenoids (1−9), together with 13 known congeners (10−22). The structures of the new compounds were elucidated by 1D and 2D NMR analysis in combination with HRESIMS data. The absolute configuration of the new natural products 1, 3, and 7 was determined using the TDDFT-ECD approach and confirmed for 1 by single-crystal X-ray determination through anomalous dispersion. The isolated compounds were tested for cytotoxicity against L5178Y, A2780, J82, and HEK-293 cell lines. Compound 1 was the most active metabolite toward L5178Y cells, with an IC50 value of 3.6 μM, and an IC50 against A2780 cells of 8.7 μM. Interestingly, 1 features a new type of indole diterpenoid scaffold with a rare 6/5/6/6/6/6/5 heterocyclic system bearing an aromatic ring C, which is suggested to be important for the cytotoxic activity of this natural product against L5278Y and A2780 cells.

JOURNAL OF NATURAL PRODUCTS

Article

Cite This: J. Nat. Prod. 2019, 82, 1412−1423

pubs.acs.org/jnp

Indole Diterpenoids from an Endophytic *Penicillium* sp.

Ni P. Ariantari,[†,‡] Elena Ancheeva,[*,†] Chenyin Wang,[§] Attila Mándi,[⊥] Tim-O. Knedel,[#] Tibor Kurtán,[⊥] Chaidir Chaidir,[∥] Werner E. G. Müller,[○] Matthias U. Kassack,[§] Christoph Janiak,[#] Georgios Daletos,[*,†] and Peter Proksch[*,†]

[†]Institute of Pharmaceutical Biology and Biotechnology, Heinrich Heine University Düsseldorf, Universitätsstrasse 1, 40225 Düsseldorf, Germany

[‡]Department of Pharmacy, Faculty of Mathematic and Natural Sciences, Udayana University, 80361 Bali, Indonesia

[§]Institute of Pharmaceutical and Medicinal Chemistry, Heinrich Heine University Düsseldorf, Universitätsstrasse 1, 40225 Düsseldorf, Germany

[⊥]Department of Organic Chemistry, University of Debrecen, P.O.B. 400, 4002 Debrecen, Hungary

[#]Institute of Inorganic Chemistry and Structural Chemistry, Heinrich Heine University Düsseldorf, Universitätsstraße 1, 40225 Düsseldorf, Germany

[∥]Center for Pharmaceutical and Medical Technology, Agency for the Assessment and Application Technology, 10340 Jakarta, Indonesia

[○]Institute of Physiological Chemistry, Universitätsmedizin der Johannes Gutenberg-Universität Mainz, Duesbergweg 6, 55128 Mainz, Germany

Supporting Information

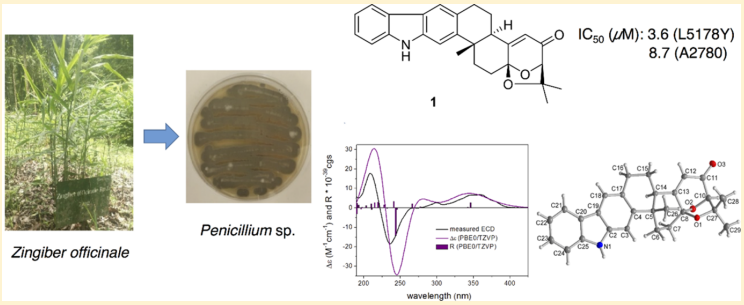

ABSTRACT: A chemical investigation of the endophyte *Penicillium* sp. (strain ZO-R1-1), isolated from roots of the medicinal plant *Zingiber officinale*, yielded nine new indole diterpenoids (**1**−**9**), together with 13 known congeners (**10**−**22**). The structures of the new compounds were elucidated by 1D and 2D NMR analysis in combination with HRESIMS data. The absolute configuration of the new natural products **1**, **3**, and **7** was determined using the TDDFT-ECD approach and confirmed for **1** by single-crystal X-ray determination through anomalous dispersion. The isolated compounds were tested for cytotoxicity against L5178Y, A2780, J82, and HEK-293 cell lines. Compound **1** was the most active metabolite toward L5178Y cells, with an IC_{50} value of 3.6 μM, and an IC_{50} against A2780 cells of 8.7 μM. Interestingly, **1** features a new type of indole diterpenoid scaffold with a rare 6/5/6/6/6/6/5 heterocyclic system bearing an aromatic ring C, which is suggested to be important for the cytotoxic activity of this natural product against L5278Y and A2780 cells.

Filamentous fungi (e.g., *Penicillium*, *Aspergillus*, and *Fusarium* sp.) are important producers of structurally unusual natural products with pharmaceutical potential.[1] Since the discovery of the antibiotic penicillin G from *Penicillium notatum*, fungi belonging to this genus have gained considerable attention with regard to their secondary metabolites and proved to be prolific sources of bioactive compounds. The discovery of the antifungal compound griseofulvin from *P. griseofulvum*, of the cholesterol-lowering agent compactin produced by *P. citrinum*, and of the immunosuppressant agent mycophenolic acid, isolated from *P. brevicompactum*, represents further success stories leading to important therapeutically used molecules from this genus.[1−5]

In our search for new bioactive compounds from fungal sources, we investigated *Penicillium* sp. (strain ZO-R1-1), an endophytic fungus isolated from the medicinal plant *Zingiber officinale* (Zingiberaceae) collected in Indonesia. Rhizomes of

Received: August 26, 2018
Published: May 22, 2019

DOI: 10.1021/acs.jnatprod.8b00723
J. Nat. Prod. 2019, 82, 1412−1423

Journal of Natural Products Article

Chart 1

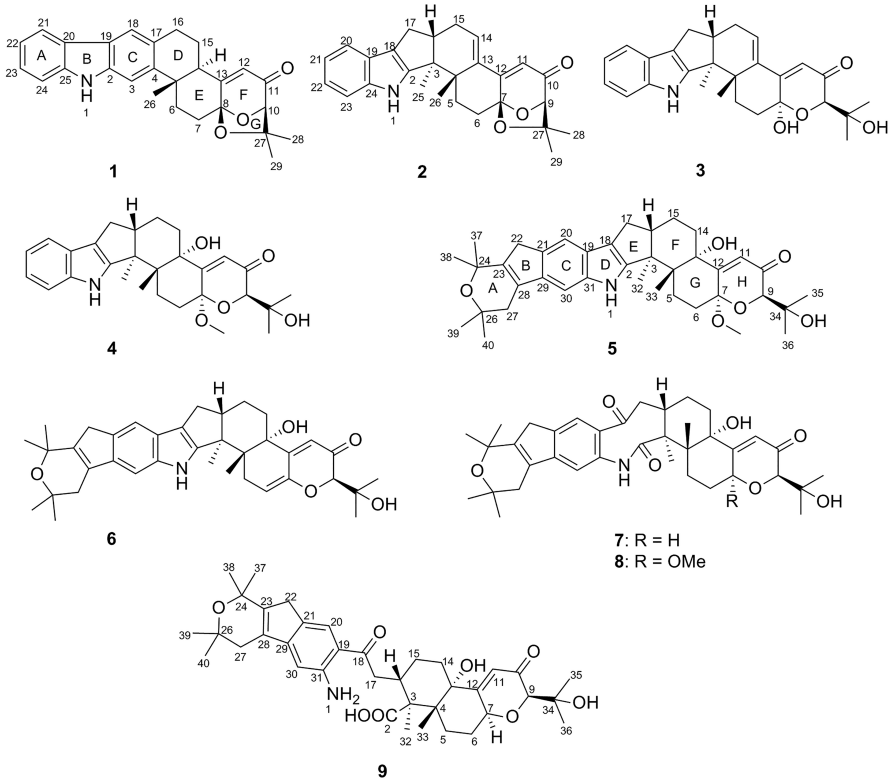

Z. officinale have been widely used in traditional medicine systems among Asian countries to treat numerous ailments, such as vertigo, common cold, cough, anorexia, and rheumatism.[6−8] A number of studies have reported antioxidant,[9] antiemetic,[10] anticancer,[7,8,11] antiarthritic,[12] and anti-inflammatory[9,11] activities, attributed to the main bioactive metabolites, gingerols and shogaols.

The HPLC-PDA analysis of the EtOAc extract of *Penicillium* sp., in combination with an in-house UV spectra library, demonstrated a series of peaks with similar UV absorptions at around 228 and 280 nm, which suggested the presence of indole diterpenoids.[13−15] Indole diterpenoids are a large class of structurally diverse fungal secondary metabolites, featuring an indole moiety fused to a diterpene skeleton.[16−18] Among them, lolitrem B,[19] paxilline,[20] paspalitrems A and B,[21] janthitrems B and C,[22−24] penitrems A−F,[25] aflatrem,[26] and paspalinine[27] are known as tremorgenic mycotoxins, causing neurological disorders in farm animals. These compounds are produced by species of fungi from the genera *Penicillium*, *Aspergillus*, *Epichloë*, and *Claviceps*[16,19,28,29] and are also known for their insecticidal properties.[16,30] Moreover, indole diterpenoids were found to be antibacterial,[31,32] inhibitors of *Candida albicans* biofilm formation,[33] antiviral (against H1N1 influenza A virus)[14] and antiproliferative with activities against human glioblastoma[34] and breast cancer cell lines.[35] Paxilline has been shown to inhibit high-conductance Ca^{2+}-activated K^+ (Maxi-K) channels,[36] which was associated with its anti-convulsant effect.[37] Synthetic derivatives of indole diterpenoids were patented as Maxi-K channel blockers for treatment of glaucoma.[38] The complex structures of these natural products and the broad range of their biological activities have inspired numerous studies, which focused on their total synthesis and on the elucidation of the biosynthetic pathways and enzymes leading to the rich chemical diversity of these intriguing secondary metabolites.[39−41]

In the present study, we describe the isolation and structure elucidation of nine new indole diterpenoid analogues (**1**−**9**) from the endophyte *Penicillium* sp. ZO-R1-1. A plausible biosynthetic pathway leading to the formation of the uncommon alkaloid diterpenoid skeleton of **1** is proposed. Furthermore, we discuss the cytotoxicity of the new and known indole diterpenoids isolated in this study.

RESULTS AND DISCUSSION

The HRESIMS spectrum of shearilicine (**1**) exhibited a prominent pseudomolecular ion peak at *m*/*z* 414.2063 $[M + H]^+$ attributed to the molecular formula $C_{27}H_{27}NO_3$ and accounting for 15 degrees of unsaturation. Investigation of the ^{1}H NMR data (Table 1) revealed the presence of one isolated NH signal, three methyl groups, four sets of methylene signals, nine methines including six aromatic, one olefinic and two further aliphatic protons. Four characteristic aromatic proton signals resonating at δ_H 8.00 (H-21), 7.19 (H-22), and 7.38 (H-23, H-24), along with the NH signal (δ_H 7.90), hinted at the presence of an indole moiety containing a 1,2-disubstituted benzene (ring A). The observed HMBC correlations from H-

DOI: 10.1021/acs.jnatprod.8b00723
J. Nat. Prod. 2019, 82, 1412−1423

Journal of Natural Products Article

Table 1. ^{1}H and ^{13}C NMR Data for 1−4

	1[a]		2[b]		3[b]		4[c]	
position	δ_C, type[d]	δ_H (J in Hz)	δ_C, type[d]	δ_H (J in Hz)	δ_C, type	δ_H (J in Hz)	δ_C, type	δ_H (J in Hz)
1-NH		7.90, s		10.84, s		10.85, s		10.76, s
2	139.8, C		148.4, C		148.8, C		152.7, C	
3	107.8, CH	7.28, s	48.7, C		47.8, C		50.4, C	
4	147.6, C		38.8, C		42.0, C		42.4, C	
5	35.9, C		28.4, CH_2	2.45, m; 1.98, ov	28.1, CH_2	2.20, m; 2.08, ov	24.9, CH_2	2.42, m; 1.81, m
6	34.5, CH_2	2.53, m	30.4, CH_2	1.98, ov; 1.84, m	32.9, CH_2	2.08, ov	27.3, CH_2	2.47, m; 1.83, ov
7	27.7, CH_2	2.24, ddd (14.0, 11.9, 9.2); 2.04, br dd (14.0, 6.3)	103.8, C		93.5, C		97.1, C	
8	103.9, C							
9			87.4, CH	4.43, d (1.2)	78.3, CH	4.13, s	78.5, CH	3.92, s
10	88.1, CH	4.35, d (1.2)	195.1, C		198.7, C		197.2, C	
11	197.5, C		117.3, CH	6.16, s	120.7, CH	5.86, s	121.3, CH	5.79, s
12	120.4, CH	5.94, br s	163.8, C		161.4, C		160.3, C	
13	171.0, C		138.4, C		140.7, C		75.7, C	
14	43.3, CH	3.04, dt (12.0, 2.6)	132.5, CH	6.52, dd (5.2, 2.7)	130.4, CH	6.07, dd (5.2, 2.4)	32.7, CH_2	1.83, m; 1.68, m
15	19.9, CH_2	2.18, m; 1.85, qd (12.0, 6.1)	27.9, CH_2	2.39, ov; 2.34, dt (19.3, 5.2)	27.5, CH_2	2.30, m; 2.26, m	21.0, CH_2	1.94, dd (11.8, 3.0); 1.64, ov
16	29.5, CH_2	3.14, m	44.5, CH	2.90, m	45.0, CH	2.82, m	49.5, CH	2.75, m
17	125.6, C		26.7, CH_2	2.74, dd (13.2, 6.7); 2.39, ov	26.5, CH_2	2.76, dd (13.1, 6.7); 2.39, dd (13.1, 10.1)	26.9, CH_2	2.62, dd (13.0, 6.0); 2.34, ov
18	119.7, CH	7.75, s	116.1, C		116.1, C		114.9, C	
19	122.2, C		124.2, C		124.2, C		124.5, C	
20	123.1, C		117.6, CH	7.32, ov	117.9, CH	7.31, d (8.0)	117.7, CH	7.27, ov
21	120.2, CH	8.00, d (7.7)	118.4, CH	6.93, ddd (8.1, 7.0, 1.2)	118.5, CH	6.92, td (8.0, 1.2)	118.4, CH	6.90, td (7.0, 1.1)
22	119.1, CH	7.19, m	119.5, CH	6.98, ddd (8.1, 7.0, 1.2)	119.7, CH	6.97, td (8.0, 1.2)	119.3, CH	6.92, td (7.0, 1.3)
23	125.8, CH	7.38, ov[e]	111.7, CH	7.32, ov	111.8, CH	7.29, d (8.0)	111.8, CH	7.27, ov
24	110.7, CH	7.38, ov	140.4, C		140.4, C		139.7, C	
25	140.1, C		14.2, CH_3	0.97, s	15.0, CH_3	0.92, s	16.3, CH_3	1.26, s
26	30.8, CH_3	1.39, s	27.2, CH_3	1.17, s	22.4, CH_3	1.09, s	19.1, CH_3	0.96, s
27	78.7, C		77.6, C		71.4, C		71.0, C	
28	22.8, CH_3	1.26, s	22.6, CH_3	1.14, s	25.8, CH_3	1.18, s	25.7, CH_3	1.20, s
29	28.7, CH_3	1.47, s	28.5, CH_3	1.39, s	26.7, CH_3	1.18, s	26.2, CH_3	1.23, s
7-OH						6.54, s		
7-OMe							49.0, CH_3	3.38, s
13-OH								4.58, s
27-OH						4.31, s		4.45, s

[a]Recorded at 600 MHz (^{1}H) and 150 MHz (^{13}C) in $CDCl_3$. [b]Recorded at 600 MHz (^{1}H) and 150 MHz (^{13}C) in DMSO-d_6. [c]Recorded at 300 MHz (^{1}H) and 75 MHz (^{13}C) in DMSO-d_6. [d]Chemical shifts extracted from HSQC and HMBC spectra. [e]ov stands for overlapped signals.

21 to C-19, C-23, and C-25, from H-23 to C-21 and C-25, and from NH to C-2 and C-20 confirmed this substructure. Two further aromatic protons appearing at δ_H 7.28 (H-3) and 7.75 (H-18) afforded HMBC correlations to C-17 and C-19 and to C-2 and C-4, respectively. These correlations suggested an additional aromatic ring C fused to the indole part at positions C-2 and C-19, thus forming a carbazole unit, which was previously described for indole sesquiterpenes from bacteria.[42,43] Detailed analysis of the COSY spectrum revealed two further spin systems, H_2-6/H_2-7 and H_2-16/H_2-15/H-14, which were connected based on the detected HMBC correlations from H_2-6 to C-14, from H_2-7 to C-5 and C-13, and from H-14 to C-5 and C-6 (Figure 1). Further HMBC correlations from H_2-6 and H_2-7 to C-8 and from H-14 to C-13 confirmed the structure of rings D and E in **1**. Furthermore, the methyl group CH_3-26 was placed at position C-5, as confirmed by the HMBC spectrum. The connection of ring D to the carbazole substructure was established by HMBC correlations from H_2-16 to C-4, C-17, and C-18, as well as

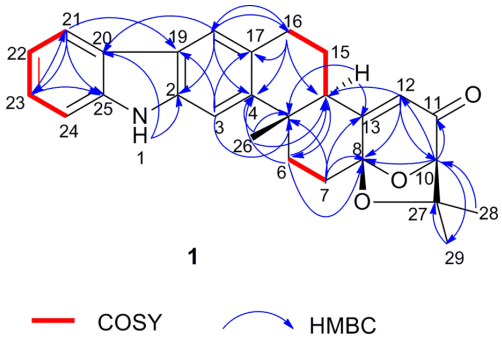

Figure 1. COSY and selected HMBC correlations of **1**.

from H_2-6 to C-4. The olefinic proton H-12 displayed correlations to the sp^3 carbons C-8 and C-10, which together with the correlations from H-10 to the ketone C-11 and to C-8

DOI: 10.1021/acs.jnatprod.8b00723
J. Nat. Prod. 2019, 82, 1412−1423

hinted at the presence of an α,β-unsaturated pyranone moiety (ring F) in **1**. Moreover, the HMBC correlations of the two methyl signals H_3-28 and H_3-29 to C-27 and C-10, in addition to the remaining degree of unsaturation, allowed the deduction of a dioxolane moiety (ring G) fused to the pyranone at C-8 and C-10. The HMBC correlations from H-10 to C-8, C-11, C-12, and C-29 confirmed the assignments of rings F and G in **1**, which were in accordance with the NMR data of the well-described indole diterpene paspalicine (**12**),[44,45] containing the same partial structure of rings D−G. The absence of a ROESY correlation between H-14 and H_3-26, together with similarity of NMR data for rings E−G of **1** with those of paspalicine, suggested that the two compounds shared the same relative configuration. Accordingly, the structure of **1** was established as a new indole diterpenoid containing a rare carbazole unit forming an unprecedented 6/5/6/6/6/6/5 heterocyclic system.

In order to elucidate the absolute configuration of **1**, the solution time-dependent density functional theory−electronic circular dichroism (TDDFT-ECD) method was applied. While ECD is mostly used to efficiently distinguish enantiomers and determine absolute configuration, it is also capable of distinguishing more than two stereoisomers in molecules with multiple chirality centers when the relative configuration is not available or obvious from NMR measurements.[46−49] In compound **1**, the two blocks of chirality, C-5/C-14 and C-8/C-10, could not be correlated by NMR, although the trans relative configuration of C-5 and C-14 and the cis relationship of the C-8 and C-10 centers of the bridged ring F were determined. Therefore, ECD calculations were carried out for the (5*S*,8*R*,10*S*,14*R*) and (5*S*,8*S*,10*R*,14*R*) stereoisomers to correlate C-5 and C-14 with ring F. The initial Merck molecular force field (MMFF) conformational search yielded two low-energy conformers for (5*S*,8*R*,10*S*,14*R*)-**1** and one low-energy conformer for (5*S*,8*S*,10*R*,14*R*)-**1** in a 21 kJ/mol energy window, which were reoptimized at the B3LYP/6-31+G(d,p) and the CAM-B3LYP/TZVP[50] PCM/MeCN levels. ECD spectra were than computed at various levels of theory (B3LYP, BH&HLYP, CAM-B3LYP, and PBE0 functionals and TZVP basis set) for all sets of conformers, which reproduced the experimental ECD spectrum for (5*S*,8*S*,10*R*,14*R*)-**1** (Figure 2) and resulted in a mirror-image spectrum for (5*S*,8*R*,10*S*,14*R*)-**1** (Figure 3). This suggests that the ECD spectrum is mainly governed by the α,β-unsaturated carbonyl chromophore and hence the C-8 and C-10 chirality centers, and the absolute configuration of **1** could not be assigned by only considering the ECD calculations. However, if the (5*S*,14*R*) absolute configuration, the same as that of paxilline, is assumed for **1**, the ECD calculation affords the (8*S*,10*R*) configuration for ring F. In order to elucidate the absolute configuration, ^{13}C NMR DFT calculations were performed on the two diastereomers above at the mPW1PW91/6-311+G(2d,p)[51] and the mPW1PW91/6-311+G(2d,p) SMD/$CHCl_3$ levels. Substantially lower average deviations at both applied levels of theory were found from the experimental data for the (5*S*,8*S*,10*R*,14*R*) stereoisomer than for the other diastereomer, allowing elucidation of the relative configuration as (5*S**,8*S**,10*R**,14*R**). This result in combination with the ECD calculation of (5*S*,8*S*,10*R*,14*R*)-**1** allowed the unambiguous configurational assignment of **1** as (5*S*,8*S*,10*R*,14*R*). Moreover, the absolute structure of compound **1** was confirmed by anomalous dispersion of Cu Kα radiation to (5*S*,8*S*,10*R*,14*R*) (Figure 4), thus unequivocally

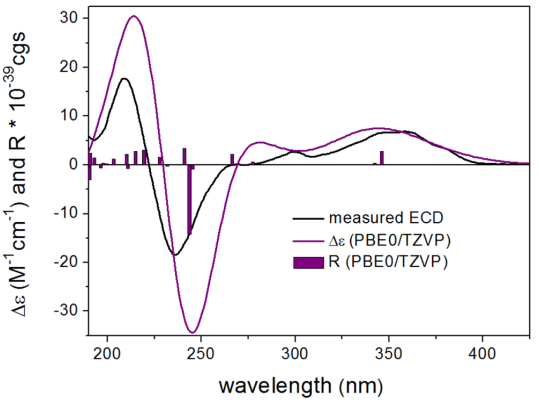

Figure 2. Experimental ECD spectrum of **1** in MeCN compared with the PBE0/TZVP PCM/MeCN ECD spectrum of (5*S*,8*S*,10*R*,14*R*)-**1** computed for the single CAM-B3LYP/TZVP PCM/MeCN conformer. Bars represent the rotational strength values.

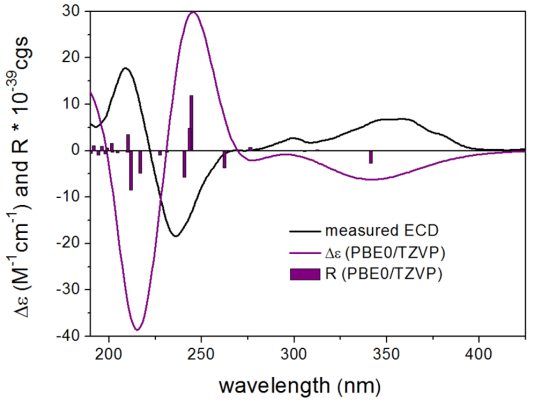

Figure 3. Experimental ECD spectrum of **1** in MeCN compared with the PBE0/TZVP PCM/MeCN ECD spectrum of (5*S*,8*R*,10*S*,14*R*)-**1** computed for the single low-energy CAM-B3LYP/TZVP PCM/MeCN conformer. Bars represent the rotational strength values.

supporting the predicted configuration. Further crystal data are listed in Table S75 (Supporting Information).

The molecular formula of paspalinine-13-ene (**2**) was established as $C_{27}H_{29}NO_3$ on the basis of the pseudomolecular ion peak at *m*/*z* 416.2215 $[M + H]^+$ in the HRESIMS spectrum, accounting for 14 degrees of unsaturation. The ^{1}H NMR data of **2** (Table 1) were similar to those of the known indole diterpenoid paspalicine,[44,45] except for an additional olefinic proton resonating at δ_H 6.52 (H-14) and the absence of the aliphatic signal at H-13, suggesting a double bond at $\Delta^{13(14)}$. The HMBC correlations from H_2-15 to two olefinic carbons C-13 and C-14 as well as to C-3 and C-16, together with correlations from H-14 to C-4, C-12, and C-16, confirmed the proposed structure of **2**. The relative configuration of **2** was deduced from the NOESY spectrum, which revealed a correlation between H-16 and H_3-26 and no correlation between H_3-25 and H-16. Compound **2** is known as a synthetic product described in a patent application together with a series of other synthetic paspalinine derivatives with

DOI: 10.1021/acs.jnatprod.8b00723
J. Nat. Prod. 2019, 82, 1412−1423

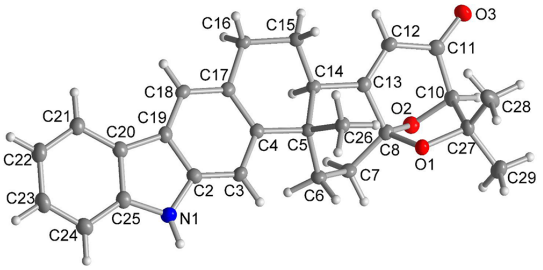

Figure 4. Molecular structure of one of the two symmetry-independent molecules in the crystal of **1** (50% thermal ellipsoids). For an image of both independent molecules in the asymmetric unit and their hydrogen-bonding interaction, see Figure S74 in the Supporting Information.

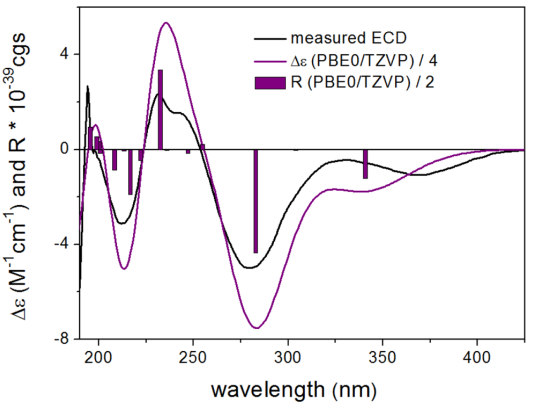

Figure 5. Experimental ECD spectrum of **3** in MeCN compared with the Boltzmann-averaged PBE0/TZVP PCM/MeCN ECD spectrum of (3*S*,4*S*,7*S*,9*R*,16*S*)-**3** computed for the low-energy (≥1%) CAM-B3LYP/TZVP PCM/MeCN conformers. Bars represent the rotational strength values of conformer A.

potent potassium channel blocking activity for use in the treatment of glaucoma.[38] In this paper, we report **2** as a new natural product for the first time and provide complete NMR data of this compound.

The HRESIMS spectrum of 7-hydroxypaxilline-13-ene (**3**) showed a prominent pseudomolecular ion peak at *m*/*z* 434.2325 $[M + H]^+$ consistent with the molecular formula $C_{27}H_{31}NO_4$, indicating 13 degrees of unsaturation. The ^1H and ^{13}C NMR data of **3** (Table 1) closely resembled those of **2**, apart from an additional hydroxy signal resonating at δ_H 6.54. The HMBC correlations from the extra hydroxy function to C-6, C-7, and C-12 suggested cleavage of the 1,3-dioxolane ring in the structure of **3**, which was in agreement with the loss of one degree of unsaturation in comparison with **2**. The cross-peak 7-OH/H-9 in the ROESY spectrum indicated the α-orientation of the hydroxy group. Moreover, the ROESY correlation H-16/H_3-26 implied a trans-3,16-ring junction as observed in former congeners.[20,52]

For the configurational assignment of **3**, the same solution TDDFT-ECD computational protocol was applied as for **1**. MMFF conformational search of (3*S*,4*S*,7*S*,9*R*,16*S*)-**3** resulted in 12 conformer clusters in a 21 kJ/mol energy window, the DFT reoptimization of which yielded three low-energy conformers over 1% population at both applied levels. ECD spectra computed at various levels for both sets of conformers reproduced the experimental ECD spectrum (Figure 5), allowing elucidation of the absolute configuration as (3*S*,4*S*,7*S*,9*R*,16*S*), which was in accordance with that of **1** and of paxilline.

The molecular formula of **4** was established on the basis of the HRESIMS as $C_{28}H_{35}NO_5$, accounting for 12 degrees of unsaturation. The ^1H and ^{13}C NMR data of **4** (Table 1) were similar to those of **3**, with additional signals of a methoxy group resonating at δ_H 3.38/δ_C 49.0 and of a hydroxy group at δ_H 4.58 in addition to the methylene protons at δ_H 1.64/1.83 (H_2-14). The methoxy group was assigned based on the observed HMBC correlation from 7-OMe to C-7. Furthermore, HMBC correlations from the hydroxy proton 13-OH to C-4, C-12, C-13, and C-14 confirmed its attachment to C-13. Accordingly, the planar structure of **4** was elucidated as 7-methoxypaxilline. The ROESY data suggested that **4** adopts the same relative configuration as **3**, and based on the displayed cross-peaks 7-OMe/H-9 and 13-OH/H_3-25, the hydroxy group 13-OH and 7-OMe are suggested to have a cofacial orientation.

The molecular formulas of 7-methoxypyrapaxilline (**5**) and pyrapaxilline-6-ene (**6**) were determined as $C_{38}H_{49}NO_6$ and $C_{37}H_{45}NO_5$, respectively, on the basis of prominent pseudomolecular ion peaks in the HRESIMS spectra. The ^1H and ^{13}C NMR data of these two metabolites (Table 2) were in good agreement with those of pyrapaxilline (**21**)[53] isolated in this study, indicating that both compounds share the same eight-membered ring skeleton characteristic of the janthitremane group of indole diterpenoids isolated from *Eupenicillium shearii*.[54] Compound **5** differed from pyrapaxilline by the presence of a methoxy group attached to C-7, instead of the oxymethine proton in the known analogue. This was confirmed by the respective HMBC correlation from 7-OMe to C-7. Further comparison of NMR data of derivatives **5** and **6** revealed that **6** displays an olefinic signal (δ_H 5.64/δ_C 110.9 and a sp^2 carbon at δ_C 145.1), instead of a 7-OMe group, that were assigned to the double bond at $\Delta^{6(7)}$, accounting for the additional degree of unsaturation of compound **6**. The NMR chemical shift data were in accordance with the recently reported shearinines L and M, bearing double bonds at the same position as well.[55] Based on the similarity of the NMR data with regard to signals of rings D−H of compounds **5** and **6**, including the NOE correlations with those of **4** and pyrapaxilline and considering their common biosynthetic origin, **5** and **6** are suggested to share the same relative configuration that is characteristic for shearinine/paspalinine derivatives. Consequently, the structures of **5** and **6** were established as new shearinine derivatives, and shearinine N and O were proposed as their trivial names, respectively.

The molecular formula of shearinine P (**7**) was determined as $C_{37}H_{47}NO_7$ on the basis of the prominent pseudomolecular ion peak at *m*/*z* 618.3416 $[M + H]^+$ in the HRESIMS spectrum. The ^1H and ^{13}C NMR data of **7** (Table 2) showed close similarity to those of pyrapaxilline.[53] However, the olefinic signals at C-18 and C-2 of pyrapaxilline were replaced by two carbonyl signals at δ_C 174.6 (C-2) and δ_C 204.6 (C-18), respectively. These signals suggested the presence of a keto-amide ring in the structure of **7**, as described for shearinine C,[54] which is presumably formed via oxidation of the indole moiety at the C-2−C-18 double bond. The presence

DOI: 10.1021/acs.jnatprod.8b00723
J. Nat. Prod. 2019, 82, 1412−1423

Table 2. ^{1}H and ^{13}C NMR Data for 5−9

	5[a]		6[b]		7[a]		8[a]		9[a]	
position	δ_C, type	δ_H (J in Hz)	δ_C, type	δ_H (J in Hz)	δ_C, type[c]	δ_H (J in Hz)	δ_C, type[c]	δ_H (J in Hz)	δ_C, type[c]	δ_H (J in Hz)
1-NH		10.60, s		10.59, s		9.09, s		9.09, s		7.28, br s (NH_2)
2	151.8, C		151.7, C		174.6, C		174.5, C		176.5, C	12.30, br s (COOH)
3	50.5, C		50.3, C		56.6, C		56.4, C		52.7, C	
4	42.5, C		42.8, C		43.3, C		43.4, C		41.7, C	
5	25.0, CH_2	2.41 m; 1.79, m	30.4, CH_2	3.01, br d (17.5); 2.43, m	24.9, CH_2	2.34, ov; 1.70, m	23.5, CH_2	2.19, td (14.1, 4.5); 1.73, m	25.0, CH_2	2.38, m; 1.53, ov
6	27.3, CH_2	2.47, m; 1.88, m	110.9, CH	5.64, br dt (6.4, 2.4)	27.8, CH_2	2.07, m; 1.54, m	26.7, CH_2	2.35, td (14.9, 3.3); 1.62, td (14.9, 4.7)	27.7, CH_2	2.06, m; 1.53, ov
7	97.2, C		145.1, C		71.9, CH	4.67, ddt (10.3, 8.0, 2.2)	96.6, C		72.1, CH	4.69, br ddt (10.0, 7.7, 2.1)
9	78.5, CH	3.92, s	85.9, CH	4.02, s	82.9, CH	3.60, d (1.9)	78.0, CH	3.86, s	82.9, CH	3.63, d (1.9)
10	197.2, C		195.1, C		197.6, C		197.1, C		197.5, C	
11	121.3, CH	5.76, s	115.9, CH	5.80, s	119.3, CH	5.66, br d (1.9)	121.7, CH	5.68, s	119.3, CH	5.77, br d (2.0)
12	160.3, C		154.5, C		168.4, C		159.7, C		168.7, C	
13	75.8, C		73.9, C		75.1, C		75.0, C		75.2, C	
14	32.6, CH_2	1.71, m; 1.64, m	31.8, CH_2	1.94, ov; 1.85, m	30.3, CH_2	1.59, m; 1.44, m	30.1, CH_2	1.51, td (13.0, 3.7); 1.45, m	29.2, CH_2	1.72, br td (13.4, 4.2); 1.53, ov
15	21.0, CH_2	1.89, m; 1.60, m	21.1, CH_2	1.94, ov; 1.66, m	24.9, CH_2	1.74, m; 1.30, br dt (9.8, 3.4)	24.9, CH_2	1.73, m; 1.30, m	22.2, CH_2	1.53, ov; 148 m
16	49.2, CH	2.68, m	49.1, CH	2.72, m	35.2, CH	2.88, ov	35.0, CH	2.92, m	33.4, CH	2.89, m
17	27.0, CH_2	2.61, dd (12.8, 6.1); 2.29, dd (12.8, 10.9)	26.8, CH_2	2.62, dd (12.8, 6.2); 2.29, dd (12.8, 11.0)	47.8, CH_2	2.88, ov; 2.34, ov	47.7, CH_2	2.88, dd (17.5, 6.6); 2.35, ov	42.6, CH_2	2.76, dd (14.9, 2.1); 2.58, m
18	114.9, C		114.8, C		204.6, C		204.8, C		200.4, C	
19	122.4, C		122.4, C		130.8, C		130.9, C		113.7, C	
20	113.0, CH	7.31, s	113.0, CH	7.31, s	122.0, CH	7.47, s	121.9, CH	7.45, s	125.0, CH	7.91, s
21	133.5, C		133.6, C		140.5, C		140.5, C		127.9, C	
22	35.6, CH_2	3.28, ov[d]	35.6, CH_2	3.29, ov	36.4, CH_2	3.44, dt (22.8, 2.5); 3.49 dt (22.8, 2.5)	36.4, CH_2	3.43, d (22.8); 3.49, d (22.8)	35.5, CH_2	3.30, ov
23	141.8, C		141.8, C		149.3, C		149.0, C		151.0, C	
24	72.9, C		73.0, C		72.9, C		72.9, C		73.0, C	
26	70.8, C		70.8, C		70.5, C		70.8, C		70.8, C	
27	33.9, CH_2	2.38, m	33.9, CH_2	2.37, t (2.8)	33.4, CH_2	2.34, m	33.4, CH_2	2.35, ov	33.3, CH_2	2.29, t (2.5)
28	131.5, C		131.5, C		130.5, C		130.7, C		130.8, C	
29	138.0, C		138.1, C		148.2, C		148.0, C		150.7, C	
30	101.3, CH	7.05, br d (0.8)	101.4, CH	7.06, d (0.8)	116.5, CH	6.88, s	116.2, CH	6.88, s	105.4, CH	6.56, s
31	139.1, C		139.3, C		136.4, C		136.2, C		150.7, C	
32	16.2, CH_3	1.23, s	16.4, CH_3	1.27, s	16.0, CH_3	1.46, s	16.1, CH_3	1.44, s	14.4, CH_3	1.38, s
33	19.1, CH_3	0.91, s	19.7, CH_3	1.01, s	19.2, CH_3	0.82, s	19.5, CH_3	0.85, s	19.4, CH_3	0.83, s
34	71.0, C		72.9, C		70.9, C		70.9, C		70.8, C	
35	25.8, CH_3	1.21, s	26.8, CH_3	1.14, s	25.6, CH_3	1.12, s	25.5, CH_3	1.15, s	25.6, CH_3	1.14, s
36	26.2, CH_3	1.23, s	27.1, CH_3	1.25, s	25.4, CH_3	1.16, s	25.8, CH_3	1.18, s	25.5, CH_3	1.18, s
37	30.4, CH_3	1.35, s	30.5, CH_3	1.35, s	30.0, CH_3	1.36, s	30.1, CH_3	1.35, s	29.8, CH_3	1.34, s
38	30.4, CH_3	1.35, s	30.6, CH_3	1.35, s	30.0, CH_3	1.36, s	30.1, CH_3	1.36, s	29.8, CH_3	1.34, s
39	29.4, CH_3	1.24, s	29.4, CH_3	1.25, s	28.8, CH_3	1.20, s	28.7, CH_3	1.20, s	28.9, CH_3	1.22, s

DOI: 10.1021/acs.jnatprod.8b00723
J. Nat. Prod. 2019, 82, 1412−1423

Table 2. continued

	5[a]		6[b]		7[a]		8[a]		9[a]	
position	δ_C type	δ_H (J in Hz)	δ_C type	δ_H (J in Hz)	δ_C type[c]	δ_H (J in Hz)	δ_C type[c]	δ_H (J in Hz)	δ_C type[c]	δ_H (J in Hz)
40	29.5, CH_3	1.24, s	29.5, CH_3	1.25, s	29.2, CH_3	1.24, s	29.2, CH_3	1.24, s	28.9, CH_3	1.22, s
7-OMe	49.0, CH_3	3.38, s					48.6, CH_3	3.32, s		
13-OH		4.56, s		4.88, s		4.92, s		4.47, s		4.90, s
34-OH		4.45, s		4.53, s		4.28, s		4.38, s		4.30, s

[a]Recorded at 600 MHz (^{1}H) and 300 MHz (^{13}C) in DMSO-d_6. [b]Recorded at 300 MHz (^{1}H) and 75 MHz (^{13}C) in DMSO-d_6. [c]Chemical shifts extracted from HSQC and HMBC spectra. [d]ov stands for overlapped signals.

of this substructure in **7** was further corroborated by HMBC correlations from H_2-17 to C-18, from H-20 to C-18, from H-30 to C-18 (long-range correlation), and from NH and H_3-32 to C-2. Moreover, **7** exhibited the same molecular formula as shearinine C.[47] The double bond in ring A, however, was switched from $\Delta^{27(28)}$ to $\Delta^{23(28)}$ for compound **7**, which was supported by HMBC correlations from H_3-37/H_3-38 to C-23, as well as from H_2-22 and H_2-27 to both olefinic carbons C-23 and C-28. Thus, the planar structure of **7** was identified as the ring-opened 7-desmethoxy derivative of **5**, in which the C-2−C-18 bond of the indole moiety was oxidized and cleaved.

The MMFF search of (3*S*,4*R*,7*S*,9*R*,13*S*,16*S*)-**7** resulted in 18 conformer clusters in a 21 kJ/mol window, the DFT reoptimization of which yielded five and six low-energy conformers above 1% at the B3LYP/6-31+G(d,p) and the CAM-B3LYP/TZVP PCM/MeCN levels, respectively. ECD spectra computed at various levels gave moderate agreement with the experimental ECD spectrum (see Figure S73). While the B3LYP and the PBE0 functionals resembled well the 197 and the 290 nm transitions, they failed to reproduce the 249 nm transition. The BH&HLYP and CAM-B3LYP functionals on the other hand gave better results for this transition but were not successful in the low-wavelength region.[48] It is possible that the real conformational distribution is somewhat different from the estimated one (results not shown). Based on the approximate overall ECD agreement, the absolute configuration was determined as (3*S*,4*R*,7*S*,9*R*,13*S*,16*S*).

The pseudomolecular ion peak of **8** was 30 amu larger than that of **7**, as evident from the HRESIMS spectrum, which was consistent with the molecular formula $C_{38}H_{49}NO_8$. The ^{1}H and ^{13}C NMR data of **8** (Table 2) were almost identical to those of **7**, with the exception of an additional methoxy signal at δ_H 3.32/δ_C 48.6 instead of the methine at position 7. The connection of this group to δ_C 96.6 (C-7) was verified by the respective HMBC correlation. Therefore, the structure of **8** was determined as a new shearinine congener, and the name 7-methoxyshearinine P was suggested. The ^{1}H and ^{13}C NMR data of shearinine Q (**9**) (Table 2) closely resembled those of **7**. Compound **9**, however, displayed an increase in the molecular weight of 18 amu compared to **7**, which together with the loss of one degree of unsaturation indicated cleavage of the keto-amide ring in the structure of **9**. This was further corroborated by the presence of free amino and carboxylic acid groups resonating at δ_H 7.28 and 12.30, respectively. Thus, the planar structure of **9** was elucidated. Based on biosynthetic considerations and on the similarity of NOESY data of **7**−**9** it is assumed that **8** and **9** share the same relative stereochemistry as **7**.

The structures of the remaining 13 known compounds were established based on their spectroscopic data, as well as by comparison with the literature. These natural products were identified as emindole SB (**10**),[14,56] shearinine F (**11**),[52,57] paspalicine (**12**),[44,45] 21-isopentenylpaxilline (**13**),[54] paxilline (**14**),[14,20,56] dehydroxypaxilline (**15**),[56] paspalinine (**16**),[27,58] 6,7-dehydropaxilline (**17**),[59] paspaline (**18**),[44,60] 7-hydroxy-13-dehydroxypaxilline (**19**),[54,61] 10β-hydroxy-13-desoxypaxilline (**20**),[61] pyrapaxilline (**21**),[53] and paspalitrem A (**22**),[62] as shown in Figure S80.

An additional experiment was performed to exclude the possibility that **4**, **5**, and **8** are artifacts arising from their corresponding analogues (paxilline, pyrapaxilline, and **7**, respectively) during the isolation process. For this purpose, 1 mg of paxilline, pyrapaxilline, or **7** was each dissolved in 1.0 mL

DOI: 10.1021/acs.jnatprod.8b00723
J. Nat. Prod. 2019, 82, 1412−1423

of MeOH, exposed to light for 72 h at room temperature, and then analyzed by HPLC and LC-MS. The results showed no additional peak in the HPLC chromatograms nor in the MS spectra, indicating that the new methoxylated analogues **4**, **5**, and **8** are true natural products and not artifacts formed through methylation when using MeOH.

The biosynthetic pathway leading to indole diterpenoids has been widely discussed in the literature. These compounds are suggested to be formed through a common intermediate, 3-geranylgeranylindole, followed by a series of epoxidation, oxidation, cyclization, and prenylation reactions, which provide their large chemical diversity.[16,18,40,41] Interestingly, compound **1** bears a rare carbazole motif, which has previously been reported for xiamycin A,[43,63] an uncommon indole sesquiterpene isolated from the bacterial endophyte *Streptomyces* sp. Following characterization of the corresponding biosynthetic gene cluster, it was suggested that a flavoprotein-catalyzed hydroxylation of the indole moiety takes place forming an indole C-3-hydroxyiminium species. Subsequently, the resulting C-2 carbanion equivalent is attacked by the C-23 olefinic function, leading to a cyclization reaction.[63] Finally, dehydration and proton loss followed by spontaneous oxidative aromatization would lead to the formation of the carbazole moiety of xiamycin A.[63] Accordingly, compound **1** is proposed to undergo a similar cyclization mechanism for geranylgeranylindole, as described for xiamycin A (Figure S81). However, considering that xiamycin A is a bacterial compound, the cyclization mechanism for geranylgeranylindole in **1** might be novel and warrants further investigation. Additional oxidation steps followed by cyclization would yield the keto function at C-11 and ketal formation at C-8, thus forming the rings F and G in **1**, which is related to paspalicine.

All isolated compounds were evaluated for their cytotoxic activity toward the murine L5178Y cell line (Table 3). Among the tested natural products, compound **1** exhibited the most pronounced activity, with an IC_{50} value of 3.6 μM, which was stronger than that of the positive control kahalalide F (IC_{50} 4.3 μM). Compounds **2**, **3**, **6**, **7**, and 7-hydroxy-13-dehydroxypaxilline (**19**) displayed cytotoxicity with IC_{50} values in the range of 5.3−8.1 μM. In addition, the cytotoxicity of the isolated compounds toward the A2780 human ovarian cancer cell line was determined (Table 3). Compounds **1**, **6**, emindole SB (**10**), and paspaline (**18**) showed pronounced activity with IC_{50} values of 5.3−8.7 μM. The remaining compounds were found to be inactive against both cell lines. The unusual motif of the indole diterpenoid scaffold in **1**, bearing an aromatic ring C, is suggested to be determinant of its strong cytotoxicity [**1** vs paspalicine (**12**)]. A double bond at $\Delta^{13(14)}$ increases the activity of paspalinine derivatives [**2** vs paspalicine (**12**)], whereas it has little influence on the cytotoxicity of paxilline derivatives [**3** vs 7-hydroxy-13-dehydroxypaxilline (**19**)]. Furthermore, a double bond at $\Delta^{6(7)}$ slightly enhances the cytotoxicity of janthitremane derivatives [**6** vs pyrapaxilline (**21**)]. Cleavage of the keto-amide ring in the seven-membered ring skeleton of indole diterpenoid leads to loss of activity, as observed in **9** vs **7**. Meanwhile, the replacement of a proton at C-7 by a methoxy group tends to attenuate the activity [pyrapaxilline (**21**) vs **5**, and **7** vs **8**]. Interestingly, Sallam et al. demonstrated the antiproliferative and antimigratory activities of emindole SB (**10**) and paspaline (**18**) against human breast cancer cells, showing no BK channel inhibitory effect, which renders these compounds interesting pharmacophores for further biological studies.[35]

Table 3. Cytotoxicity (IC_{50} in μM) of 1−10, 13, 15, 18−22 toward L5178Y, A2780, J82, and HEK-293 Cell Lines

	1	2	3	4	5	6	7	8	9	10	13	15	18	19	20	21	22
L5178Y[a]	3.6	5.3	5.3	*f*	*f*	8.1	7.6	*f*	*f*	18.3	12.9	*f*	*f*	6.2	*f*	10.9	*f*
A2780[b]	8.7 (3.3)[e]	12.2 (1.8)[e]	*f*	12.2	32.2	7.8 (4.8)[e]	11.9 (2.4)[e]	19.4	51.5	8.2 (5.4)[e]	*f*	17.1	5.3 (8.1)[e]	*f*	28.5	12.8	19.8
J82[c]	40.6	42.1	*g*	55.3	96.7	31.7	29.4	73.0	*f*	*g*	*g*	*g*	*g*	*g*	*g*	*g*	*g*
HEK-293[d]	28.5	21.7	27.9	*g*	*g*	37.4	28.3	*g*	*g*	44.6	*g*	*g*	43.0	39.8	*g*	*g*	*g*

[a]Kahalalide F (IC_{50} 4.3 μM) as positive control. Cisplatin (IC_{50} 1.2 μM,[b] 0.8 μM,[c] and 6.2 μM[d]) as positive control. [e]Selectivity index (SI): IC_{50} values against HEK-293 cells divided by IC_{50} value against the A2780 cell line. [f]Inactive. [g]Not tested.

DOI: 10.1021/acs.jnatprod.8b00723
J. Nat. Prod. 2019, 82, 1412−1423

A high-content analysis-based fluorescent live/dead assay of the new compounds was applied to the human urothelial bladder cancer cell line J82 (Table 3). Bladder cancer is known to rapidly develop chemoresistance. Thus, compounds active against bladder cancer cell lines are of high scientific interest. In the fluorescent live/dead assay, direct counts of live and dead cells were acquired by the fluorescent imaging system. Most of the tested compounds gave IC_{50} values between 30 and 100 μM toward J82 cells, thus showing considerably lower potency compared to their activity against L5178Y or A2780 cells (Figures S86 and S87).

Furthermore, active compounds with IC_{50} values of <10 μM against L5178Y or A2780 cells [**1**–**3**, **6**, **7**, emindole SB (**10**), paspaline (**18**), and 7-hydroxy-13-dehydroxypaxilline (**19**)] were tested against the human embryonic kidney cell line HEK-293 for preliminary estimation of their selectivity index (SI). Compounds **1**, **6**, emindole SB (**10**), and paspaline (**18**) showed the highest selectivity among tested compounds with SI values in the range from 3.3 to 8.1, comparable to that of the positive control cisplatin (SI = 5.2), which merits further pharmacological investigation.

EXPERIMENTAL SECTION

General Experimental Procedures. Optical rotations were determined with a Jasco P-2000 polarimeter. ^{1}H (600 and 300 MHz), ^{13}C (150 and 75 MHz), and 2D NMR were recorded on Bruker AVANCE DMX 600 or 300 NMR spectrometers. The chemical shifts (δ) were referred to the residual solvent peaks at δ_H 2.50 (DMSO-d_6) and δ_H 7.26 ($CDCl_3$) ppm for ^{1}H, and δ_C 39.5 (DMSO-d_6) and δ_C 77.2 ($CDCl_3$) ppm for ^{13}C. Mass spectra (ESI) were measured with a Finnigan LCQ Deca mass spectrometer, and HRMS (ESI) spectra were recorded with an FTHRMS-Orbitrap (Thermo-Finnigan) mass spectrometer. HPLC analysis was performed with a Dionex UltiMate 3000 HPLC system with an UltiMate 3000 pump coupled to a photodiode array detector (DAD 3000 RS), with the detection wavelength set at 235, 254, 280, and 340 nm. The column was prefilled with Eurospher 100-10 C_{18}, 125 × 4 mm (Knauer, Germany). The following gradient was used for routine analysis (MeOH: 0.1% HCOOH in H_2O): 0 min (65% MeOH); 2 min (65% MeOH); 25.5 min (100% MeOH); 35.5 min (100% MeOH). Semipreparative HPLC was performed with a Merck Hitachi Chromaster HPLC system (UV detector 5410; pump 5110; column Eurospher 100-10 C_{18}, 300 × 8 mm, Knauer, Germany; flow rate 5 mL/min). Column chromatography was performed on silica 60 M (0.040–0.063 mm; Macherey-Nagel, Germany) and on Sephadex LH-20 stationary phases. TLC plates precoated with silica gel 60 F_{254} (Macherey-Nagel, Germany) were used for analysis; detection was under UV 254 and 366 nm. ECD spectra were recorded on a J-810 spectropolarimeter.

Fungal Material. The fungus *Penicillium* sp. (strain ZO-R1-1) was isolated[64] from healthy roots of *Zingiber officinale*, collected in May 2016 at Banyumas, the Central Java Province, Indonesia. The taxonomic identification of the fungus was conducted according to a molecular biology protocol by DNA amplification and gene sequencing in the ITS region as previously described,[64] followed by BlastN search in the NCBI database. The sequence was submitted to GenBank (accession no. MH602299). The fungus strain was deposited in one of the author's laboratory (P.P.).

Fermentation, Extraction, and Isolation. The fungus was inoculated on solid rice medium, which was prepared by autoclaving 100 g of rice in 100 mL of demineralized water in a 1 L Erlenmeyer flask. The fermentation was performed in 5 flasks under static conditions at room temperature for 3 weeks. The fungal culture was extracted with 500 mL of ethyl acetate added to each flask, and the extract was subsequently dried under vacuum to afford 7.6 g. Fat was removed from the extract by liquid–liquid separation between *n*-hexane and 90% aqueous MeOH. The MeOH fraction (4.6 g) was subjected to vacuum liquid chromatography over silica gel 60 using a step gradient elution, employing mixtures of *n*-hexane–EtOAc followed by CH_2Cl_2–MeOH to yield 16 fractions. Fractions 80HEA, 70HEA, 60HEA, and 50HEA eluted with *n*-hexane–EtOAc (8:2), (7:3), (6:4), and (5:5), respectively, were selected for further separation according to their HPLC chromatograms. Separation of fraction 80HEA (173.2 mg) was carried out on Sephadex LH-20 employing CH_2Cl_2–MeOH as mobile phase, followed by purification using semipreparative HPLC with MeOH–H_2O as mobile phase to yield the new compounds **1** (2.4 mg) and **2** (1.3 mg), along with known compounds shearinine F (1.1 mg), paspalicine (4.1 mg), paspalinine (11.7 mg), and paspalitrem A (3.0 mg). Following the same procedure, emindole SB (3.5 mg), dehydroxypaxilline (1.9 mg), and paspaline (1.9 mg) were obtained from fraction 70HEA (398.2 mg). The new compounds **3** (3.7 mg), **4** (7.0 mg), **5** (10.9 mg), **6** (4.5 mg), **7** (4.5 mg), **8** (1.4 mg), and **9** (2.5 mg), as well as known analogues 21-isopentenylpaxilline (11.2 mg), paxilline (38.0 mg), 6,7-dehydropaxilline (1.8 mg), 7-hydroxy-13-dehydroxypaxilline (3.2 mg), and pyrapaxilline (19.8 mg), were afforded from fraction 60HEA (513.9 mg). In the same manner, chromatographic separation of fraction 50HEA (133.9 mg), yielded the known compound 10β-hydroxy-13-desoxypaxilline (6.7 mg).

*Shearilicine (**1**):* colorless, crystal; $[\alpha]_D^{20}$ +201 (*c* 0.27, $CHCl_3$); UV (MeOH, photodiode array) λ_{max} 301, 261, 239 nm; ECD (MeCN, λ [nm] ($\Delta\varepsilon$), *c* 0.121 mM) 379sh (+3.57), 358 (+6.87), 345sh (+6.54), 332sh (+4.43), 300 (+2.69), 246sh (−11.68), 236 (−18.43), 208 (+17.70); ^{1}H and ^{13}C NMR data, see Table 1; HRESIMS *m*/*z* 414.2063 [M + H]$^+$ (calcd for $C_{27}H_{28}NO_3$, 414.2064).

*Paspalinine-13-ene (**2**):* colorless, crystal; $[\alpha]_D^{20}$ −63 (*c* 0.10, $CHCl_3$); UV (MeOH, photodiode array) λ_{max} 299, 229 nm; ECD (MeCN, λ [nm] ($\Delta\varepsilon$), *c* 0.175 mM) 369 (+4.59), 302sh (−12.62), 294 (−13.17), 249 (+0.72), 227sh (+2.72), 215sh (+3.20), 204 (+3.35); ^{1}H and ^{13}C NMR data, see Table 1; HRESIMS *m*/*z* 416.2215 [M + H]$^+$ (calcd for $C_{27}H_{30}NO_3$, 416.2220).

*7-Hydroxypaxilline-13-ene (**3**):* white, amorphous powder; $[\alpha]_D^{20}$ −365 (*c* 0.10, $CHCl_3$); UV (MeOH, photodiode array) λ_{max} 287, 229 nm; ECD (MeCN, λ [nm] ($\Delta\varepsilon$), *c* 0.346 mM) 402sh (−0.34), 369 (−1.07), 290sh (−4.24), 279 (−5.00), 244sh (+1.51), 231 (+2.34), 219sh (−2.12), 212 (−3.12); ^{1}H and ^{13}C NMR data, see Table 1; HRESIMS *m*/*z* 434.2325 [M + H]$^+$ (calcd for $C_{27}H_{32}NO_4$, 434.2326).

*7-Methoxypaxilline (**4**):* yellow, amorphous powder; $[\alpha]_D^{20}$ +11 (*c* 0.10, MeOH); UV (MeOH, photodiode array) λ_{max} 281, 230 nm; ECD (MeCN, λ [nm] ($\Delta\varepsilon$), *c* 0.054 mM) 368 (−0.62), 300 (+1.00), 247 (+3.42), 233 (−3.57), 223 (+2.57), 205 (−12.00); ^{1}H and ^{13}C NMR data, see Table 1; HRESIMS *m*/*z* 466.2587 [M + H]$^+$ (calcd for $C_{28}H_{36}NO_5$, 466.2588).

*Shearinine N (**5**):* yellow, amorphous powder; $[\alpha]_D^{20}$ +5 (*c* 0.10, MeOH); UV (MeOH, photodiode array) λ_{max} 306, 238 nm; ECD (MeCN, λ [nm] ($\Delta\varepsilon$), *c* 0.162 mM) 359 (−0.30), 303 (+1.20), 264 (−2.11), 240 (+3.82), 212 (−8.49); ^{1}H and ^{13}C NMR data, see Table 2; HRESIMS *m*/*z* 616.3620 [M + H]$^+$ (calcd for $C_{38}H_{50}NO_6$, 616.3633).

*Shearinine O (**6**):* yellow, amorphous powder; $[\alpha]_D^{20}$ −5 (*c* 0.10, MeOH); UV (MeOH, photodiode array) λ_{max} 308, 257, 241 nm; ECD (MeCN, λ [nm] ($\Delta\varepsilon$), *c* 0.128 mM) 375 (−3.99), 318 (+6.15), 254sh (−3.49), 248 (−3.54), 220 (+1.69), 203 (−2.59); ^{1}H and ^{13}C NMR data, see Table 2; HRESIMS *m*/*z* 584.3361 [M + H]$^+$ (calcd for $C_{37}H_{46}NO_5$, 584.3370).

*Shearinine P (**7**):* white, amorphous powder; $[\alpha]_D^{20}$ −76 (*c* 0.20, $CHCl_3$); UV (MeOH, photodiode array) λ_{max} 309, 243 nm; ECD (MeCN, λ [nm] ($\Delta\varepsilon$), *c* 0.081 mM) 341 (−2.46), 294 (+9.42), 250 (−30.80), 231sh (−19.32), 213sh (+1.82); ^{1}H and ^{13}C NMR data, see Table 2; HRESIMS *m*/*z* 618.3416 [M + H]$^+$ (calcd for $C_{37}H_{48}NO_7$, 618.3425).

*7-Methoxyshearinine P (**8**):* white, amorphous powder; $[\alpha]_D^{20}$ −19 (*c* 0.05, MeOH); UV (MeOH, photodiode array) λ_{max} 309, 224 nm; ECD (MeCN, λ [nm] ($\Delta\varepsilon$), *c* 0.077 mM) 367sh (−0.88), 340 (−1.12), 292 (+3.12), 256 (−8.17), 212 (−8.86); ^{1}H and ^{13}C NMR

DOI: 10.1021/acs.jnatprod.8b00723
J. Nat. Prod. 2019, 82, 1412–1423

data, see Table 2; HRESIMS m/z 648.3523 $[M + H]^+$ (calcd for $C_{38}H_{50}NO_8$, 648.3531).

Shearinine Q (9): yellow, amorphous powder; $[\alpha]_D^{20}$ −33 (c 0.20, $CHCl_3$); UV (MeOH, photodiode array) λ_{max} 381, 306, 245 nm; ^1H and ^{13}C NMR data, see Table 2; HRESIMS m/z 636.3530 $[M + H]^+$ (calcd for $C_{37}H_{50}NO_8$, 636.3531).

Cytotoxicity Assay. Cytotoxicity toward the murine lymphoma cell line L5178Y was tested by the MTT method with kahalalide F as positive control and media with 0.1% DMSO as negative control as described earlier.[65] The rate of cell survival of the ovarian cancer cell line A2780 and of the human embryonic kidney cell line HEK-293 under the action of test substances was evaluated by an improved MTT assay as previously described.[66] The A2780 and HEK-293 cells were seeded into 96-well plates (Sarstedt, Germany) and incubated overnight. Then, cells were exposed to increasing concentrations of compounds in phosphate-buffered saline (PBS) and positive control cisplatin. After 72 h treatment, 25 μL of MTT solution (5 mg/mL) was added into each well and incubated for 15 min. The formazan precipitate was dissolved in 75 μL of DMSO per well. Absorbance was then measured at 544 and 690 nm using the BMG FLUOstar microplate reader (BMG Labtechnologies Offenburg, Germany).

High Content Analysis Based Fluorescent Live/Dead Assay. Live and dead cells were assayed by high content analysis (HCA). Briefly, the urothelial bladder cancer cell line J82 was treated with increasing concentrations of compounds in 96-well plates (Sarstedt, Germany). After 72 h treatment, cells were stained with a mixture of Hoechst 33342 (Sigma-Aldrich, St. Louis, MO, USA), calcein AM (Merck Millipore, Germany), and propidium iodide (Santa Cruz Biotechnology, Heidelberg) for cell nuclei and live and dead cells, respectively. The staining solution was replaced by PBS after 20 min. Images were acquired with the ArrayScan XTI Live High Content Platform (Thermo Fisher Scientific Inc., USA) using excitation filters of 386 nm (Hoechst 33342), 485 nm (calcein AM), and 560 nm (propidium iodide), respectively. Results were analyzed using HCS Studio: Cellomics Scan (Thermo Fisher Scientific Inc., USA).

Computational Section. Mixed torsional/low-frequency mode conformational searches were carried out by means of the Macromodel 10.8.011 software by using the MMFF with an implicit solvent model for $CHCl_3$.[67] Geometry reoptimizations were carried out at the B3LYP/6-31+G(d,p) level in vacuo and CAM-B3LYP/TZVP[50] levels with the PCM solvent model for MeCN with the Gaussian 09 package.[68] TDDFT-ECD calculations were run with various functionals (B3LYP, BH&HLYP, CAM-B3LYP, and PBE0) and the TZVP basis set with the same or no solvent model as in the preceding DFT optimization step. ECD spectra were generated as sums of Gaussians with 2400−3600 cm^{-1} half-height widths using dipole-velocity-computed rotational strength values.[69] NMR shift values were computed at the mPW1PW91/6-311+G(2d,p) and the mPW1PW91/6-311+G(2d,p) SMD/$CHCl_3$ levels. Computed ^{13}C NMR data were corrected with I = 185.4855 and S = −1.0306 in the gas phase and I = 186.5242 and S = −1.0533 in the SMD calculations.[70,71] Boltzmann distributions were estimated from the B3LYP and the CAM-B3LYP energies. The MOLEKEL software package was used for visualization of the results.[72]

X-ray Crystallographic Analysis of 1. Crystals were afforded by slow evaporation from methanol solution. Data Collection: Compound **1** was measured with a Bruker Kappa APEX2 CCD diffractometer with a microfocus tube and Cu Kα radiation (λ = 0.710 73 Å). For data collection APEX2, for cell refinement and data reduction SAINT,[73] and for experimental absorption correction SADABS were used.[74] The structure was solved by intrinsic phasing using SHELXT,[75] and refinement was done by full-matrix least-squares on F^2 using SHELXL-2016/6.[76] The hydrogen atoms were positioned geometrically (with C−H = 0.95 Å for aromatic CH, 1.00 Å for aliphatic CH, 0.99 Å for CH_2, and 0.98 Å for CH_3) and refined using riding models (AFIX 43, 13, 23, 137, respectively), with $U_{iso}(H) = 1.2U_{eq}$(CH, CH_2), and $1.5U_{eq}(CH_3)$. The hydrogen atoms in amine groups were refined with $U_{iso}(H) = 1.5U_{eq}$.

The absolute structure configuration of **1** was solved using anomalous dispersion from Cu Kα, resulting in a Flack parameter of x = −0.01(7) using Parsons quotient method. All graphics were drawn using DIAMOND.[77] The structural data have been deposited in the Cambridge Crystallographic Data Center (CCDC No. 1862565).

■ ASSOCIATED CONTENT

Supporting Information

The Supporting Information is available free of charge on the ACS Publications website at DOI: 10.1021/acs.jnatprod.8b00723.

HPLC chromatograms, UV, HRESIMS, NMR spectra of **1**−**9**, structure of the single conformer of **1**, results of ^{13}C NMR DFT calculations of **1**, structure and population of the low-energy conformers of **3**, ECD spectrum of **7**, results of the X-ray analysis of **1** as well as results of the cell viability assay of **1**, **2**, and **4**−**9** (PDF)

Crystallographic data of **1** (CIF)

■ AUTHOR INFORMATION

Corresponding Authors

*Tel: +49 211 81 14175. E-mail: Elena.Ancheeva@uni-duesseldorf.de.

*Tel: +49 211 81 14173. E-mail: Georgios.Daletos@uni-duesseldorf.de.

*Tel: +49 211 81 14163. Fax: +49 211 81 11923. E-mail: proksch@uni-duesseldorf.de.

ORCID

Elena Ancheeva: 0000-0002-2440-4427

Attila Mándi: 0000-0002-7867-7084

Christoph Janiak: 0000-0002-6288-9605

Georgios Daletos: 0000-0002-1636-6424

Present Address

G. Daletos: Department of Chemical Engineering, Massachusetts Institute of Technology, 25 Ames Street, Cambridge, Massachusetts 02139, United States.

Notes

The authors declare no competing financial interest.

■ ACKNOWLEDGMENTS

The scholarship granted to N.P.A. by DAAD under the Program Biodiversity and Health is gratefully acknowledged. This study was supported by the Bundesministerium für Bildung und Forschung (BMBF, Germany, project BALIPEND, grant number 16GW0107K to P.P. and grant number 16GW0108 to M.U.K.) and by the Deutsche Forschungsgemeinschaft (DFG, Germany) for funding the ThermoFisher Arrayscan XTI (Grant INST 208/690-1-FUGG) to M.U.K. The research of the Hungarian authors was supported by the EU and cofinanced by the European Regional Development Fund under the project GINOP-2.3.2-15-2016-00008. The Governmental Information-Technology Development Agency (KIFÜ) is acknowledged for CPU time. We wish to thank Harwoko (Institute of Pharmaceutical Biology and Biotechnology, Heinrich Heine University Düsseldorf, Germany) for collection of the plant material.

■ REFERENCES

(1) Berdy, J. *J. Antibiot.* **2005**, *58*, 1−26.

(2) Finkelstein, E.; Amichai, B.; Grunwald, M. H. *Int. J. Antimicrob. Agents* **1996**, *6*, 189−194.

(3) Demain, A. L. *J. Ind. Microbiol. Biotechnol.* **2014**, *41*, 185−201.

DOI: 10.1021/acs.jnatprod.8b00723
J. Nat. Prod. 2019, 82, 1412−1423

(4) Cragg, G. M.; Newman, D. J. *Biochim. Biophys. Acta, Gen. Subj.* **2013**, *1830*, 3670−3695.
(5) Dias, D. A.; Urban, S.; Roessner, U. *Metabolites* **2012**, *2*, 303−336.
(6) Elfahmi; Woerdenbag, H. J.; Kayser, O. *J. Herb. Med.* **2014**, *4*, 51−73.
(7) Chen, C. Y.; Yang, Y. H.; Kuo, S. Y. *J. Nat. Prod.* **2010**, *73*, 1370−1374.
(8) Zhang, F.; Thakur, K.; Hu, F.; Zhang, J. G.; Wei, Z. J. *J. Agric. Food Chem.* **2017**, *65*, 2089−2099.
(9) Dugasani, S.; Pichika, M. R.; Nadarajah, V. D.; Balijepalli, M. K.; Tandra, S.; Korlakunta, J. N. *J. Ethnopharmacol.* **2010**, *127*, 515−520.
(10) Yang, Y.; Kinoshita, K.; Koyama, K.; Takahashi, K.; Kondo, S.; Watanabe, K. *Phytomedicine* **2002**, *9*, 146−152.
(11) Sang, S.; Hong, J.; Wu, H.; Liu, J.; Yang, C. S.; Pan, M. H.; Badmaev, V.; Ho, C. T. *J. Agric. Food Chem.* **2009**, *57*, 10645−10650.
(12) Funk, J. L.; Frye, J. B.; Oyarzo, J. N.; Timmermann, B. N. *J. Nat. Prod.* **2009**, *72*, 403−407.
(13) Selala, M. I.; Musuku, A.; Schepens, P. J. C. *Anal. Chim. Acta* **1991**, *244*, 1−8.
(14) Fan, Y.; Wang, Y.; Liu, P.; Fu, P.; Zhu, T.; Wang, W.; Zhu, W. *J. Nat. Prod.* **2013**, *76*, 1328−1336.
(15) Uhlig, S.; Egge-Jacobsen, W.; Vrålstad, T.; Miles, C. O. *Rapid Commun. Mass Spectrom.* **2014**, *28*, 1621−1634.
(16) Saikia, S.; Nicholson, M. J.; Young, C.; Parker, E. J.; Scott, B. *Mycol. Res.* **2008**, *112*, 184−199.
(17) Matsuda, Y.; Abe, I. *Nat. Prod. Rep.* **2016**, *33*, 26−53.
(18) Xu, W.; Gavia, D. J.; Tang, Y. *Nat. Prod. Rep.* **2014**, *31*, 1474−1487.
(19) Philippe, G. *Toxins* **2016**, *8*, 47.
(20) Springer, J. P.; Clardy, J.; Wells, J. M.; Cole, R. J.; Kirksey, J. W. *Tetrahedron Lett.* **1975**, *16*, 2531−2534.
(21) Cole, R. J.; Dorner, J. W.; Lansden, J. A.; Cox, R. H.; Pape, C.; Cunfer, B.; Nicholson, S. S.; Bedell, D. M. *J. Agric. Food Chem.* **1977**, *25*, 1197−1201.
(22) Gallagher, R. T.; Latch, G. C. M.; Keogh, R. G. *Appl. Environ. Microbiol.* **1980**, *39*, 272−273.
(23) Wilkins, A. L.; Miles, C. O.; Ede, R. M.; Gallagher, R. T.; Munday, S. C. *J. Agric. Food Chem.* **1992**, *40*, 1307−1309.
(24) Penn, J.; Swift, R.; Wigley, L. J.; Mantle, P. G.; Bilton, J. N.; Sheppard, R. N. *Phytochemistry* **1993**, *32*, 1431−1434.
(25) González, M. C.; Lull, C.; Moya, P.; Ayala, I.; Primo, J.; Yufera, E. P. *J. Agric. Food Chem.* **2003**, *51*, 2156−2160.
(26) Gallagher, R. T.; Clardy, J.; Wilson, B. J. *Tetrahedron Lett.* **1980**, *21*, 239−242.
(27) Gallagher, R. T.; Finer, J.; Clardy, J.; Leutwiler, A.; Weibel, F.; Acklin, W.; Arigoni, D. *Tetrahedron Lett.* **1980**, *21*, 235−238.
(28) Mantle, P. G. *Phytochemistry* **2009**, *70*, 7−10.
(29) Bennett, J. W.; Klich, M. *Clin. Microbiol. Rev.* **2003**, *16*, 497−516.
(30) Singh, S. B.; Ondeyka, J. G.; Jayasuriya, H.; Zink, D. L.; Ha, S. N.; Dahl-Roshak, A.; Greene, J.; Kim, J. A.; Smith, M. M.; Shoop, W.; Tkacz, J. S. *J. Nat. Prod.* **2004**, *67*, 1496−1506.
(31) Qiao, M. F.; Ji, N. Y.; Liu, X. H.; Li, K.; Zhu, Q. M.; Xue, Q. Z. *Bioorg. Med. Chem. Lett.* **2010**, *20*, 5677−5680.
(32) Ogata, M.; Ueda, J. Y.; Hoshi, M.; Hashimoto, J.; Nakashima, T.; Anzai, K.; Takagi, M.; Shin-ya, K. *J. Antibiot.* **2007**, *60*, 645−648.
(33) You, J.; Du, L.; King, J. B.; Hall, B. E.; Cichewicz, R. H. *ACS Chem. Biol.* **2013**, *8*, 840−848.
(34) Abdullaev, I. F.; Rudkouskaya, A.; Mongin, A. A.; Kuo, Y. H. *PLoS One* **2010**, *5*, e12304.
(35) Sallam, A. A.; Houssen, W. E.; Gissendanner, C. R.; Orabi, K. Y.; Foudah, A. I.; El Sayed, K. A. *MedChemComm* **2013**, *4*, 1360−1369.
(36) Knaus, H. G.; McManus, O. B.; Lee, S. H.; Schmalhofer, W. A.; Garcia-Calvo, M.; Helms, L. M.; Sanchez, M.; Giangiacomo, K.; Reuben, J. P.; Smith, A. B., III; Kaczorowski, G. J.; Garcia, M. L. *Biochemistry* **1994**, *33*, 5819−5828.
(37) Sheehan, J. J.; Benedetti, B. L.; Barth, A. L. *Epilepsia* **2009**, *50*, 711−720.
(38) Brnardic, E.; Doherty, J. B.; Dorsey, J.; Ellwood, C.; Fillmore, M.; Malaska, M.; Nelson, K.; Soukri, M. Maxi-K channel blockers and methods of use. Patent WO2009/048559 A1, 2009.
(39) Corsello, M. A.; Kim, J.; Garg, N. K. *Chem. Sci.* **2017**, *8*, 5836−5844.
(40) Tang, M. C.; Lin, H. C.; Li, D.; Zou, Y.; Li, J.; Xu, W.; Cacho, R. A.; Hillenmeyer, M. E.; Garg, N. K.; Tang, Y. *J. Am. Chem. Soc.* **2015**, *137*, 13724−13727.
(41) Liu, C.; Minami, A.; Dairi, T.; Gomi, K.; Scott, B.; Oikawa, H. *Org. Lett.* **2016**, *18*, 5026−5029.
(42) Ding, L.; Münch, J.; Goerls, H.; Maier, A.; Fiebig, H. H.; Lin, W. H.; Hertweck, C. *Bioorg. Med. Chem. Lett.* **2010**, *20*, 6685−6687.
(43) Ding, L.; Maier, A.; Fiebig, H. H.; Lin, W. H.; Hertweck, C. *Org. Biomol. Chem.* **2011**, *9*, 4029−4031.
(44) Fehr, T.; Acklin, W. *Helv. Chim. Acta* **1966**, *49*, 1907−1910.
(45) Springer, J. P.; Clardy, J. P. *Tetrahedron Lett.* **1980**, *21*, 231−234.
(46) Ancheeva, E.; Küppers, L.; Akone, S. H.; Ebrahim, W.; Liu, Z.; Mándi, A.; Kurtán, T.; Lin, W.; Orfali, R.; Rehberg, N.; Kalscheuer, R.; Daletos, G.; Proksch, P. *Eur. J. Org. Chem.* **2017**, *2017*, 3256−3264.
(47) Liu, Y.; Kurtán, T.; Mándi, A.; Weber, H.; Wang, C.; Hartmann, R.; Lin, W.; Daletos, G.; Proksch, P. *Tetrahedron Lett.* **2018**, *59*, 632−636.
(48) Tóth, L.; Mándi, A.; Váradi, D.; Kovács, T.; Szabados, A.; Kiss-Szikszai, A.; Gong, Q.; Zhang, H.; Mátyus, P.; Antus, S.; Kurtán, T. *Chirality* **2018**, *30*, 866−874.
(49) Zhang, P.; Meng, L. H.; Mándi, A.; Kurtán, T.; Li, X. M.; Liu, Y.; Li, X.; Li, C. S.; Wang, B. G. *Eur. J. Org. Chem.* **2014**, *2014*, 4029−4036.
(50) Yanai, T.; Tew, D. P.; Handy, N. C. *Chem. Phys. Lett.* **2004**, *393*, 51−57.
(51) Adamo, C.; Barone, V. *J. Chem. Phys.* **1998**, *108*, 664−675.
(52) Smetanina, O. F.; Kalinovsky, A. I.; Khudyakova, Y. V.; Pivkin, M. V.; Dmitrenok, P. S.; Fedorov, S. N.; Ji, H.; Kwak, J. Y.; Kuznetsova, T. A. *J. Nat. Prod.* **2007**, *70*, 906−909.
(53) Matsui, C.; Ikeda, Y.; Iinuma, H.; Kushida, N.; Kunisada, T.; Simizu, S.; Umezawa, K. *J. Antibiot.* **2014**, *67*, 787−790.
(54) Belofsky, G. N.; Gloer, J. B.; Wicklow, D. T.; Dowd, P. F. *Tetrahedron* **1995**, *51*, 3959−3968.
(55) Dhodary, B.; Schilg, M.; Wirth, R.; Spiteller, D. *Chem. - Eur. J.* **2018**, *24*, 4445−4452.
(56) Nozawa, K.; Nakajima, S.; Kawai, K. I.; Udagawa, S. I. *J. Chem. Soc., Perkin Trans. 1* **1988**, 2607−2610.
(57) Xu, M.; Gessner, G.; Groth, I.; Lange, C.; Christner, A.; Bruhn, T.; Deng, Z.; Li, X.; Heinemann, S. H.; Grabley, S.; Bringmann, G.; Sattler, I.; Lin, W. *Tetrahedron* **2007**, *63*, 435−444.
(58) Smith, A. B., III; Kingery-Wood, J.; Leenay, T. L.; Nolen, E. G.; Sunazuka, T. *J. Am. Chem. Soc.* **1992**, *114*, 1438−1449.
(59) Gao, N.; Shang, Z. C.; Yu, P.; Luo, J.; Jian, K. L.; Kong, L. Y.; Yang, M. H. *Chin. Chem. Lett.* **2017**, *28*, 1194−1199.
(60) Munday-Finch, S. C.; Wilkins, A. L.; Miles, C. O. *Phytochemistry* **1996**, *41*, 327−332.
(61) Mantle, P. G.; Weedon, C. M. *Phytochemistry* **1994**, *36*, 1209−1217.
(62) Bills, G. F.; Giacobbe, R. A.; Lee, S. H.; Peláez, F.; Tkacz, J. S. *Mycol. Res.* **1992**, *96*, 977−983.
(63) Li, H.; Zhang, Q.; Li, S.; Zhu, Y.; Zhang, G.; Zhang, H.; Tian, X.; Zhang, S.; Ju, J.; Zhang, C. *J. Am. Chem. Soc.* **2012**, *134*, 8996−9005.
(64) Kjer, J.; Debbab, A.; Aly, A. H.; Proksch, P. *Nat. Protoc.* **2010**, *5*, 479−490.
(65) Chen, H.; Daletos, G.; Abdel-Aziz, M. S.; Thomy, D.; Dai, H.; Brötz-Oesterhelt, H.; Lin, W.; Proksch, P. *Phytochem. Lett.* **2015**, *12*, 35−41.
(66) Rönsberg, D.; Debbab, A.; Mandi, A.; Vasylyeva, V.; Böhler, P.; Stork, B.; Engelke, L.; Hamacher, A.; Sawadogo, R.; Diederich, M.;

DOI: 10.1021/acs.jnatprod.8b00723
J. Nat. Prod. 2019, 82, 1412−1423

Wray, V.; Lin, W.; Kassack, M. U.; Janiak, C.; Scheu, S.; Wesselborg, S.; Kurtán, T.; Aly, A. H.; Proksch, P. *J. Org. Chem.* **2013**, *78*, 12409−12425.
(67) *MacroModel*; Schrödinger, LLC, 2015; http://www.schrodinger.com/MacroModel.
(68) Frisch, M. J.; Trucks, G. W.; Schlegel, H. B.; Scuseria, G. E.; Robb, M. A.; Cheeseman, J. R.; Scalmani, G.; Barone, V.; Mennucci, B.; Petersson, G. A.; Nakatsuji, H.; Caricato, M.; Li, X.; Hratchian, H. P.; Izmaylov, A. F.; Bloino, J.; Zheng, G.; Sonnenberg, J. L.; Hada, M.; Ehara, M.; Toyota, K.; Fukuda, R.; Hasegawa, J.; Ishida, M.; Nakajima, T.; Honda, Y.; Kitao, O.; Nakai, H.; Vreven, T.; Montgomery, J. A., Jr.; Peralta, J. E.; Ogliaro, F.; Bearpark, M.; Heyd, J. J.; Brothers, E.; Kudin, K. N.; Staroverov, V. N.; Kobayashi, R.; Normand, J.; Raghavachari, K.; Rendell, A.; Burant, J. C.; Iyengar, S. S.; Tomasi, J.; Cossi, M.; Rega, N.; Millam, J. M.; Klene, M.; Knox, J. E.; Cross, J. B.; Bakken, V.; Adamo, C.; Jaramillo, J.; Gomperts, R.; Stratmann, R. E.; Yazyev, O.; Austin, A. J.; Cammi, R.; Pomelli, C.; Ochterski, J. W.; Martin, R. L.; Morokuma, K.; Zakrzewski, V. G.; Voth, G. A.; Salvador, P.; Dannenberg, J. J.; Dapprich, S.; Daniels, A. D.; Farkas, O.; Foresman, J. B.; Ortiz, J. V.; Cioslowski, J.; Fox, D. J. *Gaussian 09*, Revision E.01; Gaussian, Inc.: Wallingford, CT, 2013.
(69) Stephens, P. J.; Harada, N. *Chirality* **2009**, *22*, 229−233.
(70) CHESHIRE CCAT, *the Chemical Shift Repository for computed NMR scaling factors*, http://cheshirenmr.info/index.htm.
(71) Lodewyk, M. W.; Siebert, M. R.; Tantillo, D. J. *Chem. Rev.* **2012**, *112*, 1839−1862.
(72) Varetto, U. *MOLEKEL* 5.4; Swiss National Supercomputing Centre: Manno, Switzerland, 2009.
(73) *Apex2*, Data Collection Program for the CCD Area-Detector System; *SAINT*, Data Reduction and Frame Integration Program for the CCD Area-Detector System; Bruker Analytical X-ray Systems: Madison, WI, USA, 1997−2012.
(74) Sheldrick, G. M. *SADABS: Area-detector absorption correction*; University of Goettingen: Germany, 1996.
(75) Sheldrick, G. M. *Acta Crystallogr., Sect. A: Found. Adv.* **2015**, *71*, 3−8.
(76) Sheldrick, G. M. *Acta Crystallogr., Sect. C: Struct. Chem.* **2015**, *71*, 3−8.
(77) Brandenburg, K. *Diamond (Version 3.2), Crystal and Molecular Structure Visualization, Crystal Impact − K*; Brandenburg & H. Putz Gbr: Bonn, Germany, 2009.

DOI: 10.1021/acs.jnatprod.8b00723
J. Nat. Prod. 2019, 82, 1412−1423

Supporting Information

Indole Diterpenoids from an Endophytic *Penicillium* sp.

Ni P. Ariantari,[†,‡] Elena Ancheeva,[*,†] Chenyin Wang,[§] Attila Mándi,[⊥], Tim-O. Knedel,[#] Tibor Kurtán,[⊥] Chaidir Chaidir, [‖] Werner E. G. Müller,[○] Matthias U. Kassack,[§] Christoph Janiak,[#] Georgios Daletos,[*,†] Peter Proksch[*,†]

[†]Institute of Pharmaceutical Biology and Biotechnology, Heinrich Heine University Düsseldorf, Universitätsstrasse 1, 40225 Düsseldorf, Germany

[‡]Department of Pharmacy, Faculty of Mathematic and Natural Sciences, Udayana University, 80361 Bali, Indonesia

[§]Institute of Pharmaceutical and Medicinal Chemistry, Heinrich Heine University Düsseldorf, Universitätsstrasse 1, 40225 Düsseldorf, Germany

[⊥]Department of Organic Chemistry, University of Debrecen, P.O.B. 400, 4002 Debrecen, Hungary

[#]Institute of Inorganic Chemistry and Structural Chemistry, Heinrich Heine University Düsseldorf, Universitätsstraße 1, 40225 Düsseldorf, Germany

[‖]Center for Pharmaceutical and Medical Technology, Agency for the Assessment and Application Technology, 10340 Jakarta, Indonesia

[○]Institute of Physiological Chemistry, Universitätsmedizin der Johannes Gutenberg-Universität Mainz, Duesbergweg 6, 55128 Mainz, Germany

[*]Corresponding author

Table of Contents

(A)

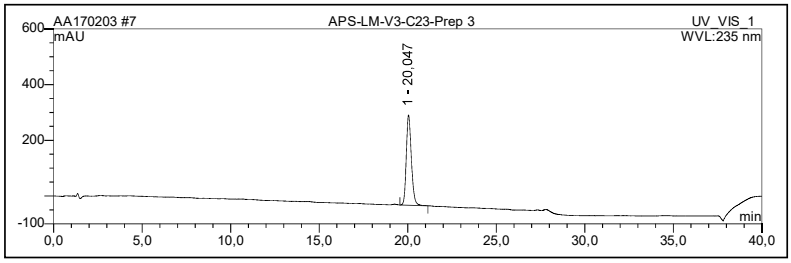

(B)

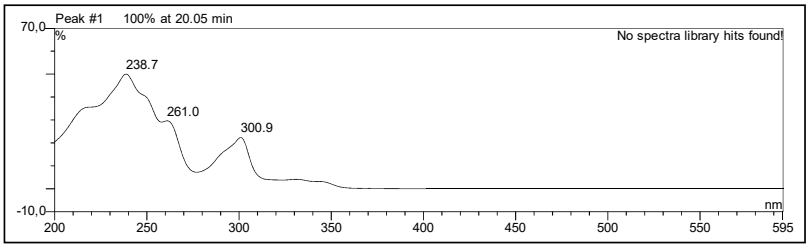

Figure S1. HPLC chromatogram (A) and UV spectrum (B) of compound **1**.

Acquisition Parameter

Source Type	ESI	Ion Polarity	Positive	Set Nebulizer	0.3 Bar
Focus	Not active	Set Capillary	4000 V	Set Dry Heater	180 °C
Scan Begin	50 m/z	Set End Plate Offset	-500 V	Set Dry Gas	4.0 l/min
Scan End	1500 m/z	Set Collision Cell RF	600.0 Vpp	Set Divert Valve	Source

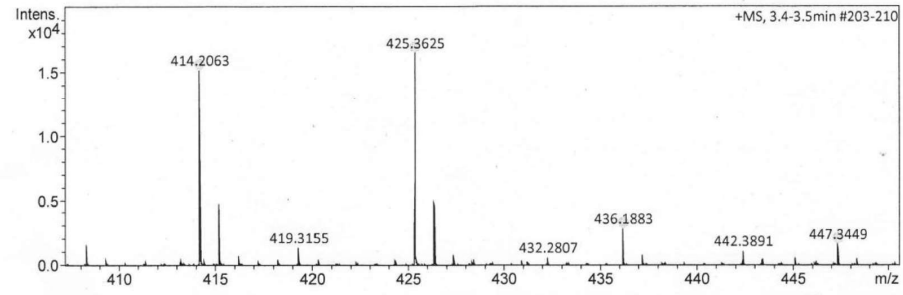

Meas. m/z	#	Ion Formula	m/z	err [ppm]	mSigma	# mSigma	Score	rdb	e⁻ Conf	N-Rule
414.2063	1	C27H28NO3	414.2064	0.1	10.3	1	100.00	14.5	even	ok
425.3625	1	C26H49O4	425.3625	-0.0	5.6	1	100.00	2.5	even	ok
	2	C27H45N4	425.3639	3.1	8.1	2	48.83	7.5	even	ok
436.1883	1	C27H27NNaO3	436.1883	0.1	29.3	1	100.00	14.5	even	ok
447.3449	1	C27H44N4Na	447.3458	2.1	27.3	1	79.45	7.5	even	ok
	2	C26H48NaO4	447.3445	-0.9	29.9	2	100.00	2.5	even	ok

Figure S2. HRESIMS spectrum of compound **1**.

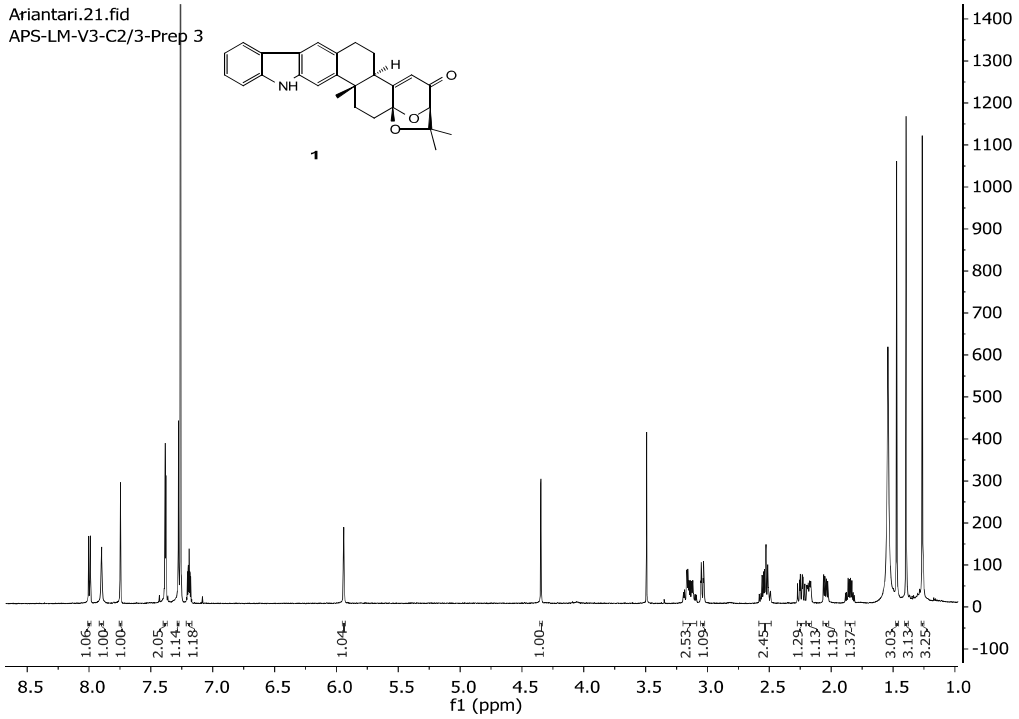

Figure S3. ^{1}H NMR (600 MHz, $CDCl_3$) spectrum of compound **1**.

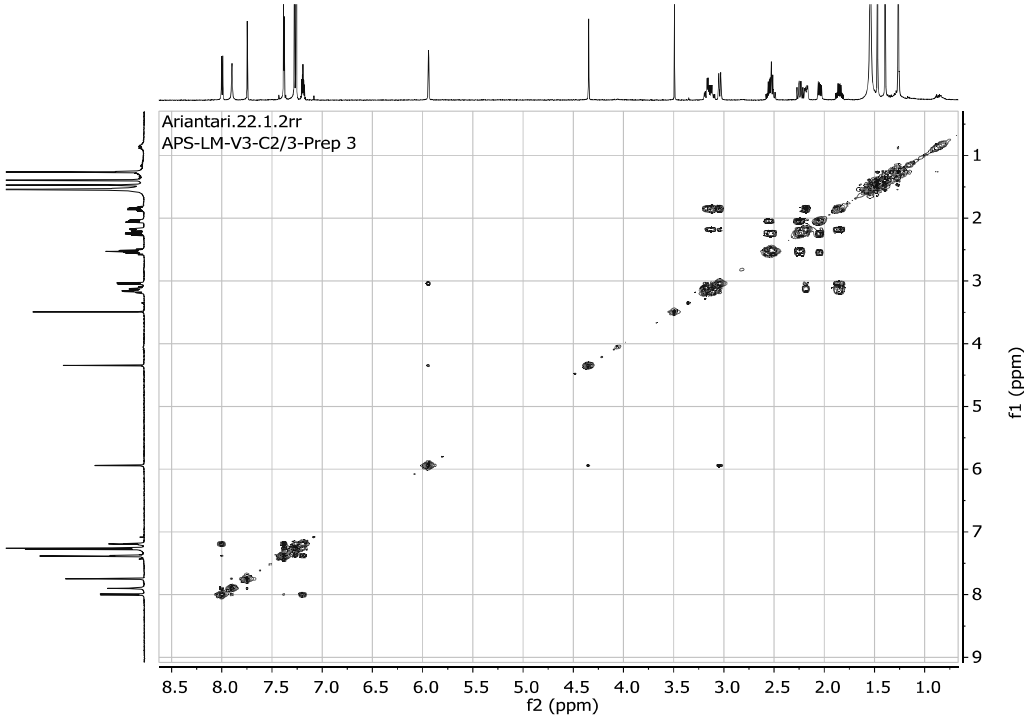

Figure S4. ^{1}H-^{1}H COSY (600 MHz, $CDCl_3$) spectrum of compound **1**.

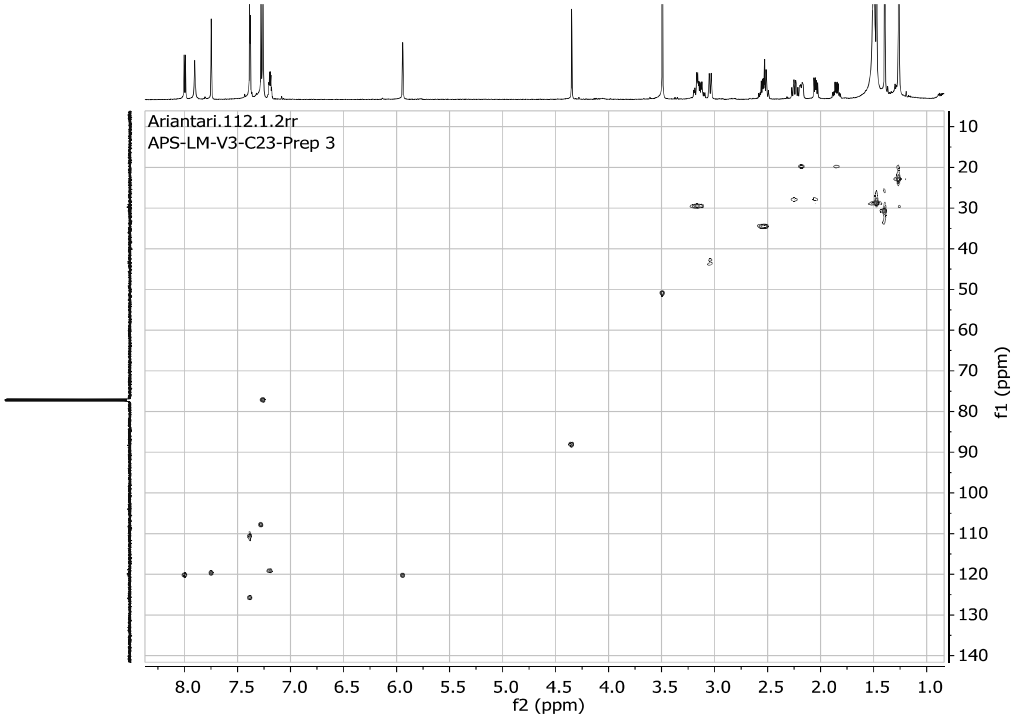

Figure S5. HSQC (600 and 150 MHz, $CDCl_3$) spectrum of compound **1**.

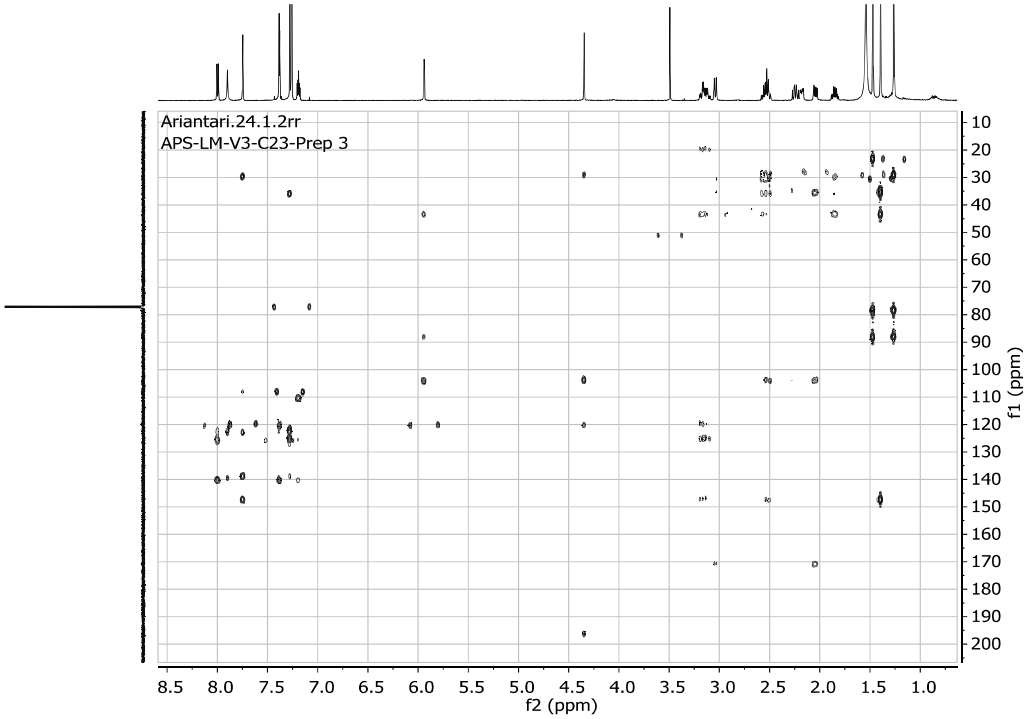

Figure S6. HMBC (600 and 150 MHz, $CDCl_3$) spectrum of compound **1**.

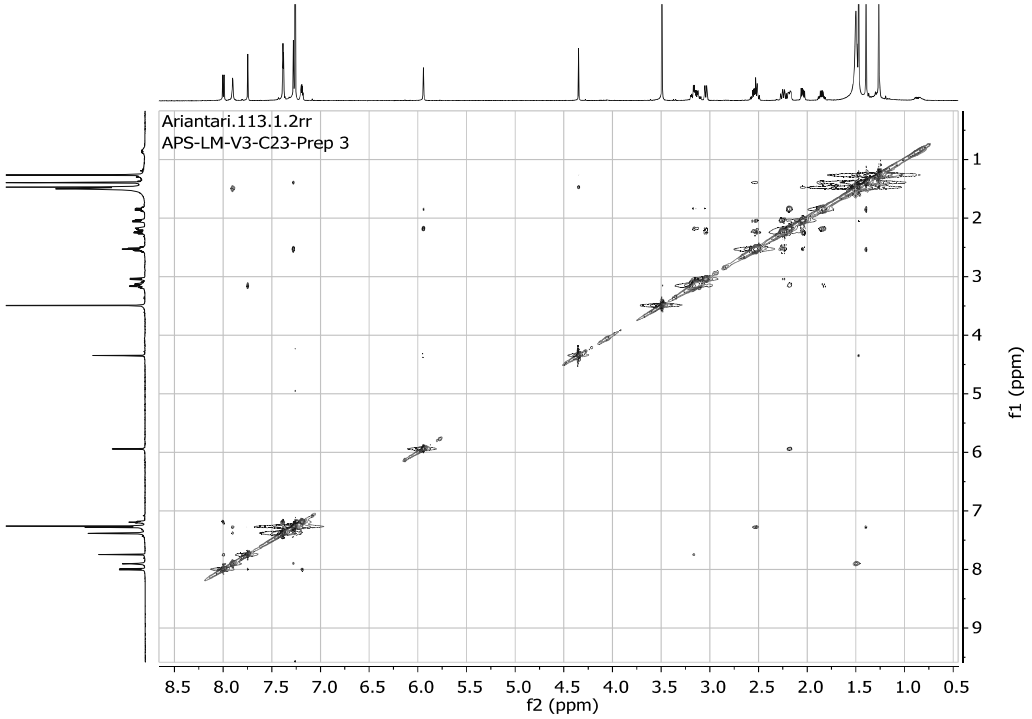

Figure S7. ROESY (600 MHz, $CDCl_3$) spectrum of compound **1**.

(A)

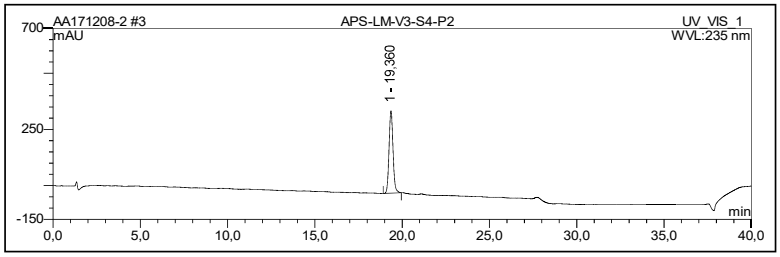

(B)

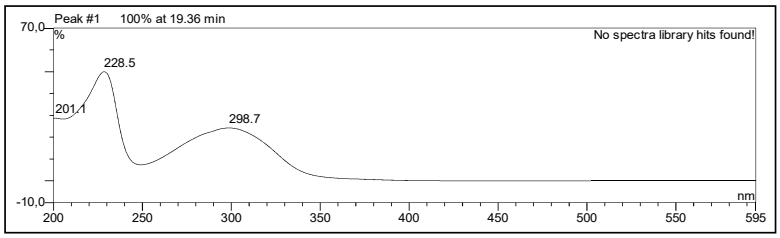

Figure S8. HPLC chromatogram (A) and UV spectrum (B) of compound **2**.

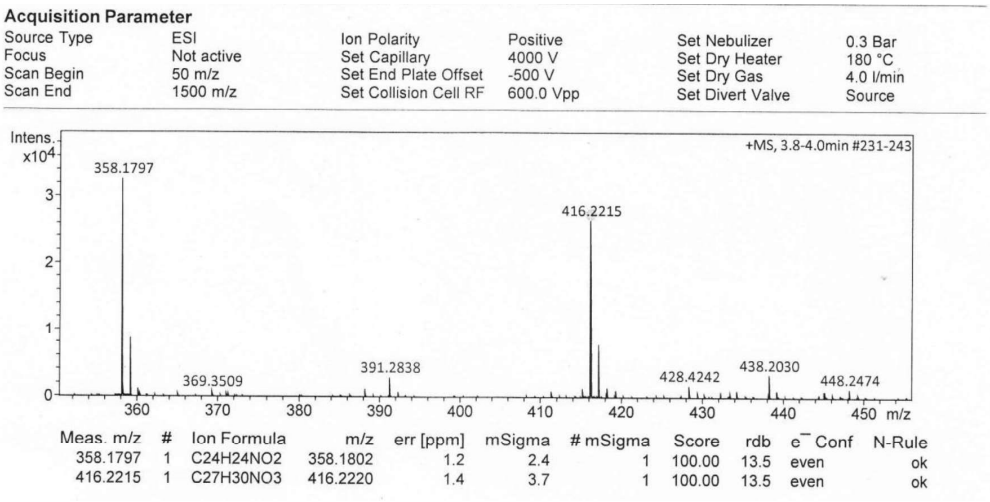

Figure S9. HRESIMS spectrum of compound **2**.

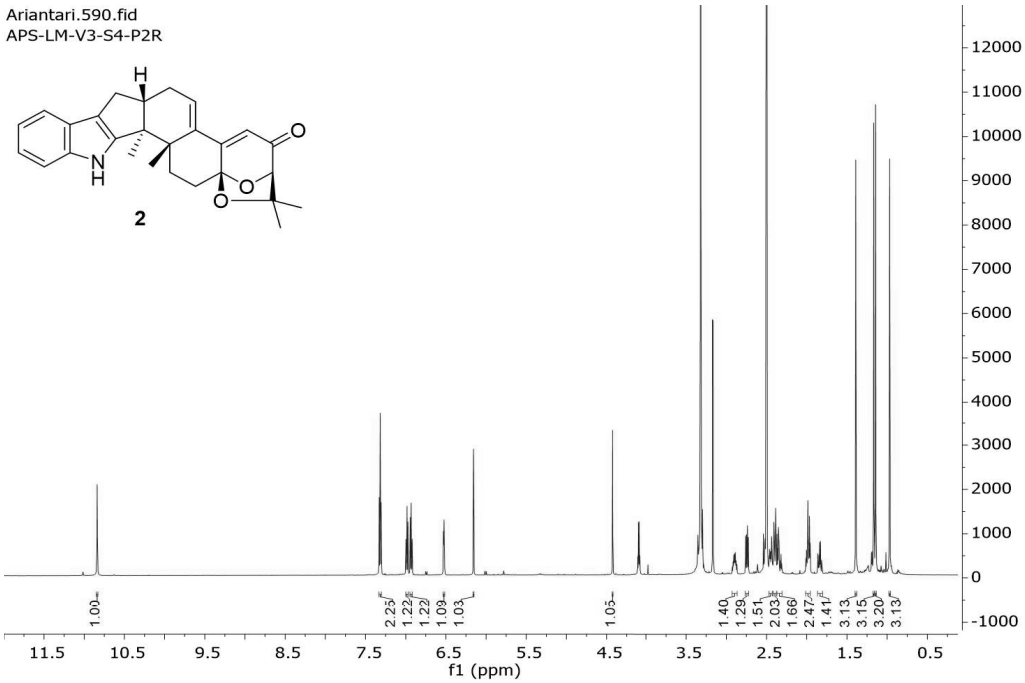

Figure S10. ^{1}H NMR (600 MHz, DMSO-d_6) spectrum of compound **2**.

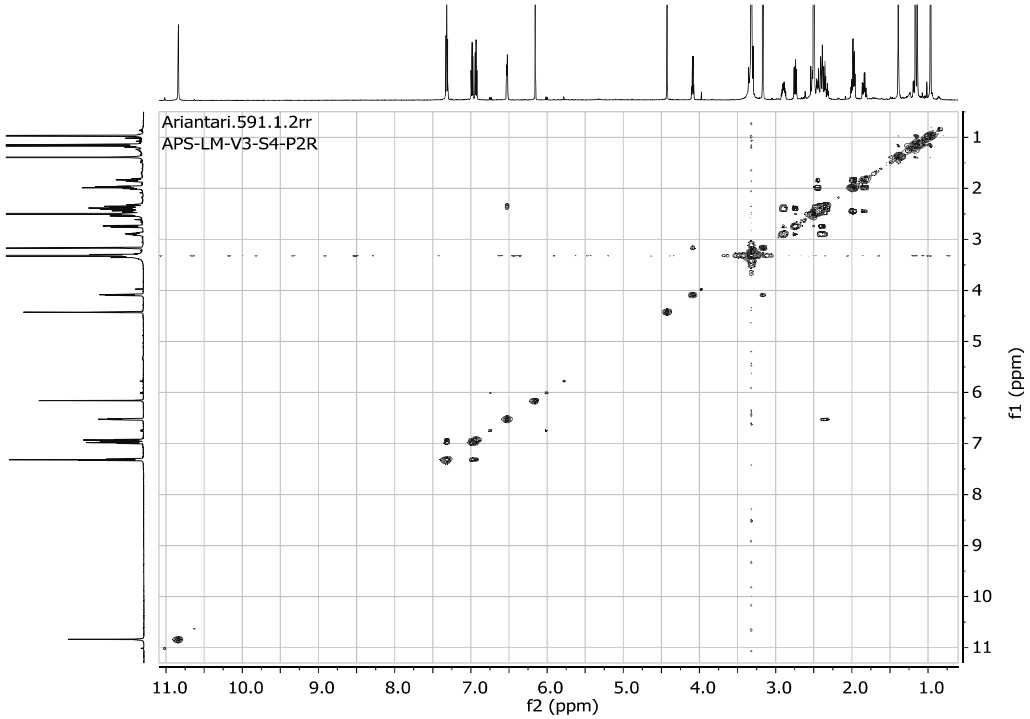

Figure S11. ^{1}H-^{1}H COSY (600 MHz, DMSO-d_6) spectrum of compound **2**.

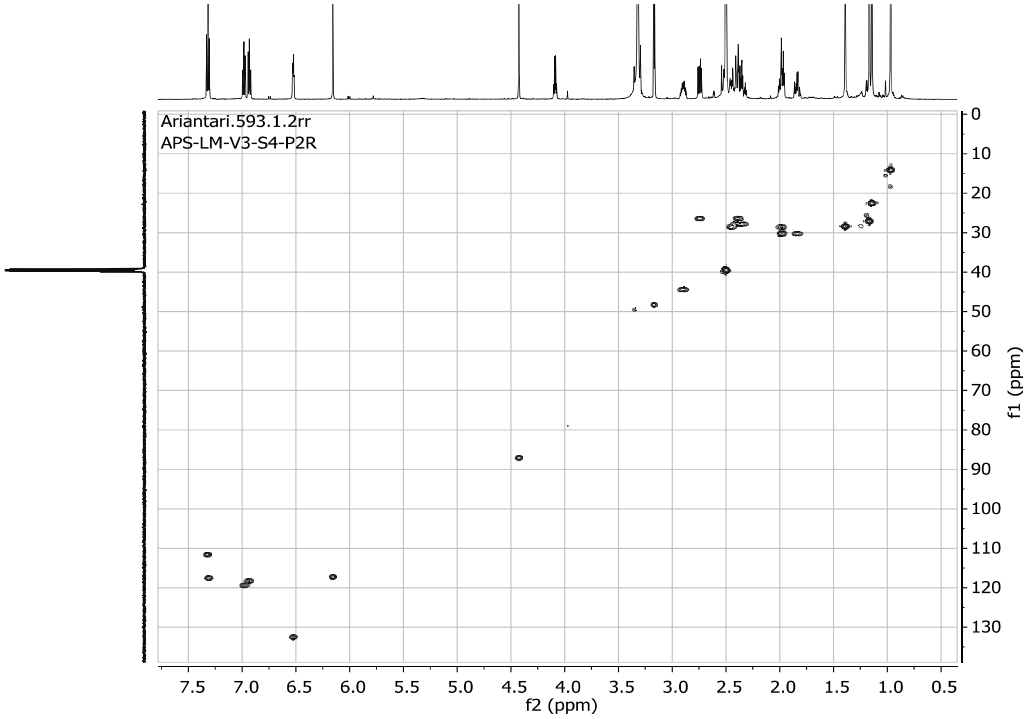

Figure S12. HSQC (600 and 150 MHz, DMSO-d_6) spectrum of compound **2**.

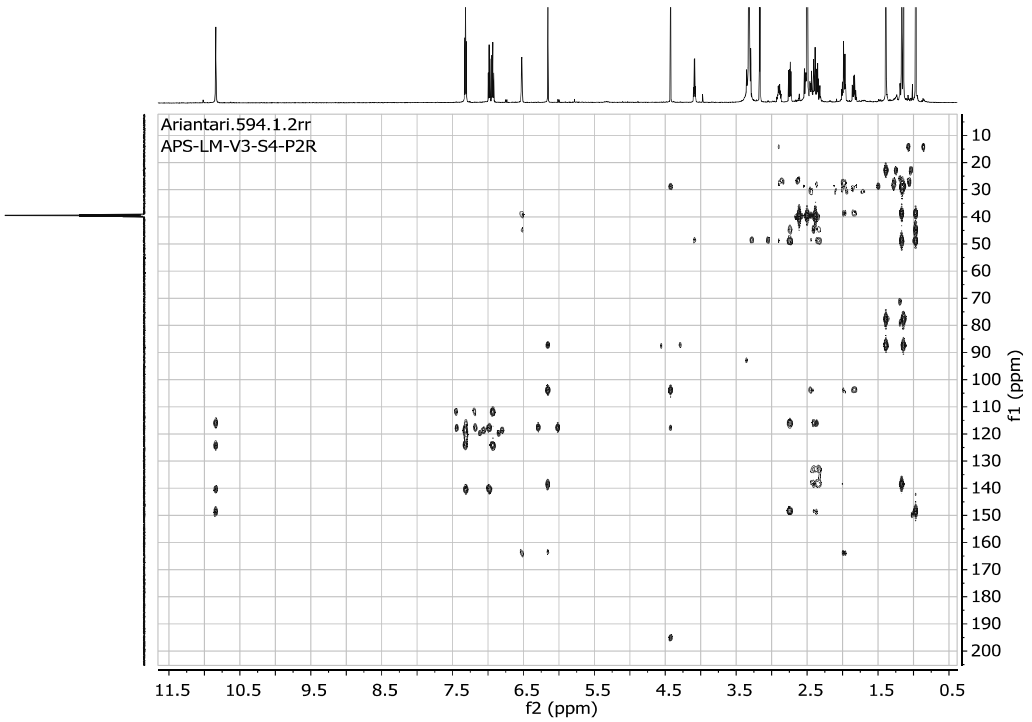

Figure S13. HMBC (600 and 150 MHz, DMSO-d_6) spectrum of compound **2**.

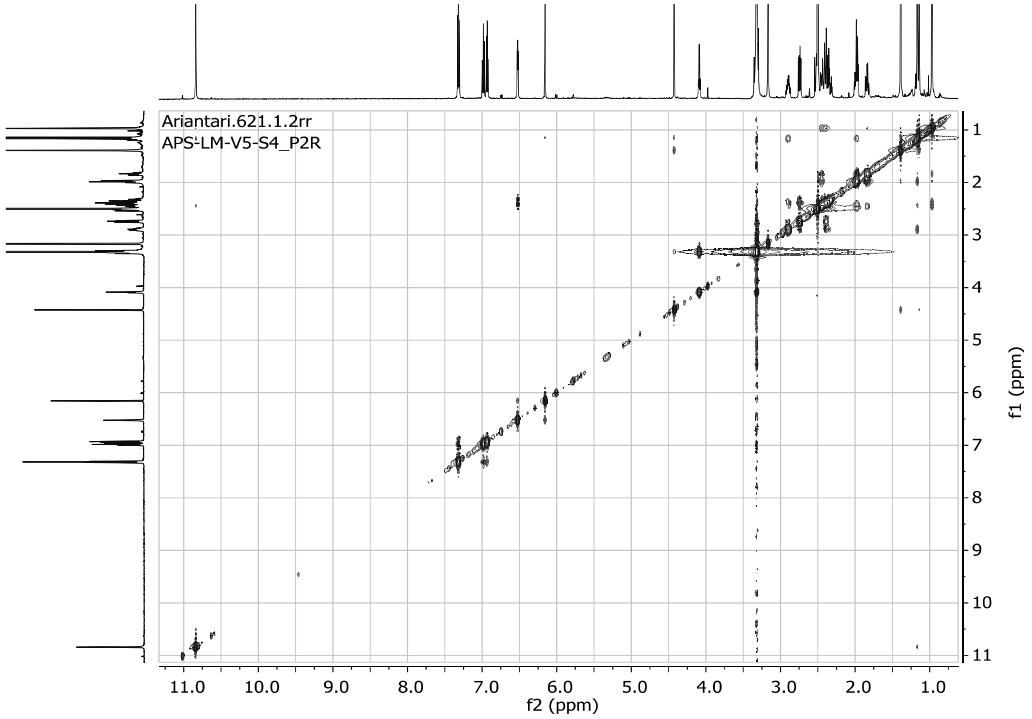

Figure S14. NOESY (600 MHz, DMSO-d_6) spectrum of compound **2**.

(A)

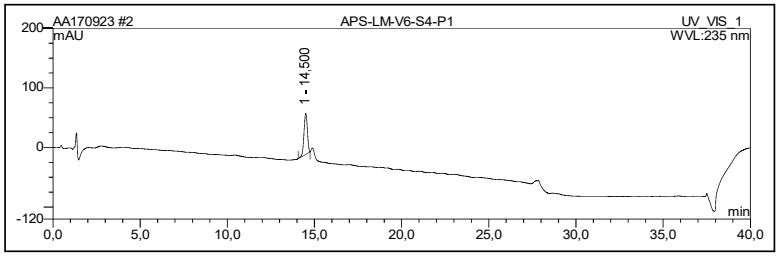

(B)

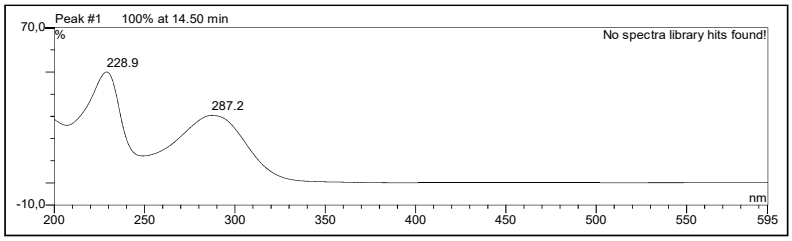

Figure S15. HPLC chromatogram (A) and UV spectrum (B) of compound **3**.

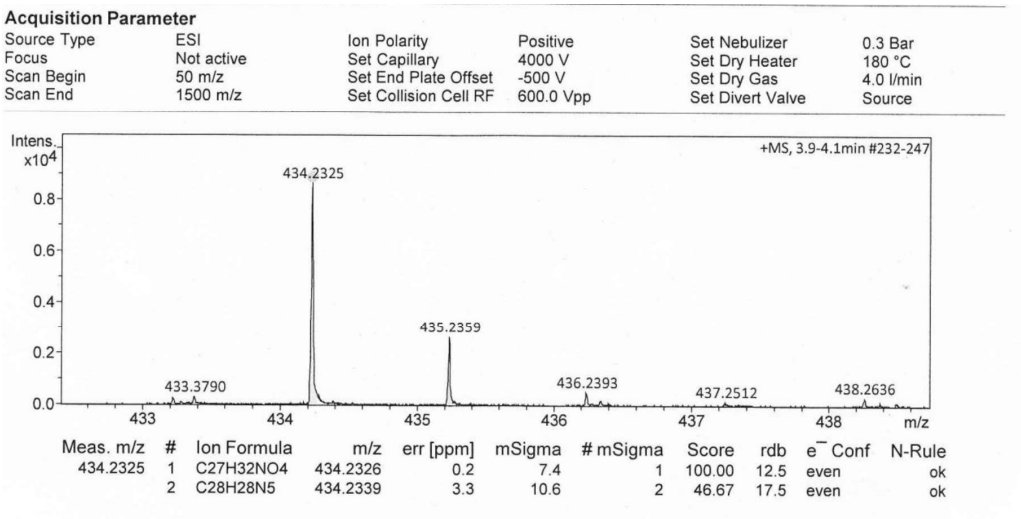

Figure S16. HRESIMS spectrum of compound **3**.

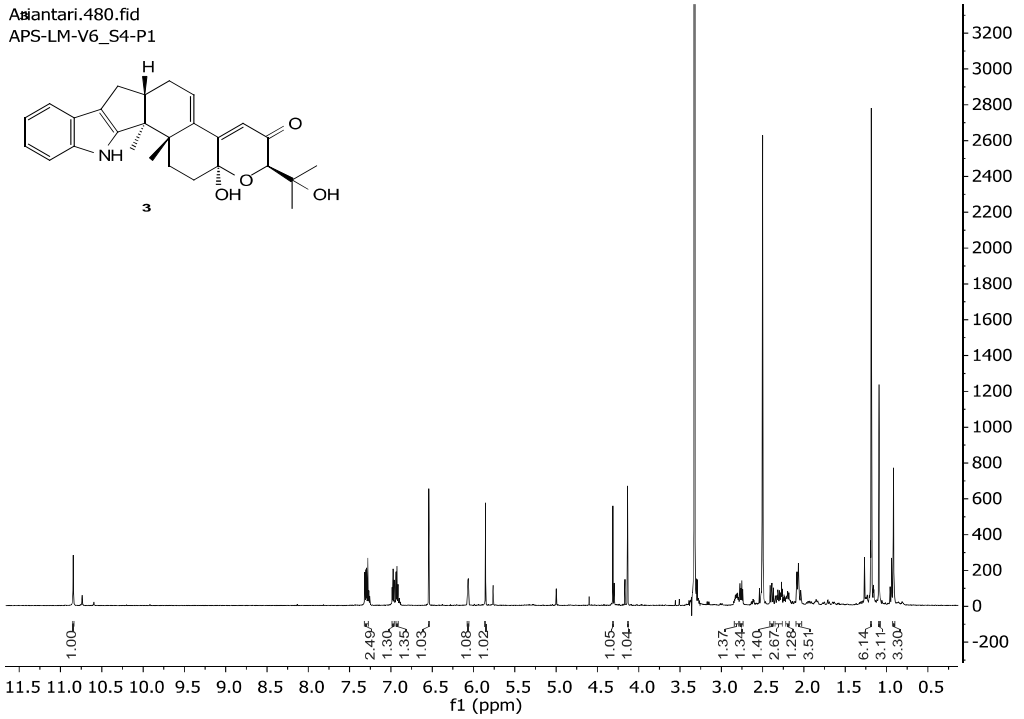

Figure S17. ^{1}H NMR (600 MHz, DMSO-d_6) spectrum of compound **3**.

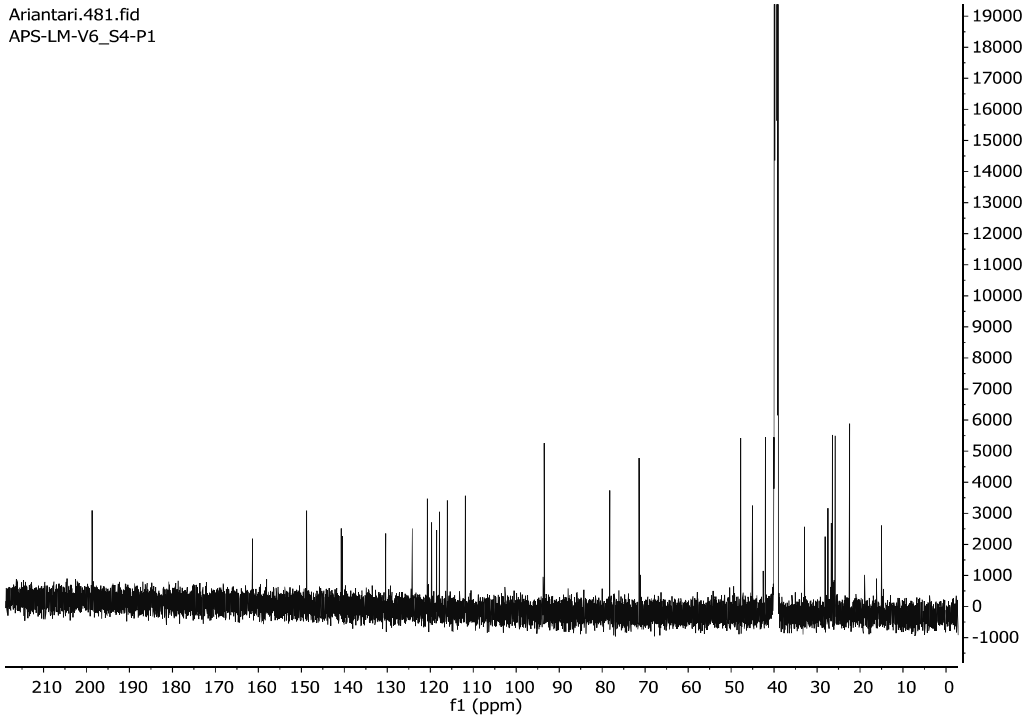

Figure S18. ^{13}C NMR (150 MHz, DMSO-d_6) spectrum of compound **3**.

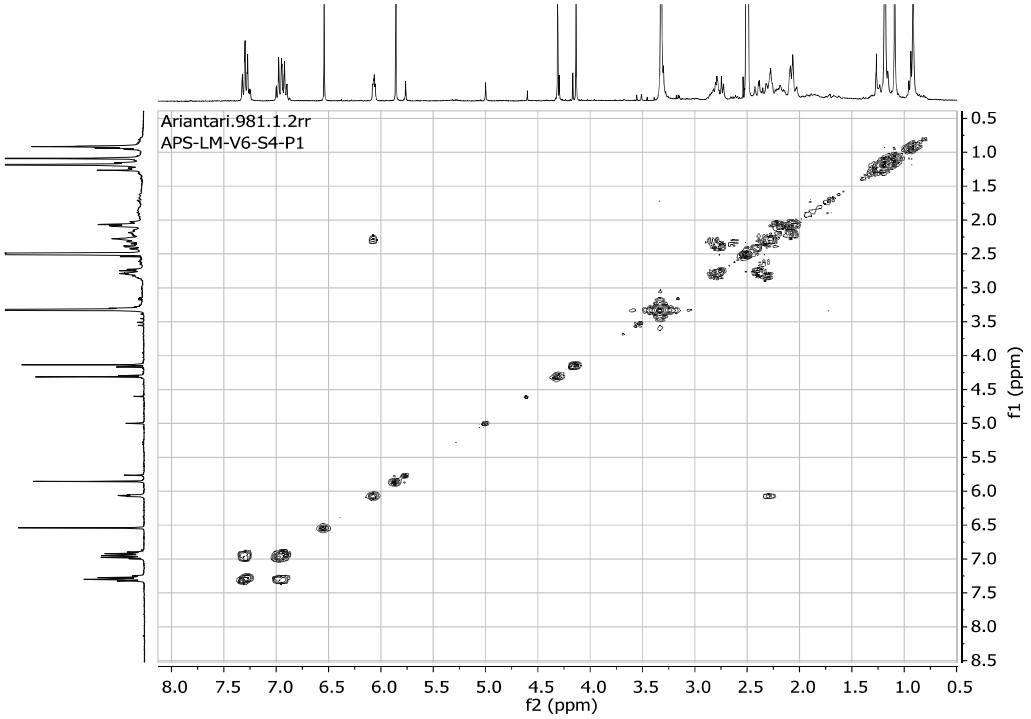

Figure S19. ^{1}H-^{1}H COSY (300 MHz, DMSO-d_6) spectrum of compound **3**.

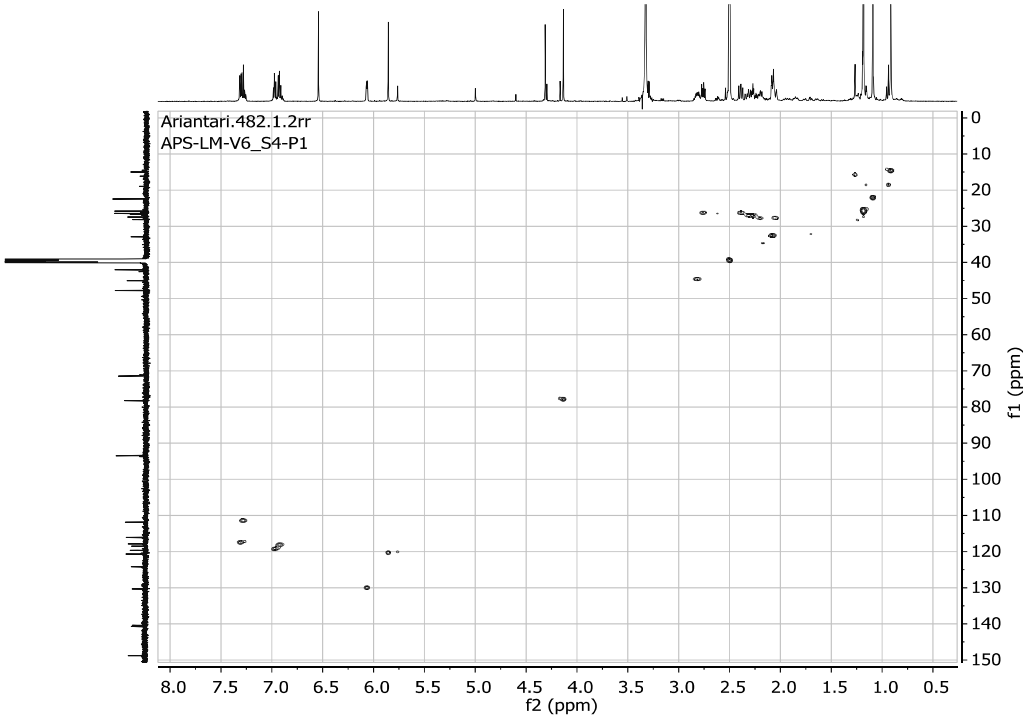

Figure S20. HSQC (600 and 150 MHz, DMSO-d_6) spectrum of compound **3**.

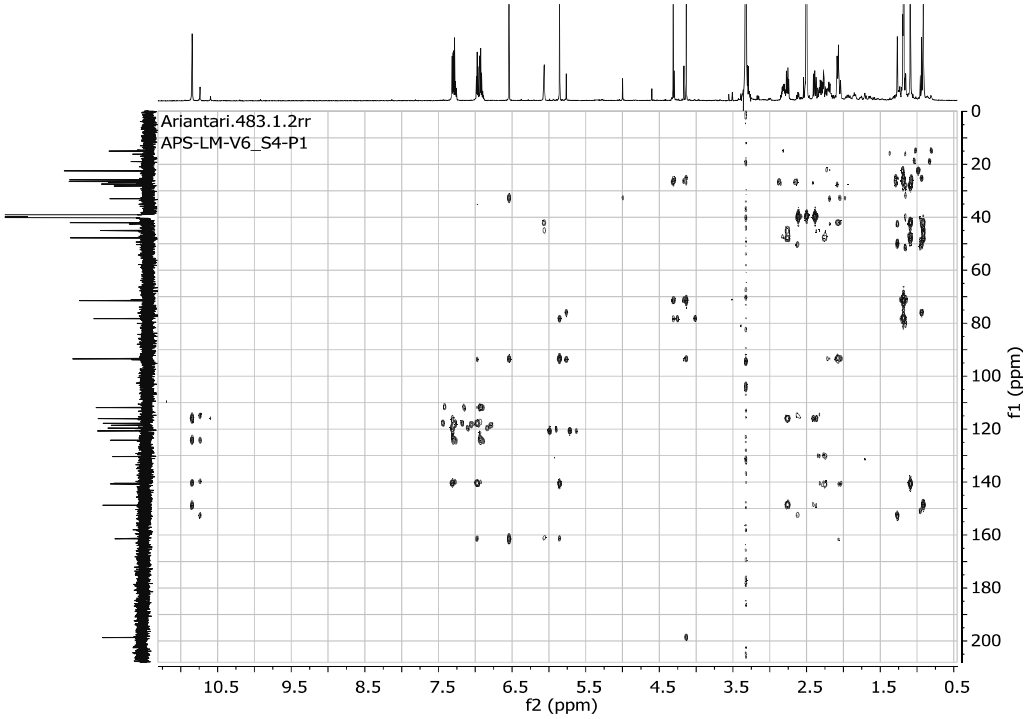

Figure S21. HMBC (600 and 150 MHz, DMSO-d_6) spectrum of compound **3**.

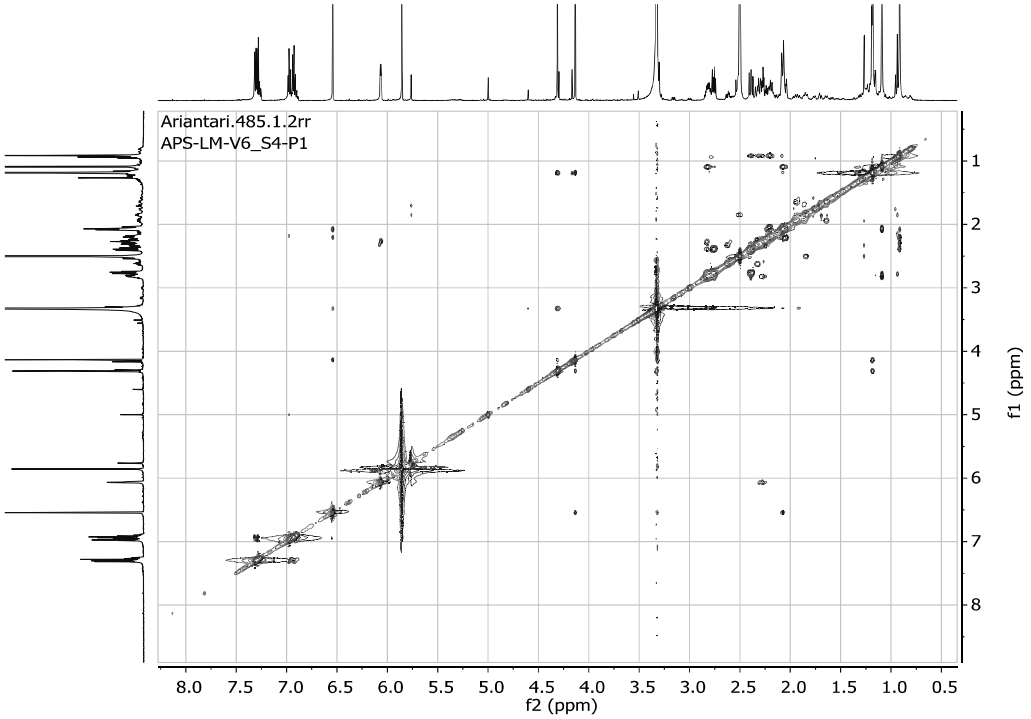

Figure S22. ROESY (600 MHz, DMSO-d_6) spectrum of compound **3**.

(A)

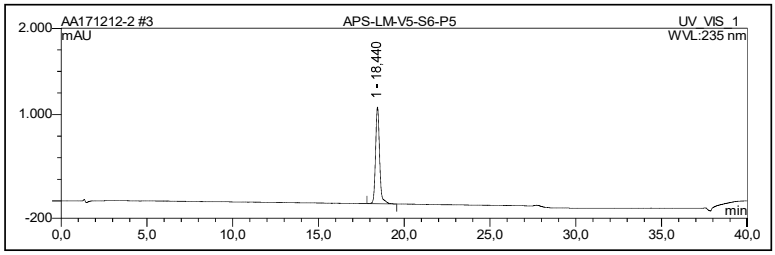

(B)

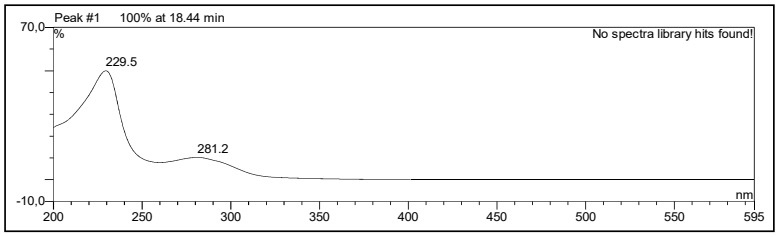

Figure S23. HPLC chromatogram (A) and UV spectrum (B) of compound **4**.

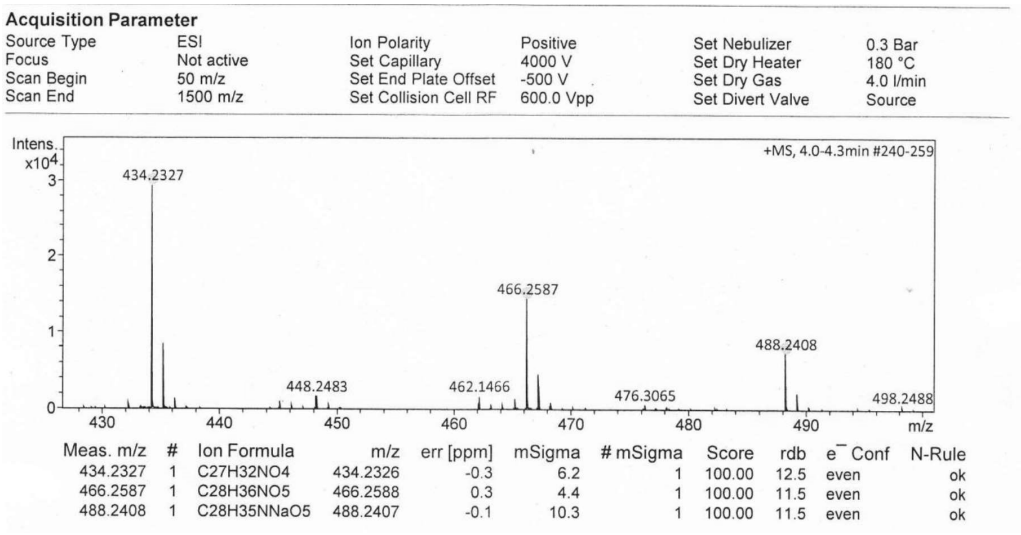

Figure S24. HRESIMS spectrum of compound **4**.

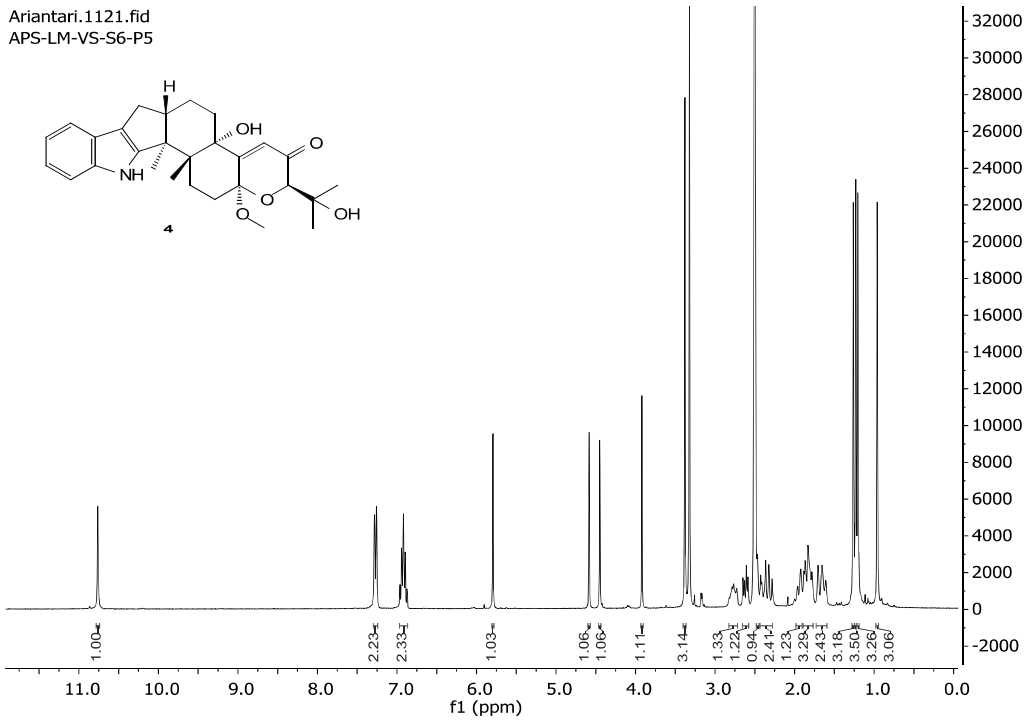

Figure S25. ^{1}H NMR (300 MHz, DMSO-d_6) spectrum of compound **4**.

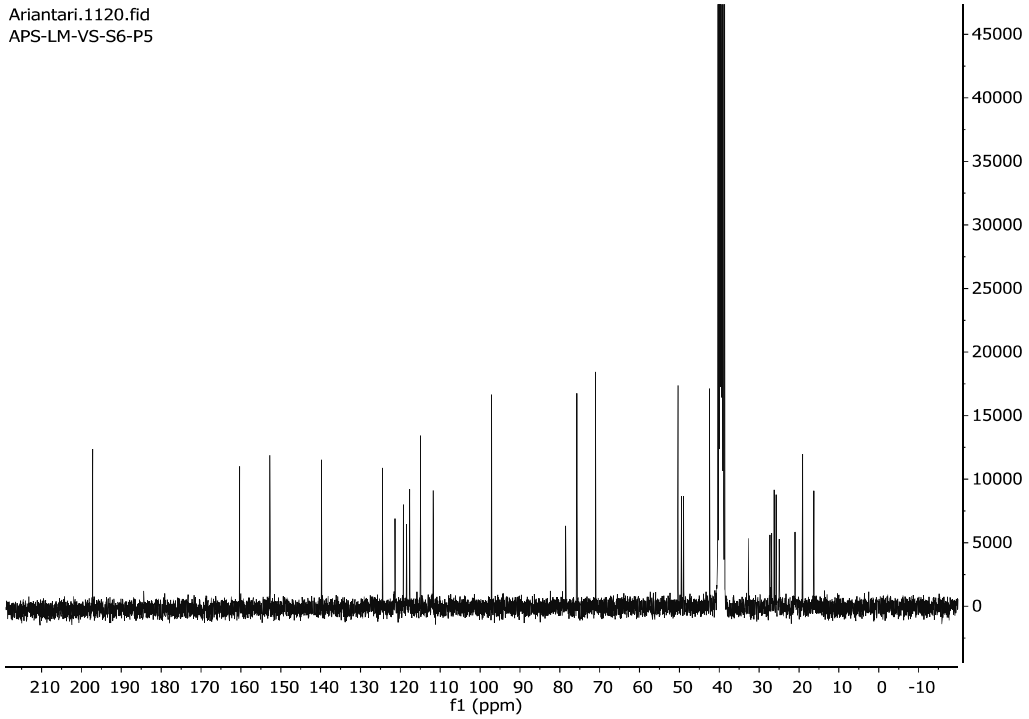

Figure S26. ^{13}C NMR (75 MHz, DMSO-d_6) spectrum of compound **4**.

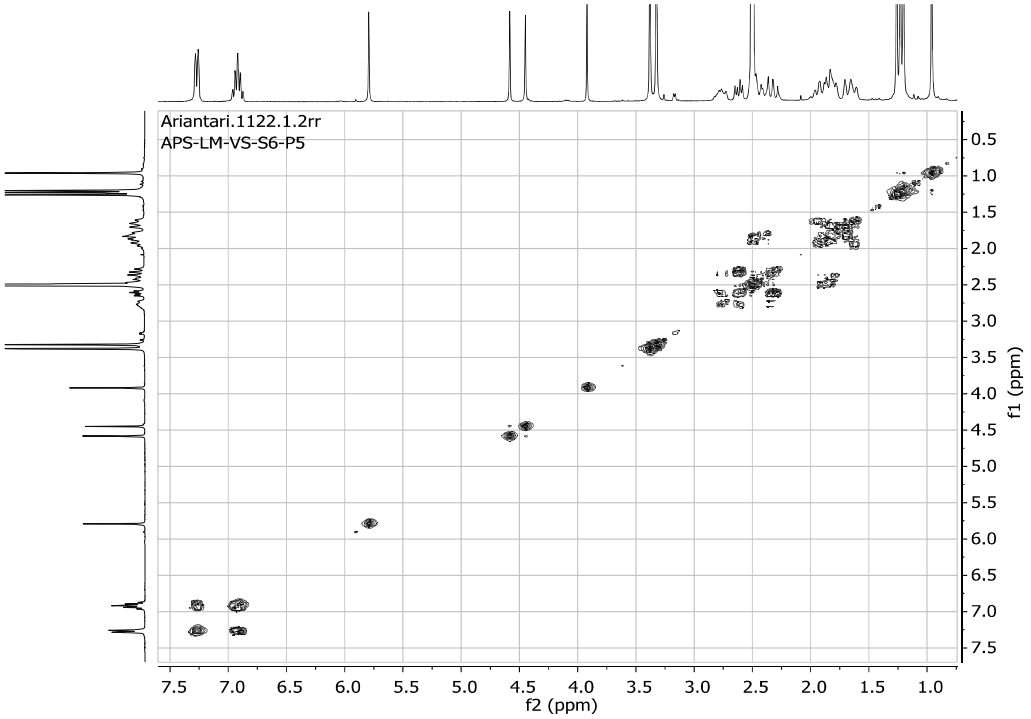

Figure S27. ^{1}H-^{1}H COSY (300 MHz, DMSO-d_6) spectrum of compound **4**.

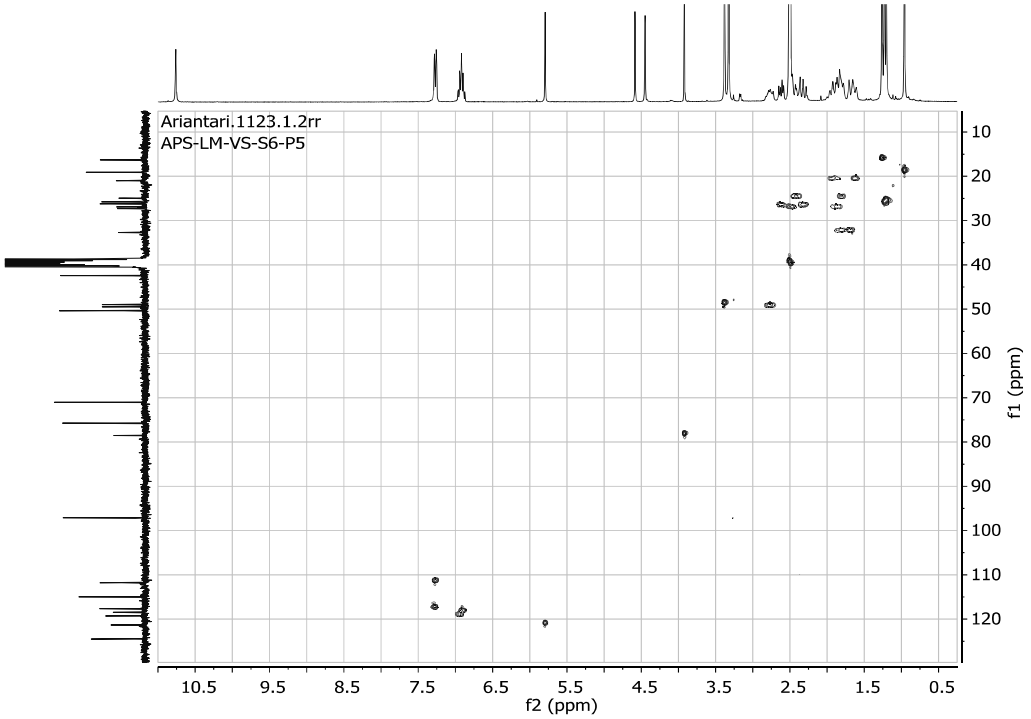

Figure S28. HSQC (300 and 75 MHz, DMSO-d_6) spectrum of compound **4**.

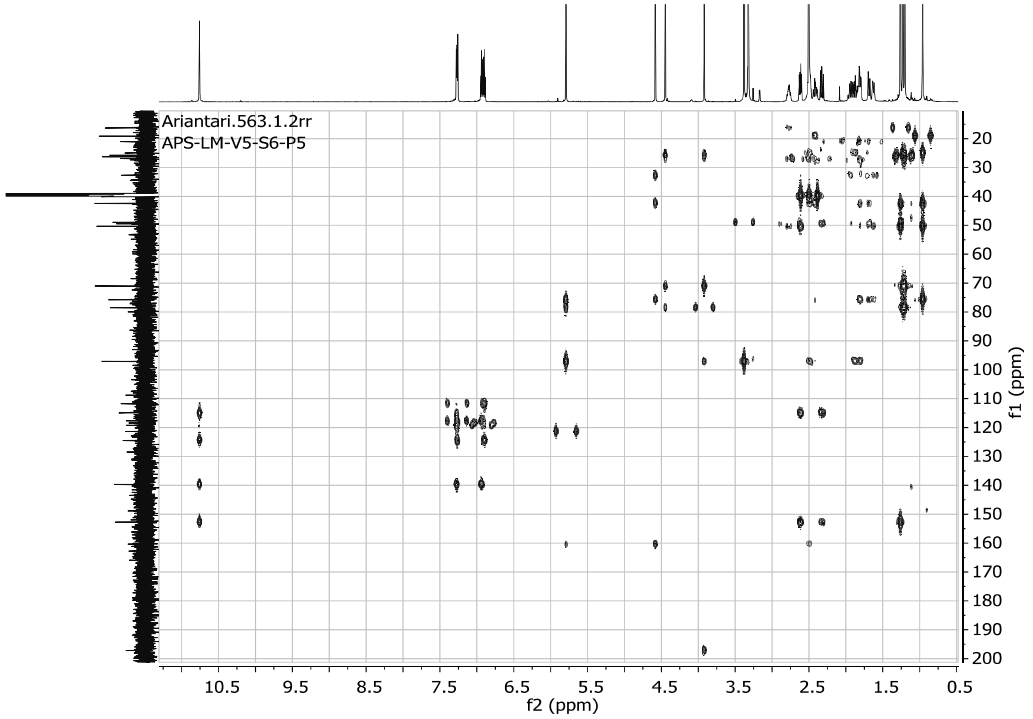

Figure S29. HMBC (600 and 150 MHz, DMSO-d_6) spectrum of compound **4**.

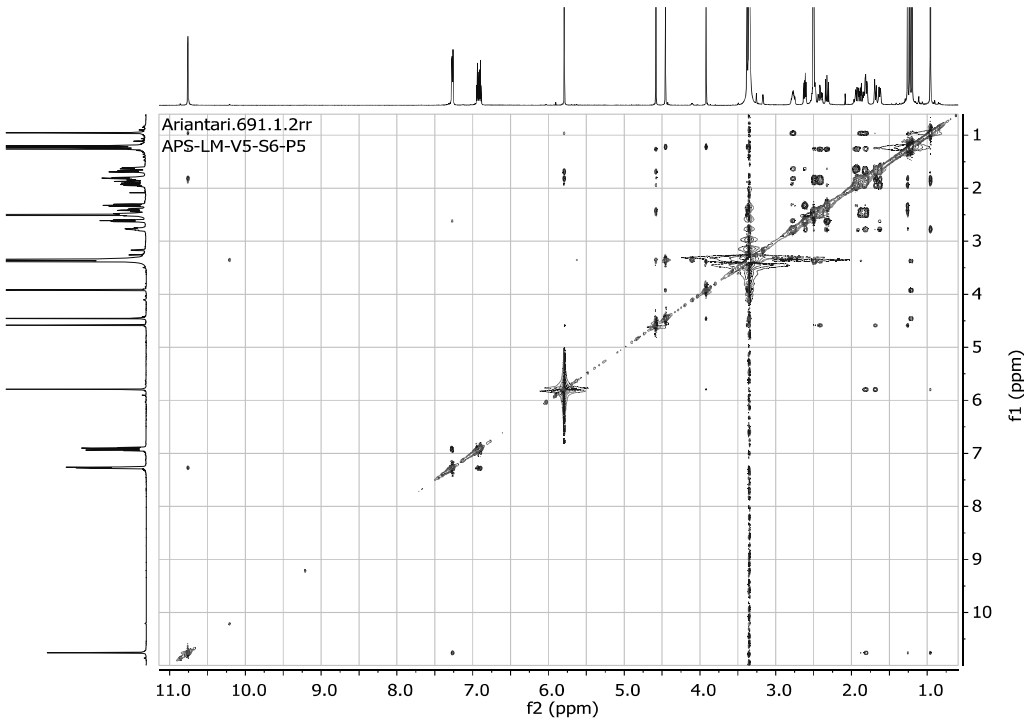

Figure S30. NOESY (600 MHz, DMSO-d_6) spectrum of compound **4**.

(A)

(B)

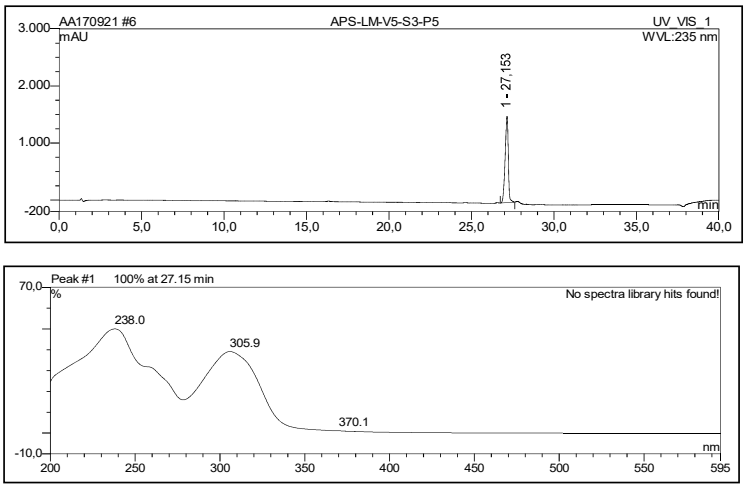

Figure S31. HPLC chromatogram (A) and UV spectrum (B) of compound **5**.

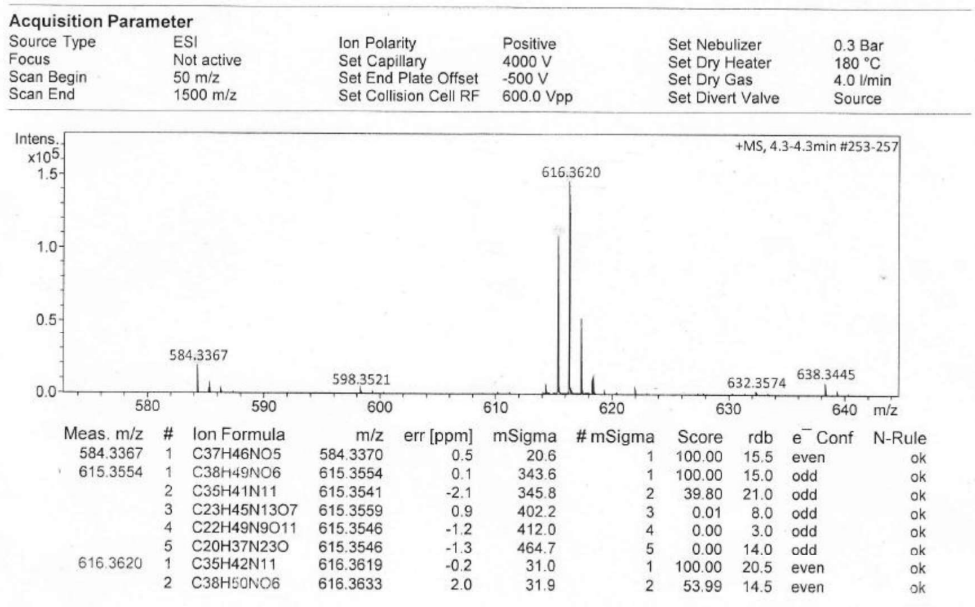

Figure S32. HRESIMS spectrum of compound **5**.

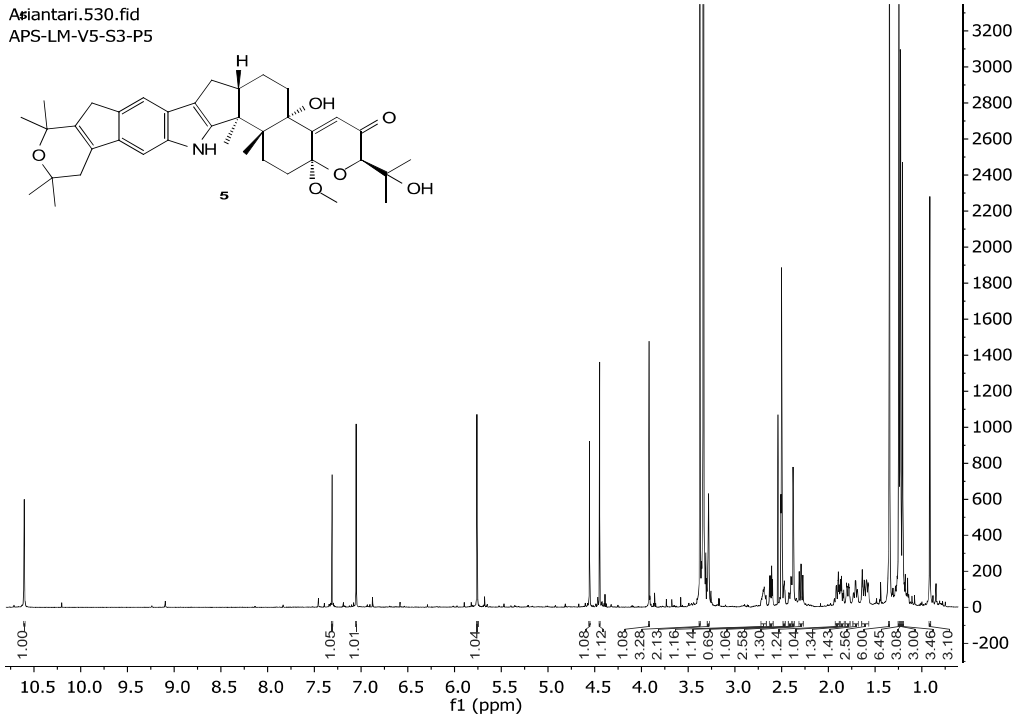

Figure S33. ^{1}H NMR (600 MHz, DMSO-d_6) spectrum of compound **5**.

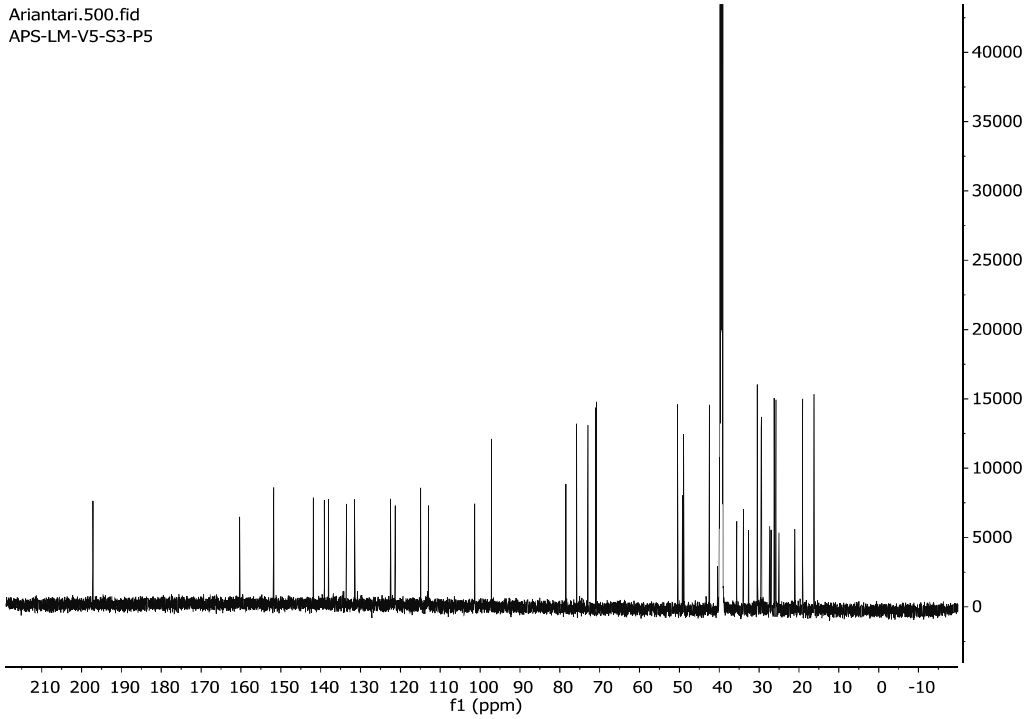

Figure S34. ^{13}C NMR (150 MHz, DMSO-d_6) spectrum of compound **5**.

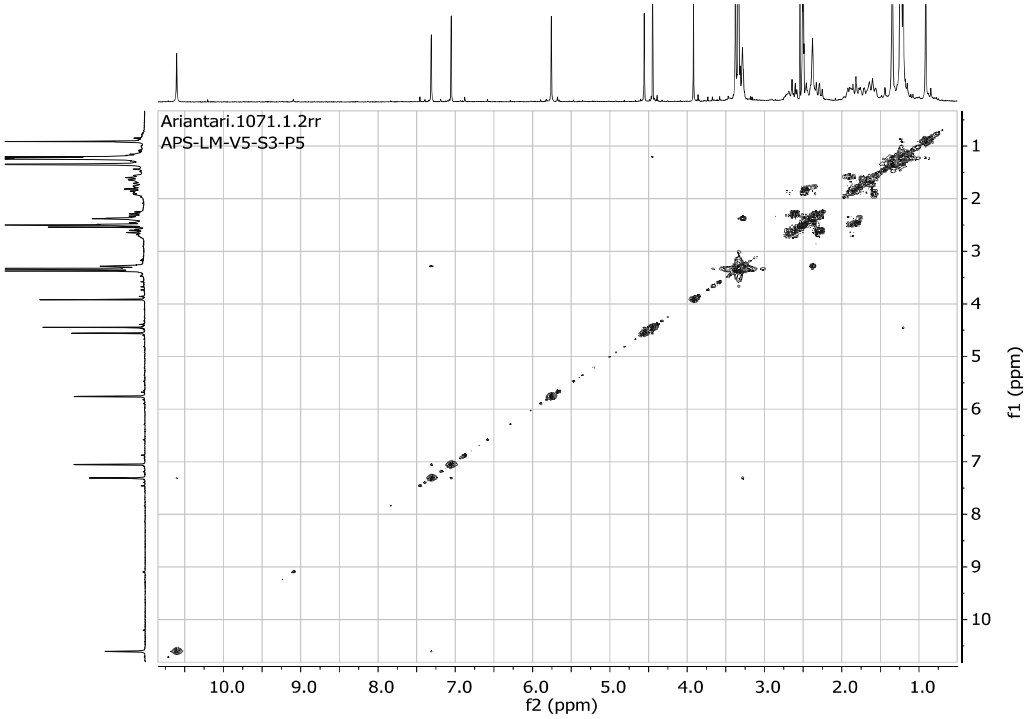

Figure S35. ^{1}H-^{1}H COSY (300 MHz, DMSO-d_6) spectrum of compound **5**.

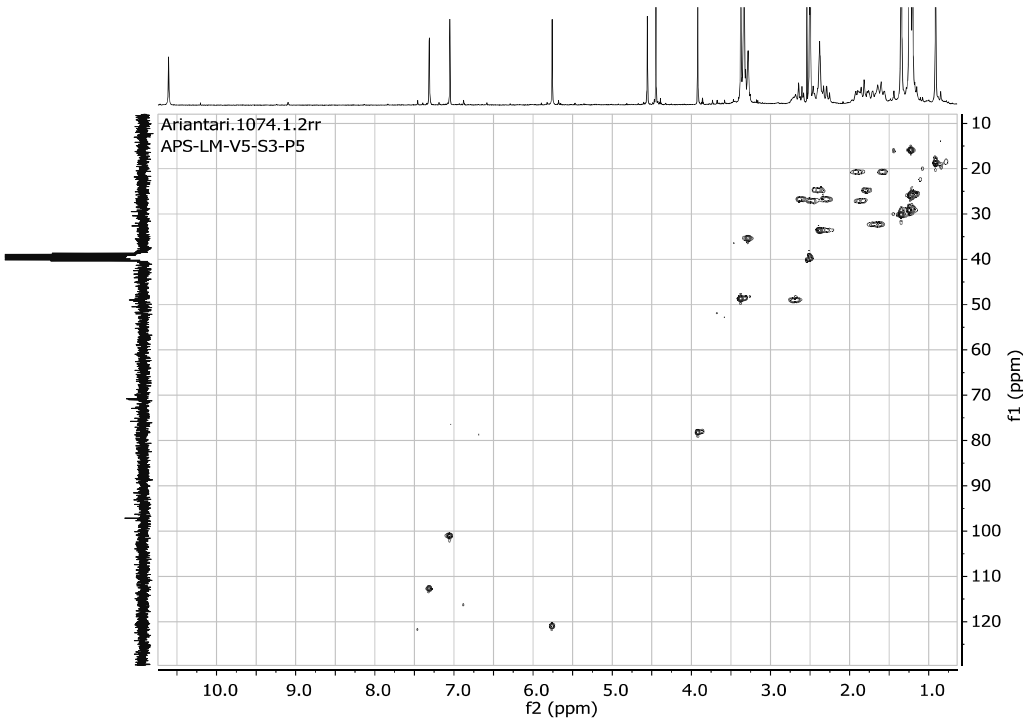

Figure S36. HSQC (300 and 75 MHz, DMSO-d_6) spectrum of compound **5**.

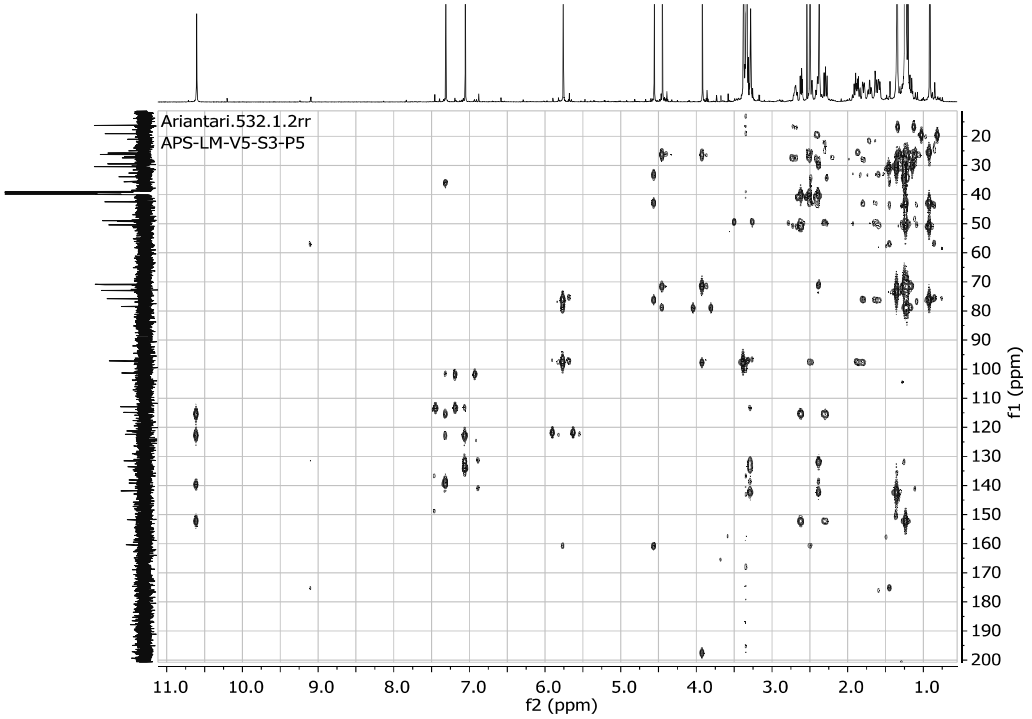

Figure S37. HMBC (600 and 150 MHz, DMSO-d_6) spectrum of compound **5**.

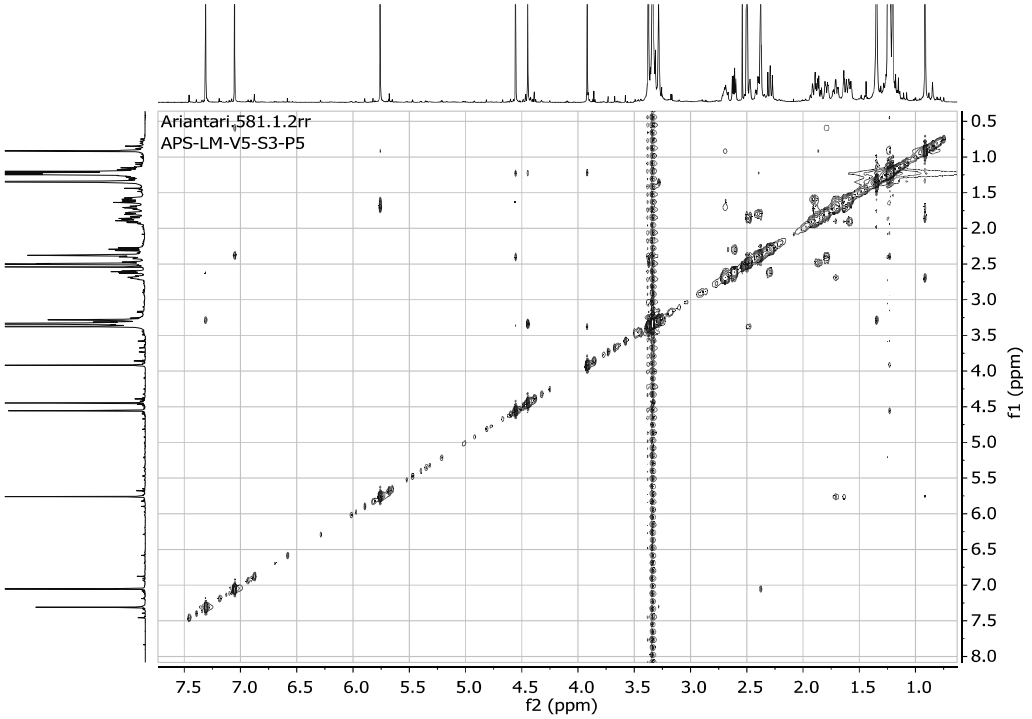

Figure S38. NOESY (600 MHz, DMSO-d_6) spectrum of compound **5**.

(A)

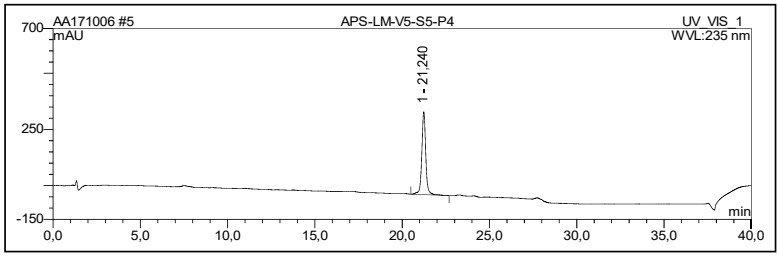

(B)

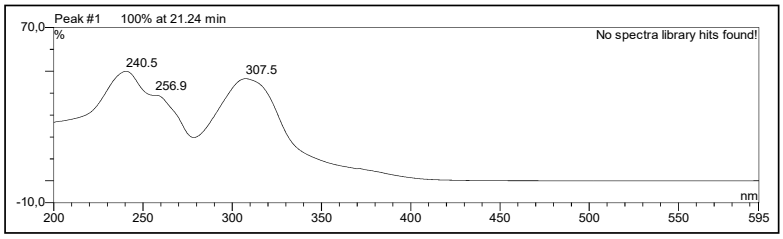

Figure S39. HPLC chromatogram (A) and UV spectrum (B) of compound **6**.

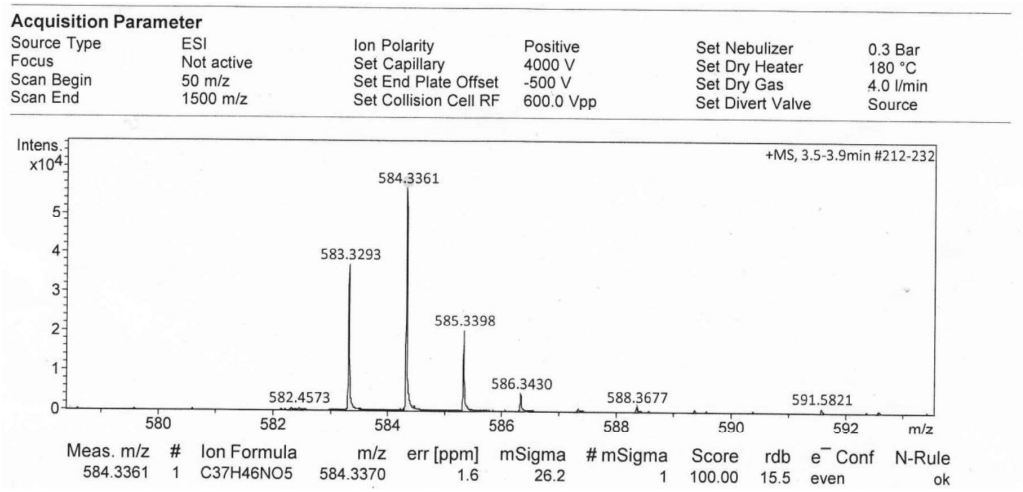

Figure S40. HRESIMS spectrum of compound **6**.

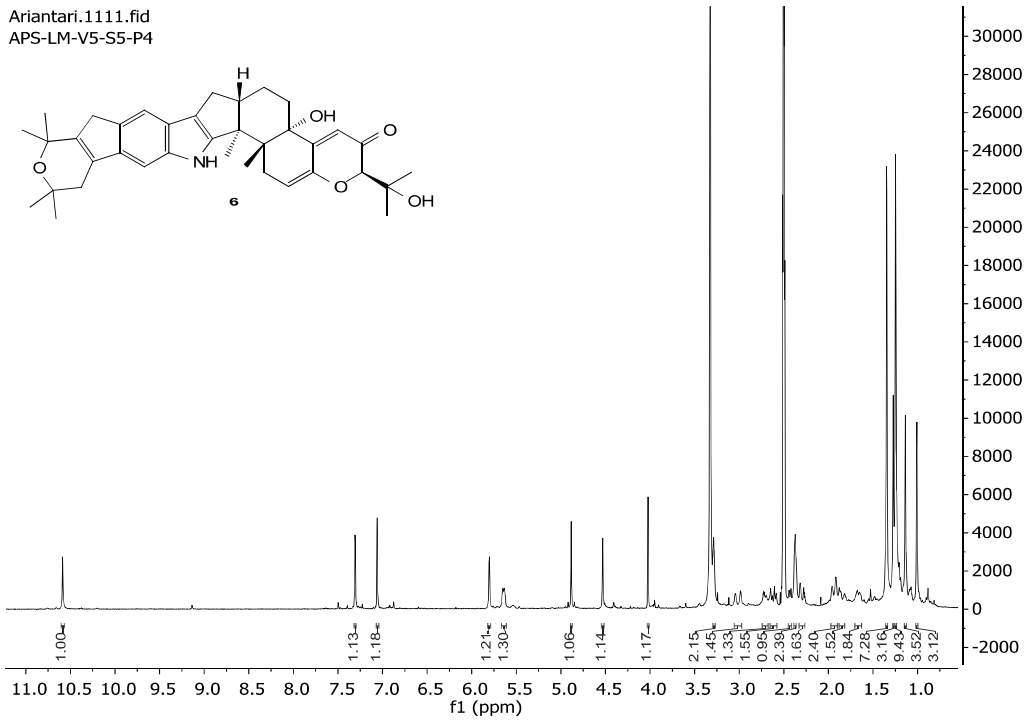

Figure S41. ^{1}H NMR (300 MHz, DMSO-d_6) spectrum of compound **6**.

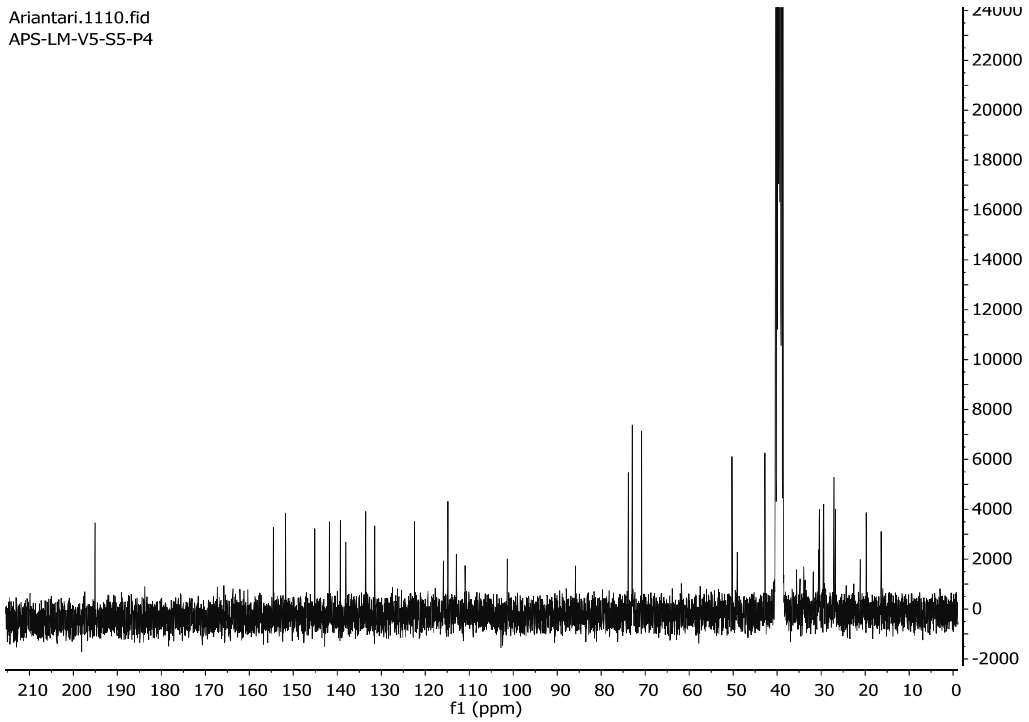

Figure S42. ^{13}C NMR (75 MHz, DMSO-d_6) spectrum of compound **6**.

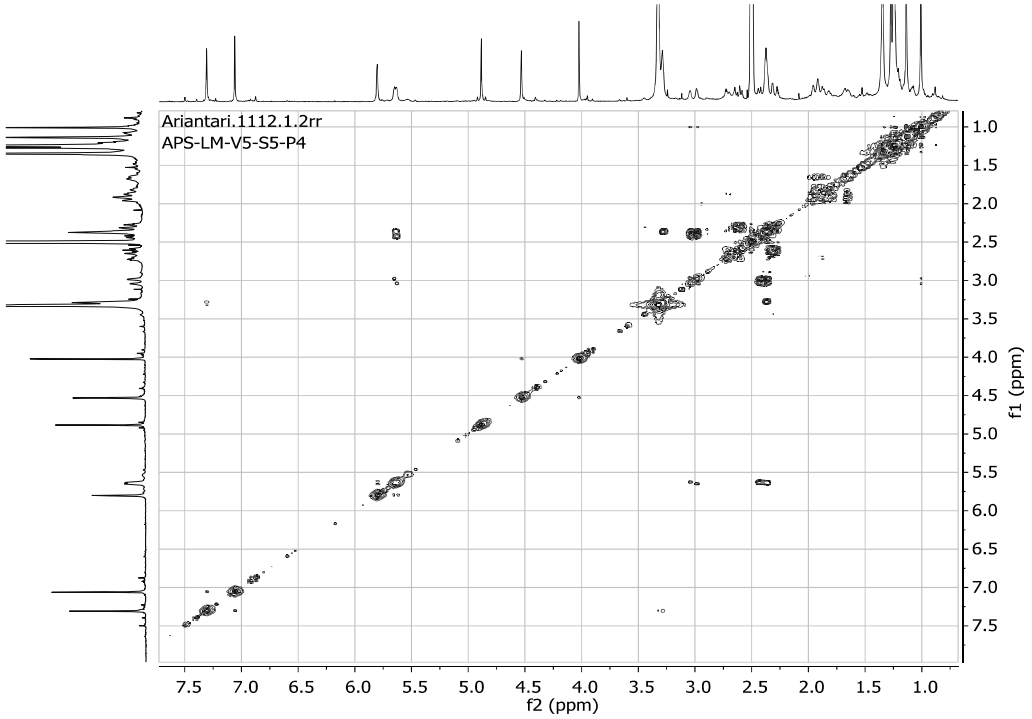

Figure S43. ^{1}H-^{1}H COSY (300 MHz, DMSO-d_6) spectrum of compound **6**.

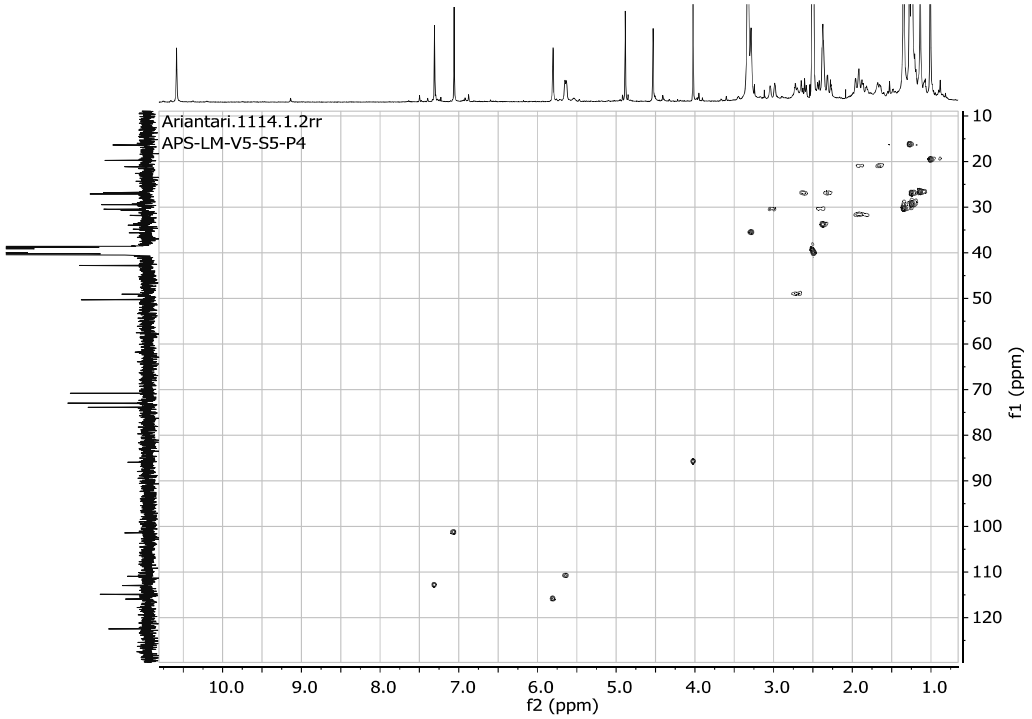

Figure S44. HSQC (300 and 75 MHz, DMSO-d_6) spectrum of compound **6**.

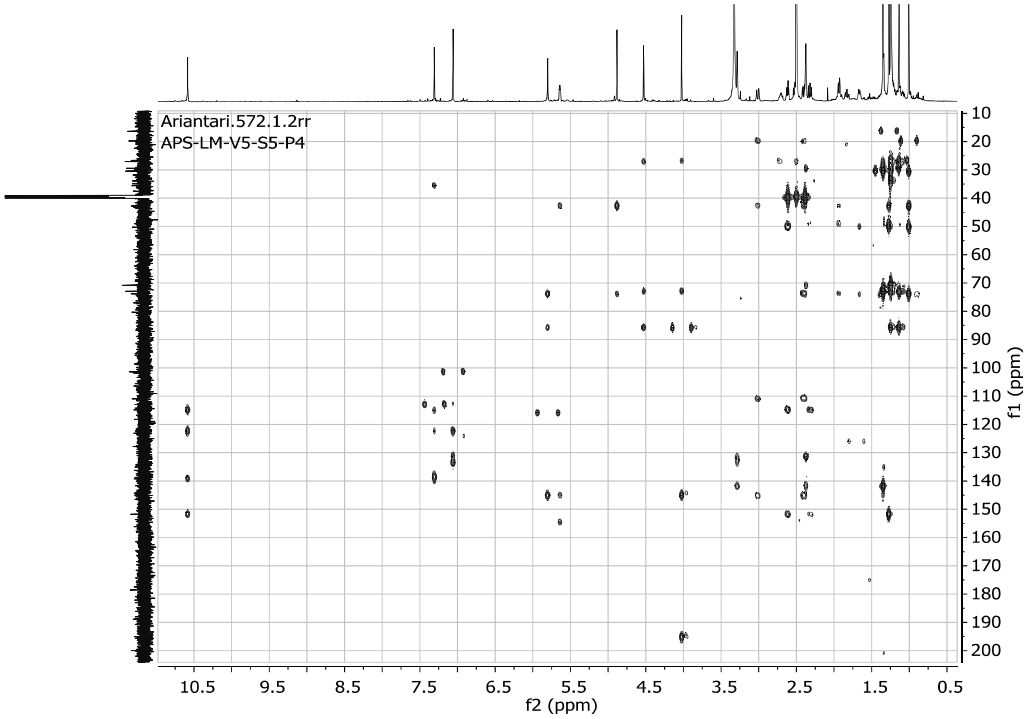

Figure S45. HMBC (600 and 150 MHz, DMSO-d_6) spectrum of compound **6**.

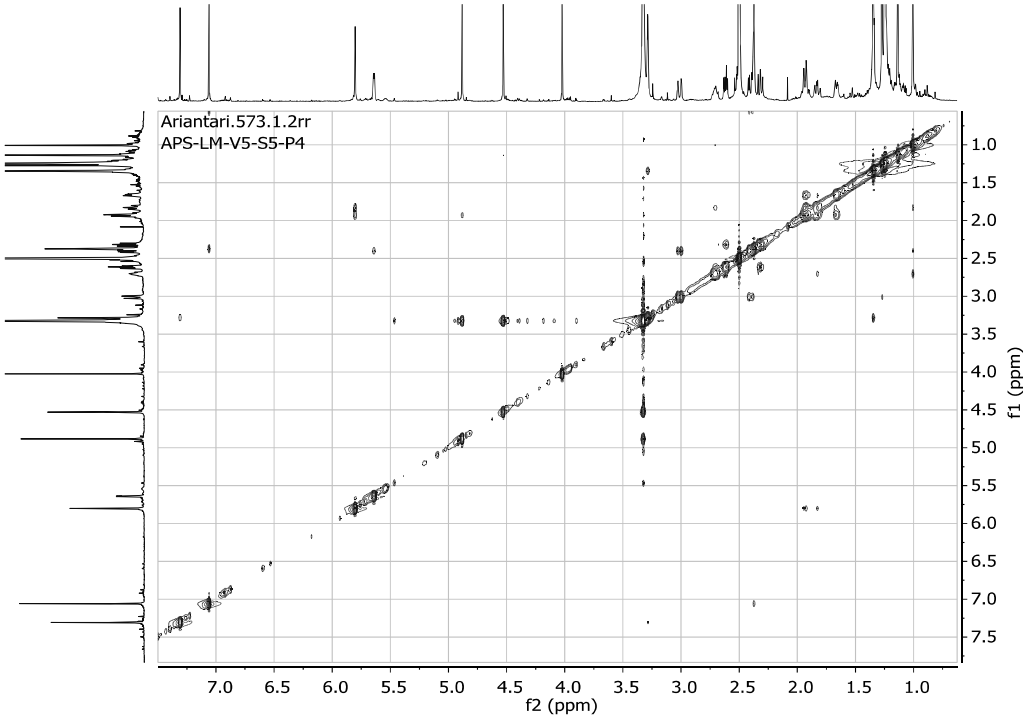

Figure S46. NOESY (600 MHz, DMSO-d_6) spectrum of compound **6**.

(A)

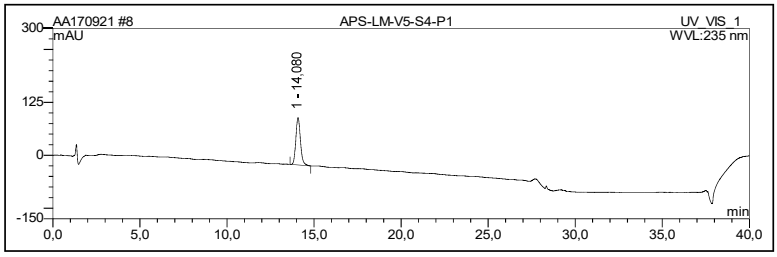

(B)

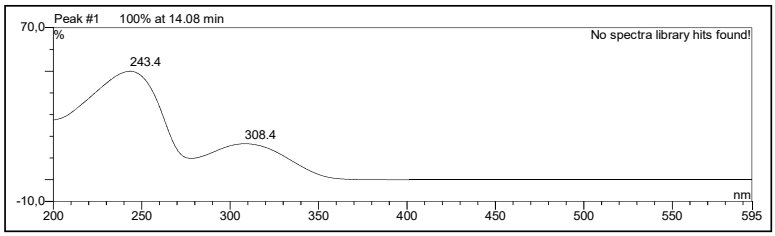

Figure S47. HPLC chromatogram (A) and UV spectrum (B) of compound **7**.

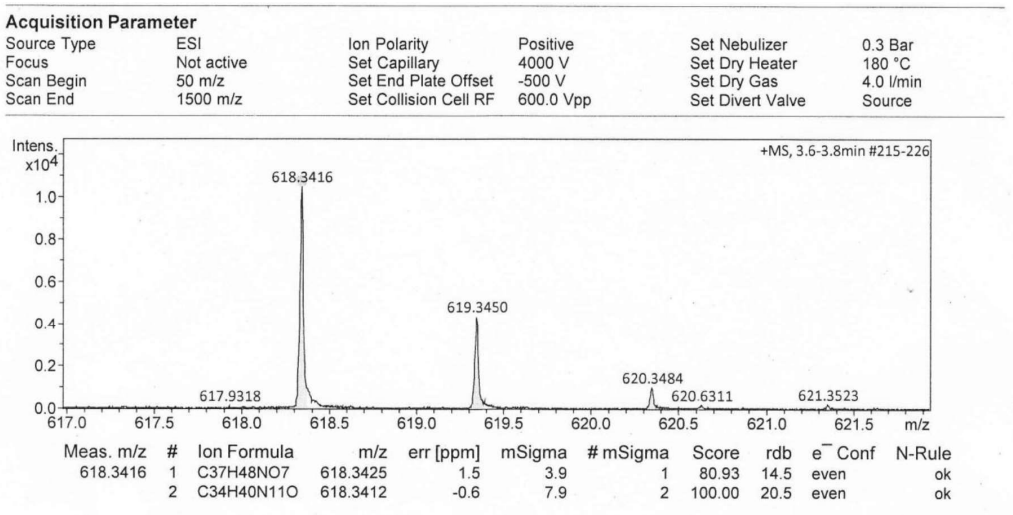

Figure S48. HRESIMS spectrum of compound **7**.

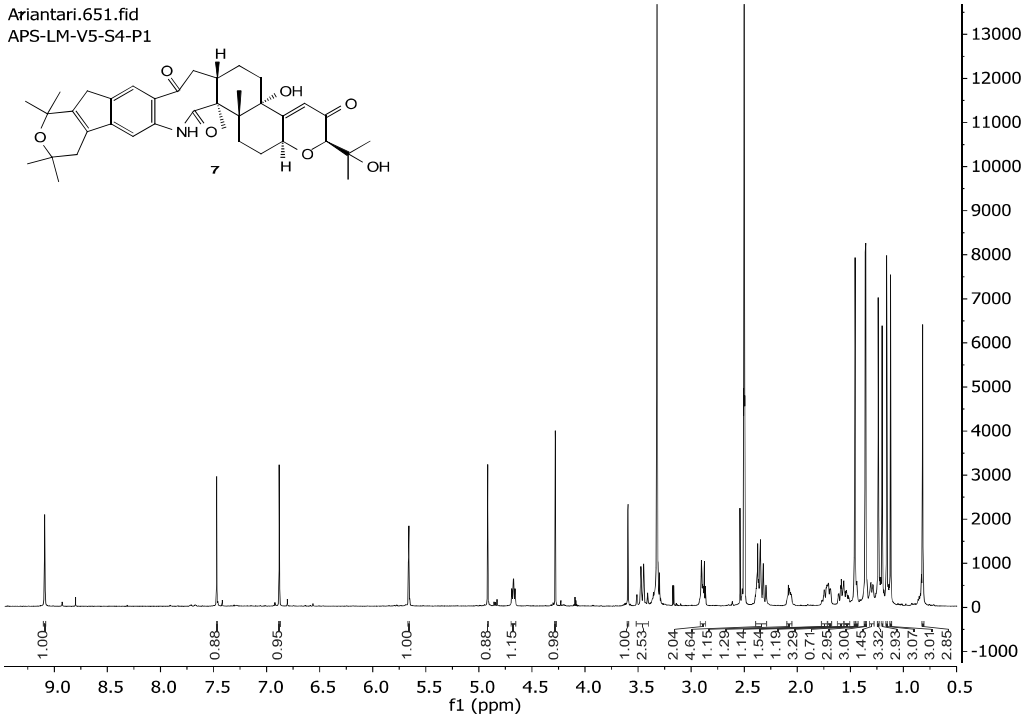

Figure S49. ^{1}H NMR (600 MHz, DMSO-d_6) spectrum of compound **7**.

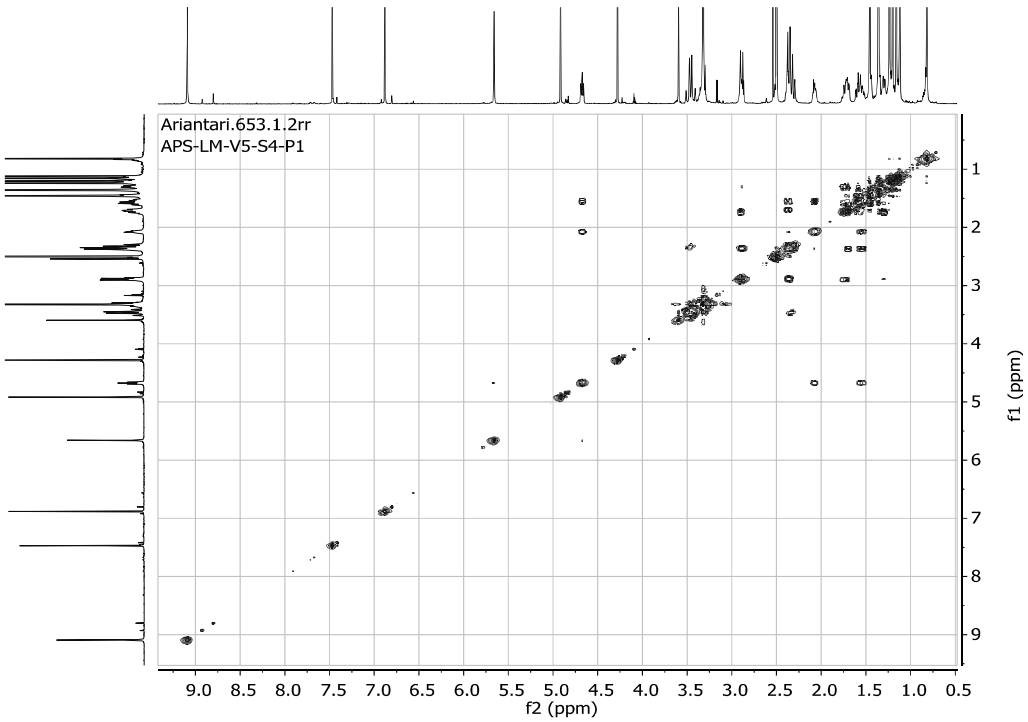

Figure S50. ^{1}H-^{1}H COSY (600 MHz, DMSO-d_6) spectrum of compound **7**.

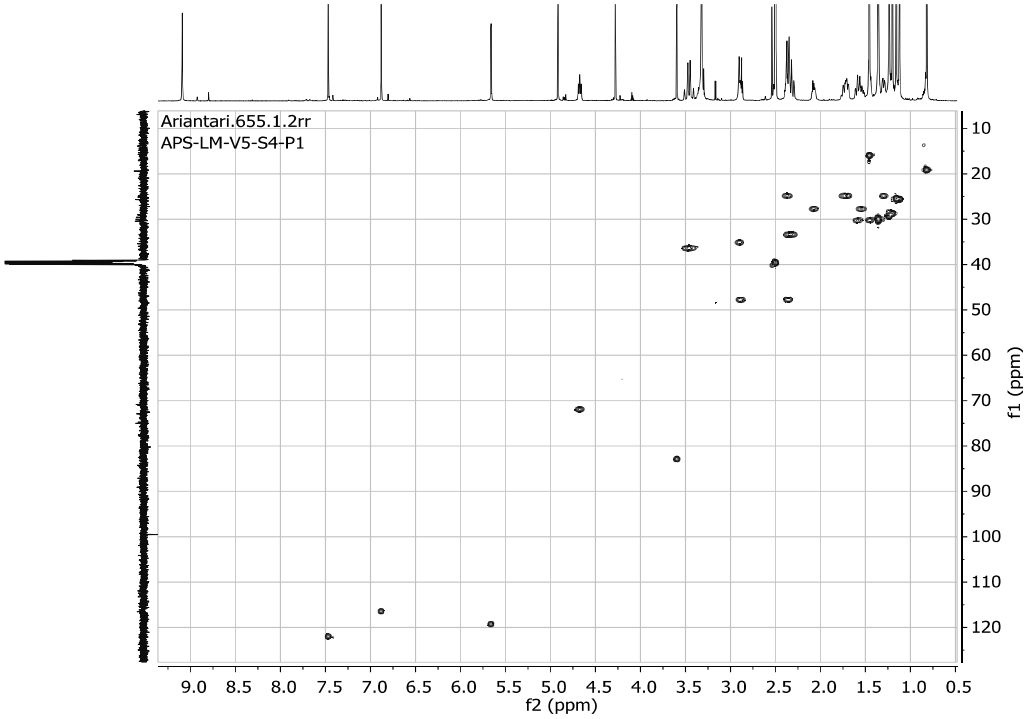

Figure S51. HSQC (600 and 150 MHz, DMSO-d_6) spectrum of compound **7**.

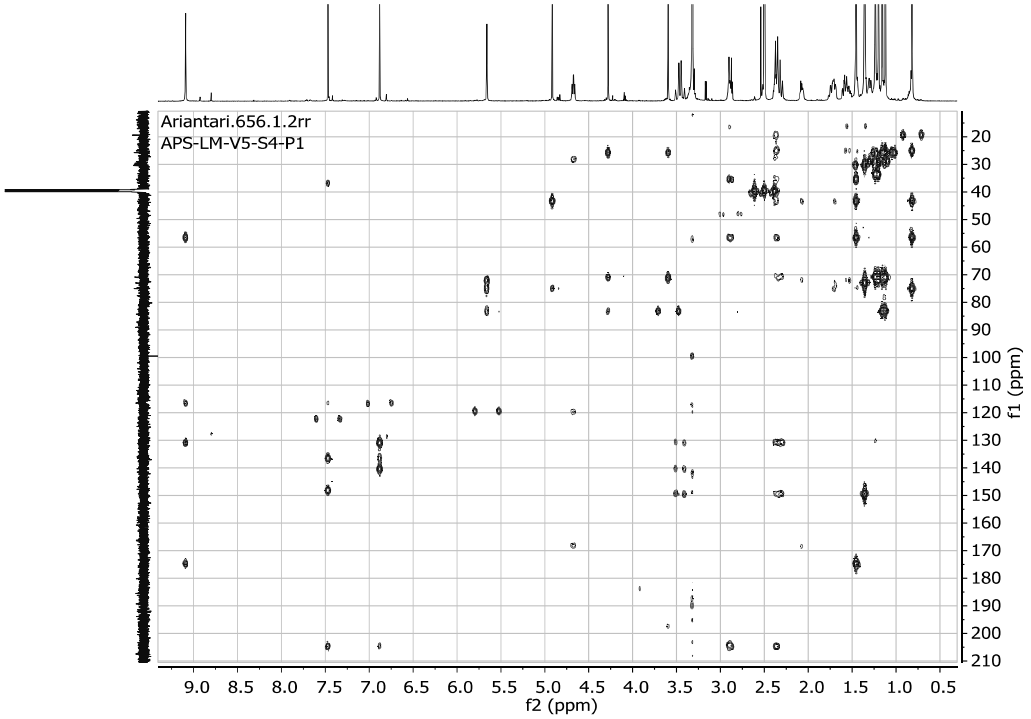

Figure S52. HMBC (600 and 150 MHz, DMSO-d_6) spectrum of compound **7**.

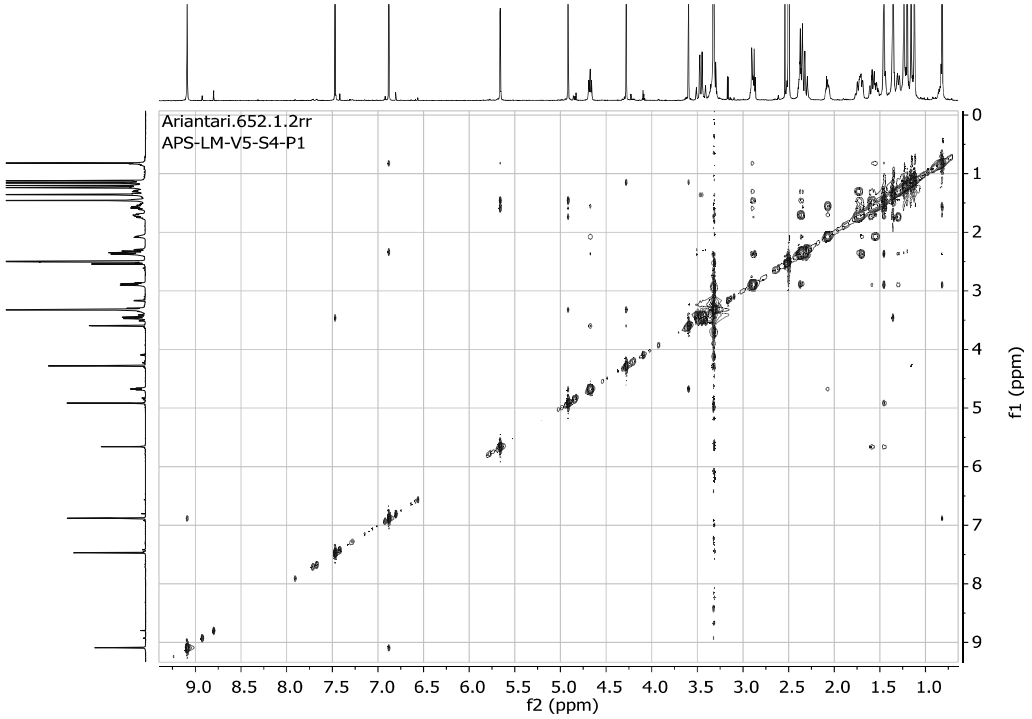

Figure S53. NOESY (600 MHz, DMSO-d_6) spectrum of compound **7**.

(A)

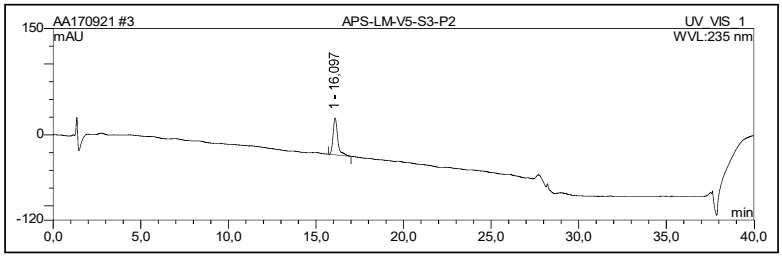

(B)

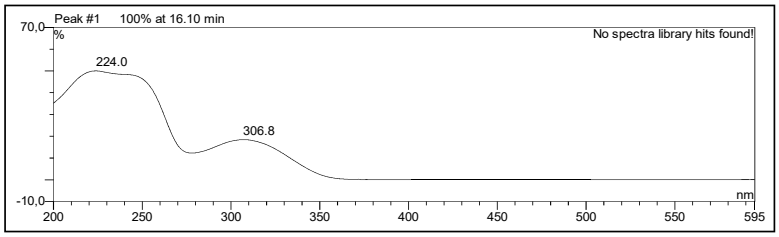

Figure S54. HPLC chromatogram (A) and UV spectrum (B) of compound **8**.

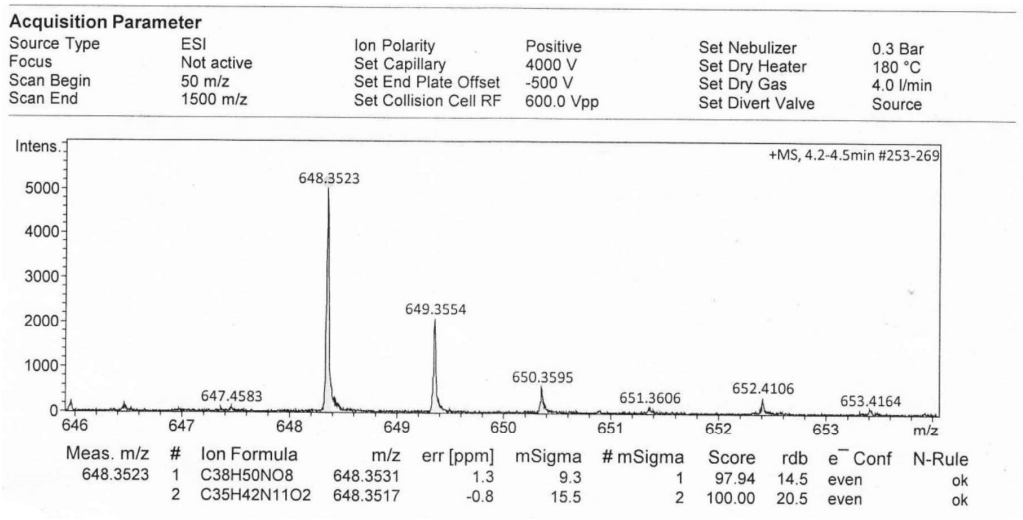

Figure S55. HRESIMS spectrum of compound **8**.

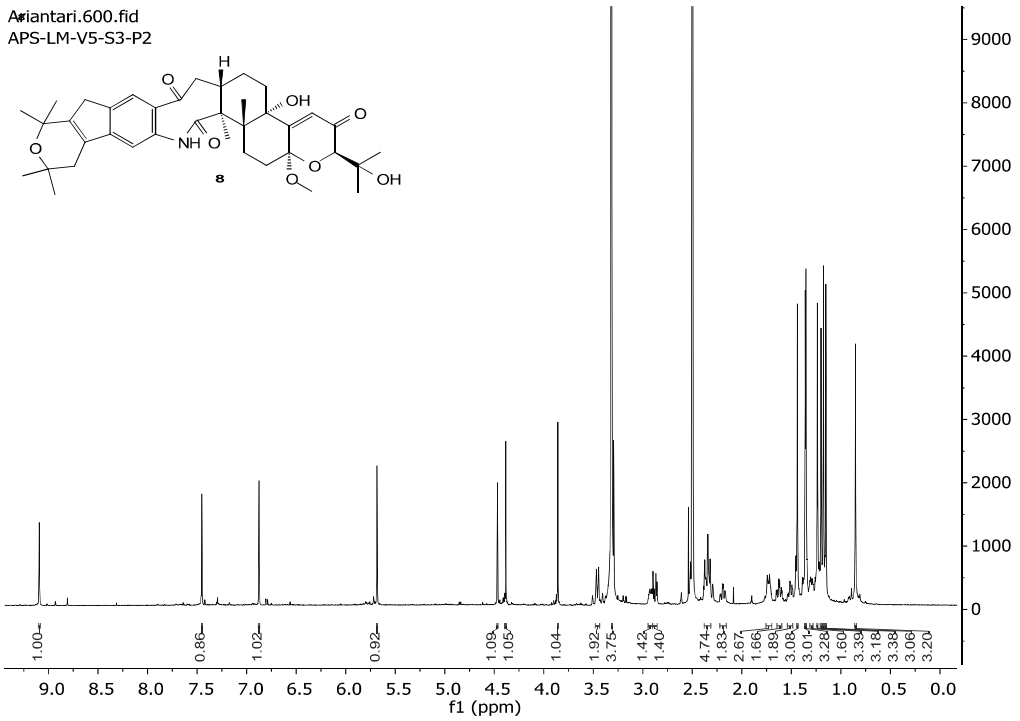

Figure S56. ^{1}H NMR (600 MHz, DMSO-d_6) spectrum of compound **8**.

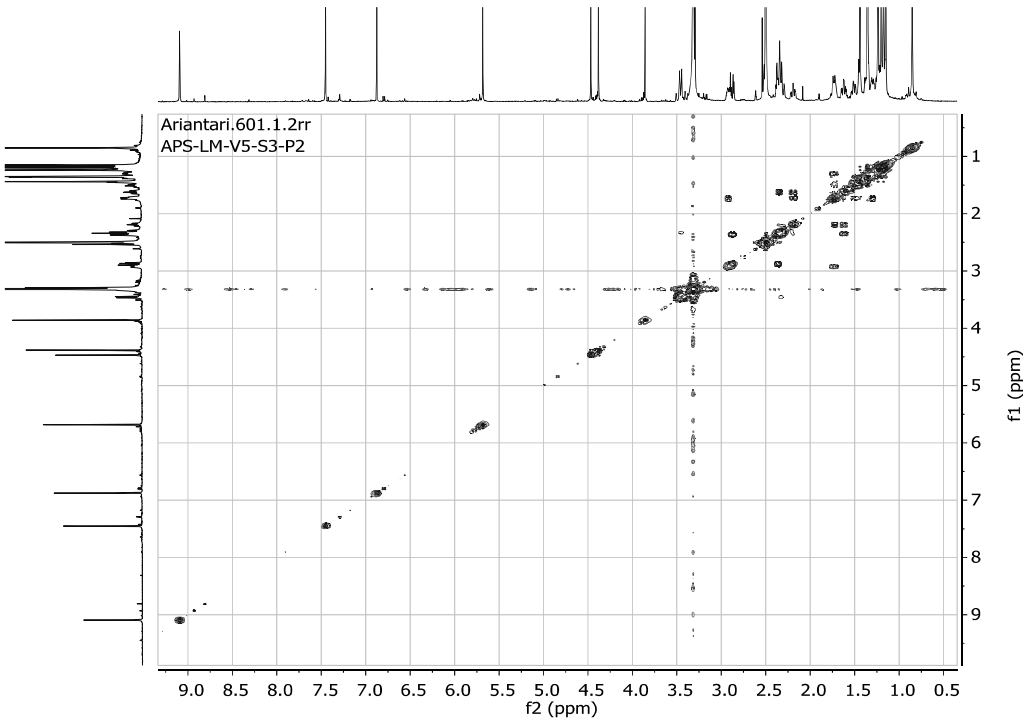

Figure S57. ^{1}H-^{1}H COSY (600 MHz, DMSO-d_6) spectrum of compound **8**.

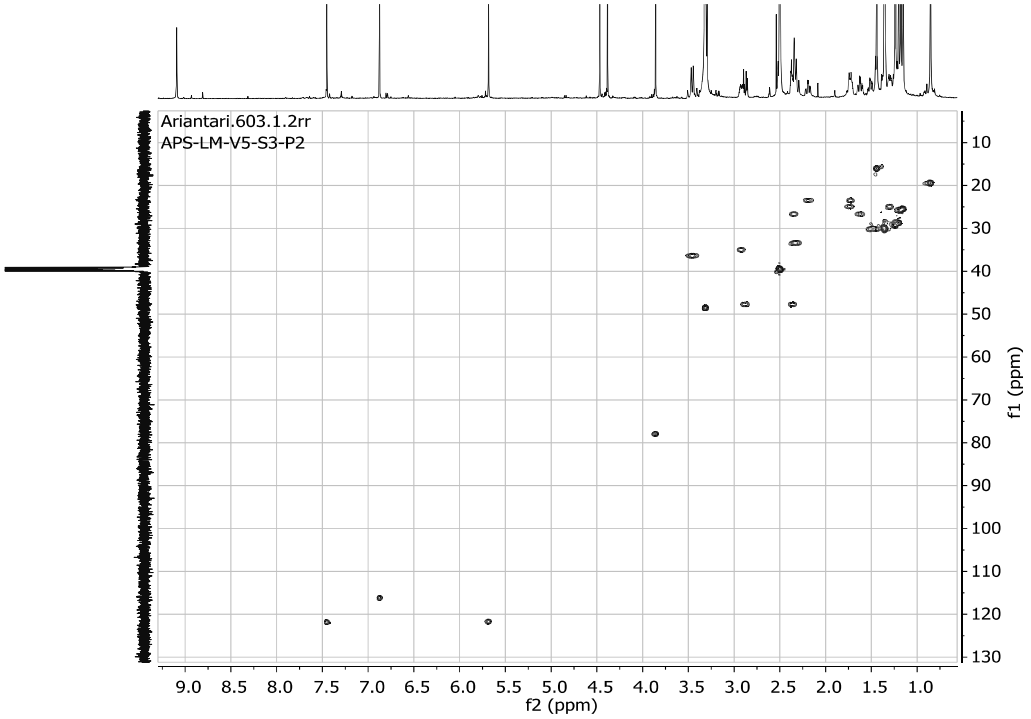

Figure S58. HSQC (600 and 150 MHz, DMSO-d_6) spectrum of compound **8**.

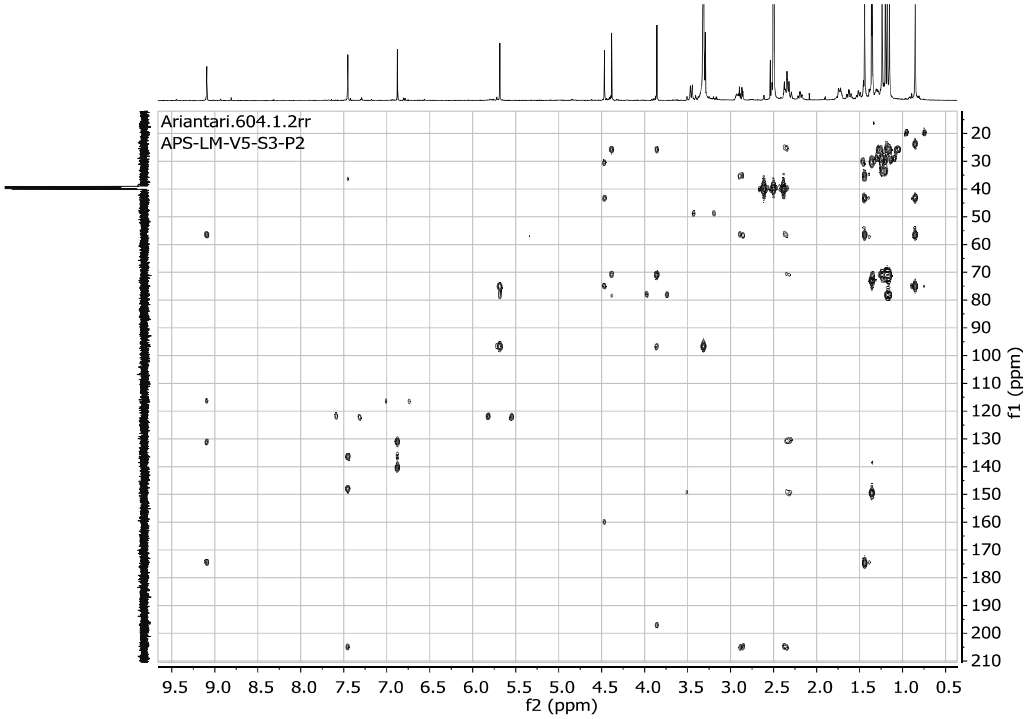

Figure S59. HMBC (600 and 150 MHz, DMSO-d_6) spectrum of compound **8**.

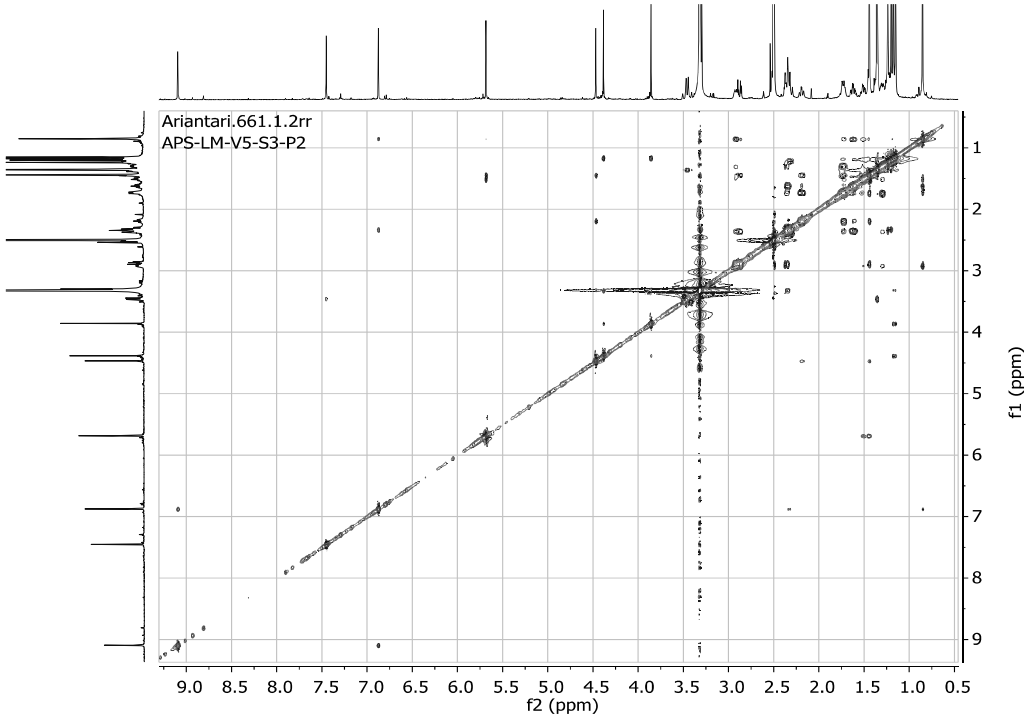

Figure S60. NOESY (600 MHz, DMSO-d_6) spectrum of compound **8**.

(A)

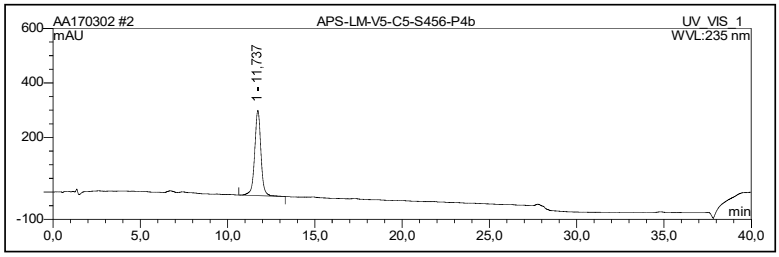

(B)

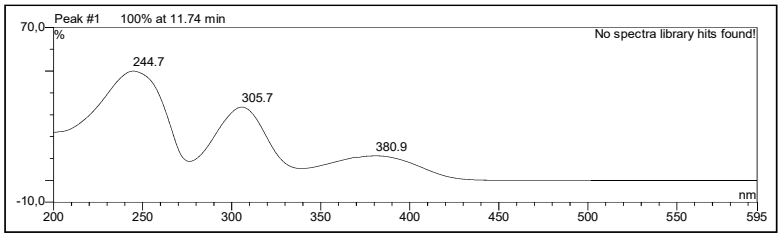

Figure S61. HPLC chromatogram (A) and UV spectrum (B) of compound **9**.

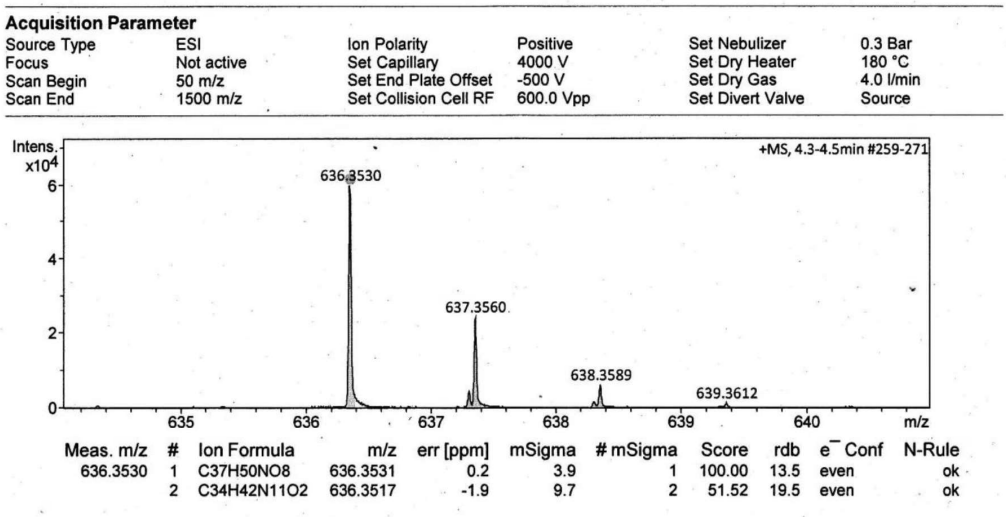

Figure S62. HRESIMS spectrum of compound **9**.

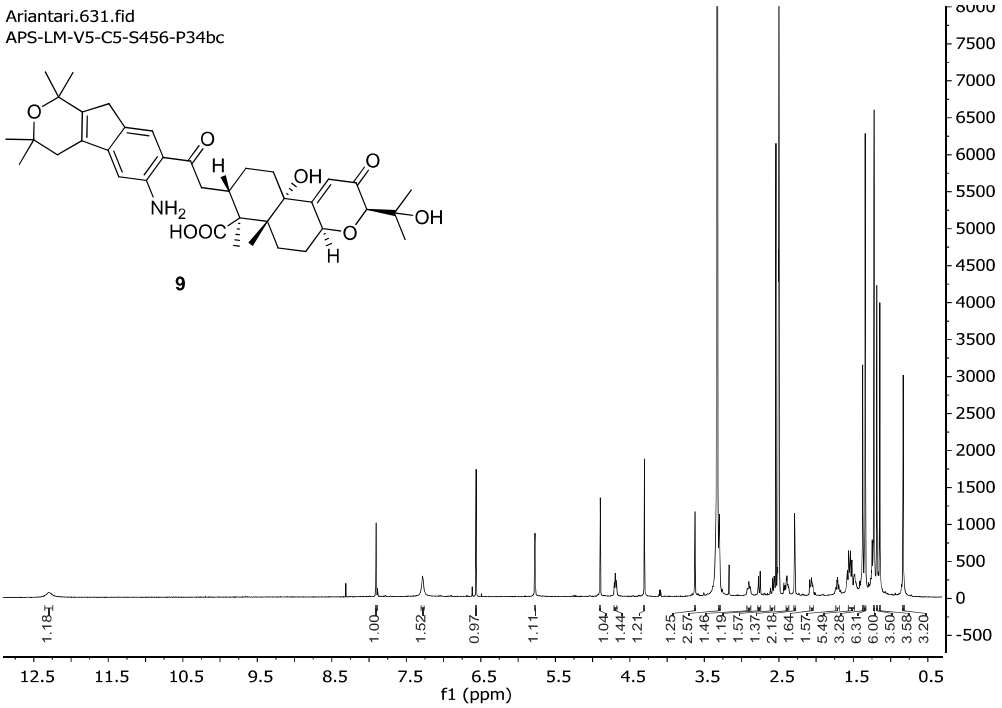

Figure S63. ^{1}H NMR (600 MHz, DMSO-d_6) spectrum of compound **9**.

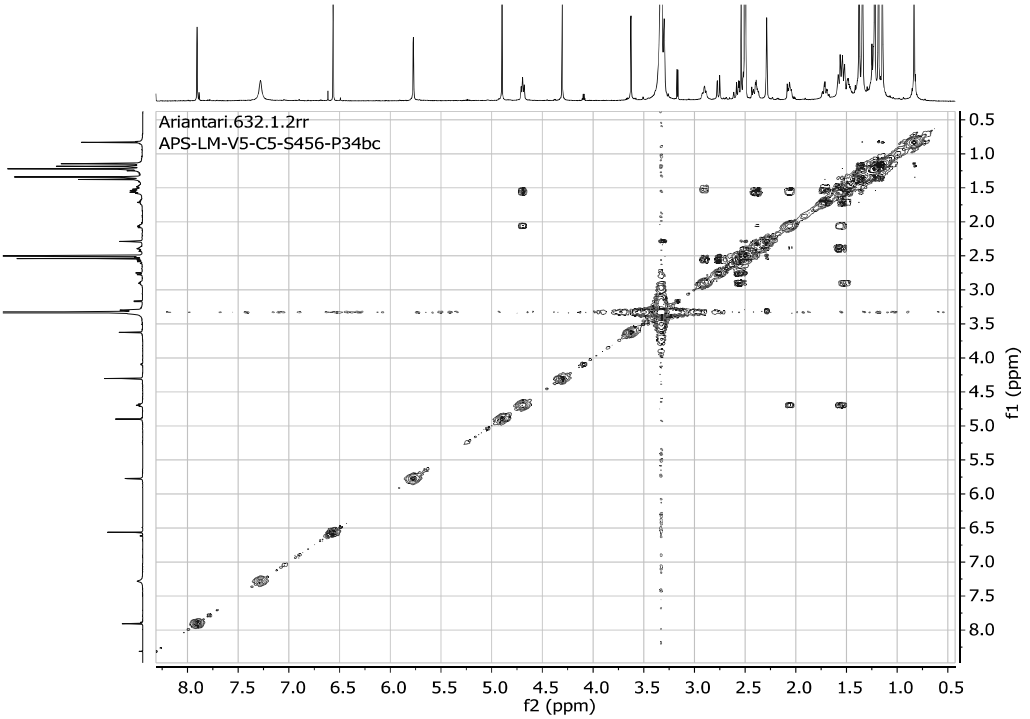

Figure S64. ^{1}H-^{1}H COSY (600 MHz, DMSO-d_6) spectrum of compound **9**.

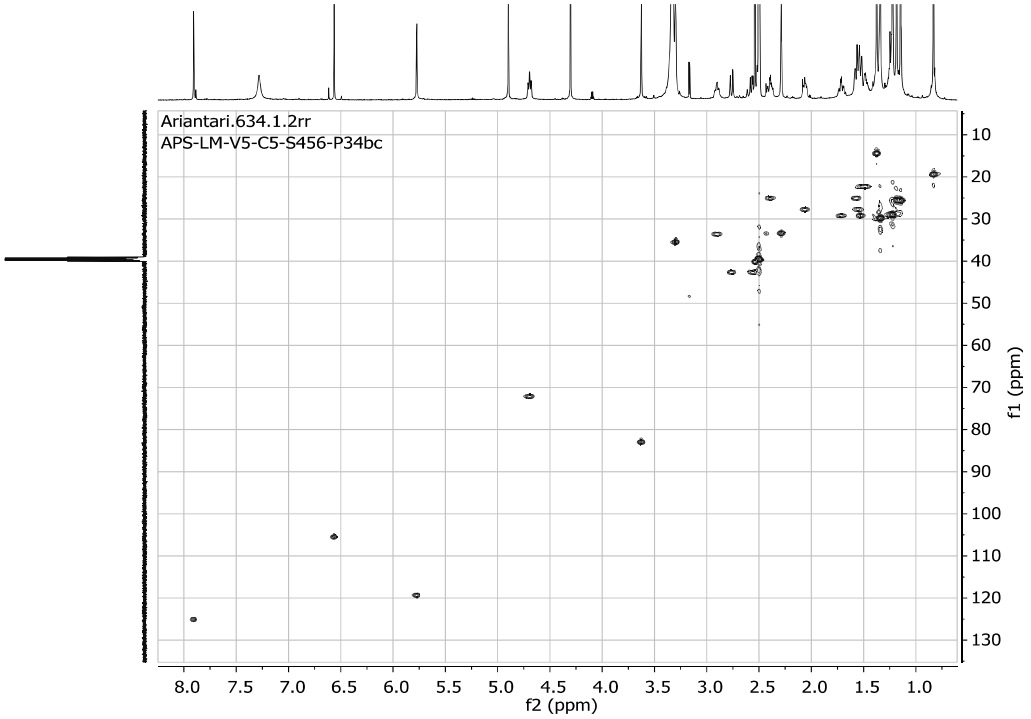

Figure S65. HSQC (600 and 150 MHz, DMSO-d_6) spectrum of compound **9**.

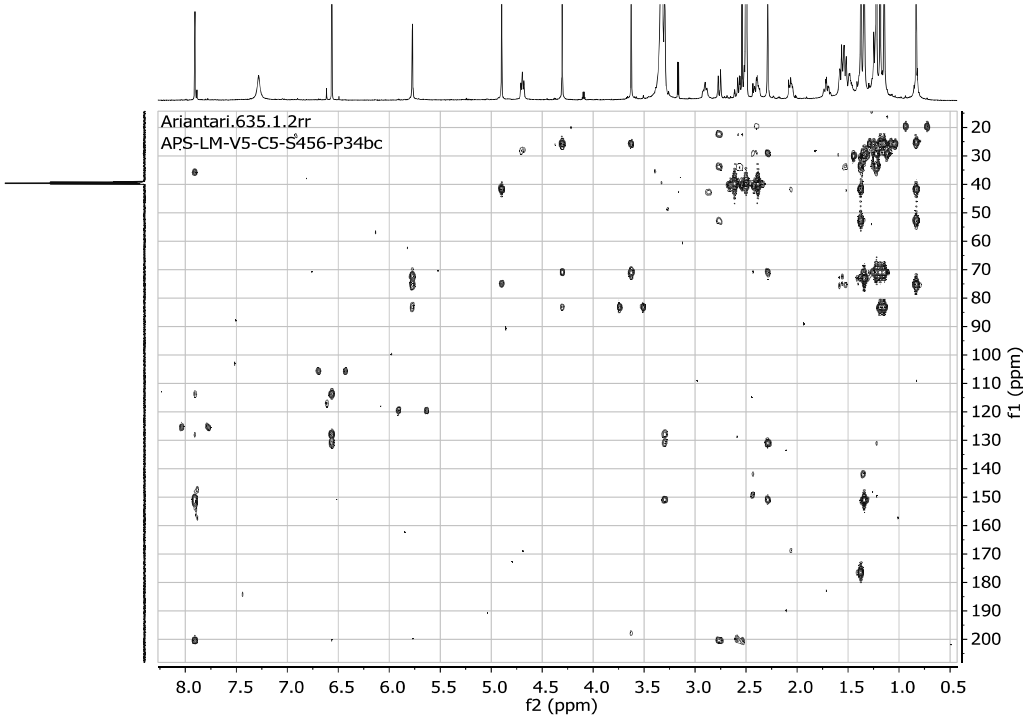

Figure S66. HMBC (600 and 150 MHz, DMSO-d_6) spectrum of compound **9**.

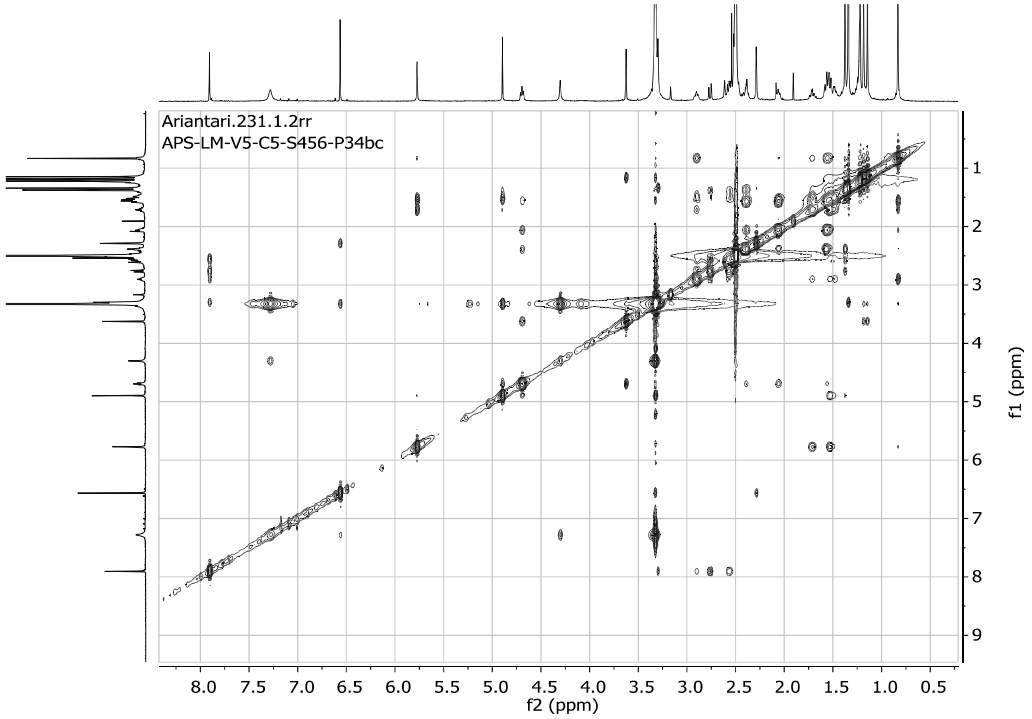

Figure S67. NOESY (600 MHz, DMSO-d_6) spectrum of compound **9**.

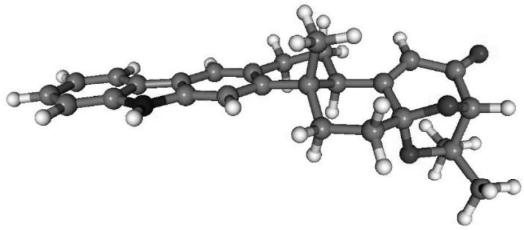

Figure S68. Structure of the single low-energy CAM-B3LYP/TZVP PCM/MeCN conformer (99.7%) of (5*S*,8*R*,10*S*,14*R*)-**1**.

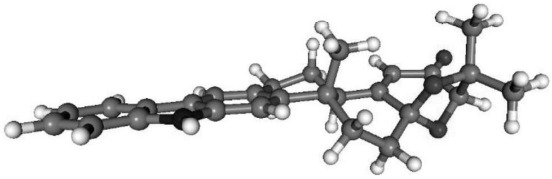

Figure S69. Structure of the single CAM-B3LYP/TZVP PCM/MeCN conformer of (5*S*,8*S*,10*R*,14*R*)-**1**.

Table S70. Comparison of the computed ^{13}C NMR data of (5*S*,8*R*,10*S*,14*R*)-**1** and (5*S*,8*S*,10*R*,14*R*)-**1** [calculated at the mPW1PW91/6-311+G(2d,p) level for the mPW1PW91/6-311+G(2d,p) conformers] with the experimental data. Corrected mean absolute error (CMAE) values were computed for all carbon atoms. For better comparison Δδ values ≥ 2.5 are highlighted with yellow and ≥ 5 with red.

Numbering	Exp	(5*S*,8*R*,10*S*,14*R*)	$\Delta\delta_{(5S,8R,10S,14R)}$	(5*S*,8*S*,10*R*,14*R*)	$\Delta\delta_{(5S,8S,10R,14R)}$
C-2	139.79	138.06	1.73	138.01	1.78
C-3	107.79	106.06	1.73	106.91	0.88
C-4	147.60	143.97	3.63	148.80	1.20
C-5	35.88	43.19	7.31	40.27	4.39
C-6	34.49	35.99	1.50	35.35	0.86
C-7	27.73	31.28	3.55	28.71	0.98
C-8	103.88	103.95	0.07	104.37	0.49
C-10	88.05	87.21	0.84	88.55	0.50
C-11	197.52	193.74	3.78	195.40	2.12
C-12	120.35	121.64	1.29	121.36	1.01
C-13	171.02	171.00	0.02	174.97	3.95
C-14	43.25	47.76	4.51	44.15	0.90
C-15	19.85	21.33	1.48	20.57	0.72
C-16	29.45	31.66	2.21	31.07	1.62
C-17	125.64	127.12	1.48	126.41	0.77
C-18	119.69	121.68	1.99	121.08	1.39
C-19	122.18	122.68	0.50	122.34	0.16
C-20	123.06	123.41	0.35	124.17	1.11
C-21	120.19	120.75	0.56	120.75	0.56
C-22	119.10	119.50	0.40	119.29	0.19
C-23	125.79	125.94	0.15	125.86	0.07
C-24	110.74	108.44	2.30	108.20	2.54
C-25	140.11	139.06	1.05	139.02	1.09
C-26	30.81	22.97	7.84	29.70	1.11
C-27	78.66	82.84	4.18	81.14	2.48
C-28	22.75	21.44	1.31	22.10	0.65
C-29	28.65	27.49	1.16	27.53	1.12
CMAE			2.11		1.28

Table S71. Comparison of the computed ^{13}C NMR data of (5*S*,8*R*,10*S*,14*R*)-**1** and (5*S*,8*S*,10*R*,14*R*)-**1** [calculated at the mPW1PW91/6-311+G(2d,p) SMD/$CHCl_3$ level for the mPW1PW91/6-311+G(2d,p) conformers] with the experimental data. Corrected mean absolute error (CMAE) values were computed for all carbon atoms. For better comparison Δδ values ≥ 2.5 are highlighted with yellow and ≥ 5 with red.

Numbering	Exp	(5*S*,8*R*,10*S*,14*R*)	$\Delta\delta_{(5S,8R,10S,14R)}$	(5*S*,8*S*,10*R*,14*R*)	$\Delta\delta_{(5S,8S,10R,14R)}$
C-2	139.79	136.31	3.48	136.19	3.60
C-3	107.79	105.63	2.16	106.60	1.19
C-4	147.60	143.18	4.42	147.67	0.07
C-5	35.88	43.74	7.86	40.57	4.69
C-6	34.49	35.57	1.08	35.32	0.83
C-7	27.73	31.52	3.79	28.76	1.03
C-8	103.88	102.84	1.04	103.26	0.62
C-10	88.05	86.26	1.79	87.66	0.39
C-11	197.52	193.47	4.05	195.02	2.50
C-12	120.35	119.64	0.71	119.39	0.96
C-13	171.02	171.95	0.93	175.98	4.96
C-14	43.25	48.20	4.95	44.47	1.22
C-15	19.85	21.42	1.57	20.65	0.80
C-16	29.45	31.52	2.07	30.93	1.48
C-17	125.64	126.36	0.72	125.68	0.04
C-18	119.69	119.73	0.04	119.13	0.56
C-19	122.18	120.00	2.18	119.70	2.48
C-20	123.06	121.27	1.79	121.97	1.09
C-21	120.19	119.17	1.02	119.20	0.99
C-22	119.10	117.22	1.88	117.06	2.04
C-23	125.79	124.17	1.62	124.13	1.66
C-24	110.74	107.99	2.75	107.82	2.92
C-25	140.11	137.51	2.60	137.48	2.63
C-26	30.81	22.94	7.87	29.52	1.29
C-27	78.66	82.43	3.77	80.64	1.98
C-28	22.75	21.21	1.54	21.85	0.90
C-29	28.65	27.38	1.27	27.45	1.20
CMAE			2.55		1.63

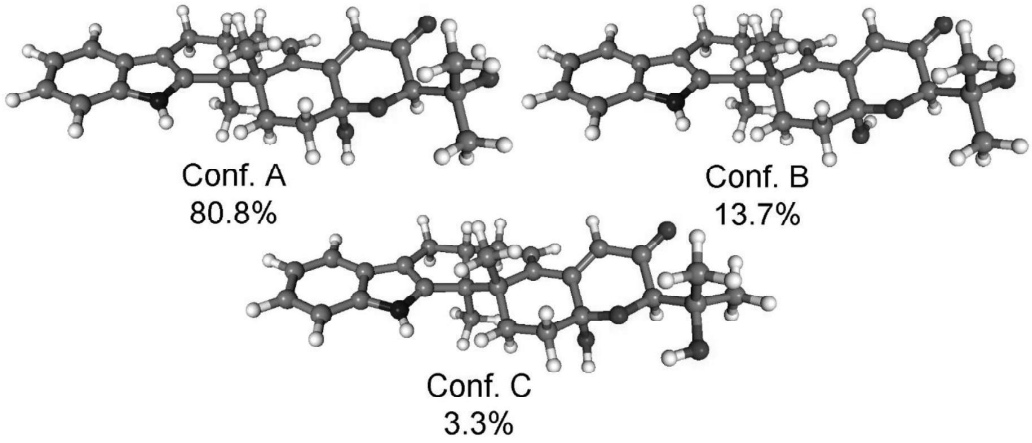

Figure S72. Structure and population of the low-energy CAM-B3LYP/TZVP PCM/MeCN conformers (≥ 1%) of (3*S*,4*S*,7*S*,9*R*,16*S*)-**3**.

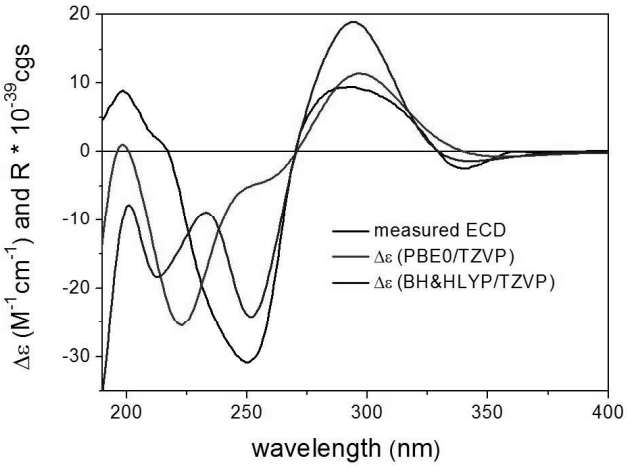

Figure S73. Experimental ECD spectrum of **7** in MeCN compared with the Boltzmann-averaged PBE0/TZVP PCM/MeCN and the BH&HLYP/TZVP PCM/MeCN ECD spectra of (3*S*,4*R*,7*S*,9*R*,13*S*,16*S*)-**7** computed for the low-energy (≥ 1%) CAM-B3LYP/TZVP PCM/MeCN conformers. Bars represent the rotational strength values of conformer A.

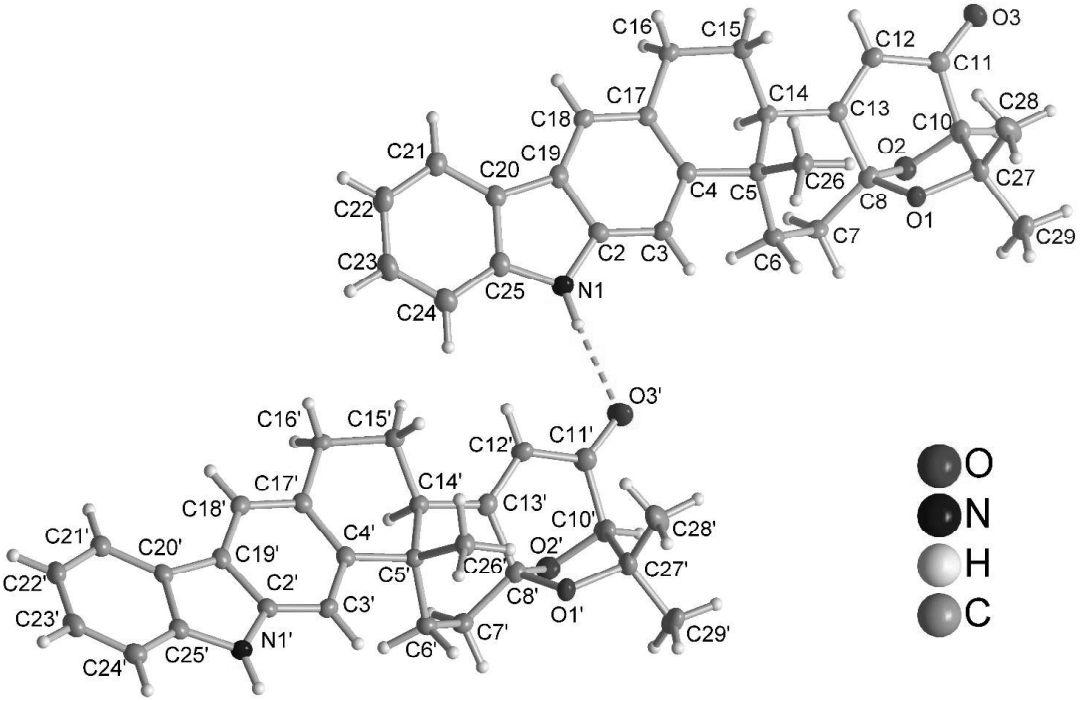

Figure S74. Molecular structures of the two independent molecules in the asymmetric unit of **1**, showing their intermolecular interaction through an N1–H1···O3' bond as dashed orange lines. Hydrogen bond details (Å, °): N1–H1 0.88(2), H1···O3' 2.18(2), N1···O3' 3.057(2), N1–H1···O3' 172(2); not shown N1'–H1' 0.87(2), H1'···O3^{i} 2.23(2), N1'···O3^{i} 3.090(2), N1'–H1'···O3^{i} 170(2); symmetry transformation i = x, y, z-1.

Table S75. Crystal data for compound **1**.

Data set	Cu_TOK_Proksch_AA102_2_0m_a
CCDC number	1862565
Empirical formula	$C_{27}H_{27}NO_3$
M [g mol^{-1}]	413.49
Crystal size [mm^3]	0.3 x 0.3 x 0.3
Temperature [K]	140
θ range [°] (completeness)	3.7 – 65.7 (0.99)
h; k; l range	±13 ; ±8 ; ±28
Crystal system	Monoclinic
Space group	$P2_1$
a [Å]	11.8611(5)
b [Å]	7.1874(3)
c [Å]	24.2244(10)
β [°]	94.496(1)
V [$Å^3$]	2058.79(15)
Z	4
D_{calc} [g cm^{-3}]	1.334
μ (Cu Kα)[mm^{-1}]	0.69
F(000)	880
Max./min. transmission	0.772/ 0.864
Reflections collected	26702
Independent reflect. (R_{int})	7034
Data/restraints/parameters	7034/ 1/ 572
Max./min. Δρ [e $Å^{-3}$] [a]	0.17/ -0.14
R_1/wR_2 [I>2σ(I)]	0.028/ 0.075
Goodness-of-fit on F^2	1.03
Flack parameter [b]	-0.01(7)

[a] Largest difference peak and hole, [b] Absolute structure parameter.

Table S76. Fractional atomic coordinates and isotropic or equivalent isotropic displacement parameters ($Å^2$) for compound **1**.

	x	y	z	U_{iso}*/U_{eq}
O1	0.01172 (10)	0.52536 (18)	0.84088 (5)	0.0212 (3)
O2	0.05671 (10)	0.28180 (18)	0.89714 (5)	0.0235 (3)
O3	0.14205 (11)	0.5885 (2)	1.00498 (5)	0.0293 (3)
N1	0.36876 (13)	0.4473 (2)	0.57614 (6)	0.0243 (3)
H1	0.305 (2)	0.447 (4)	0.5551 (9)	0.037*
C2	0.38243 (14)	0.4808 (3)	0.63254 (7)	0.0205 (4)
C3	0.30175 (14)	0.4841 (3)	0.67120 (7)	0.0206 (4)
H3	0.223634	0.474706	0.659469	0.025*
C4	0.33648 (14)	0.5016 (2)	0.72747 (7)	0.0180 (4)
C5	0.24540 (14)	0.5062 (3)	0.76923 (7)	0.0179 (4)
C6	0.14953 (14)	0.3625 (3)	0.75297 (7)	0.0217 (4)
H6A	0.086741	0.428490	0.731912	0.026*
H6B	0.179312	0.268786	0.727931	0.026*
C7	0.10155 (14)	0.2601 (3)	0.80181 (7)	0.0219 (4)
H7A	0.024928	0.213289	0.789988	0.026*
H7B	0.150024	0.151331	0.811986	0.026*
C8	0.09489 (14)	0.3822 (3)	0.85181 (7)	0.0201 (4)
C10	0.02837 (15)	0.4301 (3)	0.93321 (7)	0.0236 (4)
H10	-0.018983	0.384146	0.962761	0.028*
C11	0.13557 (15)	0.5230 (3)	0.95797 (7)	0.0229 (4)
C12	0.22731 (15)	0.5328 (3)	0.92115 (7)	0.0229 (4)
H12	0.298187	0.585331	0.933785	0.027*
C13	0.21052 (14)	0.4671 (2)	0.86948 (7)	0.0188 (4)
C14	0.29863 (13)	0.4569 (3)	0.82798 (7)	0.0179 (3)
H14	0.321942	0.323376	0.826471	0.021*
C15	0.40592 (14)	0.5668 (3)	0.84483 (7)	0.0197 (4)
H15A	0.435146	0.529938	0.882657	0.024*
H15B	0.387961	0.701289	0.845350	0.024*
C16	0.49650 (14)	0.5315 (3)	0.80463 (7)	0.0191 (4)
H16A	0.553313	0.632448	0.808912	0.023*
H16B	0.535468	0.413340	0.814993	0.023*
C17	0.45269 (14)	0.5206 (2)	0.74440 (7)	0.0174 (3)

C18	0.53153 (14)	0.5216 (2)	0.70479 (7)	0.0182 (4)
H18	0.609546	0.534923	0.716271	0.022*
C19	0.49832 (14)	0.5034 (2)	0.64875 (7)	0.0185 (4)
C20	0.55752 (14)	0.4870 (3)	0.59868 (7)	0.0198 (4)
C21	0.67136 (15)	0.4948 (3)	0.58723 (7)	0.0227 (4)
H21	0.728442	0.521751	0.615829	0.027*
C22	0.69957 (15)	0.4627 (3)	0.53366 (7)	0.0279 (4)
H22	0.776231	0.472202	0.525214	0.033*
C23	0.61596 (16)	0.4162 (3)	0.49176 (7)	0.0287 (4)
H23	0.637419	0.390496	0.455565	0.034*
C24	0.50318 (17)	0.4070 (3)	0.50193 (8)	0.0259 (4)
H24	0.447056	0.374046	0.473480	0.031*
C25	0.47429 (14)	0.4477 (3)	0.55532 (7)	0.0213 (4)
C26	0.19661 (14)	0.7056 (3)	0.76850 (7)	0.0208 (4)
H26A	0.137010	0.713266	0.794237	0.031*
H26B	0.164899	0.735931	0.731013	0.031*
H26C	0.256969	0.793954	0.779804	0.031*
C27	-0.04025 (15)	0.5619 (3)	0.89229 (7)	0.0245 (4)
C28	-0.03063 (19)	0.7674 (3)	0.90579 (8)	0.0342 (5)
H28A	-0.062755	0.791537	0.941157	0.051*
H28B	-0.072085	0.839439	0.876444	0.051*
H28C	0.049177	0.804177	0.908507	0.051*
C29	-0.16262 (15)	0.4977 (4)	0.88487 (8)	0.0341 (5)
H29A	-0.199180	0.519363	0.919202	0.051*
H29B	-0.165032	0.364672	0.876016	0.051*
H29C	-0.202539	0.567749	0.854609	0.051*
O1'	0.01754 (10)	0.48928 (19)	0.33598 (5)	0.0225 (3)
O2'	0.06470 (10)	0.23197 (19)	0.38549 (5)	0.0261 (3)
O3'	0.14797 (11)	0.4909 (2)	0.50334 (5)	0.0350 (4)
N1'	0.37079 (12)	0.6233 (2)	0.07457 (6)	0.0216 (3)
H1'	0.3062 (19)	0.628 (4)	0.0547 (9)	0.032*
C2'	0.38481 (14)	0.5764 (3)	0.13030 (7)	0.0189 (4)
C3'	0.30568 (14)	0.5579 (3)	0.16919 (7)	0.0197 (4)
H3'	0.227188	0.565343	0.158108	0.024*
C4'	0.34213 (14)	0.5282 (2)	0.22488 (7)	0.0178 (4)
C5'	0.25174 (14)	0.5137 (3)	0.26665 (7)	0.0176 (4)

C6'	0.15716 (14)	0.3738 (3)	0.24526 (7)	0.0208 (4)
H6C	0.092790	0.445518	0.227623	0.025*
H6D	0.187042	0.294584	0.216317	0.025*
C7'	0.11261 (14)	0.2464 (3)	0.28994 (7)	0.0215 (4)
H7C	0.037435	0.197266	0.276504	0.026*
H7D	0.164502	0.139361	0.296455	0.026*
C8'	0.10293 (14)	0.3484 (3)	0.34352 (7)	0.0202 (4)
C10'	0.03457 (15)	0.3673 (3)	0.42553 (7)	0.0275 (4)
H10'	-0.013979	0.311017	0.453047	0.033*
C11'	0.14120 (15)	0.4518 (3)	0.45396 (7)	0.0254 (4)
C12'	0.23212 (14)	0.4849 (3)	0.41762 (7)	0.0221 (4)
H12'	0.300816	0.541794	0.431606	0.026*
C13'	0.21706 (14)	0.4340 (2)	0.36448 (7)	0.0190 (4)
C14'	0.30526 (13)	0.4405 (3)	0.32296 (6)	0.0176 (3)
H14'	0.326932	0.308296	0.316449	0.021*
C15'	0.41434 (14)	0.5409 (3)	0.34247 (7)	0.0197 (4)
H15C	0.442326	0.494097	0.379473	0.024*
H15D	0.399512	0.675854	0.345634	0.024*
C16'	0.50390 (14)	0.5085 (3)	0.30144 (7)	0.0183 (4)
H16C	0.565118	0.601088	0.308578	0.022*
H16D	0.537269	0.383480	0.308087	0.022*
C17'	0.45901 (14)	0.5223 (2)	0.24134 (7)	0.0173 (3)
C18'	0.53671 (14)	0.5304 (2)	0.20126 (7)	0.0183 (4)
H18'	0.615171	0.520075	0.212122	0.022*
C19'	0.50145 (14)	0.5533 (2)	0.14556 (7)	0.0177 (4)
C20'	0.55933 (14)	0.5762 (3)	0.09538 (7)	0.0187 (4)
C21'	0.67179 (15)	0.5571 (3)	0.08281 (7)	0.0225 (4)
H21'	0.728362	0.518927	0.110419	0.027*
C22'	0.69938 (15)	0.5948 (3)	0.02934 (7)	0.0259 (4)
H22'	0.775158	0.579727	0.020022	0.031*
C23'	0.61652 (16)	0.6549 (3)	-0.01089 (7)	0.0262 (4)
H23'	0.637717	0.684509	-0.046869	0.031*
C24'	0.50433 (17)	0.6724 (3)	0.00030 (8)	0.0236 (4)
H24'	0.448700	0.714852	-0.027167	0.028*
C25'	0.47583 (14)	0.6254 (3)	0.05331 (7)	0.0202 (4)
C26'	0.20182 (15)	0.7100 (3)	0.27381 (7)	0.0209 (4)

H26D	0.138611	0.702601	0.297464	0.031*
H26E	0.174787	0.759735	0.237492	0.031*
H26F	0.260386	0.792255	0.291031	0.031*
C27'	-0.03258 (15)	0.5134 (3)	0.38839 (7)	0.0275 (4)
C28'	-0.01789 (19)	0.7154 (4)	0.40664 (9)	0.0383 (5)
H28D	-0.048418	0.731978	0.442752	0.057*
H28E	-0.058466	0.796656	0.379343	0.057*
H28F	0.062675	0.747361	0.409561	0.057*
C29'	-0.15653 (16)	0.4597 (4)	0.38012 (8)	0.0407 (6)
H29D	-0.193339	0.484527	0.414198	0.061*
H29E	-0.162835	0.326948	0.371135	0.061*
H29F	-0.193419	0.532822	0.349705	0.061*

Table S77. Atomic displacement parameters (Å^2) for compound **1**.

	U^{11}	U^{22}	U^{33}	U^{12}	U^{13}	U^{23}
O1	0.0185 (6)	0.0286 (7)	0.0169 (6)	0.0021 (5)	0.0030 (5)	0.0004 (5)
O2	0.0239 (6)	0.0255 (7)	0.0217 (6)	-0.0038 (5)	0.0052 (5)	0.0025 (5)
O3	0.0288 (7)	0.0435 (9)	0.0157 (6)	0.0004 (6)	0.0017 (5)	-0.0022 (6)
N1	0.0205 (7)	0.0356 (9)	0.0169 (7)	-0.0001 (7)	0.0008 (6)	0.0008 (7)
C2	0.0224 (8)	0.0211 (9)	0.0178 (8)	0.0008 (8)	0.0014 (6)	-0.0004 (7)
C3	0.0160 (8)	0.0260 (10)	0.0197 (8)	0.0010 (7)	0.0001 (6)	0.0012 (7)
C4	0.0185 (8)	0.0167 (8)	0.0187 (8)	0.0005 (7)	0.0019 (6)	0.0012 (7)
C5	0.0161 (8)	0.0211 (9)	0.0163 (8)	-0.0011 (7)	0.0001 (6)	-0.0014 (7)
C6	0.0207 (8)	0.0249 (9)	0.0196 (8)	-0.0031 (7)	0.0013 (7)	-0.0033 (8)
C7	0.0194 (8)	0.0228 (9)	0.0234 (9)	-0.0054 (7)	0.0012 (7)	-0.0029 (7)
C8	0.0183 (8)	0.0232 (9)	0.0190 (8)	-0.0011 (7)	0.0026 (6)	0.0033 (7)
C10	0.0221 (8)	0.0314 (10)	0.0180 (8)	-0.0004 (8)	0.0053 (7)	0.0015 (8)
C11	0.0240 (9)	0.0279 (10)	0.0165 (8)	0.0023 (7)	-0.0002 (7)	0.0036 (7)
C12	0.0178 (8)	0.0309 (10)	0.0199 (8)	-0.0023 (7)	0.0005 (7)	0.0000 (8)
C13	0.0188 (8)	0.0184 (9)	0.0191 (8)	0.0007 (7)	0.0011 (6)	0.0024 (7)
C14	0.0176 (8)	0.0186 (8)	0.0174 (8)	-0.0005 (7)	0.0009 (6)	0.0004 (7)
C15	0.0189 (8)	0.0237 (10)	0.0163 (8)	-0.0016 (7)	0.0007 (6)	-0.0002 (7)
C16	0.0163 (8)	0.0213 (9)	0.0193 (8)	-0.0014 (7)	-0.0006 (6)	0.0007 (7)
C17	0.0195 (8)	0.0149 (8)	0.0177 (8)	0.0007 (7)	0.0012 (6)	0.0014 (7)
C18	0.0163 (8)	0.0168 (9)	0.0211 (8)	0.0007 (7)	-0.0004 (6)	0.0012 (7)
C19	0.0200 (8)	0.0158 (9)	0.0200 (8)	0.0020 (7)	0.0043 (6)	0.0024 (7)
C20	0.0230 (8)	0.0168 (8)	0.0199 (8)	0.0009 (7)	0.0035 (7)	0.0021 (7)

C21	0.0222 (8)	0.0225 (9)	0.0239 (9)	0.0010 (7)	0.0044 (7)	0.0023 (8)
C22	0.0251 (9)	0.0325 (11)	0.0272 (9)	0.0012 (8)	0.0093 (7)	0.0024 (9)
C23	0.0319 (9)	0.0337 (11)	0.0217 (8)	0.0029 (9)	0.0095 (7)	0.0008 (8)
C24	0.0292 (9)	0.0292 (10)	0.0195 (8)	0.0009 (8)	0.0029 (6)	0.0014 (8)
C25	0.0226 (8)	0.0213 (9)	0.0204 (8)	0.0021 (7)	0.0043 (6)	0.0033 (7)
C26	0.0198 (8)	0.0216 (9)	0.0214 (8)	0.0005 (7)	0.0029 (6)	0.0012 (7)
C27	0.0211 (9)	0.0360 (11)	0.0166 (8)	0.0034 (8)	0.0036 (7)	-0.0022 (8)
C28	0.0406 (11)	0.0373 (12)	0.0237 (9)	0.0118 (10)	-0.0034 (8)	-0.0054 (9)
C29	0.0214 (9)	0.0590 (15)	0.0221 (9)	0.0012 (10)	0.0040 (7)	-0.0007 (9)
O1’	0.0183 (6)	0.0308 (7)	0.0187 (6)	0.0035 (5)	0.0038 (4)	0.0000 (5)
O2’	0.0254 (6)	0.0296 (7)	0.0237 (6)	-0.0062 (6)	0.0045 (5)	0.0036 (6)
O3’	0.0300 (7)	0.0589 (10)	0.0161 (6)	-0.0051 (7)	0.0027 (5)	-0.0008 (6)
N1’	0.0184 (7)	0.0300 (9)	0.0161 (7)	-0.0003 (6)	-0.0004 (5)	0.0006 (6)
C2’	0.0202 (8)	0.0193 (9)	0.0172 (8)	-0.0007 (7)	0.0012 (6)	-0.0023 (7)
C3’	0.0161 (8)	0.0227 (9)	0.0198 (8)	0.0015 (7)	-0.0006 (6)	-0.0007 (7)
C4’	0.0191 (8)	0.0160 (8)	0.0185 (8)	0.0001 (7)	0.0022 (6)	-0.0014 (7)
C5’	0.0166 (8)	0.0191 (9)	0.0166 (8)	0.0001 (7)	-0.0004 (6)	-0.0016 (7)
C6’	0.0195 (8)	0.0248 (9)	0.0179 (8)	-0.0012 (7)	0.0004 (6)	-0.0023 (7)
C7’	0.0185 (8)	0.0222 (9)	0.0237 (9)	-0.0035 (7)	0.0012 (6)	-0.0022 (7)
C8’	0.0191 (8)	0.0224 (9)	0.0196 (8)	-0.0010 (7)	0.0034 (6)	0.0032 (7)
C10’	0.0235 (9)	0.0405 (11)	0.0194 (8)	-0.0057 (9)	0.0065 (7)	0.0008 (8)
C11’	0.0242 (9)	0.0332 (11)	0.0187 (8)	0.0008 (8)	0.0012 (7)	0.0030 (8)
C12’	0.0187 (8)	0.0282	0.0191 (8)	-0.0013	-0.0002	0.0021 (8)

		(10)		(8)	(6)	
C13’	0.0184 (8)	0.0178 (8)	0.0207 (8)	0.0020 (7)	0.0016 (6)	0.0035 (7)
C14’	0.0177 (8)	0.0186 (8)	0.0165 (8)	0.0007 (7)	0.0006 (6)	0.0004 (7)
C15’	0.0188 (8)	0.0234 (9)	0.0169 (8)	-0.0018 (7)	0.0008 (6)	-0.0005 (7)
C16’	0.0167 (8)	0.0197 (9)	0.0180 (8)	-0.0016 (7)	-0.0019 (6)	0.0001 (7)
C17’	0.0200 (8)	0.0146 (8)	0.0175 (8)	0.0001 (7)	0.0019 (6)	-0.0004 (7)
C18’	0.0170 (8)	0.0171 (9)	0.0206 (8)	0.0013 (7)	0.0002 (6)	-0.0009 (7)
C19’	0.0196 (8)	0.0156 (9)	0.0181 (8)	0.0003 (7)	0.0030 (6)	-0.0011 (7)
C20’	0.0217 (8)	0.0163 (8)	0.0184 (8)	-0.0007 (7)	0.0030 (6)	-0.0027 (7)
C21’	0.0211 (8)	0.0247 (10)	0.0218 (8)	-0.0004 (7)	0.0019 (7)	-0.0040 (8)
C22’	0.0228 (9)	0.0317 (11)	0.0242 (9)	-0.0033 (8)	0.0077 (7)	-0.0049 (8)
C23’	0.0307 (9)	0.0292 (10)	0.0196 (8)	-0.0051 (8)	0.0073 (7)	-0.0029 (8)
C24’	0.0267 (8)	0.0251 (9)	0.0189 (8)	-0.0026 (8)	0.0006 (6)	-0.0006 (7)
C25’	0.0215 (8)	0.0198 (9)	0.0195 (8)	-0.0008 (7)	0.0027 (6)	-0.0033 (7)
C26’	0.0208 (8)	0.0210 (9)	0.0212 (8)	0.0015 (7)	0.0037 (6)	0.0009 (7)
C27’	0.0210 (9)	0.0436 (12)	0.0184 (8)	0.0033 (8)	0.0047 (7)	-0.0039 (8)
C28’	0.0383 (11)	0.0467 (14)	0.0293 (10)	0.0143 (10)	-0.0004 (8)	-0.0121 (10)
C29’	0.0203 (9)	0.0778 (18)	0.0246 (9)	-0.0026 (11)	0.0058 (7)	-0.0023 (11)

Table S78. Geometric parameters (Å, º) for compound **1**.

O1—C8	1.436 (2)	O1'—C8'	1.434 (2)
O1—C27	1.456 (2)	O1'—C27'	1.454 (2)
O2—C8	1.418 (2)	O2'—C8'	1.419 (2)
O2—C10	1.435 (2)	O2'—C10'	1.439 (2)
O3—C11	1.229 (2)	O3'—C11'	1.225 (2)
N1—C2	1.384 (2)	N1'—C25'	1.385 (2)
N1—C25	1.386 (2)	N1'—C2'	1.389 (2)
N1—H1	0.88 (2)	N1'—H1'	0.87 (2)
C2—C3	1.391 (2)	C2'—C3'	1.387 (2)
C2—C19	1.409 (2)	C2'—C19'	1.414 (2)
C3—C4	1.398 (2)	C3'—C4'	1.400 (2)
C3—H3	0.9500	C3'—H3'	0.9500
C4—C17	1.414 (2)	C4'—C17'	1.413 (2)
C4—C5	1.537 (2)	C4'—C5'	1.534 (2)
C5—C26	1.545 (2)	C5'—C26'	1.545 (2)
C5—C14	1.552 (2)	C5'—C14'	1.551 (2)
C5—C6	1.563 (2)	C5'—C6'	1.564 (2)
C6—C7	1.540 (2)	C6'—C7'	1.542 (2)
C6—H6A	0.9900	C6'—H6C	0.9900
C6—H6B	0.9900	C6'—H6D	0.9900
C7—C8	1.503 (2)	C7'—C8'	1.503 (2)
C7—H7A	0.9900	C7'—H7C	0.9900
C7—H7B	0.9900	C7'—H7D	0.9900
C8—C13	1.531 (2)	C8'—C13'	1.537 (2)
C10—C11	1.518 (3)	C10'—C11'	1.518 (3)
C10—C27	1.555 (3)	C10'—C27'	1.560 (3)
C10—H10	1.0000	C10'—H10'	1.0000
C11—C12	1.462 (2)	C11'—C12'	1.464 (2)
C12—C13	1.338 (2)	C12'—C13'	1.337 (2)
C12—H12	0.9500	C12'—H12'	0.9500
C13—C14	1.508 (2)	C13'—C14'	1.508 (2)
C14—C15	1.526 (2)	C14'—C15'	1.524 (2)
C14—H14	1.0000	C14'—H14'	1.0000
C15—C16	1.527 (2)	C15'—C16'	1.528 (2)

C15—H15A	0.9900	C15'—H15C	0.9900
C15—H15B	0.9900	C15'—H15D	0.9900
C16—C17	1.512 (2)	C16'—C17'	1.514 (2)
C16—H16A	0.9900	C16'—H16C	0.9900
C16—H16B	0.9900	C16'—H16D	0.9900
C17—C18	1.391 (2)	C17'—C18'	1.391 (2)
C18—C19	1.390 (2)	C18'—C19'	1.391 (2)
C18—H18	0.9500	C18'—H18'	0.9500
C19—C20	1.453 (2)	C19'—C20'	1.452 (2)
C20—C21	1.401 (2)	C20'—C21'	1.398 (2)
C20—C25	1.412 (2)	C20'—C25'	1.409 (2)
C21—C22	1.385 (2)	C21'—C22'	1.387 (2)
C21—H21	0.9500	C21'—H21'	0.9500
C22—C23	1.403 (3)	C22'—C23'	1.397 (3)
C22—H22	0.9500	C22'—H22'	0.9500
C23—C24	1.381 (3)	C23'—C24'	1.384 (3)
C23—H23	0.9500	C23'—H23'	0.9500
C24—C25	1.395 (3)	C24'—C25'	1.395 (3)
C24—H24	0.9500	C24'—H24'	0.9500
C26—H26A	0.9800	C26'—H26D	0.9800
C26—H26B	0.9800	C26'—H26E	0.9800
C26—H26C	0.9800	C26'—H26F	0.9800
C27—C28	1.515 (3)	C27'—C29'	1.518 (3)
C27—C29	1.520 (3)	C27'—C28'	1.523 (3)
C28—H28A	0.9800	C28'—H28D	0.9800
C28—H28B	0.9800	C28'—H28E	0.9800
C28—H28C	0.9800	C28'—H28F	0.9800
C29—H29A	0.9800	C29'—H29D	0.9800
C29—H29B	0.9800	C29'—H29E	0.9800
C29—H29C	0.9800	C29'—H29F	0.9800
C8—O1—C27	107.61 (13)	C8'—O1'—C27'	107.84 (13)
C8—O2—C10	101.43 (13)	C8'—O2'—C10'	101.21 (14)
C2—N1—C25	108.64 (14)	C25'—N1'—C2'	108.75 (14)
C2—N1—H1	126.8 (15)	C25'—N1'—H1'	124.8 (14)
C25—N1—H1	123.5 (14)	C2'—N1'—H1'	125.4 (14)

N1—C2—C3	129.36 (16)	C3'—C2'—N1'	130.36 (16)
N1—C2—C19	109.36 (15)	C3'—C2'—C19'	120.77 (15)
C3—C2—C19	121.20 (15)	N1'—C2'—C19'	108.84 (14)
C2—C3—C4	119.50 (15)	C2'—C3'—C4'	119.64 (15)
C2—C3—H3	120.3	C2'—C3'—H3'	120.2
C4—C3—H3	120.3	C4'—C3'—H3'	120.2
C3—C4—C17	119.83 (15)	C3'—C4'—C17'	119.91 (15)
C3—C4—C5	118.36 (15)	C3'—C4'—C5'	117.82 (15)
C17—C4—C5	121.78 (15)	C17'—C4'—C5'	122.18 (15)
C4—C5—C26	107.12 (14)	C4'—C5'—C26'	107.81 (14)
C4—C5—C14	110.01 (13)	C4'—C5'—C14'	110.13 (13)
C26—C5—C14	110.32 (14)	C26'—C5'—C14'	110.19 (14)
C4—C5—C6	110.77 (14)	C4'—C5'—C6'	110.19 (13)
C26—C5—C6	110.20 (13)	C26'—C5'—C6'	110.67 (14)
C14—C5—C6	108.41 (14)	C14'—C5'—C6'	107.87 (14)
C7—C6—C5	115.31 (14)	C7'—C6'—C5'	115.17 (13)
C7—C6—H6A	108.4	C7'—C6'—H6C	108.5
C5—C6—H6A	108.4	C5'—C6'—H6C	108.5
C7—C6—H6B	108.4	C7'—C6'—H6D	108.5
C5—C6—H6B	108.4	C5'—C6'—H6D	108.5
H6A—C6—H6B	107.5	H6C—C6'—H6D	107.5
C8—C7—C6	112.70 (15)	C8'—C7'—C6'	111.70 (15)
C8—C7—H7A	109.1	C8'—C7'—H7C	109.3
C6—C7—H7A	109.1	C6'—C7'—H7C	109.3
C8—C7—H7B	109.1	C8'—C7'—H7D	109.3
C6—C7—H7B	109.1	C6'—C7'—H7D	109.3
H7A—C7—H7B	107.8	H7C—C7'—H7D	107.9
O2—C8—O1	104.54 (13)	O2'—C8'—O1'	104.21 (13)
O2—C8—C7	111.56 (15)	O2'—C8'—C7'	112.41 (15)
O1—C8—C7	110.41 (14)	O1'—C8'—C7'	109.62 (14)
O2—C8—C13	108.65 (13)	O2'—C8'—C13'	108.80 (13)
O1—C8—C13	110.67 (15)	O1'—C8'—C13'	110.77 (14)
C7—C8—C13	110.84 (14)	C7'—C8'—C13'	110.85 (14)
O2—C10—C11	109.80 (14)	O2'—C10'—C11'	109.51 (15)
O2—C10—C27	101.57 (13)	O2'—C10'—C27'	102.06 (14)
C11—C10—C27	111.36 (16)	C11'—C10'—	111.23 (17)

		C27’	
O2—C10—H10	111.2	O2’—C10’—H10’	111.2
C11—C10—H10	111.2	C11’—C10’—H10’	111.2
C27—C10—H10	111.2	C27’—C10’—H10’	111.2
O3—C11—C12	123.47 (17)	O3’—C11’—C12’	123.68 (17)
O3—C11—C10	121.63 (16)	O3’—C11’—C10’	121.54 (16)
C12—C11—C10	114.87 (15)	C12’—C11’—C10’	114.77 (15)
C13—C12—C11	119.37 (16)	C13’—C12’—C11’	119.03 (16)
C13—C12—H12	120.3	C13’—C12’—H12’	120.5
C11—C12—H12	120.3	C11’—C12’—H12’	120.5
C12—C13—C14	125.51 (15)	C12’—C13’—C14’	125.93 (16)
C12—C13—C8	117.82 (15)	C12’—C13’—C8’	118.40 (15)
C14—C13—C8	116.52 (14)	C14’—C13’—C8’	115.54 (14)
C13—C14—C15	113.79 (14)	C13’—C14’—C15’	115.10 (14)
C13—C14—C5	110.29 (13)	C13’—C14’—C5’	109.85 (13)
C15—C14—C5	113.45 (14)	C15’—C14’—C5’	113.03 (14)
C13—C14—H14	106.2	C13’—C14’—H14’	106.0
C15—C14—H14	106.2	C15’—C14’—H14’	106.0
C5—C14—H14	106.2	C5’—C14’—H14’	106.0
C14—C15—C16	110.91 (14)	C14’—C15’—C16’	110.04 (14)
C14—C15—H15A	109.5	C14’—C15’—H15C	109.7
C16—C15—H15A	109.5	C16’—C15’—H15C	109.7
C14—C15—H15B	109.5	C14’—C15’—H15D	109.7
C16—C15—H15B	109.5	C16’—C15’—H15D	109.7
H15A—C15—H15B	108.0	H15C—C15’—H15D	108.2

C17—C16—C15	114.74 (14)	C17'—C16'—C15'	113.92 (14)
C17—C16—H16A	108.6	C17'—C16'—H16C	108.8
C15—C16—H16A	108.6	C15'—C16'—H16C	108.8
C17—C16—H16B	108.6	C17'—C16'—H16D	108.8
C15—C16—H16B	108.6	C15'—C16'—H16D	108.8
H16A—C16—H16B	107.6	H16C—C16'—H16D	107.7
C18—C17—C4	119.55 (15)	C18'—C17'—C4'	119.39 (15)
C18—C17—C16	117.81 (15)	C18'—C17'—C16'	118.14 (15)
C4—C17—C16	122.58 (15)	C4'—C17'—C16'	122.47 (14)
C19—C18—C17	121.25 (15)	C19'—C18'—C17'	121.11 (15)
C19—C18—H18	119.4	C19'—C18'—H18'	119.4
C17—C18—H18	119.4	C17'—C18'—H18'	119.4
C18—C19—C2	118.61 (15)	C18'—C19'—C2'	118.77 (15)
C18—C19—C20	134.78 (16)	C18'—C19'—C20'	134.43 (16)
C2—C19—C20	106.42 (15)	C2'—C19'—C20'	106.56 (14)
C21—C20—C25	119.28 (16)	C21'—C20'—C25'	119.71 (16)
C21—C20—C19	134.31 (16)	C21'—C20'—C19'	133.87 (16)
C25—C20—C19	106.35 (14)	C25'—C20'—C19'	106.41 (15)
C22—C21—C20	119.11 (17)	C22'—C21'—C20'	118.88 (17)
C22—C21—H21	120.4	C22'—C21'—H21'	120.6
C20—C21—H21	120.4	C20'—C21'—H21'	120.6
C21—C22—C23	120.59 (17)	C21'—C22'—C23'	120.48 (16)
C21—C22—H22	119.7	C21'—C22'—	119.8

		H22’	
C23—C22—H22	119.7	C23’—C22’—H22’	119.8
C24—C23—C22	121.47 (17)	C24’—C23’—C22’	121.72 (17)
C24—C23—H23	119.3	C24’—C23’—H23’	119.1
C22—C23—H23	119.3	C22’—C23’—H23’	119.1
C23—C24—C25	117.87 (18)	C23’—C24’—C25’	117.67 (18)
C23—C24—H24	121.1	C23’—C24’—H24’	121.2
C25—C24—H24	121.1	C25’—C24’—H24’	121.2
N1—C25—C24	129.17 (17)	N1’—C25’—C24’	129.42 (17)
N1—C25—C20	109.18 (15)	N1’—C25’—C20’	109.27 (15)
C24—C25—C20	121.55 (16)	C24’—C25’—C20’	121.28 (16)
C5—C26—H26A	109.5	C5’—C26’—H26D	109.5
C5—C26—H26B	109.5	C5’—C26’—H26E	109.5
H26A—C26—H26B	109.5	H26D—C26’—H26E	109.5
C5—C26—H26C	109.5	C5’—C26’—H26F	109.5
H26A—C26—H26C	109.5	H26D—C26’—H26F	109.5
H26B—C26—H26C	109.5	H26E—C26’—H26F	109.5
O1—C27—C28	109.32 (16)	O1’—C27’—C29’	108.21 (15)
O1—C27—C29	107.95 (14)	O1’—C27’—C28’	108.78 (17)
C28—C27—C29	112.12 (18)	C29’—C27’—C28’	111.62 (18)
O1—C27—C10	101.52 (13)	O1’—C27’—C10’	101.42 (14)
C28—C27—C10	115.46 (16)	C29’—C27’—C10’	110.49 (18)
C29—C27—C10	109.73 (17)	C28’—C27’—C10’	115.61 (16)
C27—C28—H28A	109.5	C27’—C28’—H28D	109.5
C27—C28—H28B	109.5	C27’—C28’—	109.5

		H28E	
H28A—C28—H28B	109.5	H28D—C28'—H28E	109.5
C27—C28—H28C	109.5	C27'—C28'—H28F	109.5
H28A—C28—H28C	109.5	H28D—C28'—H28F	109.5
H28B—C28—H28C	109.5	H28E—C28'—H28F	109.5
C27—C29—H29A	109.5	C27'—C29'—H29D	109.5
C27—C29—H29B	109.5	C27'—C29'—H29E	109.5
H29A—C29—H29B	109.5	H29D—C29'—H29E	109.5
C27—C29—H29C	109.5	C27'—C29'—H29F	109.5
H29A—C29—H29C	109.5	H29D—C29'—H29F	109.5
H29B—C29—H29C	109.5	H29E—C29'—H29F	109.5

Table S79. Hydrogen-bond geometry (Å, º) for compound **1**.

D—H···A	D—H	H···A	D···A	D—H···A
N1′—H1′···O3^{i}	0.87 (2)	2.23 (2)	3.090 (2)	170 (2)
N1—H1···O3′	0.88 (2)	2.18 (2)	3.057 (2)	172 (2)
C28′—H28D···O3′^{ii}	0.98	2.61	3.404 (2)	138

Symmetry codes: (i) x, y, z-1; (ii) -x, y+1/2, -z+1.

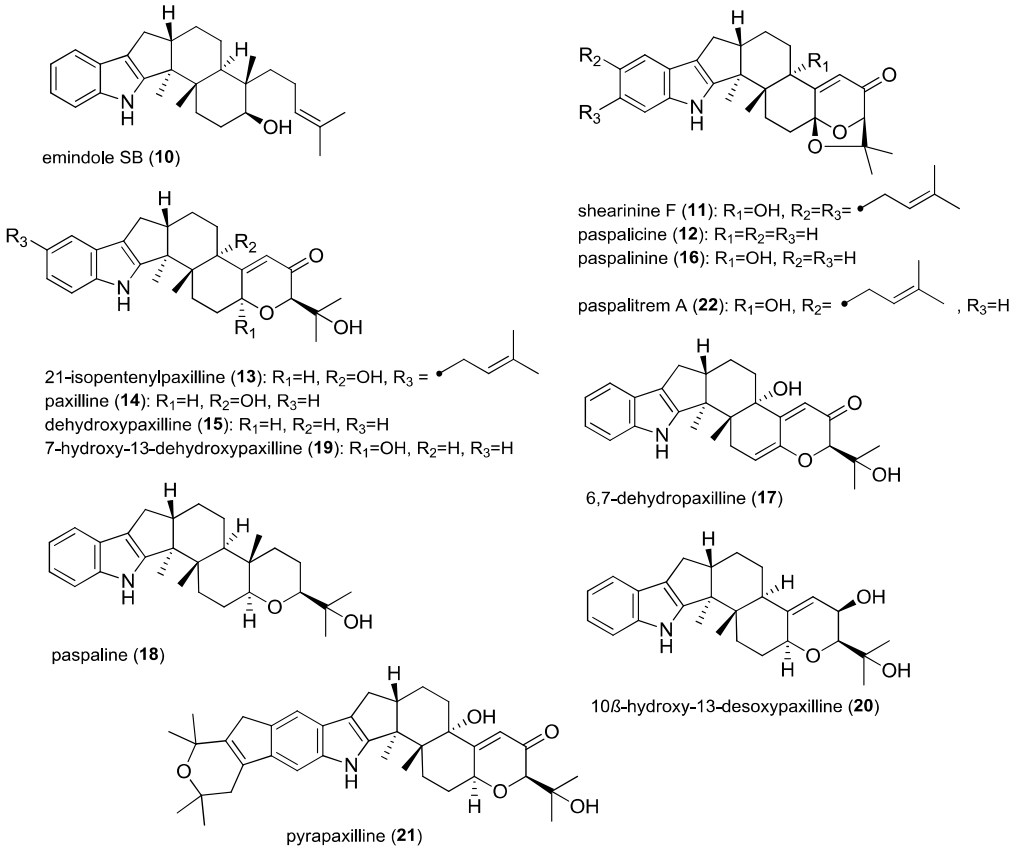

Figure S80. Structures of known compounds isolated from *Penicillium* sp.

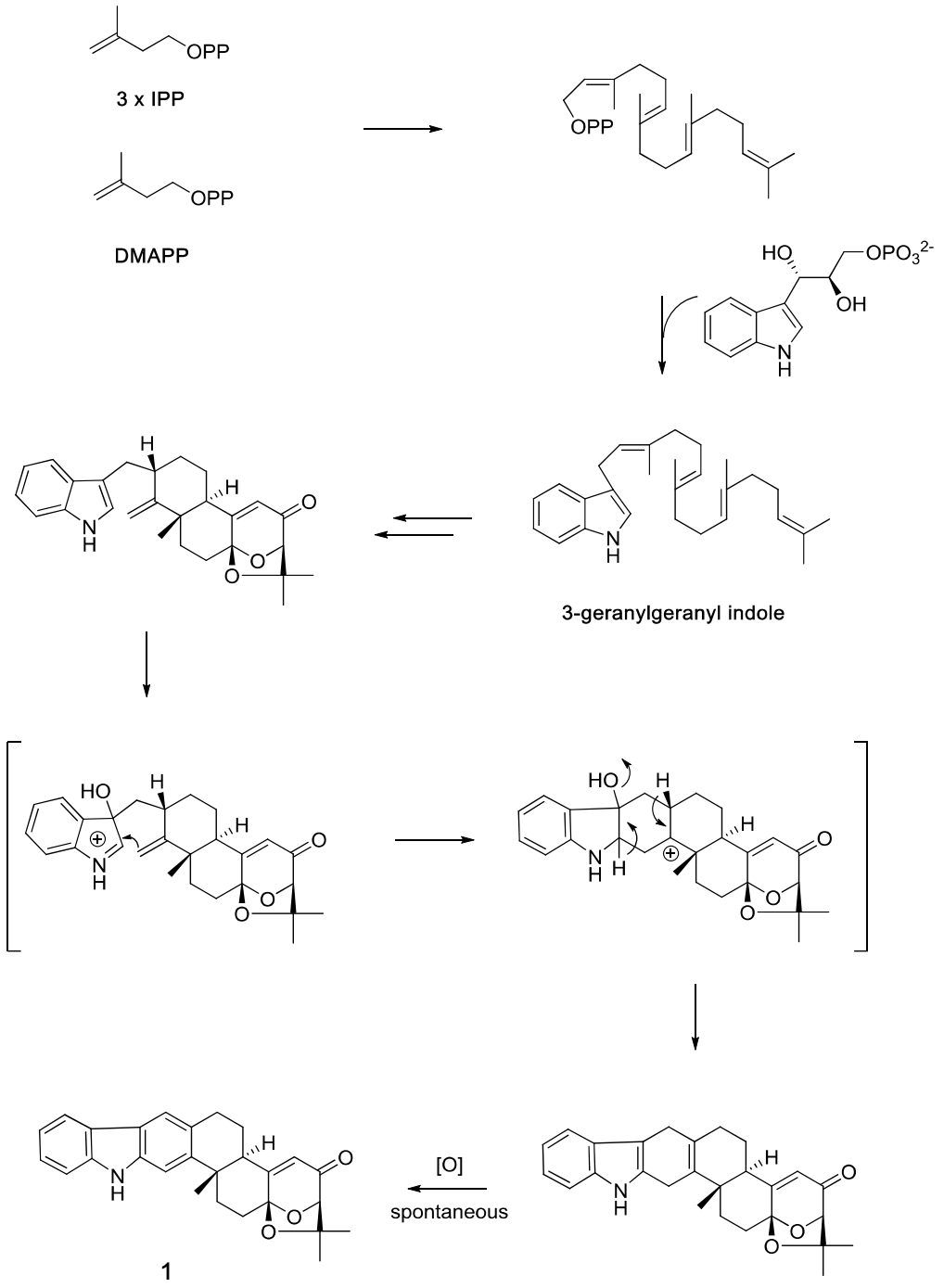

Figure S81. Proposed biosynthesis of the compound **1**.

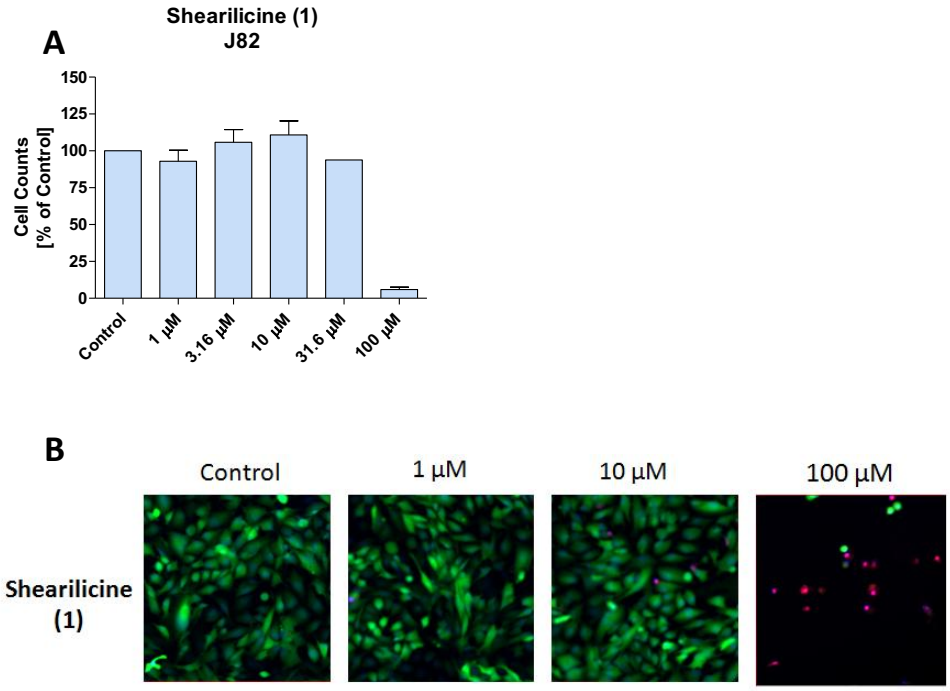

Figure S82. Cell viability assay of **1** in urothelial bladder cancer cell line J82.
(A) Percentage of control cell counts of J82 after 72 h treatment with **1** using High Content Analysis-based fluorescent live/dead assay. (B) Staining of live (calcein-AM, green) and dead (PI, red) J82 cells after 72 h treatment with different concentrations of **1**. Data shown in A are mean +/- SEM from 2 independent experiments each with 3 replicates.

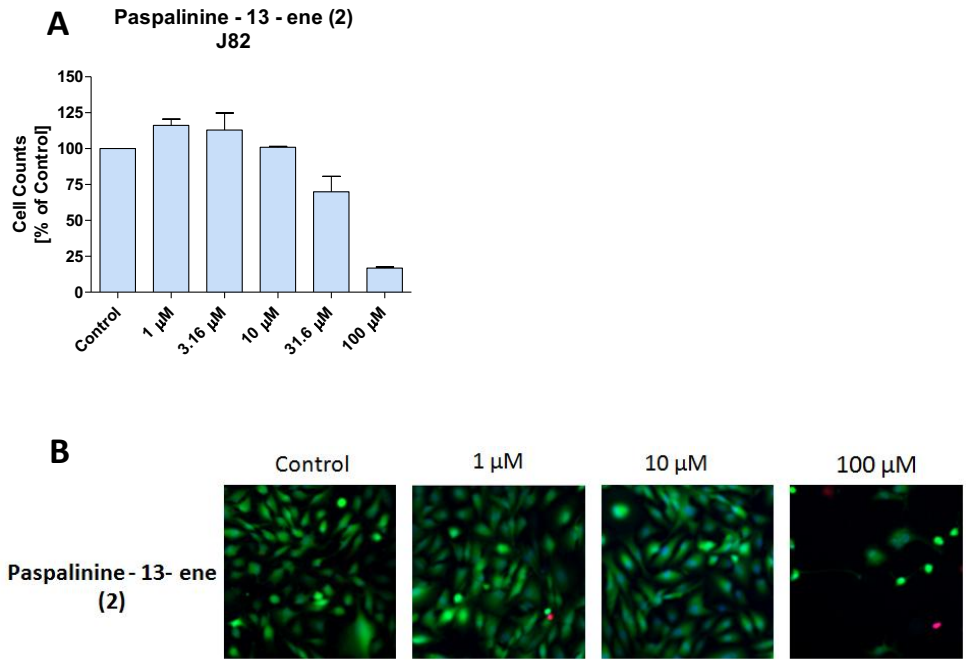

Figure S83. Cell viability assay of **2** in urothelial bladder cancer cell line J82.

(A) Percentage of control cell counts of J82 after 72 h treatment with **2** using High Content Analysis-based fluorescent live/dead assay. (B) Staining of live (calcein-AM, green) and dead (PI, red) J82 cells after 72 h treatment with different concentrations of **2**. Data shown in A are mean +/- SEM from 2 independent experiments each with 3 replicates.

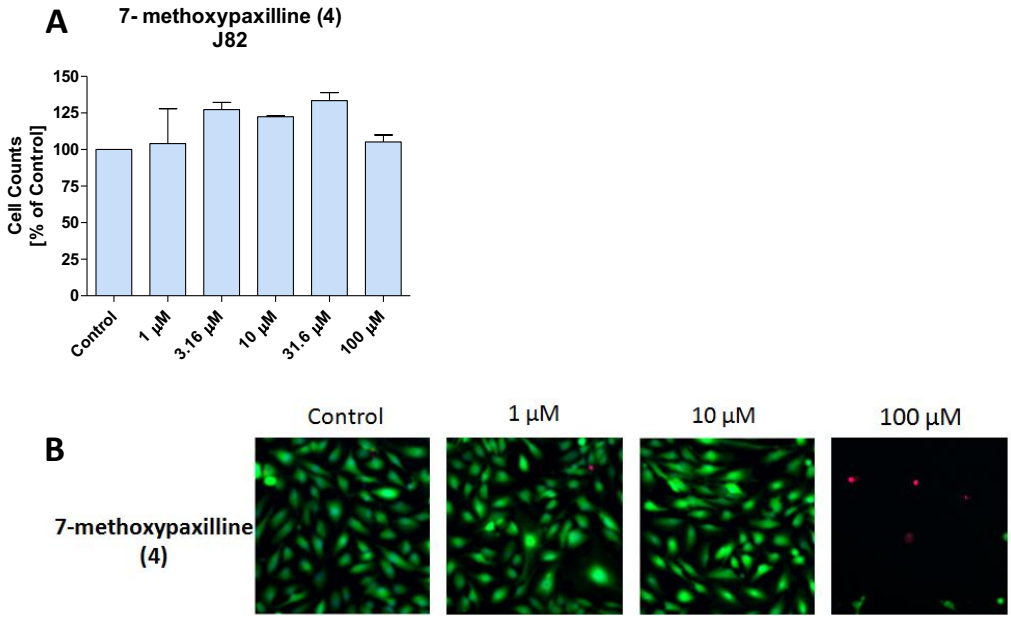

Figure S84. Cell viability assay of **4** in urothelial bladder cancer cell line J82.
(A) Percentage of control cell counts of J82 after 72 h treatment with **4** using High Content Analysis-based fluorescent live/dead assay. (B) Staining of live (calcein-AM, green) and dead (PI, red) J82 cells after 72 h treatment with different concentrations of **4**. Data shown in A and B are mean +/- SEM from 2 independent experiments each with 3 replicates.

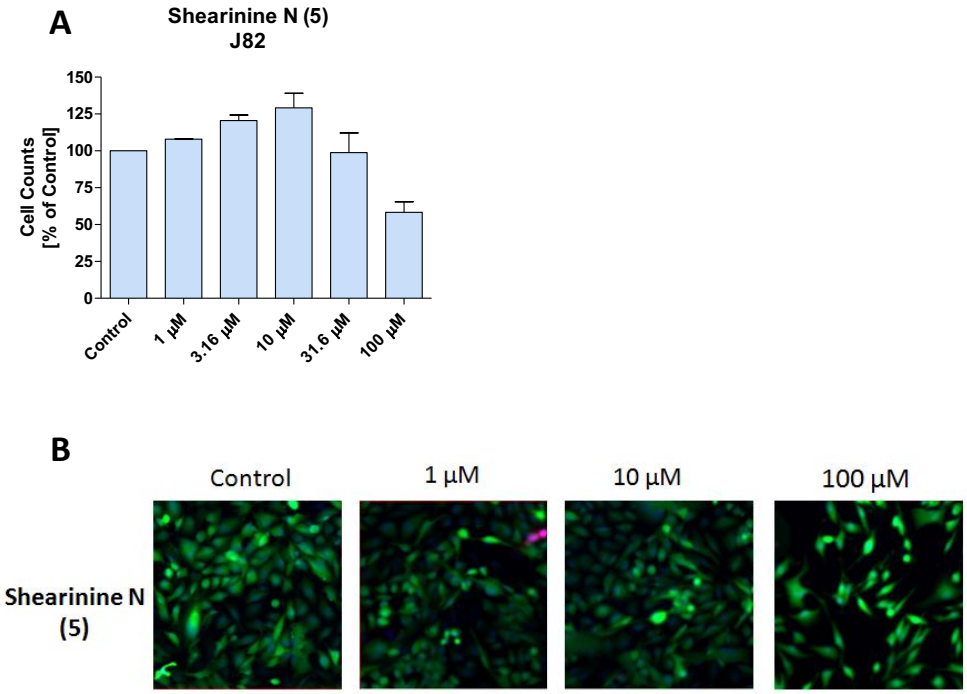

Figure S85. Cell viability assay of **5** in urothelial bladder cancer cell line J82.
(A) Percentage of control cell counts of J82 after 72 h treatment with **5** using High Content Analysis-based fluorescent live/dead assay. (B) Staining of live (calcein-AM, green) and dead (PI, red) J82 cells after 72 h treatment with different concentrations of **5**. Data shown in A are mean +/- SEM from 2 independent experiments each with 3 replicates.

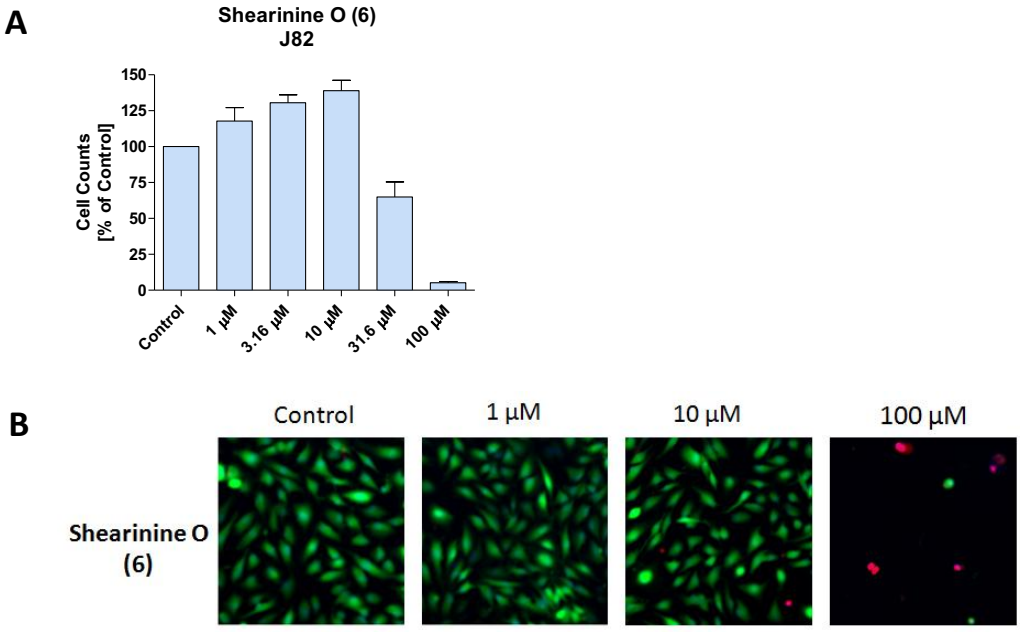

Figure S86. Cell viability assay of **6** in urothelial bladder cancer cell line J82. Percentage of control cell counts of J82 after 72 h treatment with **6** using High Content Analysis-based fluorescent live/dead assay. Staining of live (calcein-AM, green) and dead (PI, red) J82 cells after 72 h treatment with different concentrations of **6**. Data shown in A are mean +/- SEM from 2 independent experiments each with 3 replicates.

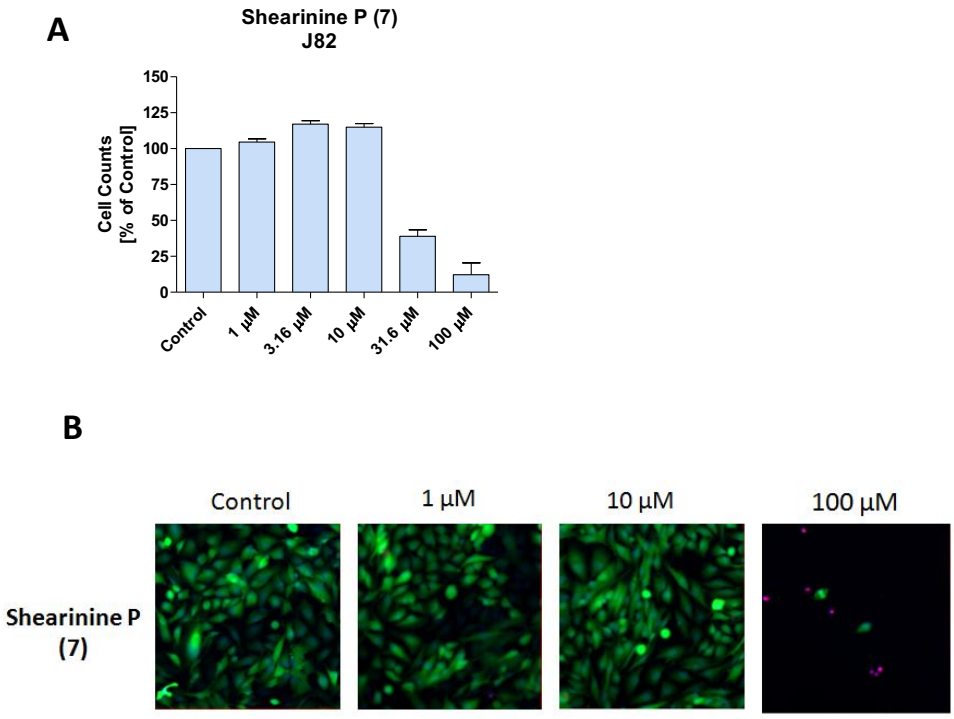

Figure S87. Cell viability assay of **7** in urothelial bladder cancer cell line J82. Percentage of control cell counts of J82 after 72 h treatment with **7** using High Content Analysis-based fluorescent live/dead assay. Staining of live (calcein-AM, green) and dead (PI, red) J82 cells after 72 h treatment with different concentrations of **7**. Data shown in A are mean +/- SEM from 2 independent experiments each with 3 replicates.

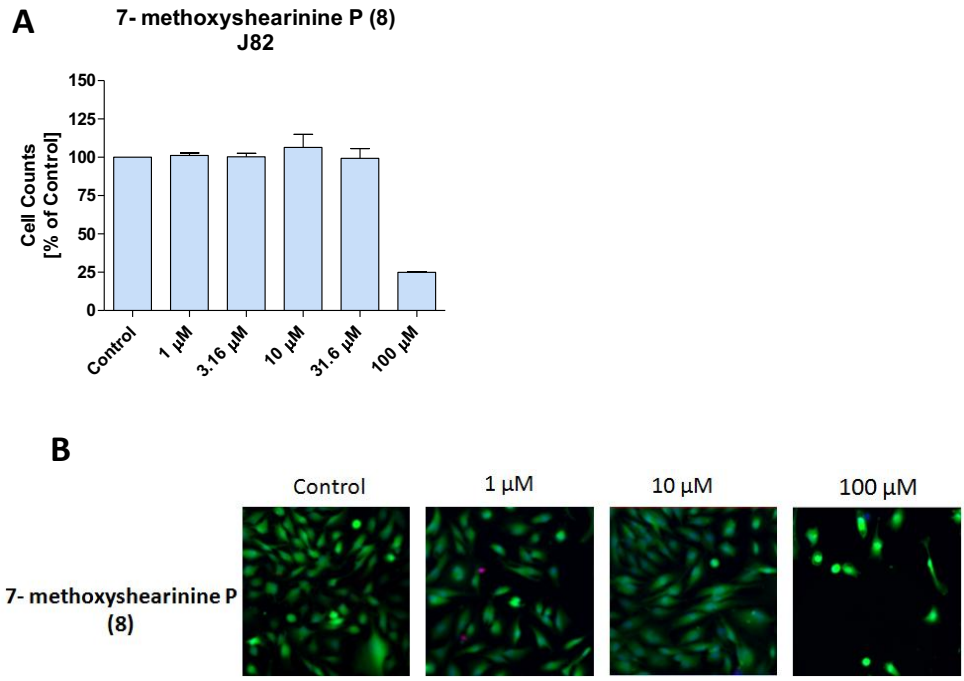

Figure S88. Cell viability assay of **8** in urothelial bladder cancer cell line J82.
(A) Percentage of control cell counts of J82 after 72 h treatment with **8** using High Content Analysis-based fluorescent live/dead assay. (B) Staining of live (calcein-AM, green) and dead (PI, red) J82 cells after 72 h treatment with different concentrations of **8**. Data shown in A are mean +/- SEM from 2 independent experiments each with 3 replicates.

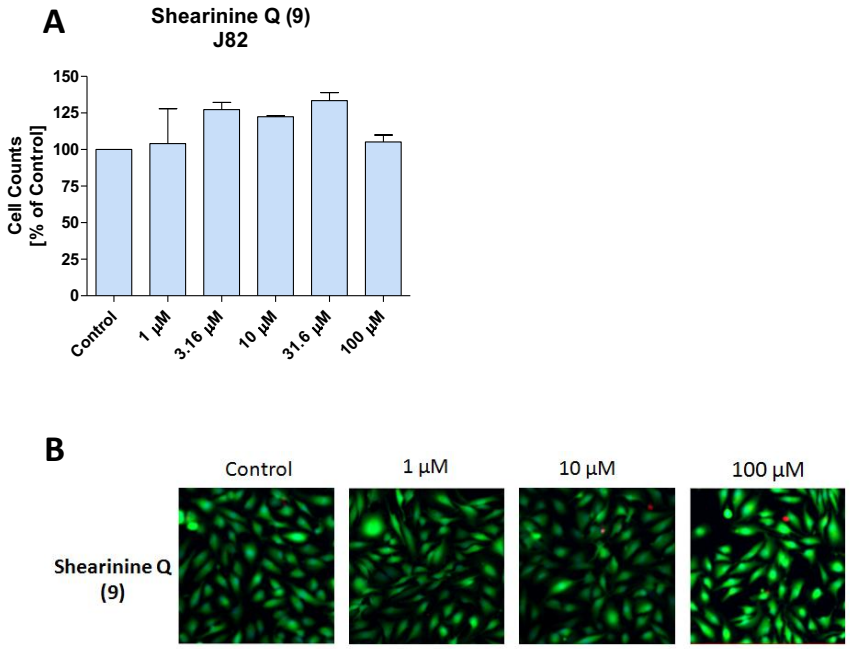

Figure S89. Cell viability assay of **9** in urothelial bladder cancer cell line J82.
(A) Percentage of control cell counts of J82 after 72 h treatment with **9** using High Content Analysis-based fluorescent live/dead assay. (B) Staining of live (calcein-AM, green) and dead (PI, red) J82 cells after 72 h treatment with different concentrations of **9**. Data shown in A are mean +/- SEM from 2 independent experiments each with 3 replicates.

4 Discussion and Conclusion

Despite the remarkable advances in improving prognosis and increasing survival rate of patients with bladder cancer in the past decades, tumor progression and recurrence due to acquired resistance against platinum-based chemotherapy remain a challenge for the management of this malignancy. Consequently, search for agents that could sensitize cisplatin-resistant bladder carcinomas or novel treatment strategies are needed for cisplatin-ineligible bladder cancer patients. This thesis deals with 2 different approaches to overcome chemoresistance in bladder cancer. First, DNMTi and HDACi were used as epigenetic modifiers to improve cisplatin sensitivity or as novel treatment combination in case of platinum-resistant cancers. Second, novel natural compounds were tested for their activity in sensitive and chemoresistant bladder cancers and a selected compound was studied for its mechanism of action in depth. To mimic chemoresistant bladder cancer in an *in vitro* model, a cisplatin resistant bladder cancer cell line was established based on protocols mimicking the clinical use of cisplatin as described previously [73]. Thus, the study was conducted using three urothelial bladder cancer cell lines: J82, the 6-fold more resistant cell line J82CisR, and RT-112.

4.1 Effects of Epigenetic Modulators on Cisplatin-Resistant Cancer Cells

Due to the exciting development of technologies on genome-wide analyses, different epigenetic patterns between normal and cancer tissues have been revealed in many malignancies including bladder cancer [77]. Increased promotor CpG island methylation levels in the tissues from bladder cancer patients were reported in a study analyzing 57 tissue samples from normal urothelial tissue and bladder cancer patients [78]. In addition, higher expression levels of HDACs have been shown in bladder cancer tissues compared to normal urothelial tissue [79]. Therefore, targeting epigenetic abnormalities such as increased CpG island methylation or condensed chromatin structure because of increased HDAC expression is a highly promising therapeutic approach for treating bladder cancer with DNMT- and / or HDAC-inhibitors. It is widely accepted that drug combinations are more effective to treat cancer than

monotherapy [80]. In this study, the DNMTi decitabine and HDACi entinostat, a class I selective HDACi) were tested alone and in combination with cisplatin to investigate an effect on chemosensitivity against cisplatin. As the data summarized in **Table 1** show, 48 h preincubation with decitabine or entinostat failed to reverse cisplatin resistance of J82CisR cells. A significantly increased cytotoxicity of cisplatin was only observed in RT-112 but not in J82 cells upon pretreatment with entinostat (shift factor 2.8). The resistance factor between J82 and J82CisR is 6, whereas the partial reversal of cisplatin resistance gave a shift factor of only 1.5 (**Table1**). In contrast to these results, another study of our group has identified novel alkoxyamide-based HDAC inhibitors (**Figure 12b**) that can completely re-sensitize the cisplatin-resistant tongue cancer cell line Cal27CisR against cisplatin (7 to 12-fold decreased IC_{50} of cisplatin upon combination with novel HDAC inhibitors) [61]. The enhanced cytotoxic effect of cisplatin by pretreatment with the novel HDACi was achieved by activation of caspase 3 and 7 as shown in **Figure 12** [61].

Table1 Summary of the IC_{50} and shift factor of decitabine and entinostat combined with cisplatin in bladder cancer cell lines (** $p \leq 0.01$).

	Cisplatin	+Decitabine		+Entinostat	
		IC_{50} [µM]	Shift Factor	IC_{50} [µM]	Shift Factor
J82	4.22	3.0	1.4	3.56	1.2
J82 CisR	16.9	9.62	1.7	11.5	1.5
RT-112	6.33	6.18	1.0	2.24	2.8 **

Since neither the DNMT inhibitor decitabine nor the HDAC inhibitor entinostat was able to reverse cisplatin resistance in J82CisR, other combination strategies were considered and evaluated in the three bladder cancer cell lines. DNA methylation accompanies histone deacetylation to maintain a tightly compacted state of chromatin which is associated with transcriptional repression [81]. This knowledge is the molecular basis for the drug combination of a DNMT inhibitor and HDAC inhibitor. In our study, a strong synergistic cytotoxic effect was observed for the combination treatment of decitabine and entinostat in all three cell lines. The combination treatment caused substantial apoptosis induction via caspase 3 and 7 activation. Altered cell cycle distribution in J82 and RT-112 cell lines was observed when the two agents were combined. Furthermore, class IIa and class IIb selective HDAC inhibitors were

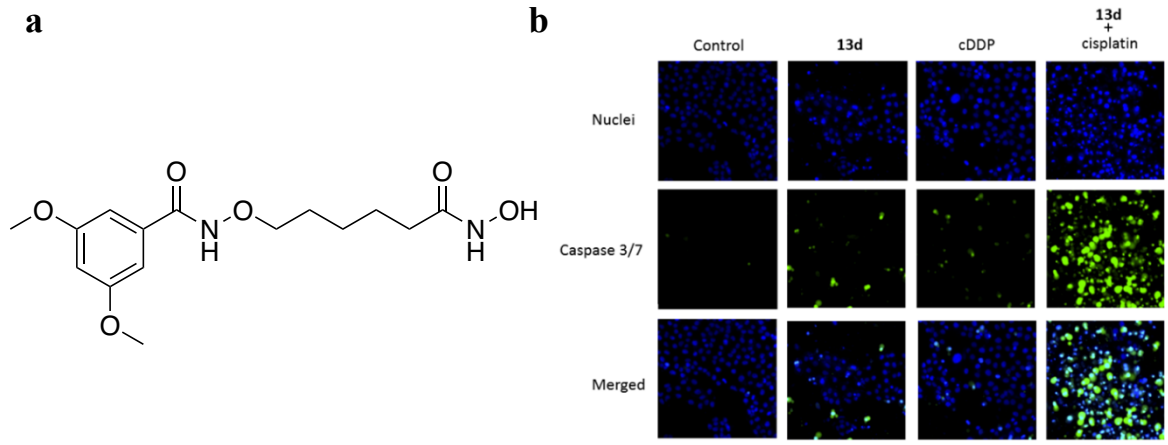

Figure 12. A Novel alkoxyamide-based HDAC inhibitor enhanced cytotoxicity of cisplatin and completely reversed chemoresistance. **a.** Structure of alkoxyamide-based HDAC inhibitor 13d. **b.** Synergistic enhancement of caspase 3 and 7 activation by the combination treatment of HDAC inhibitor 13d and cisplatin in Cal27CisR cell line.

also tested in combination with decitabine. In contrast to the results of entinostat, neither TMP269 (a class IIa selective HDAC inhibitor) nor tubastatin A (a class IIb selective HDAC inhibitor) act synergistically with decitabine to induce cytotoxicity (**Table2**), confirming the important role of class I HDACs in connection with DNMTs in impeding compound-induced cytotoxicity and apoptosis. These results are consistent with findings that HDAC1 and HDAC2 are core components of the NuRD (Mi-2/nucleosome remodeling and deacetylase) complex which cooperates with DNMTs to maintain a silencing of tumor suppressor genes [82].

Table2 Summary of the IC_{50} and shift factor of TMP269 and tubastatin A combined with decitabine in bladder cancer cell lines

	TMP269	**+Decitabine**		**Tubastatin A**	**+Decitabine**	
	IC_{50} [µM]	IC_{50} [µM]	Shift Factor	IC_{50} [µM]	IC_{50} [µM]	Shift Factor
J82	40.8	39.5	1.0	25.1	23.9	1.1
J82 CisR	20.8	24.6	0.8	9.95	7.96	1.3
RT-112	34.0	39.6	0.9	17.9	11.2	1.6

A previous study of us investigated novel HDAC inhibitors in bladder cancer cell lines and strengthened the finding that targeting class I HDACs is essential for an anti-cancer effect of HDAC inhibitors [83]. A major contribution of class IIa HDAC inhibition for an anti-cancer effect could be ruled out by using the class IIa selective inhibitor TMP269 and by establishing an HDAC4-overexpressing cell line. In contrast to class I HDACs, HDAC4 overexpression – and not inhibition – might be beneficial for anticancer effects in bladder cancer cells.

Moreover, our study identified that forkhead box class O1 (FoxO1) plays an essential role

in regulating the death of bladder cancer cells in response to the treatment with decitabine and entinostat. FoxO1 is a transcription factor regulating multiple genes involved in many cellular processes [84]. FoxO1 is phosphorylated by Akt (also named protein kinase B, PKB) and by that negatively regulated resulting in its translocation from the nucleus to the cytoplasm (**Figure 13**). Inactivation of FoxO1 by phosphorylation

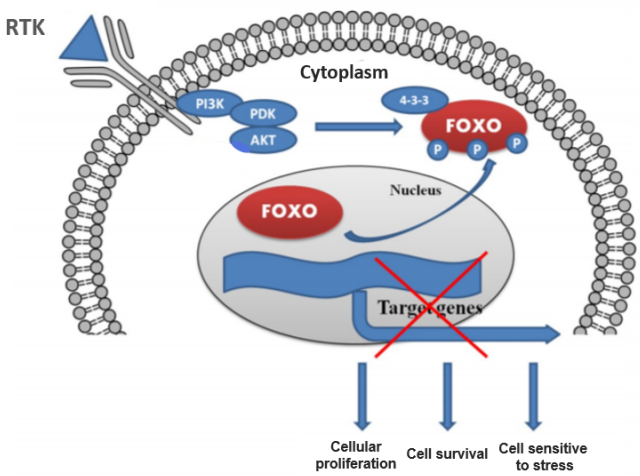

Figure 13. FoxO signaling pathway (modified from **ref. [85]**)

blocks the transcription of genes controlling apoptosis, cell cycle progression, and metabolism [85]. Our gene expression data showed a significant upregulation of FoxO1 in all three bladder cancer cell lines after treatment with decitabine and entinostat and in particular with their combination. Notably, downstream targets of FoxO1, Bim and p21, were subsequently upregulated in the three cell lines even though to a different extent. RNA and protein expression data were in good accordance for FoxO1 and its downstream genes Bim and p21. The linkage between FoxO1 upregulation and upregulation of Bim and p21 was shown by the effect of the FoxO1 inhibitor AS1842856: AS1842856 prevented the upregulation of Bim and / or p21. Interestingly, the mechanisms by which decitabine plus entinostat showed increased cytotoxicity and apoptosis were distinct in J82 and J82CisR cell lines. Since Akt is the upstream regulator of FoxO1, it was expected that increased FoxO1 would go in parallel with decreased p-Akt (phosphorylated Akt). Surprisingly, less p-Akt was only observed in J82CisR but not in J82 and not in RT-112 cells, indicating a p-Akt independent activation of FoxO1 in J82 and RT-112. The different mechanisms in the upregulation of FoxO1 are further underlined by the analysis of the expression levels of p-FoxO1. FoxO1 is phosphorylated by p-Akt leading to the formation of inactive p-FoxO1 (**FoxO signaling pathway modified from ref. [85]**). Since decreased

expression of p-Akt occurred in J82CisR under combined decitabine/entinostat treatment, p-FoxO1 was reduced correspondingly. In J82 and RT-112 cell lines, conversely, reduced p-Akt and reduced p-FoxO1 were not observed. In addition, J82CisR showed reduced expression of survivin under treatment with decitabine plus entinostat. Taken together, expression analysis of genes from the FoxO1 pathway after decitabine plus entinostat treatment suggests distinct mechanisms of cytotoxicity and apoptosis induction in different bladder cancer cells involving FoxO1 as master switch for increased Bim, increased p21, and reduced survivin.

Figure 14 summarizes part 1 of this thesis dealing with epigenetic modulation of bladder cancer cell lines including the cisplatin-resistant bladder cancer model J82CisR showing a resistance factor of 6. These in vitro cellular models were used for the investigation of the epigenetic agents decitabine and entinostat. The results of apoptosis assay, cell cycle analysis, and drug combination study revealed that decitabine and entinostat act synergistically in reducing the cell viability of urothelial bladder cancer cells including the resistant cells. Mechanistically, gene expression analysis suggested that the cytotoxic effect of the epigenetic treatment is associated with changes in expression of FoxO1, Bim, p21, and survivin.

Taken together, part 1 of the thesis demonstrates that epigenetic modulation with the approved DNMTi decitabine and the phase 3 HDACi entinostat has the potential to serve as novel treatment strategies in bladder cancer, particularly in cisplatin-resistant bladder cancers.

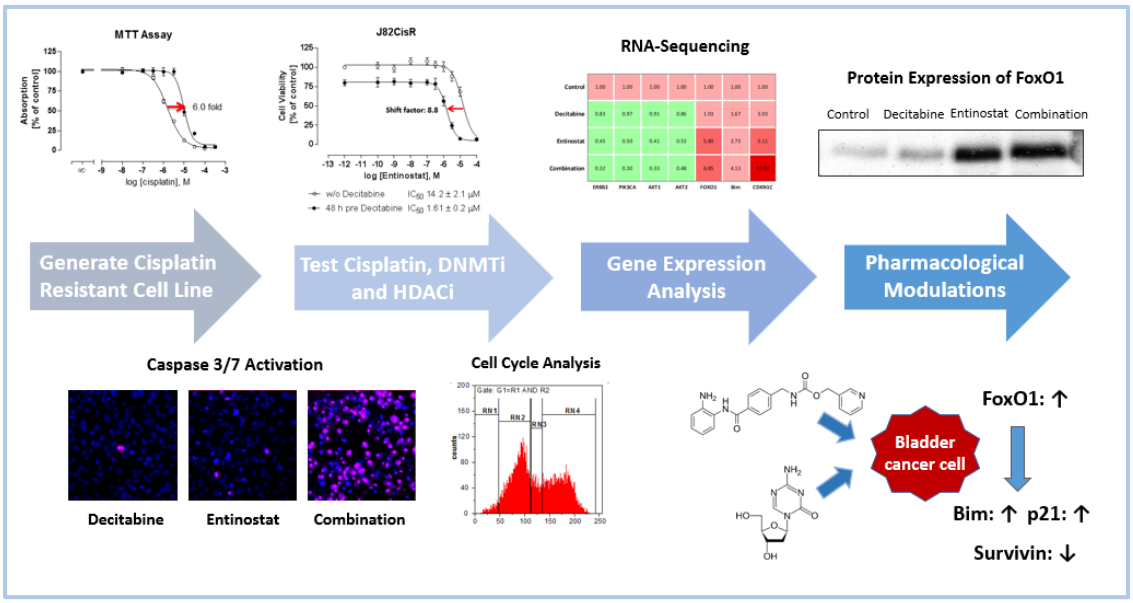

Figure 14. Workflow of the investigation of epigenetic agents in bladder cancer cells

4.2 Effects of Natural Products on Cisplatin-Resistant Cancer Cells

Nature-derived compounds are a rich source for developing anticancer agents as shown by approved drugs of paclitaxel and eribulin [63, 70]. In the group of Professor Proksch, University of Duesseldorf, a tetrahydroxanthone dimer named phomoxanthone (PXA) has been previously isolated from the endophytic fungus *Phomopsis longicolla* A [71]. PXA has been previously investigated and exhibits potent cytotoxic activity, antibiotic activity, and immunostimulatory effects [71]. This thesis unveiled potent activity of PXA against different types of cisplatin-resistant cancer cell lines, including bladder cancer cells (second publication)[86]. 5 Pairs of cisplatin-sensitive and -resistant cancer cell lines were used. Notably, PXA is equipotent (or slightly more potent) in cisplatin-resistant compared to cisplatin-sensitive cancer cell lines. Moreover, the mechanism of the cytotoxicity of PXA was investigated in depth in 2 pairs of cisplatin sensitive and resistant ovarian and bladder cancer cell lines. PXA leads to an increase in cytosolic Ca^{2+} concentration released from intracellular stores within few minutes and in a time scale that is comparable to the mitochondrial membrane potential breakdown. Consequential effects of the damaged mitochondrial membrane potential included caspase 3/7 activation and apoptosis and were detected in all four cell lines.

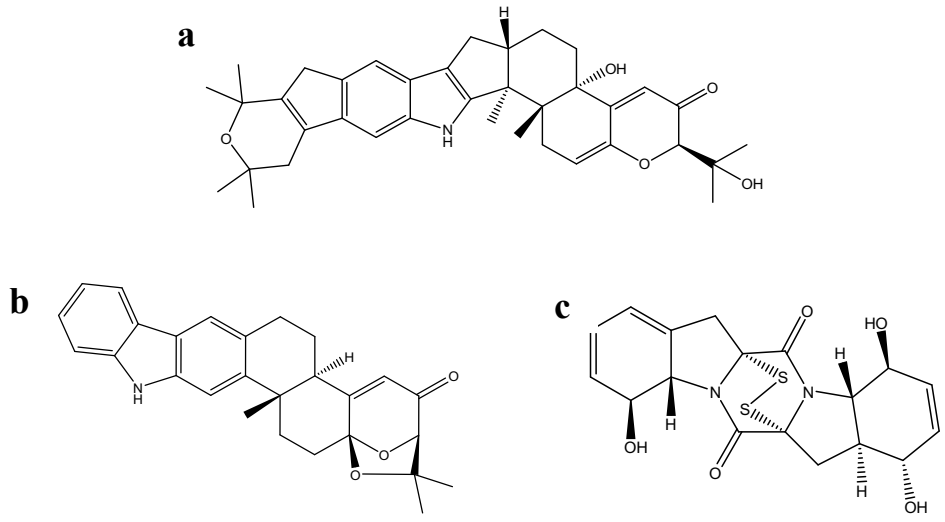

Figure 15. Structures of natural products whose anti-cancer activities were identified in this thesis.

The question remained how PXA would destroy the mitochondrial membrane potential. Boehler et al. reported in 2018 about the destruction of the inner mitochondrial membrane by

PXA [76]. However, they could not yet identify the molecular target of PXA. In this thesis, in a collaboration with the group of Professor Gohlke, University of Duesseldorf, configurational free energy computations were undertaken to judge if PXA could act as a proton shuttle. Indeed, computational results suggested that PXA could act as a proton shuttle and dissipate the proton gradient along the inner mitochondrial membrane [86]. Three protonation states of PXA were examined (uncharged, singly, and doubly deprotonated). The simulation results revealed that both the neutral and singly negatively charged PXA allowed membrane partitioning and could penetrate the inner mitochondrial membrane. The only drawback of PXA is a limited stability that may however be overcome by smart pharmaceutical formulations [76]. In conclusion, our study suggests a mechanism by which PXA can destroy the inner mitochondrial membrane and provides evidence that PXA has the potential to serve as lead structure for novel anti-cancer drugs in particular for the treatment of cisplatin-resistant cancers.

Besides PXA, a number of natural product compounds were examined for activity against cancer cells. For example, two novel indole diterpenoids isolated from *Zingiber officinale* (**Figure 15a, b**) by the group of Professor Proksch, exhibited effective anti-cancer activities in the human ovarian cancer cell line A2780 with IC_{50} values in the low micromolar range (third publication) [87]. Moreover, a new diketopiperazine (**Figure 15c**) isolated from the mangrove-derived endophytic fungus showed potent cytotoxicity with sub-μM IC_{50} values of 664 nM and 661 nM in A2780 and A2780CisR, respectively [88]. These studies indicate that compounds derived from natural sources are furthermore treasures worth to be exploited and will contribute to future cancer chemotherapy as natural compounds in the past did, too.

In summary, this thesis initially set up a cisplatin-resistant bladder cancer *in vitro* model and, in the first part, identified a promising epigenetic approach and, in the second part, characterized promising nature-derived compounds to be developed as therapeutic strategies bladder cancer, especially for those patients who are not eligible for cisplatin-based chemotherapy or exhibit chemoresistance. Further studies have to be undertaken regarding the precise mechanism of action in the complex epigenetic network, and comprehensive toxicological evaluation is necessary for promoting these compounds to clinical drug candidate for bladder cancer.

5 References

1. Kamat AM, Hahn NM, Efstathiou JA, Lerner SP, Malmstrom PU, Choi W, et al. Bladder cancer. Lancet. 2016;388(10061):2796-810.
2. Chandrasekar T, Erlich A, Zlotta AR. Molecular Characterization of Bladder Cancer. Curr Urol Rep. 2018;19(12):107.
3. Babjuk M, Oosterlinck W, Sylvester R, Kaasinen E, Bohle A, Palou-Redorta J, et al. EAU guidelines on non-muscle-invasive urothelial carcinoma of the bladder. Eur Urol. 2008;54(2):303-14.
4. Calabro F, Sternberg CN. Neoadjuvant and adjuvant chemotherapy in muscle-invasive bladder cancer. Eur Urol. 2009;55(2):348-58.
5. Sylvester RJ, van der MA, Lamm DL. Intravesical bacillus Calmette-Guerin reduces the risk of progression in patients with superficial bladder cancer: a meta-analysis of the published results of randomized clinical trials. J Urol. 2002;168(5):1964-70.
6. Vale CL. Neoadjuvant Chemotherapy in Invasive Bladder Cancer: Update of a Systematic Review and Meta-Analysis of Individual Patient Data: Advanced Bladder Cancer (ABC) Meta-analysis Collaboration. European Urology. 2005;48(2):202-6.
7. International Collaboration of T, Medical Research Council Advanced Bladder Cancer Working P, European Organisation for R, Treatment of Cancer Genito-Urinary Tract Cancer G, Australian Bladder Cancer Study G, National Cancer Institute of Canada Clinical Trials G, et al. International phase III trial assessing neoadjuvant cisplatin, methotrexate, and vinblastine chemotherapy for muscle-invasive bladder cancer: long-term results of the BA06 30894 trial. J Clin Oncol. 2011;29(16):2171-7.
8. von der Maase H, Sengelov L, Roberts JT, Ricci S, Dogliotti L, Oliver T, et al. Long-term survival results of a randomized trial comparing gemcitabine plus cisplatin, with methotrexate, vinblastine, doxorubicin, plus cisplatin in patients with bladder cancer. J Clin Oncol. 2005;23(21):4602-8.
9. Spiess PE, Agarwal N, Bangs R, Boorjian SA, Buyyounouski MK, Clark PE, et al. Bladder Cancer, Version 5.2017, NCCN Clinical Practice Guidelines in Oncology. J Natl Compr Canc Netw. 2017;15(10):1240-67.
10. Bellmunt J, Powles T, Vogelzang NJ. A review on the evolution of PD-1/PD-L1 immunotherapy for bladder cancer: The future is now. Cancer Treat Rev. 2017;54:58-67.
11. Massard C, Gordon MS, Sharma S, Rafii S, Wainberg ZA, Luke J, et al. Safety and Efficacy of Durvalumab (MEDI4736), an Anti-Programmed Cell Death Ligand-1 Immune Checkpoint Inhibitor, in Patients With Advanced Urothelial Bladder Cancer. J Clin Oncol. 2016;34(26):3119-25.
12. Sharma P, Retz M, Siefker-Radtke A, Baron A, Necchi A, Bedke J, et al. Nivolumab in metastatic urothelial carcinoma after platinum therapy (CheckMate 275): a multicentre, single-arm, phase 2 trial. Lancet Oncol. 2017;18(3):312-22.
13. Chabner BA. Barnett Rosenberg: In Memoriam (1924–2009). Cancer Res. 2010;70(1):428.
14. Loehrer PJ, Einhorn LH. Drugs five years later. Cisplatin. Ann Intern Med. 1984;100(5):704-13.
15. Dasari S, Tchounwou PB. Cisplatin in cancer therapy: molecular mechanisms of action. Eur J Pharmacol. 2014;740:364-78.
16. Ishida S, Lee J, Thiele DJ, Herskowitz I. Uptake of the anticancer drug cisplatin mediated by the copper transporter Ctr1 in yeast and mammals. Proc Natl Acad Sci U S A. 2002;99(22):14298-302.
17. Kelland LR. New platinum antitumor complexes. Critical Reviews in Oncology/Hematology. 1993;15(3):191-219.
18. Siddik ZH. Cisplatin: mode of cytotoxic action and molecular basis of resistance. Oncogene.

2003;22(47):7265-79.
19. Wang Z, Zhu G. DNA Damage Repair Pathways and Repair of Cisplatin-Induced DNA Damage. Reference Module in Chemistry, Molecular Sciences and Chemical Engineering: Elsevier; 2018.
20. Amable L. Cisplatin resistance and opportunities for precision medicine. Pharmacol Res. 2016;106:27-36.
21. Galluzzi L, Senovilla L, Vitale I, Michels J, Martins I, Kepp O, et al. Molecular mechanisms of cisplatin resistance. Oncogene. 2012;31(15):1869-83.
22. Friedberg EC. DNA damage and repair. Nature. 2003;421(6921):436-40.
23. Olaussen KA, Dunant A, Fouret P, Brambilla E, Andre F, Haddad V, et al. DNA repair by ERCC1 in non-small-cell lung cancer and cisplatin-based adjuvant chemotherapy. N Engl J Med. 2006;355(10):983-91.
24. Bellmunt J, Paz-Ares L, Cuello M, Cecere FL, Albiol S, Guillem V, et al. Gene expression of ERCC1 as a novel prognostic marker in advanced bladder cancer patients receiving cisplatin-based chemotherapy. Ann Oncol. 2007;18(3):522-8.
25. Sakai W, Swisher EM, Jacquemont C, Chandramohan KV, Couch FJ, Langdon SP, et al. Functional restoration of BRCA2 protein by secondary BRCA2 mutations in BRCA2-mutated ovarian carcinoma. Cancer Res. 2009;69(16):6381-6.
26. Shen DW, Pouliot LM, Hall MD, Gottesman MM. Cisplatin resistance: a cellular self-defense mechanism resulting from multiple epigenetic and genetic changes. Pharmacol Rev. 2012;64(3):706-21.
27. Swisher EM, Sakai W, Karlan BY, Wurz K, Urban N, Taniguchi T. Secondary BRCA1 mutations in BRCA1-mutated ovarian carcinomas with platinum resistance. Cancer Res. 2008;68(8):2581-6.
28. Holzer AK, Manorek GH, Howell SB. Contribution of the major copper influx transporter CTR1 to the cellular accumulation of cisplatin, carboplatin, and oxaliplatin. Mol Pharmacol. 2006;70(4):1390-4.
29. Ishida S, McCormick F, Smith-McCune K, Hanahan D. Enhancing tumor-specific uptake of the anticancer drug cisplatin with a copper chelator. Cancer Cell. 2010;17(6):574-83.
30. Chen HH, Yan JJ, Chen WC, Kuo MT, Lai YH, Lai WW, et al. Predictive and prognostic value of human copper transporter 1 (hCtr1) in patients with stage III non-small-cell lung cancer receiving first-line platinum-based doublet chemotherapy. Lung Cancer. 2012;75(2):228-34.
31. Taniguchi K, Wada M, Kohno K, Nakamura T, Kawabe T, Kawakami M, et al. A human canalicular multispecific organic anion transporter (cMOAT) gene is overexpressed in cisplatin-resistant human cancer cell lines with decreased drug accumulation. Cancer Res. 1996;56(18):4124-9.
32. Nakayama K, Kanzaki A, Ogawa K, Miyazaki K, Neamati N, Takebayashi Y. Copper-transporting P-type adenosine triphosphatase (ATP7B) as a cisplatin based chemoresistance marker in ovarian carcinoma: comparative analysis with expression of MDR1, MRP1, MRP2, LRP and BCRP. Int J Cancer. 2002;101(5):488-95.
33. Filipits M, Haddad V, Schmid K, Huynh A, Dunant A, Andre F, et al. Multidrug resistance proteins do not predict benefit of adjuvant chemotherapy in patients with completely resected non-small cell lung cancer: International Adjuvant Lung Cancer Trial Biologic Program. Clin Cancer Res. 2007;13(13):3892-8.
34. Goto S, Kamada K, Soh Y, Ihara Y, Kondo T. Significance of nuclear glutathione S-transferase pi in resistance to anti-cancer drugs. Jpn J Cancer Res. 2002;93(9):1047-56.
35. Kasahara K, Fujiwara Y, Nishio K, Ohmori T, Sugimoto Y, Komiya K, et al. Metallothionein content correlates with the sensitivity of human small cell lung cancer cell lines to cisplatin. Cancer Res. 1991;51(12):3237-42.
36. Siegsmund MJ, Marx C, Seemann O, Schummer B, Steidler A, Toktomambetova L, et al. Cisplatin-resistant bladder carcinoma cells: enhanced expression of metallothioneins. Urol Res. 1999;27(3):157-63.
37. Dawson MA, Kouzarides T. Cancer epigenetics: from mechanism to therapy. Cell. 2012;150(1):12-27.
38. Ehrlich M, Lacey M. DNA hypomethylation and hemimethylation in cancer. Adv Exp Med Biol. 2013;754:31-56.

39. Baylin SB. DNA methylation and gene silencing in cancer. Nat Clin Pract Oncol. 2005;2 Suppl 1:S4-11.
40. Baylin SB, Jones PA. Epigenetic Determinants of Cancer. Cold Spring Harb Perspect Biol. 2016;8(9).
41. Segura-Pacheco B, Perez-Cardenas E, Taja-Chayeb L, Chavez-Blanco A, Revilla-Vazquez A, Benitez-Bribiesca L, et al. Global DNA hypermethylation-associated cancer chemotherapy resistance and its reversion with the demethylating agent hydralazine. J Transl Med. 2006;4:32.
42. Almouzni G, Cedar H. Maintenance of Epigenetic Information. Cold Spring Harb Perspect Biol. 2016;8(5).
43. Baylin SB, Jones PA. A decade of exploring the cancer epigenome - biological and translational implications. Nat Rev Cancer. 2011;11(10):726-34.
44. Bose P, Dai Y, Grant S. Histone deacetylase inhibitor (HDACI) mechanisms of action: emerging insights. Pharmacol Ther. 2014;143(3):323-36.
45. Chueh AC, Tse JW, Togel L, Mariadason JM. Mechanisms of Histone Deacetylase Inhibitor-Regulated Gene Expression in Cancer Cells. Antioxid Redox Signal. 2015;23(1):66-84.
46. Perez de Heredia F, Sanchez J, Priego T, Larque E, Portillo MP, Palou A, et al. Adiponectin is associated with serum and adipose tissue fatty acid composition in rats. J Endocrinol Invest. 2009;32(8):659-65.
47. Strahl BD, Allis CD. The language of covalent histone modifications. Nature. 2000;403(6765):41-5.
48. Yoo CB, Jones PA. Epigenetic therapy of cancer: past, present and future. Nat Rev Drug Discov. 2006;5(1):37-50.
49. Niegisch G, Knievel J, Koch A, Hader C, Fischer U, Albers P, et al. Changes in histone deacetylase (HDAC) expression patterns and activity of HDAC inhibitors in urothelial cancers. Urol Oncol. 2013;31(8):1770-9.
50. Fraga MF, Ballestar E, Villar-Garea A, Boix-Chornet M, Espada J, Schotta G, et al. Loss of acetylation at Lys16 and trimethylation at Lys20 of histone H4 is a common hallmark of human cancer. Nat Genet. 2005;37(4):391-400.
51. de Ruijter AJ, van Gennip AH, Caron HN, Kemp S, van Kuilenburg AB. Histone deacetylases (HDACs): characterization of the classical HDAC family. Biochem J. 2003;370(Pt 3):737-49.
52. Rosato RR, Maggio SC, Almenara JA, Payne SG, Atadja P, Spiegel S, et al. The histone deacetylase inhibitor LAQ824 induces human leukemia cell death through a process involving XIAP down-regulation, oxidative injury, and the acid sphingomyelinase-dependent generation of ceramide. Mol Pharmacol. 2006;69(1):216-25.
53. Chen S, Dai Y, Pei XY, Grant S. Bim upregulation by histone deacetylase inhibitors mediates interactions with the Bcl-2 antagonist ABT-737: evidence for distinct roles for Bcl-2, Bcl-xL, and Mcl-1. Mol Cell Biol. 2009;29(23):6149-69.
54. Dasmahapatra G, Lembersky D, Kramer L, Fisher RI, Friedberg J, Dent P, et al. The pan-HDAC inhibitor vorinostat potentiates the activity of the proteasome inhibitor carfilzomib in human DLBCL cells in vitro and in vivo. Blood. 2010;115(22):4478-87.
55. Li H, Wu X. Histone deacetylase inhibitor, Trichostatin A, activates p21WAF1/CIP1 expression through downregulation of c-myc and release of the repression of c-myc from the promoter in human cervical cancer cells. Biochem Biophys Res Commun. 2004;324(2):860-7.
56. Jones PA, Issa JP, Baylin S. Targeting the cancer epigenome for therapy. Nat Rev Genet. 2016;17(10):630-41.
57. Johnstone RW. Histone-deacetylase inhibitors: novel drugs for the treatment of cancer. Nat Rev Drug Discov. 2002;1(4):287-99.
58. Stenzel K, Hamacher A, Hansen FK, Gertzen CGW, Senger J, Marquardt V, et al. Alkoxyurea-Based Histone Deacetylase Inhibitors Increase Cisplatin Potency in Chemoresistant Cancer Cell Lines. J Med Chem. 2017;60(13):5334-48.
59. Yoon CY, Park MJ, Lee JS, Lee SC, Oh JJ, Park H, et al. The histone deacetylase inhibitor trichostatin A synergistically resensitizes a cisplatin resistant human bladder cancer cell line. J Urol. 2011;185(3):1102-11.

60. Marek L, Hamacher A, Hansen FK, Kuna K, Gohlke H, Kassack MU, et al. Histone deacetylase (HDAC) inhibitors with a novel connecting unit linker region reveal a selectivity profile for HDAC4 and HDAC5 with improved activity against chemoresistant cancer cells. J Med Chem. 2013;56(2):427-36.
61. Asfaha Y, Schrenk C, Alves Avelar LA, Lange F, Wang C, Bandolik JJ, et al. Novel alkoxyamide-based histone deacetylase inhibitors reverse cisplatin resistance in chemoresistant cancer cells. Bioorganic & Medicinal Chemistry. 2019:115108.
62. Newman DJ, Cragg GM, Snader KM. The influence of natural products upon drug discovery. Nat Prod Rep. 2000;17(3):215-34.
63. Mann J. Natural products in cancer chemotherapy: past, present and future. Nat Rev Cancer. 2002;2(2):143-8.
64. Ma P, Mumper RJ. Anthracycline Nano-Delivery Systems to Overcome Multiple Drug Resistance: A Comprehensive Review. Nano Today. 2013;8(3):313-31.
65. Schiff PB, Fant J, Horwitz SB. Promotion of microtubule assembly in vitro by taxol. Nature. 1979;277(5698):665-7.
66. Debbab A, Aly AH, Lin WH, Proksch P. Bioactive compounds from marine bacteria and fungi. Microb Biotechnol. 2010;3(5):544-63.
67. Uemura D, Takahashi K, Yamamoto T, Katayama C, Tanaka J, Okumura Y, et al. Norhalichondrin A: an antitumor polyether macrolide from a marine sponge. Journal of the American Chemical Society. 1985;107(16):4796-8.
68. Gitlitz BJ, Tsao-Wei DD, Groshen S, Davies A, Koczywas M, Belani CP, et al. A phase II study of halichondrin B analog eribulin mesylate (E7389) in patients with advanced non-small cell lung cancer previously treated with a taxane: a California cancer consortium trial. J Thorac Oncol. 2012;7(3):574-8.
69. Kuznetsov G, TenDyke K, Yu M, Littlefield B. Antiproliferative effects of halichondrin B analog eribulin mesylate (E7389) against paclitaxel-resistant human cancer cells <em>in vitro</em&gt. Mol Cancer Ther. 2007;6(11 Supplement):C58.
70. Schoffski P, Chawla S, Maki RG, Italiano A, Gelderblom H, Choy E, et al. Eribulin versus dacarbazine in previously treated patients with advanced liposarcoma or leiomyosarcoma: a randomised, open-label, multicentre, phase 3 trial. Lancet. 2016;387(10028):1629-37.
71. Ronsberg D, Debbab A, Mandi A, Vasylyeva V, Bohler P, Stork B, et al. Pro-apoptotic and immunostimulatory tetrahydroxanthone dimers from the endophytic fungus Phomopsis longicolla. J Org Chem. 2013;78(24):12409-25.
72. Frank M, Niemann H, Bohler P, Stork B, Wesselborg S, Lin W, et al. Phomoxanthone A--From Mangrove Forests to Anticancer Therapy. Curr Med Chem. 2015;22(30):3523-32.
73. Gosepath EM, Eckstein N, Hamacher A, Servan K, von Jonquieres G, Lage H, et al. Acquired cisplatin resistance in the head-neck cancer cell line Cal27 is associated with decreased DKK1 expression and can partially be reversed by overexpression of DKK1. Int J Cancer. 2008;123(9):2013-9.
74. Chang X, Monitto CL, Demokan S, Kim MS, Chang SS, Zhong X, et al. Identification of hypermethylated genes associated with cisplatin resistance in human cancers. Cancer Res. 2010;70(7):2870-9.
75. Juergens RA, Wrangle J, Vendetti FP, Murphy SC, Zhao M, Coleman B, et al. Combination epigenetic therapy has efficacy in patients with refractory advanced non-small cell lung cancer. Cancer Discov. 2011;1(7):598-607.
76. Bohler P, Stuhldreier F, Anand R, Kondadi AK, Schlutermann D, Berleth N, et al. The mycotoxin phomoxanthone A disturbs the form and function of the inner mitochondrial membrane. Cell Death Dis. 2018;9(3):286.
77. Kandimalla R, van Tilborg AA, Zwarthoff EC. DNA methylation-based biomarkers in bladder cancer. Nat Rev Urol. 2013;10(6):327-35.

78. Nishiyama N, Arai E, Chihara Y, Fujimoto H, Hosoda F, Shibata T, et al. Genome-wide DNA methylation profiles in urothelial carcinomas and urothelia at the precancerous stage. Cancer Sci. 2010;101(1):231-40.
79. Ozawa A, Tanji N, Kikugawa T, Sasaki T, Yanagihara Y, Miura N, et al. Inhibition of bladder tumour growth by histone deacetylase inhibitor. BJU Int. 2010;105(8):1181-6.
80. Lane D. Designer combination therapy for cancer. Nat Biotechnol. 2006;24(2):163-4.
81. Jones PL, Veenstra GJ, Wade PA, Vermaak D, Kass SU, Landsberger N, et al. Methylated DNA and MeCP2 recruit histone deacetylase to repress transcription. Nat Genet. 1998;19(2):187-91.
82. Cai Y, Geutjes EJ, de Lint K, Roepman P, Bruurs L, Yu LR, et al. The NuRD complex cooperates with DNMTs to maintain silencing of key colorectal tumor suppressor genes. Oncogene. 2014;33(17):2157-68.
83. Kaletsch A, Pinkerneil M, Hoffmann MJ, Jaguva Vasudevan AA, Wang C, Hansen FK, et al. Effects of novel HDAC inhibitors on urothelial carcinoma cells. Clin Epigenetics. 2018;10(1):100.
84. Eijkelenboom A, Burgering BM. FOXOs: signalling integrators for homeostasis maintenance. Nat Rev Mol Cell Biol. 2013;14(2):83-97.
85. Farhan M, Wang H, Gaur U, Little PJ, Xu J, Zheng W. FOXO Signaling Pathways as Therapeutic Targets in Cancer. Int J Biol Sci. 2017;13(7):815-27.
86. Wang C, Engelke L, Bickel D, Hamacher A, Frank M, Proksch P, et al. The tetrahydroxanthone-dimer phomoxanthone A is a strong inducer of apoptosis in cisplatin-resistant solid cancer cells. Bioorg Med Chem. 2019;27(19):115044.
87. Ariantari NP, Ancheeva E, Wang C, Mandi A, Knedel TO, Kurtan T, et al. Indole Diterpenoids from an Endophytic Penicillium sp. J Nat Prod. 2019;82(6):1412-23.
88. Meng LH, Wang CY, Mandi A, Li XM, Hu XY, Kassack MU, et al. Three Diketopiperazine Alkaloids with Spirocyclic Skeletons and One Bisthiodiketopiperazine Derivative from the Mangrove-Derived Endophytic Fungus Penicillium brocae MA-231. Org Lett. 2016;18(20):5304-7.

List of Publications

1. **Wang, C**.; Engelke, L. H.; Bickel, D.; et al, The tetrahydroxanthone-dimer phomoxanthone A is a strong inducer of apoptosis in solid cancer cell. *Bioorganic & Medicinal Chemistry*, 2019, 27(19), 115044
2. **Wang, C**.; Hamacher, A.; Petzsch, P.; et al, Combination of Decitabine and Entinostat Synergistically Inhibit Urothelial Bladder Cancer Cells via Activation of FoxO1. *Cancers*, 2019, ready for submission.
3. Ariantari, Ni P.; Ancheeva, E.; **Wang, C.**; et al, Indole diterpenoids from the fungal endophyte *Penicilium* sp. *Journal of Natural Products*, 2019, 82 (6), 1412.
4. Asfaha, Y.; Schrenk, C.; Alves Avelar, L. A.; Lange, F.; **Wang, C.**; et al, Novel alkoxyamide-based histone deacetylase inhibitors reverse cisplatin resistance in chemoresistant cancer cells. Bioorganic & Medicinal Chemistry 2019, 115108.
5. Kaletsch, A.; Pinkerneil, M.; Hoffmann, M. J.; Jaguva Vasudevan, A. A.; **Wang, C.**; et al, Effects of novel HDAC inhibitors on urothelial carcinoma cells. *Clinical Epigenetics*, 2018, 10 (1), 100.
6. Li, H. L.; Li, X. M.; Li, X.; **Wang, C**.; et al, Antioxidant hydroanthraquinones from the marine algal-derived endophytic fungus *Talaromyces islandicus* EN-501. *Journal of Natural Products*, 2017, 80(1), 162.
7. Meng, L. H.; **Wang, C.**; Mandi, A.; et al, Three diketopiperazine alkaloids with spirocyclic skeletons and one bisthiodiketopiperazine derivative from the mangrove-derived endophytic fungus *Penicillium brocae* MA-231. *Organic Letters*, 2016, 18(20), 5304.

Conference Presentation and Poster

1. **Wang, C.;** Hamacher, A.; Petzsch, P.; et al, Combining epigenetic therapy and immune therapy as a potential strategy for the treatment of bladder cancer (**Poster**). 9th Mildred Scheel Cancer Conference, May 15-16, 2019, Bonn, Germany.
2. **Wang, C.,** Application of high-content imaging for the study of apoptosis induction by novel anti-cancer agents (**Presentation**). High Content Analysis User Meeting-SLAS Europe, June 26-29, 2018, Brussels, Belgium.
3. **Wang, C.,** High-content screening: a powerful technology for novel anti-cancer drug discovery (**Presentation**). 2nd Symposium of Research Training Group 2158 (GRK2158), September 18-20, 2018, Beijing, China.
4. **Wang, C.,** Strategy to overcome cisplatin resistance in urothelial bladder cancer (**Presentation**). 1st Symposium of Research Training Group 2158 (GRK2158), September 20-22, 2017, Düsseldorf, Germany.
5. **Wang, C.,** Phomoxanthone A: a promising anticancer compound from the mangrove-associated fungus *Phomopsis longicolla* (**Poster**). 8th Mildred Scheel Cancer Conference, June 14-16, 2017, Bonn, Germany.

Acknowledgement

First of all, I would like to acknowledge my supervisor Prof. Dr. Matthias U. Kassack that offering me this great chance join his research group and study here. Over the past years, he provided me with invaluable support and patient guidance that keeping my research project move on. My sincere thankfulness also goes to Prof. Dr. Peter Proksch (Institute of Pharmaceutical Biology and Biotechnology). I would like to express my heartfelt gratitude for his precious suggestions to my study and to my life as well.

I would like to give my special thanks to Dr. Alexandra Hamacher for her valuable and intensive support during the past years. The joyous moment that spent with you will become great memory in my future life.

My earnest appreciation also goes to my colleagues Parichat Sureechatchaiyan, Ana Julieta Rodrigues Moita, Kaharina (Hüppe) Gohr, Magdalena Matyja, Fritz Lange, David Müller, Jan Bandolik, Alexander Skerhut, Christian Schrenk, Nadine Horstick Muche, Kathrin Christoph, Laura Engelke.

Out of the institute, I want to thank Prof. Dr. Karl Köhrer, Dr. Patrick Petzsch, Prof. Dr. Wolfgang Schulz, Dr. Michele J. Hoffmann, and Marian Frank for their kind support on my research project.

I also would like to thank my friends Dr. Huiqin Chen, Dr. Yang Liu, Dr. Shuai Liu, Dr. Hao Wang, Dr. Zhen Liu, Haiqian Yu, Nam Michael Tran-Cong, Dr. Feng Pan, Xiaoqin Yu, Ying Gao, Lei Wang.

I want to express my appreciation to all of my colleagues and friends in the graduate collage GRK2158. It is a great pleasure to be a member of the family of GRK2158. Particularly, I want to thank Dr. Martina Holz for her generous support.

In the end, I am heartily thankful to my parents and Qi for supporting me and being my side whenever I need.

1 Introduction

1.1 Bladder Cancer

Bladder cancer comprises several types of cancers growing from the wall of the urinary bladder and is the 4th most common malignancy in men and the 11th most in women [1]. To date, urothelial carcinoma is the most common type of bladder cancer, which accounts for over 90% cases of bladder cancer. Other types of bladder cancers, including squamous cell carcinoma, adenocarcinoma, small cell carcinoma, account for less than 10% among all of this disease [2]. The stage of bladder cancer is defined by how far they have spread into the bladder wall. Depending on the location of cancers grown into the bladder, it is described as non-muscle invasive bladder cancer (NMIBC) or superficial (cancers only can be found in the inner layer of the bladder wall) and muscle invasive bladder cancer (MIBC, cancers have grown into deeper layers of the bladder wall) [3]. The stages can be specified to T0/T1 (NMIBC) and T2/T3/T4 (MIBC). Although only 30% of newly diagnosed bladder cancer cases are advanced, another 15-30% of high-grade superficial bladder cancers develop to muscle invasive carcinomas with poor long-te

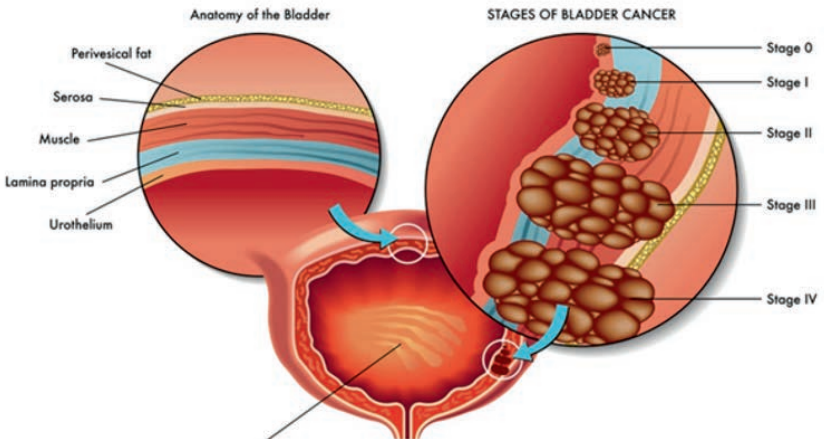

Figure 1. Anatomy of the bladder and stages of bladder cancer

Treatment Options of Bladder Cancer

The treatment of bladder cancer depends on the stage of the disease. A complete

1.2 Cisplatin

1.2.1 Cisplatin in Cancer

Cisplatin [cis-diamminedichloroplatinum (II)] is one of the most widely used chemotherapy drugs for cancer. The history of cisplatin initiates in 1845 by an Italian chemist Michele Peyrone who synthesized it for the first time. However, the inhibition of cell proliferation effect of cisplatin was accidentally discovered by Barnett Rosenberg in 1965, which triggered the study of cisplatin developed as anti-cancer agent eventually [13]. The successful results of clinical trials led the approval of cisplatin for testicular cancer treatment by FDA in 1978 [14]. In the past four decades, cisplatin has been approved for the treatment of a wide range of solid tumors, such as ovarian cancer, bladder cancer, and breast cancer. Moreover, cisplatin-based chemotherapy has become the backbone of drug combination treatments in cancer [15].

Cisplatin induces the cytotoxicity by targeting the DNA directly. Once it enters the cell, the drug is activated when the chloride atoms on cisplatin are displaced by water molecules due to the lower chloride concentration (2-30 mM) within the cell compared to the outside of the cell (100 mM). The positively charged aquated product reacts easily with any nucleophile including the nitrogen donor atoms on nucleic acids [16]. The interaction between aquated cisplatin with N7-positions of purine bases in DNA leads to the formation of DNA adducts and thus induces interstrand and intrastrand crosslinks **(Figure 2)**. It is generally agreed that, the intrastrand DNA adduct is the most prevalent nuclear lesion caused by cisplatin since 1,2-intrastrand ApG and GpG crosslinks account for 85-90% of total lesions [17]. These DNA damages induced by cisplatin lead to accumulation of DNA damage recognition proteins and regulate pathways and finally promote apoptosis and cell cycle arrest [18].

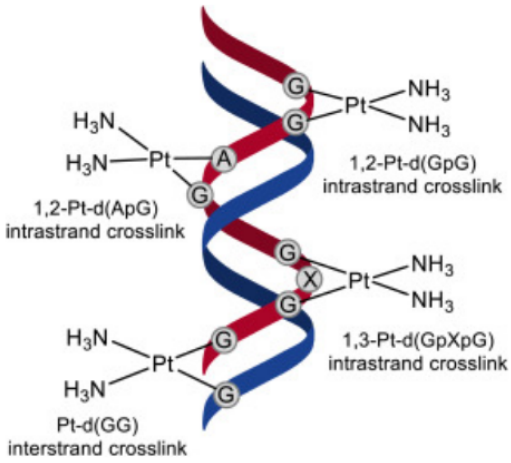

Figure 2. Different types of cisplatin-DNA adducts [19]

1.2.2 Cisplatin Resistance

Although most patients initially have good response to cisplatin, the development of drug resistance, either intrinsic or acquired, attenuates its effectiveness and eventually causes cancer relapse. The development of cisplatin resistance is a multifactorial process with alterations of many proteins and pathways. It is generally accepted that three molecular mechanisms contribute to the reduced sensitivity of tumors to cisplatin. These mechanisms are (**Figure 3**): increased DNA repair, reduced drug accumulation, cytosolic inactivation of cisplatin, and defects in the apoptotic signaling pathway [20, 21].

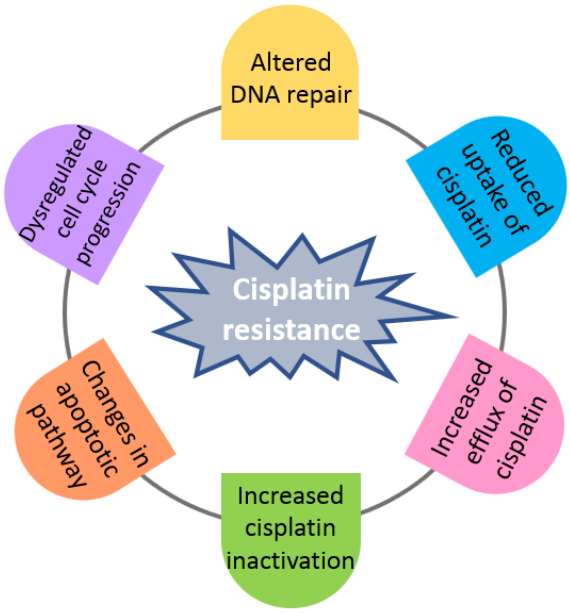

Figure 3. Mechanisms related to cisplatin resistance

glutathione conjugates. A correlation between MRP2 expression and cisplatin resistance has been found in hepatocellular, colorectal, and esophageal cancers. However, no correlation between MRP2 expression level and cisplatin response was found in ovarian and lung cancer [32, 33].

c. increased inactivation of cisplatin

In the cytoplasm, glutathione (GSH) serves as antioxidant by reducing sulfhydryl groups to keep the redox environment. The strong electrophilic property of aquated cisplatin is prone to bind GSH and other cysteine-rich proteins. As a consequence, cisplatin-GSH conjugates, catalyzed by GSTs (Glutathione-S-transferases), are pumped out by MRP transporters, resulting in the reduction of cisplatin binding to DNA [20]. The association between increased cisplatin resistance and increased expression of GSTP1, a member of the GST family, has been demonstrated in ovarian, head and neck, and lung cancers [34]. In addition, MTs (metallothioneins) inactivate cisplatin utilizing its ability to bind heavy metal ions. Up-regulated MTs have been observed in a number of cell lines including lung and bladder cancer cells which are resistant to cisplatin [35, 36].

1.3 Epigenetic Modifications and Cancer

The term “epigenetics” refers to heritable changes in gene expressions that are independent of alterations in the DNA sequence [37]. Over a long period of time, the accumulation of genetic mutations was thought to be the major cause of cancer. However, in recent decades, many studies have focused on epigenetic alterations, such as DNA methylation and histone deacetylation, and elucidated its critical role played in cancer initiation and progression.

1.3.1 DNA Methylation and Cancer

Aberrant patterns of DNA methylation, a methyl group covalently added to the 5’ carbon of cytosine resulting in 5-methylcytosine, 5mC, is one of the most frequently observed epigenetic events in cancer (**Figure 5**).

Furthermore, many studies have shown that DNA hypermethylation-induced gene silencing occurs during long-term exposure to chemotherapeutic agents. For example, in the adriamycin-resistant breast cancer cell line MCF-7, increased DNA methyltransferase activity and global DNA hypermethylation was found when compared with its parental cell line MCF-7. The sensitivity of adriamycin was restored by the treatment of the DNA methylation inhibitor hydralazine [41].

1.3.2 DNA Methyltransferases and Inhibitors

Given that DNA hypermethylation in CpG islands of promoter regions is a common event and essential to tumorigenesis, reversing or inhibiting the aberrant DNA hypermethylation is a therapeutic strategy for cancer. Three DNA methyltransferases (DNMTs), DNMT1, DNMT3a, and DNMT3b, are found in mammalian cells and catalyze the methylation on cytosine. The functional differences among the DNMTs are the responsibilities to either maintain (DNMT1) or establish (DNMT 3a and 3b) DNA methylation [42]. Several DNMT inhibitors, such as the cytosine analogue azacytidine and its deoxy derivative decitabine (**Figure 7**), were developed and some of them have already been approved for cancer treatment. Azacitidine is approved for the treatment of myelodysplastic syndromes and decitabine is approved for acute myeloid leukemia. The mode of action of azacytidine and decitabine is known as follows: both compounds are incorporated into DNA (azacitidine also into RNA) during replication and then bind covalently to the catalytic site of DNMTs [43].

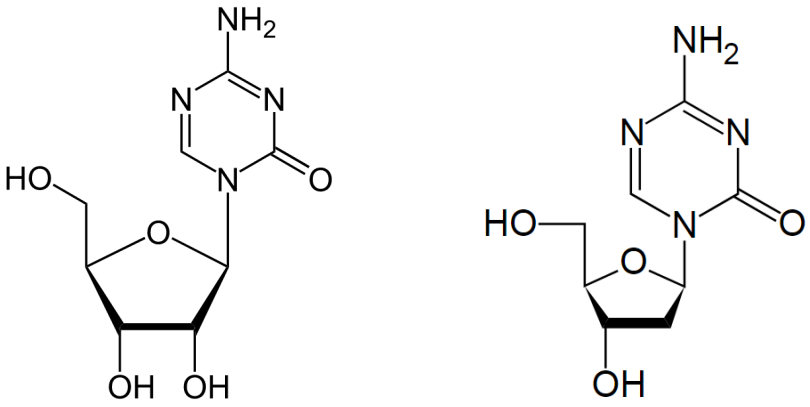

Figure 7. Structure of Azacitidine (Left) and Decitabine (Right)

1.4 Histone Modifications

1.4.1 Histone Deacetylation and Cancer

As the fundamental component of nucleosomes, modifications on histones play a major role in regulating gene expression. Histone acetylation is one of the key molecular events among these modifications. Acetylation of lysine residues of histones is mediated by histone acetyltransferases (HATs) and associated with a relaxed conformation of chromatin and promotes the recruitment of proteins and protein complexes responsible for activating transcription (**Figure 8**). The histone deacetylases (HDACs), on the other hand, are responsible for removing the acetyl groups from lysine residues to maintain a repressive chromatin environment [44]. In general, two mechanisms account for the regulation of transcription achieved by histone acetylation. First, acetylation removes the positive charge on lysine and thereby reduces its interaction with negatively charged DNA phosphate groups, eventually establishing a relaxed chromatin structure [45]. Second, hyperacetylation of histones facilitates the recognition and interaction of bromodomain (BRD)-containing proteins [46]. Binding of BRD-containing proteins with acetylated lysine residues can affect the gene transcription by initiating transcription elongation (BRD4) [47]. However, in cancers, lack or even loss of histone lysine acetylation induced by HDACs has been frequently found and causes a tightly compacted chromatin structure and gene silencing [48]. The dysregulation of the HDACs has been observed in many cancer types including bladder cancer [49, 50]. A study analyzing the mRNA expression level of HDACs in 18 bladder cancer cell lines revealed frequent upregulation of class I HDACs [49]. HDACs comprise separate groups which include class I (HDAC1, 2, 3, and 8), class IIa (HDAC4, 5, 7, and 9), class IIb (HDAC6 and 10), and class IV (HDAC11) [51].

1.4.2 Histone deacetylase inhibitors

Because of the major role of HDACs in gene transcription, HDACs inhibitors have been developed and evaluated in many cancer types. Although the exact mechanism of the anti-tumor effect induced by HDAC inhibitors remains to be elucidated, a number of studies has shown

JOURNAL OF NATURAL PRODUCTS

Article

Cite This: J. Nat. Prod. 2019, 82, 1412−1423

pubs.acs.org/jnp

Indole Diterpenoids from an Endophytic *Penicillium* sp.

Ni P. Ariantari,[†,‡] Elena Ancheeva,[*,†] Chenyin Wang,[§] Attila Mándi,[⊥] Tim-O. Knedel,[#] Tibor Kurtán,[⊥] Chaidir Chaidir,[∥] Werner E. G. Müller,[○] Matthias U. Kassack,[§] Christoph Janiak,[#] Georgios Daletos,[*,†] and Peter Proksch[*,†]

[†]Institute of Pharmaceutical Biology and Biotechnology, Heinrich Heine University Düsseldorf, Universitätsstrasse 1, 40225 Düsseldorf, Germany

[‡]Department of Pharmacy, Faculty of Mathematic and Natural Sciences, Udayana University, 80361 Bali, Indonesia

[§]Institute of Pharmaceutical and Medicinal Chemistry, Heinrich Heine University Düsseldorf, Universitätsstrasse 1, 40225 Düsseldorf, Germany

[⊥]Department of Organic Chemistry, University of Debrecen, P.O.B. 400, 4002 Debrecen, Hungary

[#]Institute of Inorganic Chemistry and Structural Chemistry, Heinrich Heine University Düsseldorf, Universitätsstraße 1, 40225 Düsseldorf, Germany

[∥]Center for Pharmaceutical and Medical Technology, Agency for the Assessment and Application Technology, 10340 Jakarta, Indonesia

[○]Institute of Physiological Chemistry, Universitätsmedizin der Johannes Gutenberg-Universität Mainz, Duesbergweg 6, 55128 Mainz, Germany

Supporting Information

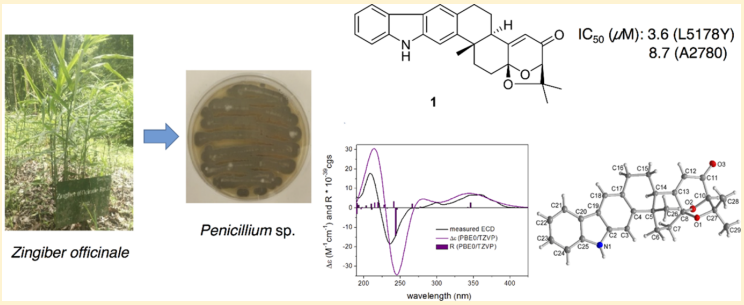

ABSTRACT: A chemical investigation of the endophyte *Penicillium* sp. (strain ZO-R1-1), isolated from roots of the medicinal plant *Zingiber officinale*, yielded nine new indole diterpenoids (**1**−**9**), together with 13 known congeners (**10**−**22**). The structures of the new compounds were elucidated by 1D and 2D NMR analysis in combination with HRESIMS data. The absolute configuration of the new natural products **1**, **3**, and **7** was determined using the TDDFT-ECD approach and confirmed for **1** by single-crystal X-ray determination through anomalous dispersion. The isolated compounds were tested for cytotoxicity against L5178Y, A2780, J82, and HEK-293 cell lines. Compound **1** was the most active metabolite toward L5178Y cells, with an IC_{50} value of 3.6 μM, and an IC_{50} against A2780 cells of 8.7 μM. Interestingly, **1** features a new type of indole diterpenoid scaffold with a rare 6/5/6/6/6/6/5 heterocyclic system bearing an aromatic ring C, which is suggested to be important for the cytotoxic activity of this natural product against L5278Y and A2780 cells.

Filamentous fungi (e.g., *Penicillium*, *Aspergillus*, and *Fusarium* sp.) are important producers of structurally unusual natural products with pharmaceutical potential.[1] Since the discovery of the antibiotic penicillin G from *Penicillium notatum*, fungi belonging to this genus have gained considerable attention with regard to their secondary metabolites and proved to be prolific sources of bioactive compounds. The discovery of the antifungal compound griseofulvin from *P. griseofulvum*, of the cholesterol-lowering agent compactin produced by *P. citrinum*, and of the immunosuppressant agent mycophenolic acid, isolated from *P. brevicompactum*, represents further success stories leading to important therapeutically used molecules from this genus.[1−5]

In our search for new bioactive compounds from fungal sources, we investigated *Penicillium* sp. (strain ZO-R1-1), an endophytic fungus isolated from the medicinal plant *Zingiber officinale* (Zingiberaceae) collected in Indonesia. Rhizomes of

Received: August 26, 2018
Published: May 22, 2019

DOI: 10.1021/acs.jnatprod.8b00723
J. Nat. Prod. 2019, 82, 1412−1423